



降雨と地震動を受ける火山灰盛土の安定性評価

メタデータ	言語: English 出版者: 公開日: 2023-12-11 キーワード (Ja): キーワード (En): 作成者: グェン, チョン ナム メールアドレス: 所属:
URL	https://doi.org/10.15118/0002000161

MURORAN INSTITUTE OF TECHNOLOGY
Graduate School of Engineering

**STABILITY EVALUATION OF VOLCANIC
EMBANKMENTS SUBJECTED TO
SEISMIC LOADINGS AND RAINFALL**

NGUYEN TRONG NAM

Stability Evaluation of Volcanic Embankments Subjected to Seismic Loadings and Rainfall

By

Nguyen Trong Nam

A dissertation submitted in partial fulfillment of the requirements for the degree of Doctor of Engineering

Examination Committee:
Professor Shima Kawamura

Professor Yukihiro Kohata

Professor Katsutoshi Kimura

MURORAN INSTITUTE OF TECHNOLOGY

August 2023

ABSTRACTS

This study aims to investigate the mechanical behavior of embankments constructed from volcanic soil under the independent and combined effect of rainfall and seismic loadings. To accomplish this purpose, a series of 1g model experiments on embankments were conducted with an apparatus that integrated both the spray nozzle and the shaking table. The soil samples were prepared using Komaoka volcanic coarse-grained soils as materials with 3 different amounts of fine particle contents ($K_{8.5A}$, K_{soil} , K_{40A}) while the initial water content was chosen at 0.9 (dry cases) and 1.1 (wet cases) of optimum water content. In the experiments, shear strain, acceleration, pore water pressure, and saturation degree were monitored and measured to provide an understanding of the influence of different fine particle contents and initial water content on the failure mechanism of the volcanic embankment subjected to rainfall and earthquake. In post-rainfall earthquake tests, the seismic loadings were applied at 3 different conditions of pore water pressure inside the embankments to clarify the effect of dissipation time between rainfall and earthquake. The results of post-rainfall earthquake cases in this study were compared with those in the cases of post-earthquake rainfall in previous research to investigate the importance of the order impact of external forces. The physical model test results were also compared with previous research including element tests and disaster reports. Besides, modern techniques of artificial intelligence were applied to predict the water retention characteristics of volcanic slopes.

The results show that the previous rainfall plays an important role in evaluating the stability of embankments under subsequent earthquakes through water retention conditions inside the slope such as rainfall-induced residual pore water pressure and saturation degree. The fine particle content has a great influence and must be taken into account when studying the stability of the volcanic embankment under the independent or combined effects of rainfall and earthquake. At the same degree of compaction, the permeability of volcanic soils decreases with the increase in the fine grain content. The earthquake resistance of the compacted volcanic embankments subjected to previous rainfall increases as the fine content increases. Even so, this increment in seismic strength is not significant when the fines content is higher than 27%. Initial water content has a great influence on the mechanical behavior, infiltration characteristics, and failure phenomenon of embankments due to rainfall and/or earthquakes. The permeability of the compacted soil on the wet side of the optimum moisture content is less than it is on the dry side when the fine grain content of the soil is sufficiently large. In contrast, embankments compacted on the wet side exhibit less resistance to subsequent earthquakes under the same shear strain due to previous rainfall. When embankments are subjected to dual disasters, the slope stability may vary for different orders of earthquake and rainfall even though the preceding received shear strain is similar. Finally, a simple method to evaluate slope stability in practice with the measured water content as the object of assessment was proposed based on the change in soil infiltration capacity. Machine learning models can be applied to predict pore water pressure values from historical data. Daily updates of the dataset and the climate data can significantly improve prediction accuracy.

TABLE OF CONTENTS

ABSTRACTS	i
TABLE OF CONTENTS.....	ii
LIST OF FIGURES	iv
LIST OF TABLES	ix
CHAPTER 1: INTRODUCTION.....	1
1.1 Overview of the research topic	1
1.2 Objectives and purpose of the research	5
1.3 Thesis outline.....	6
CHAPTER 2: LITERATURE REVIEW	9
2.1 Introduction	9
2.2 Definitions and classifications.....	9
2.3 Overview of model tests in geotechnical engineering.....	13
2.4 Previous studies on the failure of embankments caused by rainfall and earthquake	14
2.4.1 Independent effect of earthquake or rainfall	14
2.4.2 Studies on the combined effect of rainfall and earthquake	20
2.5 Research of physical and mechanical properties of volcanic soils.....	38
2.6 Summary.....	41
CHAPTER 3: SOIL MATERIALS AND TESTING METHODS	43
3.1 Introduction	43
3.2 Test materials	43
3.3 Test apparatus and procedures	47
3.3.1 Test equipment	47
3.3.2 Model embankment preparation.....	51
3.3.3 Test conditions	52
3.3.4 Similarity laws of model tests	55
3.3.5 Test procedures	60
3.4 Summary.....	60
CHAPTER 4: PHYSICAL MODEL TEST RESULTS AND ANALYSIS	62
4.1 Introduction	62
4.2 Influence of initial water content and fines content on the stability of volcanic embankments under rainfall and earthquake	62
4.2.1 Effect of fines content on slope stability during rainfall	63
4.2.2 Failure of embankments with different fine contents under post-rainfall earthquake	72
4.3 Effect of dissipation time between rainfall and earthquake	81

4.4 Effects of different orders of rainfall and earthquakes on slope failures.....	86
4.5 Summary.....	88
CHAPTER 5: DISCUSSIONS ON STABILITY EVALUATION OF VOLCANIC SLOPES	89
5.1 Introduction	89
5.2 Model test results in comparison with previous research.....	89
5.3 Stability evaluation method.....	91
5.4 Prediction of water retention characteristic of Komaoka soil	94
5.4.1 Pore water pressure forecasting.....	94
5.4.2 Water content prediction based on soil images	121
5.5 Summary	128
CHAPTER 6: CONCLUSIONS AND SUGGESTIONS	129
6.1 Introduction	129
6.2 Conclusions	129
6.3 Suggestions for future research	130
ACKNOWLEDGEMENT	131
REFERENCES	132

LIST OF FIGURES

Figure 1.1 Damage situation in Sapporo city in the 2018 Hokkaido Eastern Iburi Earthquake (from the report of JGS)	2
Figure 1.2 Test scheme and flow of discussions	6
Figure 1.3 Research outline	7
Figure 2.1 Distributions of volcanic soils deposited in Hokkaido (Matsumura (2014) [43])	10
Figure 2.2 The standard structure for embankments and cut slopes of expressways specified by Nexco Research Institute (2012) [54]	11
Figure 2.3 Typical model shapes (60- and 65-degree slopes) and setting positions of measurement devices (Kawamura and Miura (2013) [27]).....	15
Figure 2.4 The typical shape of failed slope for Komaoka volcanic soil: (a) 45-degree slope and (b) 65-degree slope (Kawamura and Miura (2013) [27]).	15
Figure 2.5 The behavior of pore water pressure during model tests for Komaoka volcanic slopes: (a) 45-degree slope and (b) 65-degree slope (Kawamura and Miura (2013) [27]).	16
Figure 2.6 Failed shapes of slopes subjected to rainfall (a) $w_0=34\%$ (side view), (b) $w_0=38\%$ (side view), (c) $w_0=43\%$ (side view), (d) $w_0=43\%$ (cross view) (Kawamura and Miura (2014a) [29]).	16
Figure 2.7 Deformation behavior at failure for Komaoka volcanic slope (a) $w_0=34\%$, (b) $w_0=38\%$, (c) $w_0=43\%$ (Kawamura and Miura (2014a) [29]).	17
Figure 2.8 Changes in the saturation degree during rainfall (a) $w_0=38\%$, (b) $w_0=43\%$ (Kawamura and Miura (2014a) [29]).	17
Figure 2.9 Changes in pore water pressure during rainfall (a) $w_0=38\%$, (b) $w_0=43\%$ (Kawamura and Miura (2014a) [29]).	17
Figure 2.10 Slope shape after cyclic loadings of 280gal: (a) $w_0=37\%$, (b) $w_0=43\%$ (Kawamura and Miura (2014a) [29]).	18
Figure 2.11 Variation of accelerations in the basement, the crown of the embankment, and shaking table (a) $w_0=37\%$ (b) $w_0=43\%$ (Kawamura and Miura (2014a) [29]). ..	19
Figure 2.12 Changes in pore water pressure during shaking table test: (a) $w_0=37\%$, (b) $w_0=43\%$ (Kawamura and Miura (2014a) [29]).	19
Figure 2.13 Frequency of each type of landslide (A) slope location (B) slope angle (Wang et al., (2004) [82])......	21
Figure 2.14 Different types of landslides in each satellite image (Lin et al., (2006) [39]).	21
Figure 2.15 Intensity–duration graph for five debris flow events in the Wenjia torrent compared with previous research (Tang et al., (2012) [71]).	23
Figure 2.16 Debris-flow formation process (Guo et al., (2021) [11]).	25
Figure 2.17 Failure situation of volcanic ashes bank at Kami-Metoki (Mishima and Kimura (1970) [49]).	26
Figure 2.18 Aerial view of earthquake-induced landslides in Miyagi, Japan in 2003 (A) Dateshita landslide, (B) Nishisaruta landslide (Uzuoka et al., (2005) [79]).	27
Figure 2.19 The Higashi Takezawa landslide and the head scarp of previous landslides (Sassa et al., (2006) [62]).	28

Figure 2.20 Decrease in Factor of Safety with Peak Ground Acceleration of the earthquake at different values of r_u (Tuladhar et al., (2007) [77]).	29
Figure 2.21 Rainfall record at the nearest station from the 2006 Leyte landslide (Sassa et al., (2007) [63]).	30
Figure 2.22 Concept of the stress-controlled dynamic-loading ring-shear apparatus (Sassa et al., (2007) [63]).	30
Figure 2.23 Horizontal and vertical displacement at slope crown (a) (d) Rainfall, (b) (e) Earthquake, (c) (f) Rainfall – Earthquake (Vickneswaran and Ravichandran (2020) [80]).	32
Figure 2.24 Movement of wetting fronts and seepage velocity of rainwater (a) post-earthquake rainfall test, (b) rainfall-only test (Tiwari et al., (2017a) [75]).	33
Figure 2.25 Variation of suction (a) post-earthquake rainfall test, (b) rainfall-only test (Tiwari et al., (2017a) [75]).	33
Figure 2.26 Comparison of safety factors in post-earthquake rainfall test and rainfall-only test (Tiwari et al., (2017a) [75]).	34
Figure 2.27 Comparison of safety factors in post-earthquake rainfall test and rainfall-only test (Tiwari et al., (2017b) [76]).	35
Figure 2.28 Changes in pore water pressure and saturation degree during rainfall test after cyclic loadings for $w_0=37\%$: (a) pore water pressure, (b) saturation degree (Kawamura and Miura (2014a) [29]).	36
Figure 2.29 Schematics of failed slope shape for $w_0=37\%$ (Kawamura and Miura (2014a) [29]).	36
Figure 2.30 Changes in pore water pressure and saturation degree during rainfall test after cyclic loadings for $w_0=43\%$: (a) pore water pressure, (b) saturation degree (Kawamura and Miura (2014a) [29]).	36
Figure 2.31 Required time until slope failure (Kawamura and Miura (2014a) [29]).	37
Figure 2.32 Changes in saturation degree in the embankment after 3 hours of rainfall (Tiwari et al., (2013) [73]).	38
Figure 2.33 Changes in cohesion with saturation degree (Tiwari et al., (2013) [73]).	38
Figure 2.34 Piping test results of Komaoka volcanic soils: (A) piping, (B) boiling (Dao (2018) [7]).	39
Figure 2.35 Change in results of Ksoil with different compaction degrees (a) velocity (b) hydraulic conductivity (Dao (2018) [7]).	39
Figure 2.36 Piping test results of Komaoka volcanic soil (A) velocity (B) hydraulic conductivity (Dao (2018) [7]).	41
Figure 2.37 Changes in the increment of finer content ΔFc after rainfall test (Kawamura and Miura (2014a) [29]).	41
Figure 3.1 Locations of sampling and monitoring site of embankment in this study	44
Figure 3.2 Grain size distribution of test samples in this study, according to [23].	45
Figure 3.3 Compaction curve of test samples in this study, according to the A-b method [16].	46
Figure 3.4 Influence of fines contents on compaction features of Komaoka volcanic soil (A) optimum water content w_{opt} , (B) and maximum dry density $\rho_{d max}$.	46

Figure 3.5 Maximum and minimum void ratio of Komaoka volcanic soils with different fine particle contents.....	47
Figure 3.6 Overall view of test apparatus in this study. (A) Overall view (B) Side view (C) Front view (D) 1-dimensional vibration loading device (E) Spray nozzle.	48
Figure 3.7 Measuring devices in this study (A) Pore water pressure transducer (B) Soil moisture meter (C) Acceleration meter	49
Figure 3.8 Soil-water characteristics curve of Komaoka volcanic soil [43]	50
Figure 3.9 Shape and dimensions of model embankments and setting positions of measuring instruments.....	51
Figure 3.10 The initial shape of the model embankments (A) front view (B) side view....	51
Figure 3.11 Slope preparation (A) Kite strings and side aluminum sashes (B) Excessive soil removal	52
Figure 3.12 Adjusted compaction curves and test conditions	53
Figure 3.13 Relationship between permeability and initial water content (Dao (2018) [7] and Matsumura (2014) [43])	53
Figure 3.14 Stress-strain relationship between prototype and model (Rocha (1957) [61])	55
Figure 3.15 Consolidated undrained triaxial test results of Komaoka volcanic soils	58
Figure 3.16 Test concept for 1g model test	59
Figure 4.1 Sieving test areas in this study.	63
Figure 4.2 Changes in saturation degree during rainfall tests (A) $K_{8.5A}$, (B) K_{soil} , and (C) K_{40A} (dry cases)	64
Figure 4.3 Water content distribution inside model embankments during and after rainfall tests (A) $K_{8.5A}$, (B) K_{soil} , and (C) K_{40A} (dry cases)	66
Figure 4.4 Change in pore water pressure during rainfall tests (A) $K_{8.5A}$, (B) K_{soil} , and (C) K_{40A} (dry cases)	66
Figure 4.5 Change in rainfall-induced shear strain (dry cases) (A) Shear strain changed with time (B) Shear strain changed with fines content.....	67
Figure 4.6 Rainfall-induced failure type of model embankments (A) $K_{8.5A}$ and (B) K_{40A} (dry cases).....	68
Figure 4.7 Grains distribution of Komaoka soils (A) $K_{8.5A}$, (B) K_{40A}	68
Figure 4.8 Change in pore water pressure during rainfall tests (A) $K_{8.5A}$, (B) K_{soil} , and (C) K_{40A} (wet cases).....	69
Figure 4.9 Changes in saturation degree during rainfall tests (A) $K_{8.5A}$, (B) K_{soil} , and (C) K_{40A} (wet cases).....	70
Figure 4.10 Change in rainfall-induced shear strain (wet cases) (A) Shear strain changed with time (B) Shear strain changed with fine content	71
Figure 4.11 Changes in the mechanical and physical behavior of volcanic soils with water content (A) dry density, (B) shear Strength, (C) and permeability [30].....	71
Figure 4.12 Variation in accelerations during earthquakes at shaking table and basement, the crown of embankments subjected to rainfall (A) $K_{8.5A}$, (B) K_{soil} , (C) K_{40A} (dry cases).....	73
Figure 4.13 Changes in saturation degree during post-rainfall earthquake tests (A) $K_{8.5A}$, (B) K_{soil} , and (C) K_{40A} (dry cases).....	74

Figure 4.14 Water content distribution inside model embankments during and after post-rainfall earthquake tests (A) $K_{8.5A}$, (B) K_{soil} , and (C) K_{40A} (dry cases).....	75
Figure 4.15 Pore water pressure during seismic loadings	75
Figure 4.16 Changes in pore water pressure during post-rainfall earthquake tests (A) $K_{8.5A}$, (B) K_{soil} , and (C) K_{40A} (dry cases).....	77
Figure 4.17 The earthquake-induced shear strain of embankments subjected to previous rainfall (dry cases) (A) Shear strain changed with number of cycles (B) Shear strain changed with fines content	77
Figure 4.18 Changes in pore water pressure during post-rainfall earthquake tests (A) $K_{8.5A}$, (B) K_{soil} , and (C) K_{40A} (wet cases).....	79
Figure 4.19 Changes in saturation degree during post-rainfall earthquake tests (A) $K_{8.5A}$, (B) K_{soil} , and (C) K_{40A} (wet cases).....	80
Figure 4.20 The earthquake-induced shear strain of embankments subjected to previous rainfall (wet cases) (A) Shear strain changed with number of cycles (B) Shear strain changed with fines content	80
Figure 4.21 Earthquake-induced failure type of model embankments subjected to rainfall (A) $K_{8.5A}$, (B) K_{40A} (wet cases).....	81
Figure 4.22 Changes in pore water pressure and saturation degree in the case of (i) (A) Dry case (B) Wet case	82
Figure 4.23 Changes in pore water pressure and saturation degree in the case of (ii) (A) Dry case (B) Wet case	83
Figure 4.24 Changes in pore water pressure and saturation degree in the case of (iii) (A) Dry case (B) Wet case	84
Figure 4.25 Model embankment at failure (A) case (i) (B) case (iii).....	85
Figure 4.26 Relationship between seismic failure time ratio and rainfall-induced shear strain in different conditions of pore water pressure (Dry case)	86
Figure 4.27 Relationship between failure time ratio and shear strain generated by previous external forces (A) Dry cases (B) Wet cases.....	87
Figure 5.1 Typical variation in the saturation degree during rainfall tests in this study.	91
Figure 5.2 Diagram of soil infiltration capacity during rainfall based on Horton's concept (Horton (1939) [17]).....	91
Figure 5.3 Relationship between water content at initial and failure conditions for Komaoka volcanic soil.	93
Figure 5.4 Full-scale cut slopes and embankments	96
Figure 5.5 Locations of monitoring instruments of cut slopes	96
Figure 5.6 Measured data of cut slope (A) Air temperature (B) Rainfall amount (C) Snow depth (D) Water content (E) Pore water pressure	98
Figure 5.7 Train-Test split	99
Figure 5.8 Time series data components	99
Figure 5.9 Moving average plot of pore water pressure data	100
Figure 5.10 Seasonal plot of pore water pressure data	101
Figure 5.11 Seasonality regressed by Month indicator	101

Figure 5.12 Seasonality regressed by Fourier features (A) 16 features (B) 4 features (C) 2 features	102
Figure 5.13 Periodogram of pore water pressure	103
Figure 5.14 Lag plots of pore water pressure	104
Figure 5.15 Partial Autocorrelation plot of pore water pressure	104
Figure 5.16 Results in long-term forecasting	109
Figure 5.17 Forecasting results with daily updated data	114
Figure 5.18 Forecasting results with daily update data and climate data	117
Figure 5.19 Forecasting results with only climate data	120
Figure 5.20 Komaoka volcanic soil (A) Wet condition (B) Dry condition.....	121
Figure 5.21 Artificial Neural Networks (ANN) and Convolutional Neural Networks (CNN)	122
Figure 5.22 Transfer learning mechanism for deep learning in this study.....	122
Figure 5.23 VGG16 architecture	123
Figure 5.24 Resnet architecture	123
Figure 5.25 Inception architecture.....	124
Figure 5.26 Training process (A) Case A (B) Case B (C) Case C	125
Figure 5.27 Test results in different input image dimensions	127
Figure 5.28 Example of prediction results	127

LIST OF TABLES

Table 1.1 Recent rainfall- and earthquake-induced failures of volcanic slopes in Hokkaido, Japan (Kawamura et al., (2019) [32]).....	3
Table 2.1 Geotechnical classification for volcanic soils by JGS Hokkaido (2011) [25]	10
Table 3.1 Physical properties of Komaoka volcanic soil and Touyouura sand.....	44
Table 3.2 Physical properties of test samples in this study.	45
Table 3.3 Soil particle density of each grain size [43].	47
Table 3.4 Specifications of the shaking table used in this study	47
Table 3.5 Specification of measuring devices in this study	50
Table 3.6 Test conditions to clarify the effect of finer contents.....	54
Table 3.7 Test conditions to clarify the effect of impact order of external force	55
Table 3.8 Similarity laws applied in 1g model experiments where the prototype soils are used as test materials	58
Table 3.9 Similarity laws were applied in this study.....	59
Table 4.1 Fines content inside embankment after 30 minutes of rainfall (dry cases)	63
Table 5.1 Values of β and γ in this study.....	93
Table 5.2 Case definition and results	111
Table 5.3 Feature importance of forecasting with daily update data and climate data	114
Table 5.4 Feature importance in the case of Forecasting with only climate data.....	120
Table 5.5 Test conditions	125
Table 5.6 Test results in different models	127

INTRODUCTION

1.1 Overview of the research topic

In recent times, temperatures and precipitation have both broken new records almost every year in Japan and throughout the world. Global warming caused by climate change has increased the number of natural disasters; and dual disasters, thus, have become more common. In particular, rainfall, when combined with other effects such as cyclic loadings or freeze-thaw actions, will cause more unpredictable consequences. That complex effect for natural or artificial soil structures has long been recognized. For example, Terzaghi (1950) [72] stated that rainfall is rarely the sole reason for failure on a long-standing slope that has experienced many heavy rainstorms in the past. Although some research has been made on the influence of dual disasters on soil structures using element tests such as triaxial experiments, studies based on the results of model tests are still quite restricted. Thanks to its ability to simulate real conditions and phenomena, the model is widely applied in the study of all geotechnical problems, especially complex mechanisms such as the impact of double disasters. Similar to other topics, the failure of embankments subjected to post-earthquake rainfall has been investigated by model experiments as in some recent studies [21, 32, 83]. This fact raises the need to use model tests to study slope stability under the effect of post-rainfall earthquakes.

Among dual hazards, post-rainfall earthquakes are not uncommon in the past and have always caused large landslides, such as the 1968 Tokachi-oki earthquake and the 2004 Niigata Chuetsu earthquake. Moreover, earthquakes that occurred after typhoons are always among the costliest disasters, such as Typhoon Hagibis in 2019, or Typhoon Jebi in combination with the 2018 Hokkaido Eastern Iwate earthquake (see Figure 1.1). The effect of the catastrophic ground disaster in 2018 was reported in the following literature. Kawamura et al., (2019) [32] analyzed the large-scale slope failure/landslide in the towns of Atsuma and Abira; including slope failure for a gentle slope, surface slope failure, river blockage, and rock slide. Besides, the mechanical and physical characteristics of the collapsed pyroclastic fall deposits spread over this area were also presented. As for the

Sapporo city area, Ishikawa et al., (2021) [21] found cracks and subsidence in the road system after the 2018 earthquake, which were not noticed in the 2003 Tokachi earthquake with a higher magnitude. According to the hypotheses of the authors, these differences in damage scenarios between two large disasters may be caused by Typhoon Jebi which occurred before the 2018 earthquake, raising groundwater levels. Similarly, Watabe and Nishimura (2020) [83] reported the liquefaction disaster caused by the 2018 earthquake in the Satozuka district where the valley was filled with Spfl pumice sand deriving from the Lake Shikotsu caldera. The effect of previous rainfall was also considered a potential factor in the scenario of the liquefaction phenomenon that occurred in Sapporo. These disaster reports posed the need to experimentally verify the influence of antecedent rainfall on the earthquake resistance of embankments. Through lessons learned from this double disaster that occurred in Hokkaido in 2018, Ishikawa et al., (2021) [21] proposed future research directions for geotechnical engineering in general and geo-disaster prevention, particularly mitigation administration. One of these is the assessment of the liquefaction risk which needs to take into account the influence of rainfall and the rise of groundwater levels due to climate change. Moreover, rainfall-induced sedimentary disaster warning maps also need to be appropriately adjusted to the occurrence of earthquakes and the peculiarity of the material properties of crushable weathered volcanic soils.

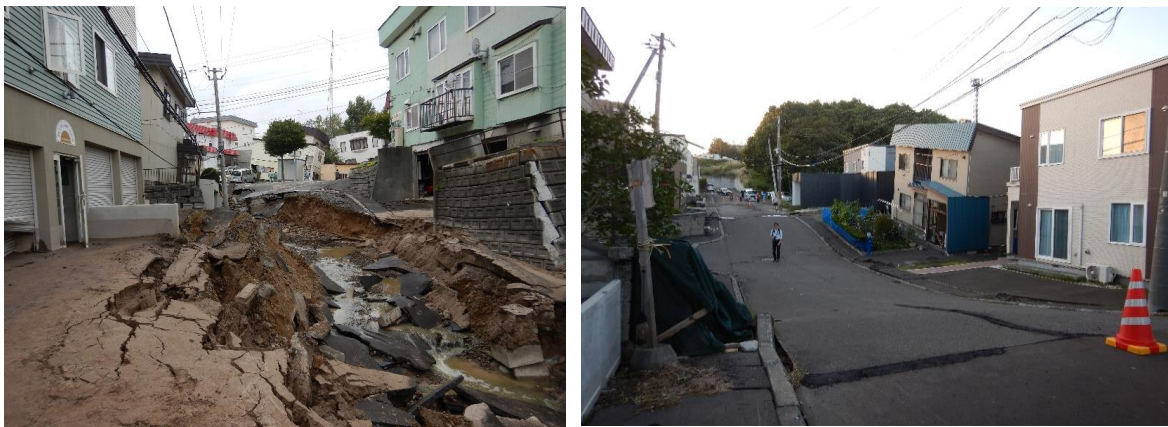


Figure 1.1 Damage situation in Sapporo city in the 2018 Hokkaido Eastern Iburi Earthquake (from the report of JGS)

Volcanic soils (pyroclastic fall deposits or pyroclastic flow deposits) are widely encountered in many countries around the world and they underlay the surface geology in several areas of high population density, which makes an understanding of their geotechnical properties of great importance. In nature, volcanic soils are often able to support slopes with high angles under normal conditions. This advantage makes it be utilized as a useful construction material, especially manmade earth structures such as road embankments or plots for housing. In Hokkaido, Japan, there are over forty Quaternary volcanoes, and

pyroclastic materials occupy about 40% of the land area. However, these natural or artificial slopes are susceptible to sudden and catastrophic failure, which leads to sediment-related disasters such as slope failures, landslides, debris flows, etc. For example, Table 1.1 shows the failures of volcanic grounds and slopes due to rainfall and earthquakes in Hokkaido over the past five decades.

Table 1.1 Recent rainfall- and earthquake-induced failures of volcanic slopes in Hokkaido, Japan (Kawamura et al., (2019) [32])

Time	Disasters	Amount of rainfall	Magnitude for JMA	Disaster type	Origin of volcanic soil
1968/5/16	Tokachi-oki earthquake	-	7.9	Liquefaction	Shikotsu pumice flow deposits
1973/9/23~24	Heavy rainfall	268mm	-	Slope failure	Komagatake fall deposits
1975/8/23	Typhoon 6th	Not clear	-	Slope failure	Komagatake fall deposits
1979/10.2	Typhoon 10th	191mm	-	Slope failure	Komagatake fall deposits
1980/8/28~31	Iburi-Heavy rainfall	600mm	-	Slope failure	Kuttara flow deposits
1990/11/5	Heavy rainfall	195mm	-	Slope failure	Komagatake fall deposits
1993/1/15	Hokkaido Kushiro-oki earthquake	-	7.8	Slope failure	Pumice flow deposits
		-		Slope failure	Kusharo pumice flow deposits
1993/7/12	Hokkaido Nansei-oki earthquake	-	7.8	Liquefaction	Komagatake flow deposits
1994/10/4	Hokkaido Toho-oki earthquake	-	8.2	Slope failure	Pumice flow deposits
1998/9/16	Typhoon 5th	305mm	-	Slope failure	Komagatake fall deposits
1999/4/13	Rainfall after freezing and thawing	380mm (including snow-melting water)	-	Slope failure	Toya pumice flow deposits, Setana formation, etc.
2000/10/3	Heavy rainfall	201mm	-	Debris flow	Komagatake fall deposits
2003/9/26	Tokachi-oki earthquake	-	8.0	Slope failure	Kusharo pumice flow deposits
		-		Liquefaction	Shikotsu pumice flow deposits
2006/8/18~19	Typhoon 10th	425mm	-	Slope failure, Debris flow	Shikotsu, Tarumae, Eniwa fall deposits
2014/9/10~11	Heavy rainfall	335mm	-	Slope failure, Debris flow	Shikotsu, Tarumae, Eniwa fall deposits
2018/9/6	Hokkaido Eastern Iburi earthquake		6.7	Liquefaction, Slope failure	Shikotsu, Tarumae, Eniwa fall deposits

As shown in Table 1.1, it can be seen that volcanic ground and slopes witnessed the most severe damage caused by geological disasters in the Hokkaido region. The failures are caused by the inexplicable performance and topography of volcanic soils which cannot be

discussed in the same category as conventional soils. For these reasons, volcanic soil is difficult to design or construct and is known as problematic soil in the field of conventional engineering. Moreover, volcanic activity is the source of this soil formation and is also one of the causes of earthquakes. As a result, sediments tend to be found in earthquake-prone countries like Japan. It should be mentioned that the damage to structures, such as roads and bridges, was minor in comparison to past earthquakes in Japan. Thus, an undesirable scenario is that the post-rainfall earthquake as discussed above could occur again in the future in Hokkaido. This situation requires an urgent need for comprehensive measures to prevent and mitigate natural disasters.

One of the existing problems with the coarse-grained volcanic soil of Hokkaido is that its fine content is easily altered by particle crushing when subjected to external factors such as consolidation, freeze-thawing, earthquakes, or compaction [20, 52]. In the above-mentioned report on the liquefaction disaster in the Satozuka district after the 2018 Hokkaido Eastern Iwate earthquake, to provide a reasonable scenario for the observed ground movements, Watabe and Nishimura (2020) [83] conducted physical and mechanical tests with soil samples prepared based on actual field conditions prior to the earthquake: the degree of compaction was 70–75%, compaction water content was 47.2%, and fine particles content was quite high of about 40%. Although a high fine-grained content may imply high seismic resistance to many geotechnical engineers, the results showed that the pumice fill was still highly susceptible to liquefaction. However, parametric studies have not been performed with different fine particles and initial water content to investigate their effect on the mechanical behavior of the soil. As can be seen, although the fine content of soils has a significant impact on the mechanical properties and hydraulic conductivity of cohesionless soils, its influence is currently ignored in design procedures. In addition, the use of the fine grains content increment as a degree of crushability, proposed by Miura and Yagi (1997) [50], has been widely applied. Therefore, assessing the effect of fine particle content is also synonymous with evaluating the influence of crushability. For these reasons, the study of the effects of fine particle content is widely performed by elemental experiments such as triaxial tests. Among these studies, Hieu et al., (2017) [16] evaluated the internal erosion and piping phenomenon of volcanic soil with different fine grain contents under the same dry density condition. However, regulations for backfill or embankments in design practice often focus on compaction degree rather than dry density. To simulate this fact, three samples of volcanic coarse-grained soil with different fine content were prepared for 1g model tests with the same degree of compaction but three different void ratios.

Besides natural disasters, the rapid development of the economy is putting heavy pressure on the natural environment and infrastructure system. Therefore, an important factor in ensuring sustainable development is the effective working of early warning systems. The experimental results in this study indicated that soil water retention characteristics such

as moisture content and pore water pressure play an important role in the evaluation of embankment stability. However, it is impossible to monitor these data in all locations at all times. This leads to the need to constantly improve and upgrade predictive models. Soil mechanics theory and geotechnical software used in analysis and design always contain human biases. In contrast, artificial intelligence models cannot focus on evaluating phenomena because they only include numerical inputs and outputs. So there may be problems these models detect while we do not. For that reason, forecasting techniques need to apply machine learning to make up the bigger picture. The determination of soil moisture currently requires the use of an oven and takes about 1 day. However, in cases where high accuracy is not required, it is very convenient to determine the water content immediately based on the image of the soil. In recent times, computer vision technology has been driven by the development of deep learning, another application of artificial intelligence. This fact facilitates the application of these techniques in moisture prediction based on soil images.

1.2 Objectives and purpose of the research

With the analysis of the actual situation in section 1.1, it is necessary to study "Stability Evaluation of Volcanic Embankments Subjected to Seismic Loadings and Rainfall". To achieve the research purpose, the thesis has solved the following specific objectives:

- ① Using the physical model test to clarify the mechanical behavior of the volcanic embankments under the independent and combined effects of rainfall and earthquake at different initial conditions such as water content, fine particle content, etc.
- ② Compare model test results with previous research including element test results and disaster reports
- ③ Proposing a method to evaluate the stability of volcanic embankments based on experimental results and modern techniques

In this study, a series of 1g model tests were conducted using an apparatus that integrated both the spray nozzle and the shaking table. In the experiments, shear strain, acceleration, pore water pressure, and saturation degree were monitored and measured to provide an understanding of the failure mechanism of the model embankment under the independent and combined action of rainfall and seismic loadings. Samples of Komaoka volcanic coarse-grained soil in Hokkaido, Japan with three different fine contents were prepared at initial water contents on the dry and wet side of the optimum water content. In particular, the slope behavior under rainfall before the earthquake was compared with that in the case of the earthquake before rainfall to clarify the role of the order of external forces on the failure mechanism of the embankment. The test scheme and flow of discussions are illustrated in Figure 1.2.

Research method: This study used quantitative data (expressed in numbers) to produce generalizable knowledge about the mechanical behavior of volcanic slopes under

the effect of rainfall and subsequent earthquakes. The controlled experimental conditions will be carefully designed and fully documented in the study so that they can be replicated by other researchers. The primary data is collected by the author, and the secondary data (used for comparison) is collected by previous researchers. The existing data were obtained through the same experimental method as this study by previous researchers. The experimental data is gathered by controlling and manipulating variables while the field monitoring descriptive data by gathering observations without intervening.

Scope of this study: The samples used in this study are Komaoka volcanic coarse-grained soil from Hokkaido, Japan. The obtained results, discussions, and conclusions will extend to volcanic soils in particular and cohesionless soils in general. In terms of time, technique and method performed with the field monitoring results from 2012 to 2014 can be used for any other periods.

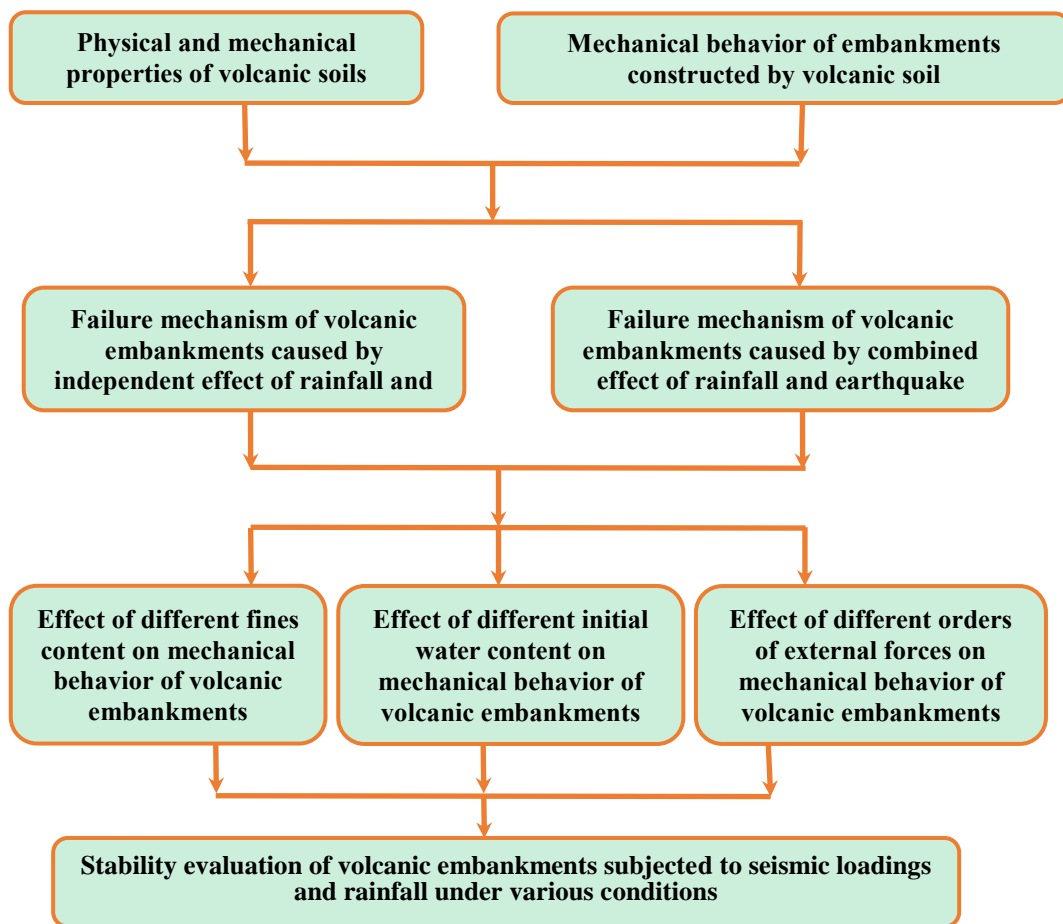


Figure 1.2 Test scheme and flow of discussions

1.3 Thesis outline

This thesis consists of six chapters as shown in Figure 1.3. The main contents of each chapter are briefly outlined as follows:

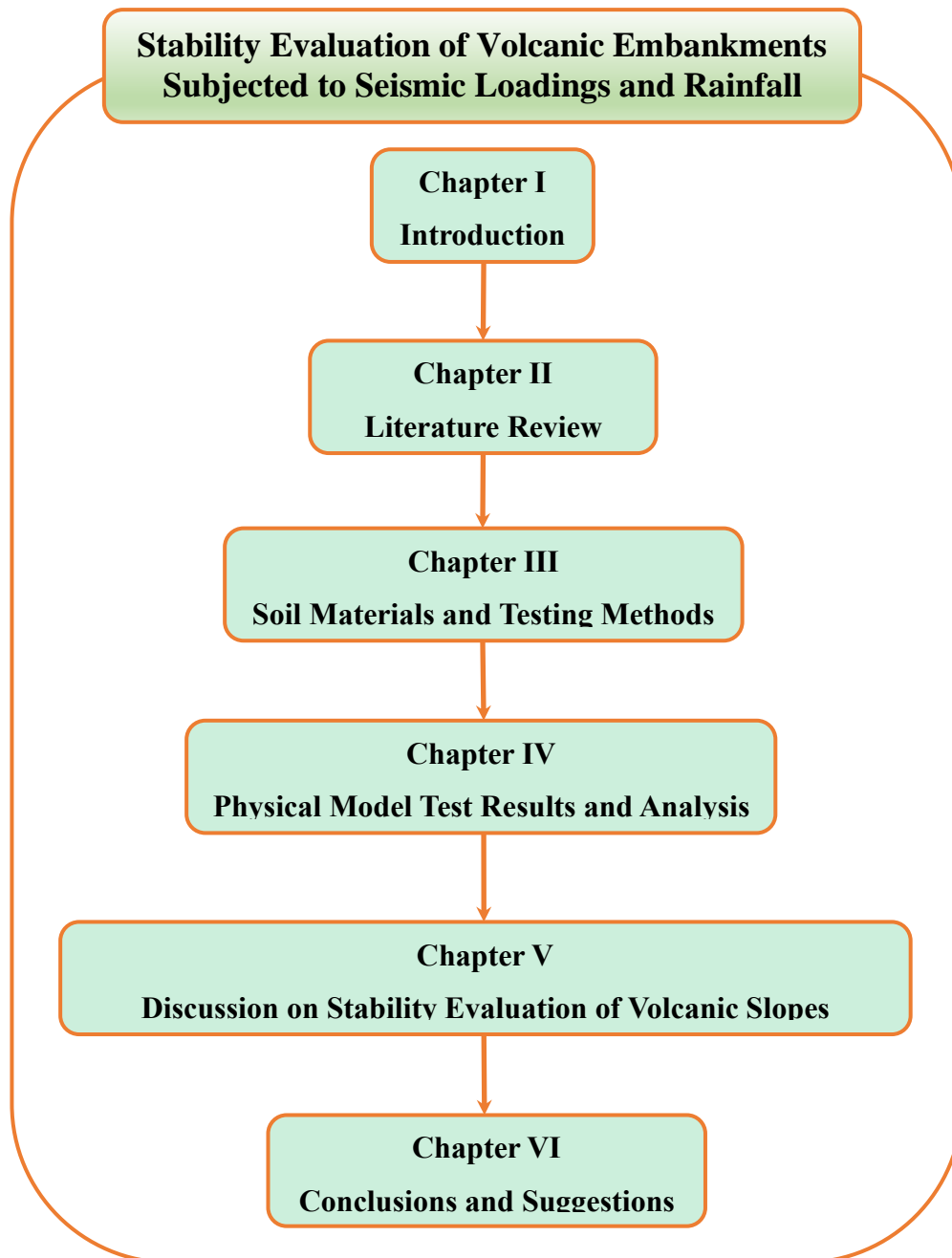


Figure 1.3 Research outline

- Chapter 1: Introduction

The current chapter introduces the topic of this study, its urgency as well as theoretical and practical implications. The general aims of the thesis are mentioned in its scope and limitations. The organization of the thesis is given to achieve the final goals.

- Chapter 2: Literature Review

The definitions used in the study and the failure mechanism of the embankments under earthquakes and rainfall are briefly presented in this chapter. Then, the author reviews previous studies investigating the effects of rainfall and earthquakes on slope stability,

especially research conducted using model experiments.

- Chapter 3: Soil Materials and Testing Methods

This chapter introduced the properties of the soil materials and the test apparatus used in the experiments of this study. Then sample preparation and testing procedures are reported so that the results can be reproduced.

- Chapter 4: Physical Model Test Results and Analysis

Based on the test samples, equipment, and procedures in the fourth chapter, the experimental results were presented and analyzed to show the influence of different conditions on the failure of the volcanic embankments under the independent and combined effect of rainfall and earthquakes.

- Chapter 5: Discussions on Stability Evaluation of Volcanic Slopes

In this chapter, the results of the model tests in Chapter 5 were compared with those of the element experiments and disaster reports. In addition, a method of assessing the stability of the embankment is proposed based on the trends obtained from the experimental results. The feasibility of applying machine learning in predicting the water content of volcanic soils was also presented.

- Chapter 6: Conclusions and Suggestions

The final chapter summarized the main results obtained in this study and discussed the suggestions and proposals in related fields. Finally, ideas for future research were also recommended.

LITERATURE REVIEW

2.1 Introduction

Due to the necessity and urgency presented in Chapter 1, the research problem has received the attention of authors around the world. Studies have been carried out using various methods and their current status is summarized in this chapter. First, general concepts related to this study were briefly defined and categorized. Then the development of the application of the modeling technique in geotechnical engineering is presented. Outstanding studies on the failure mechanism of embankments subjected to rainfall and/or earthquakes are summarized, especially studies based on the results of model experiments. Among the studies on slope stability under the effect of dual hazards, the remaining issues will be analyzed to highlight the content that this study wants to convey in the next chapters.

2.2 Definitions and classifications

Volcanic soils and distribution in Hokkaido, Japan

In geology, tephra is volcanic soil in a wide sense, which mainly refers to volcanic ash and pumice, which are solid elements included in volcanic gas produced by explosive volcano eruptions. In other words, tephra is clastic debris blasted by volcanoes and carried through the air, as opposed to lava. Tephra deposits are roughly classified into two classes based on the methods by which they originate, namely "pyroclastic fall deposits" (fa) and "pyroclastic flow deposits" (fl). The term "pyroclastic fall deposits" (fa) refers to the depositing product of volcanic ash and pumice created during the airborne transport of volcanic ejecta. Following an eruption with a volcanic column rising over the volcano, volcanic ash and pumice erupted and began descending to deposit on the ground when gravity and air resistance balanced. Then, because each volcanic product has a range of grain sizes and densities, those are chosen based on their proximity to the volcano. As a result, the grain size distribution in the Tephra fall deposit is very consistent. The phrase "pyroclastic flow deposits" (fl) denotes pumice, volcanic ash, and scoria yielded to gravity action generated by a flow or avalanche down the flank of a volcano. As a result, the pyroclastic flow deposit is often constituted of fine-grained soils.

Figure 2.1 depicts a distribution map of tephra deposits in Hokkaido, distinguishing between the tephra fall deposit and the pyroclastic flow deposit (Matsumura (2014 [43])). The sampling site of soils utilized in this study, Komaoka districts ((8) Shikotsu pyroclastic flow deposit), is also highlighted in the picture. It can be seen that the tephra fall deposits extend eastward across broad distances due to the westerlies, whilst the pyroclastic flow deposits remain closer to the volcanoes.

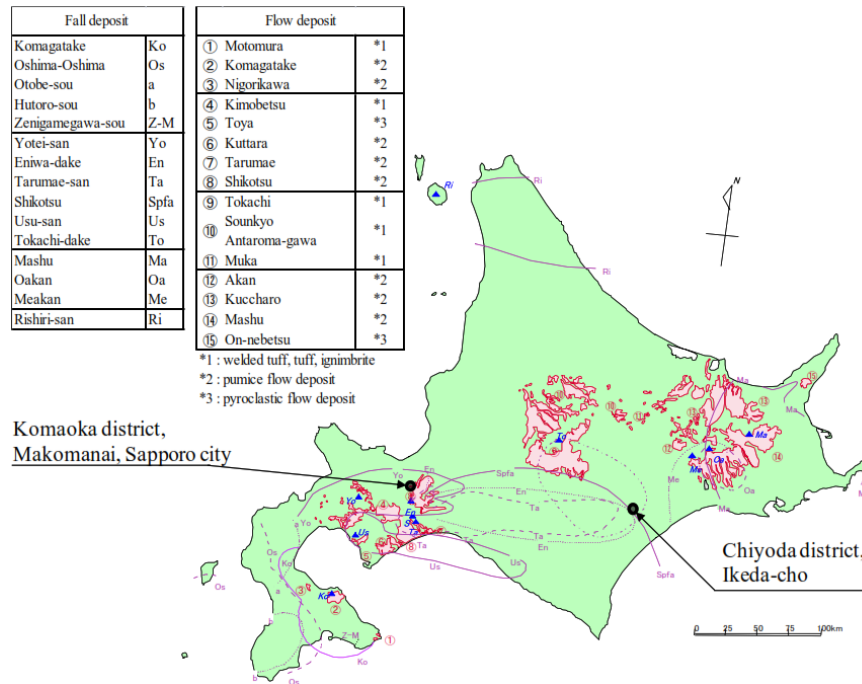


Figure 2.1 Distributions of volcanic soils deposited in Hokkaido (Matsumura (2014) [43])

Table 2.1 Geotechnical classification for volcanic soils by JGS Hokkaido (2011) [25]

Classification by Fines content F_c	$F_c \geq 50\%$: Fine-grained soil		$F_c < 50\%$: Coarse-grained soil	
	Volcanic cohesive soil {V}		Organic soil {O}	
	Low liquid limit (VL) $w_L > 50\%$		Organic, dark-colored soil with an organic smell	
	$50 < w_L < 80$	$w_L \geq 80$	$5\% \leq F_c < 15\%$	$15\% \leq F_c < 50\%$
	Type I (VH ₁)	Type II (VH ₂)	Organic-volcanic ash soil (OV)	(G-V, S-V) (GV, SV)
Classification by Stratum, Unusual soil, Local soil colloquial term	Shirasu		Kanto loam	Hachinohe loam
	(SV)		(VH ₁ , VH ₂)	(VL)

Apart from the producing method, sedimentary structure, components, distributional area, and degrees of weathering vary substantially with the depositional environment and influence the mechanical characteristics of volcanic soils. As stated in Table 2.1, the Hokkaido section of the Japanese Geotechnical Society (JGS) [25] also offers a geotechnical categorization of volcanic soils based on fines content F_c (%) ($< 75\mu\text{m}$) and liquid limit w_L , among other factors. In terms of fines content, through investigation of the property and application of volcanic soil in Hokkaido, JGS differentiated volcanic soils with $F_c < 50\%$ and $F_c \geq 50\%$ as "volcanic coarse-grained soil" and "volcanic fine-grained soil," respectively. Which, the volcanic coarse-grained soil is the primary or secondary sediment produced by volcanic ash, pumice, and scoria, whereas the volcanic fine-grained soil is the weathered volcanic coarse-grained soil. The term "primary sediment" refers to the product that falls and deposits following an eruption, whereas "secondary sediment" refers to the re-deposition of the primary sediment on the ground or in water as a consequence of gravity action or water movement.

Embankment

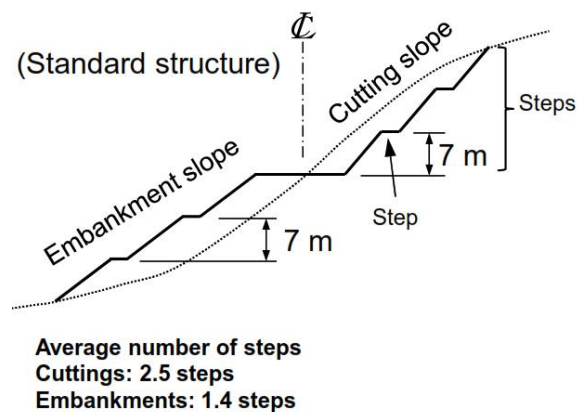


Figure 2.2 The standard structure for embankments and cut slopes of expressways specified by Nexco Research Institute (2012) [54]

In geology and geography, embankments may refer to:

- A levee: an artificial bank elevated above the nearby land that frequently follows a river's path in its floodplain or along low-lying beaches. Its goal is to prevent rivers from altering their course and to safeguard against floods in the region around the river or the shore.
- Fill dam: a sizable man-made dam that is often built by placing and compacting a complicated semi-plastic mound made of several types of soil or rock. It features a solid, impermeable core and a natural waterproof layer that is semi-permeable. This renders the dam resistant to seepage or surface erosion. Such a

dam is made up of separate material fragments. Instead of using a cementing agent, friction and particle contact combine the particles into a stable mass.

- Embankment in earthworks: a compacted earth structure built higher than the surrounding terrain to support a road, railway, or canal at the intended height through a low-lying or swampy area. In cases when the land was initially higher than needed, a cutting is employed for the same reason. An example of a standard structure for embankments and cut slopes in highways required by Nippon Expressway Company (Nexco) is shown in Figure 2.2.

Depending on the degree of direct water exposure and precipitation, the requirements for core material, surface, drainage system, ... in embankment design are different.

Slope stability and failure

Slope stability is the capacity of slopes that are inclined and covered with soil or rocks to endure and experience movement. Slope instability or slope failure is the opposite state. The ratio between the active shear stress and the available shear strength, which may be represented in terms of a safety factor if these numbers are integrated across a possible (or real) sliding surface, fundamentally determines how stable a slope is. If the safety factor, calculated along every conceivable sliding surface extending from the top of the slope to its toe, is always more than 1, then the slope may be said to be globally stable. A slope that was previously stable may first be impacted by preparation variables, rendering the slope conditionally unstable, either by raising the shear stress or by reducing the shear strength, and can ultimately lead to slope failure. Hydrologic events (such as prolonged or intense rain, rapid snowmelt, progressive soil saturation, and an increase in water pressure within the slope), earthquakes (including aftershocks), internal erosion (piping), surface or toe erosion, artificial slope loading (due to the construction of a building), slope cutting (to make room for roads, railroads, or buildings), or slope flooding (for example) are some of the factors that can cause a slope to fail.

Rainfall

A primary type of precipitation is rainfall, which is made up of water droplets that have condensed from atmospheric water vapor and subsequently descend to the ground due to gravity. The movement of moisture along three-dimensional areas of temperature and moisture differences known as weather fronts is the primary factor in the formation of rain. Additionally, it is possible for substantial precipitation to occur in mountainous places where upslope flow is maximum inside windward sides of the topography at elevation, forcing moist air to concentrate and fall out as rainfall along the sides of mountains. Downwind of cities, the urban heat island effect causes an increase in rainfall, both in volume and severity. The worldwide precipitation pattern is changing as a result of global warming. Rain gauges are used to measure rainfall. Weather radar can anticipate how much rain will fall. The amount of rain that falls over time is gauged by the intensity of the precipitation. The height

of the water layer that gradually covers the ground over time serves as a proxy for rain's intensity. It implies that a layer of a specific height would form if the rain stays where it falls.

Earthquakes

The shaking of the Earth's surface that results from a rapid release of energy in the Earth's lithosphere that generates seismic waves is known as an earthquake, quake, tremor, or temblor. Earthquakes cause the ground to shake, move, or otherwise be disturbed at the Earth's surface. The bottom may be sufficiently moved to generate a tsunami when a big earthquake's epicenter is offshore. Landslides can also be brought on by earthquakes. One of the natural causes of earthquakes is volcanic activity. Tectonic faults and magma circulation in volcanoes both contribute to the frequent occurrence of earthquakes in volcanic areas. Such earthquakes can be used to predict volcanic eruptions in advance.

Physical model tests

The assessment of one or more properties of a given product, process, or service via a predetermined protocol is the basis of a physical test, which might be qualitative or quantitative in nature. Physics, engineering, and quality control all frequently use physical testing. Performance testing, which includes a variety of engineering or functional assessments if a material, product, or system is not specified by precise material or component requirements, is a type of physical testing. The final quantifiable performance criteria are instead highlighted. Testing is a process that can be qualitative or quantitative. Performance testing is a common component of acceptance testing methodologies.

A physical model that is geometrically comparable to an object (sometimes referred to as the prototype) is called a scale model. Scale models might be bigger than small prototypes, although they are often smaller than giant prototypes. In many different industries, scale models are utilized for a variety of tasks, including tools for engineering design and testing. Despite the fact that structural engineering has been studied for thousands of years and that many significant problems have been resolved using analytical and numerical methods, many problems are still too complex to be understood analytically or the current numerical methods do not have sufficient real-world support. According to the notion of similitude, a number of specified quantities must be scaled for engineering scale models. The loading, shape, and material qualities of these variables can be roughly divided into three groups. To achieve the similitude criteria of scale model manufacture and testing, engineering scale models might employ a variety of strategies.

2.3 Overview of model tests in geotechnical engineering

In most sciences, experiments provide input to theories and test them. The problem of geotechnical engineering in particular and civil engineering in general is the scarcity of information about the performance of natural or man-made structures. While soil mechanics is required to assume simplified hypotheses about actual phenomena, field monitoring faces technical and economic difficulties, especially with disasters such as earthquakes. This

situation puts the engineers at a disadvantage and leads to damage to the structure or waste due to excessive safety. This leads to the belief that the application of physical model experiments in geotechnical engineering brings even greater value than studying structures by model. Rocha (1957) [61] was a pioneer in considering the possibilities of employing physical modeling experiments to solve soil mechanics issues. After that, the application of the model has been widely accepted in the world thanks to its higher reliability and practicality compared with element experiments. Many researchers have discussed physical modeling for model tests (e.g., Zelikson (1969) [86]; Iai (1989) [18]). Kokusho (2014) [34] summarized several patterns of physical modelings for geo-materials. Along with the development of technology, measuring devices for physical modeling experiments in the geotechnical field are constantly being researched and improved. Minardo et al., (2021) [48] used the distributed optical fiber sensors in flume tests with volcanic sand subjected to rainfall as well as in the monitoring of a coastal cliff to propose its application in the early warning system. Zhang et al., (2018) [87] presented the potential for measurement of deep deformation in landslide model tests of a flexible inclinometer probe, a design that includes gravity acceleration sensors. As discussed above, one of the driving forces behind the use of the model is cost savings compared to field monitoring. Therefore, when studying soil mechanics, 1g model tests are usually performed before further steps. Not only the economic advantages, the simplicity in operation and results of the 1g model test lead to its importance in both research and education. For these reasons, 1g modeling experiments are still widely carried out in the identification of the mechanism of the phenomenon in all areas of geotechnical engineering, although centrifugal modeling tests have been proposed and studied for a long time after Schofield (1980) [64]. Because of the practicality and similarity with this study, the research based on the results of model experiments will be presented in more detail in this Chapter.

2.4 Previous studies on the failure of embankments caused by rainfall and earthquake

2.4.1 Independent effect of earthquake or rainfall

2.4.1.1. Rainfall only

In recent years, sediment-related disasters such as landslides, debris flows, etc. caused by far-than-expected heavy rainfalls have frequently occurred, leading to the need for comprehensive measures to prevent and mitigate the adverse impacts of these natural disasters. Along with the development of measuring equipment, experiment apparatus, and computers; a huge number of studies on rainfall-induced slope failure have been carried out over the past 60 years using a variety of methods: Theoretical studies; Case studies of disasters; In-situ field monitoring and measurements: Laboratory experiments; Numerical simulations; and some other special methods. Among them, Song and Hao (2017) [68] used numerical simulation on a sandy slope to clarify the influence of rainfall intensity and duration on the stability and mechanical behavior of railway slopes. Robinson et al., (2017)

[60] provided warning and raised awareness by comparing the slope stability under rainfall with intensity from history and climate change scenarios. Kusaka and Takahashi (2018) [35] conducted a parametric study to determine the influencing factors and the degree of influence of each factor on the water level of road embankments under rainfall. Slope height is proportional to convergent water level, time to start rising, and convergent time while rainfall intensity and saturated permeability are inversely proportional to these. Zhang et al., (2019) [88] analyzed the slopes that have weak interlayers during rainfall infiltration with the strength reduction technique. After rainwater infiltrates, the weak interlayer is readily plastically deformed to create a slip surface, making this type of slope more susceptible to damage than others. Mori et al., (2020) [52] presented a method to calculate the runout distance of landslides in the conditions of different soil properties and recorded rainfall by using smoothed particle hydrodynamics simulation. Through the probabilistic approach, surrounding areas that may be affected will be alerted as a result of this study.

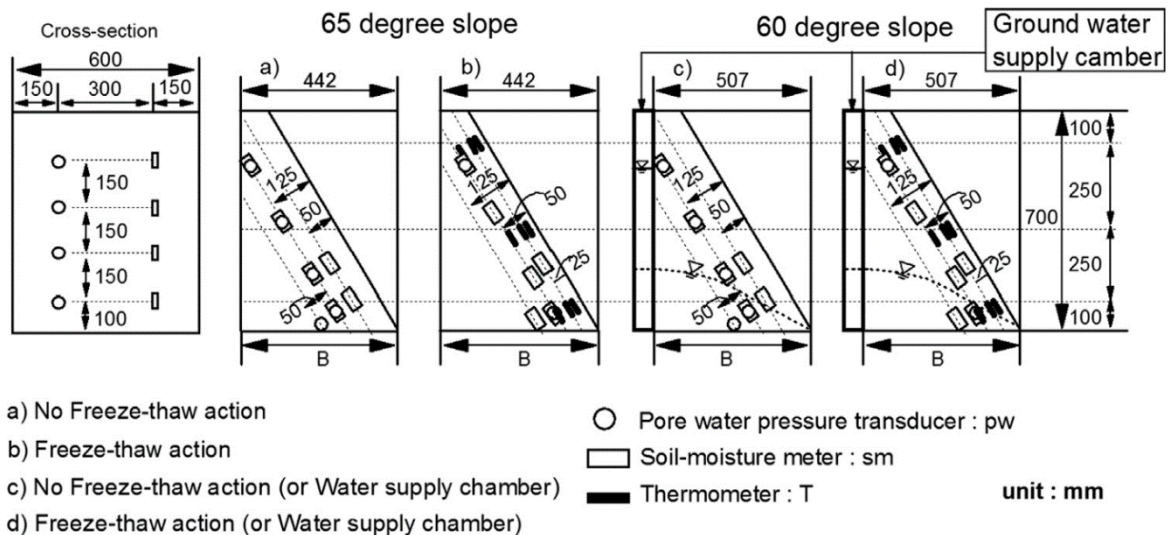


Figure 2.3 Typical model shapes (60- and 65-degree slopes) and setting positions of measurement devices (Kawamura and Miura (2013) [27]).

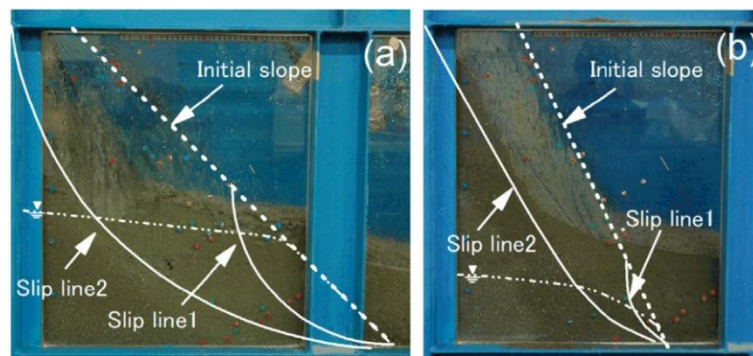


Figure 2.4 The typical shape of failed slope for Komaoka volcanic soil: (a) 45-degree slope and (b) 65-degree slope (Kawamura and Miura (2013) [27]).

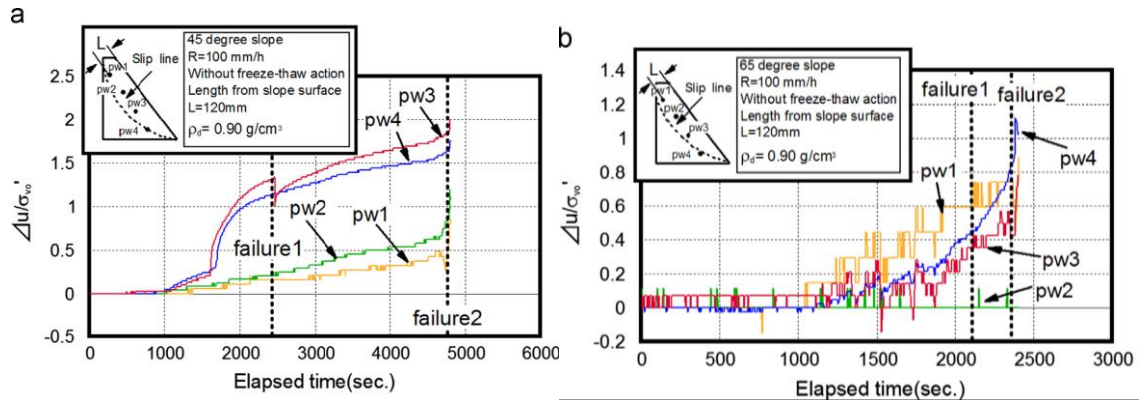


Figure 2.5 The behavior of pore water pressure during model tests for Komaoka volcanic slopes: (a) 45-degree slope and (b) 65-degree slope (Kawamura and Miura (2013) [27]).

Kawamura and Miura (2013) [27] presented the influence of slope angle on the failure mechanism of embankments constructed by many kinds of volcanic soils including Komaoka (see Figure 2.3). The deformation behavior and failure shape of Komaoka volcanic slopes with the angle of 45- and 65-degree slopes are shown in Figure 2.4 (a) and (b). The depths of the collapse region for the 65-degree slope are shallower than those for the 45-degree slope, as indicated in the image, and are similar to those of the other volcanic soils. The difference in failure patterns between Komaoka and other volcanic soils such as Touhoro was that the first failure (slip line 1) was generated at the toe of slopes, and the second failure (slip line 2) was induced with an increase in groundwater level for each slope regardless of slope angle. In terms of pore water pressure behavior, the pressure ratios around the slip line steadily grew until $\Delta u/\sigma'_{v0}$ reached 1 or higher, and then the ratios around slip line 2 similarly increased, as illustrated in Figure 2.5. Although the variation in behavior appears to be based on soil material qualities, the behavior of pore water pressure still can effectively explain the aforementioned failure occurrence. Based on those results, it is critical to understand the water retention capacity properties of soil materials as well as how saturation and pore water pressure develop in slopes.

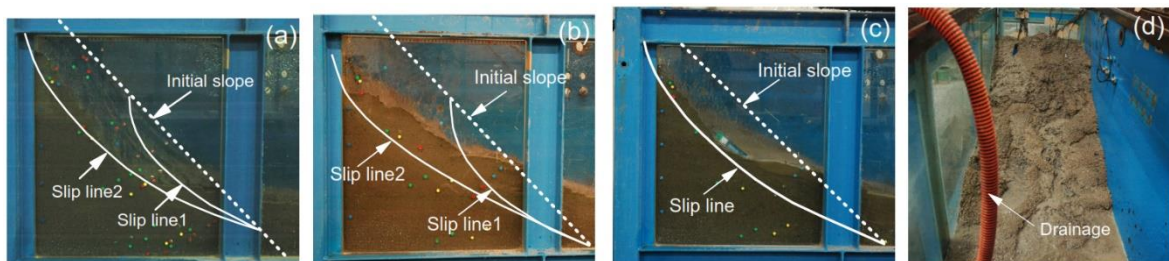


Figure 2.6 Failed shapes of slopes subjected to rainfall (a) $w_0=34\%$ (side view), (b) $w_0=38\%$ (side view), (c) $w_0=43\%$ (side view), (d) $w_0=43\%$ (cross view) (Kawamura and Miura (2014a) [29]).

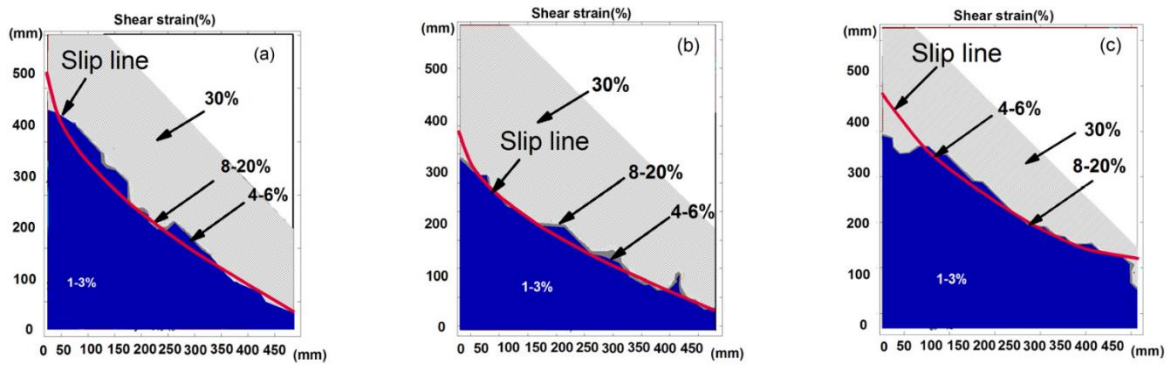


Figure 2.7 Deformation behavior at failure for Komaoka volcanic slope (a) $w_0=34\%$, (b) $w_0=38\%$, (c) $w_0=43\%$ (Kawamura and Miura (2014a) [29]).

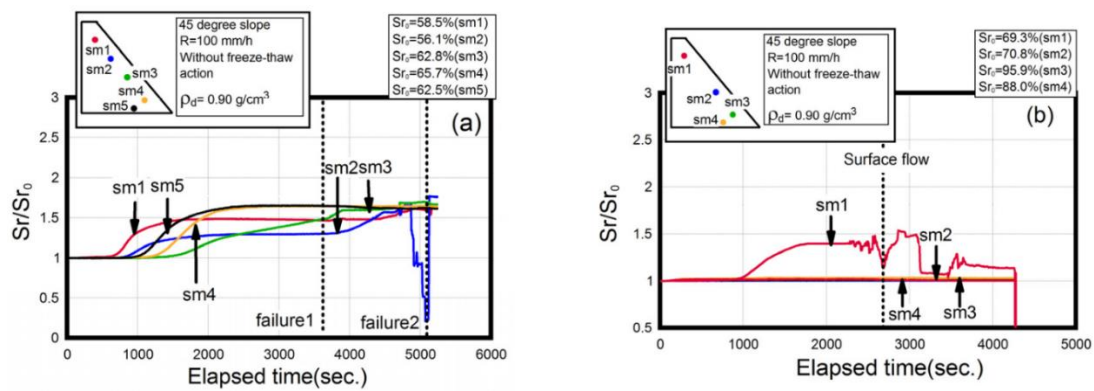


Figure 2.8 Changes in the saturation degree during rainfall (a) $w_0=38\%$, (b) $w_0=43\%$ (Kawamura and Miura (2014a) [29]).

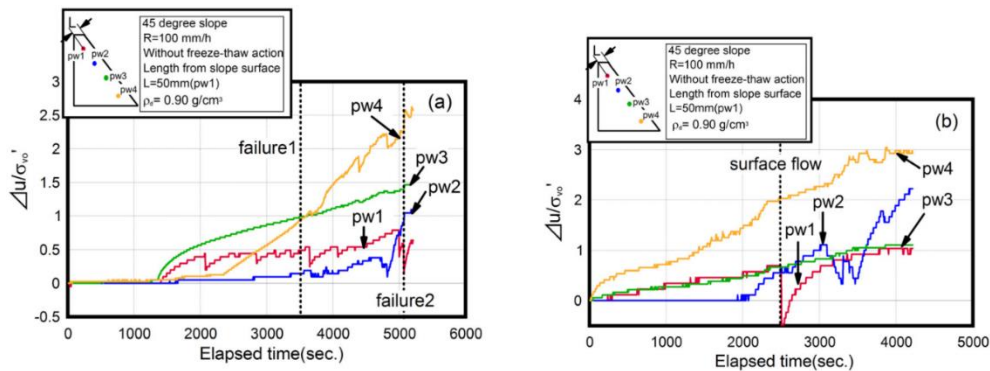


Figure 2.9 Changes in pore water pressure during rainfall (a) $w_0=38\%$, (b) $w_0=43\%$ (Kawamura and Miura (2014a) [29]).

Using Komaoka and some other kinds of volcanic soils, Kawamura and Miura (2014a) [29] clarified the effect of initial water content on the behavior of pore water pressure and saturation degree in volcanic slopes during rainfall. Figures 2.6 and 2.7 show typical failed forms and shear strain distributions at slope failure for Komaoka volcanic soils. In the cases

of lower water contents of $w_0=34\%$ and 38% , the first failure (Slip line 1) is formed at the toe of slopes, and the second failure (Slip line 2, circular failure) is swiftly induced with an increase in pore water pressure. Nevertheless, slope failure with circular slip is not verified in the case of the high water content of $w_0=43\%$. Surface flow with gully erosion proceeded until the Slip line indicated in Figure 2.6(c) for the case of high water content, and the elapsed time was 9,000 seconds (see Figure 2.6(d)) when the model test was continued until the same depth as the slip line 2 for $w_0=34\%$ and 38% (see Figure 2.7(a) and (b)). As shown in the compaction curves of that study, the optimum water content is 40.5% . The difference can also be seen from the changes in the development of saturation degree in Figure 2.8 and excess pore water pressure in Figure 2.9. Pore water pressure for $w_0=38\%$ is suddenly increased compared with that for $w_0=43\%$. Owing to the difference in the initial water content, different slope failure types can be explained by the permeability that generally decreases for higher water content over the optimum water content.

2.4.1.2. Earthquake only

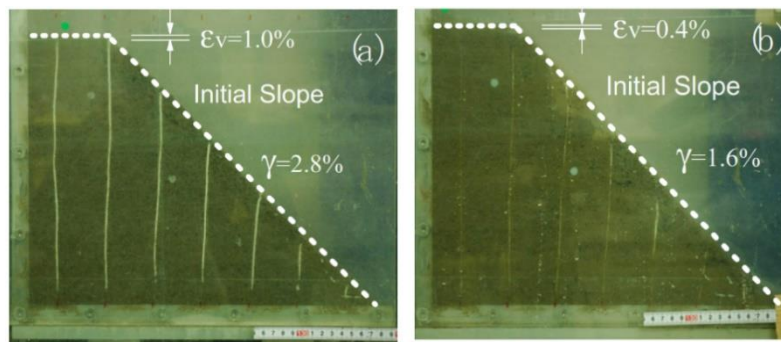


Figure 2.10 Slope shape after cyclic loadings of 280gal: (a) $w_0=37\%$, (b) $w_0=43\%$ (Kawamura and Miura (2014a) [29]).

Studies on the mechanical behavior of slopes under earthquakes performed in many different ways have contributed to increasing knowledge of the seismic resistance of embankments. Similar to rainfall, studies on the effect of earthquakes performed by numerical simulation are more numerous than those performed by laboratory experiments. Notable studies: Muraleetharan et al., (2004) [53] monitored the dynamic deformations of embankment centrifugation models with different relative densities and slope angles. These experiments show that the medium-dense sand embankment and lighter slope have greater displacement and an increase in pore water pressure. Lee et al., (2019) [38] compared the seismic deformation results calculated from computer software based on the finite difference method with the measured data from the centrifuge experiments, and the conformity increases confidence in the program's predictability. Shinoda et al., (2020) [67] assessed the practical seismic risk by presenting a simple approach for estimating the earthquake fragility of unreinforced and reinforced embankments using sensitivity analysis. Chakraborty et al.,

(2020) [4] investigated the stability of slope in hydraulic fill dams under earthquakes and concluded that the slip surface with the lowest factor of safety for static loading may not be the most dangerous for seismic action. After finding that the reliability index decreases linearly with an increase in horizontal seismic coefficient, the authors proposed a method of estimating the reliability index, which is expected to significantly reduce computational time and effort.

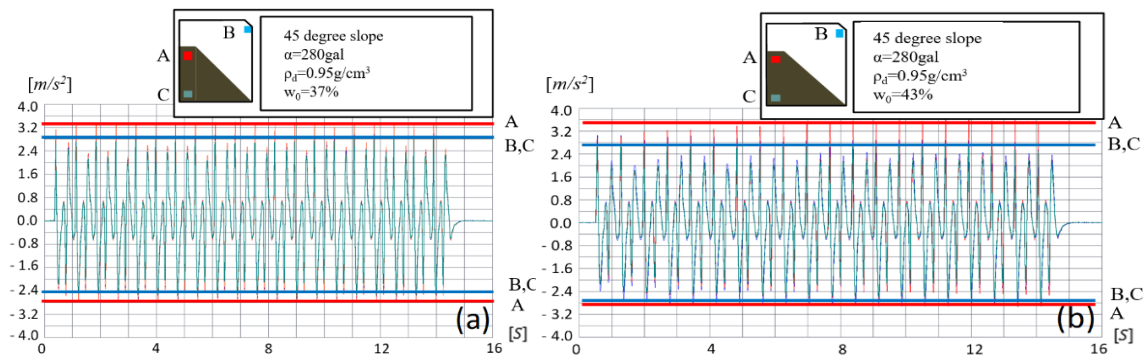


Figure 2.11 Variation of accelerations in the basement, the crown of the embankment, and shaking table (a) $w_0=37\%$ (b) $w_0=43\%$ (Kawamura and Miura (2014a) [29]).

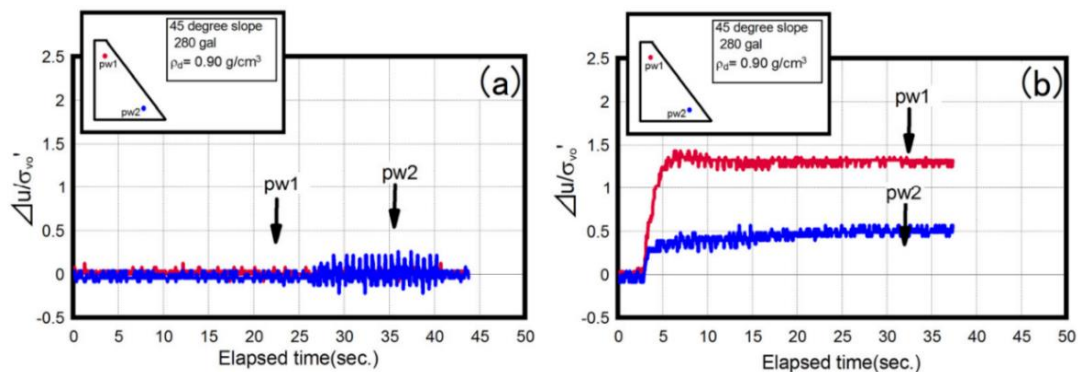


Figure 2.12 Changes in pore water pressure during shaking table test: (a) $w_0=37\%$, (b) $w_0=43\%$ (Kawamura and Miura (2014a) [29]).

In Kawamura and Miura (2014a) [29], the fundamentals of the mechanical behavior of volcanic slopes during cyclic loadings were examined with two kinds of initial water content. The typical slope failure shape after cyclic loadings of 280 gals for each water content is shown in Figure 2.10. Shear strain generated for $w_0=37\%$ and 43% was $\gamma=2.8\%$ and 1.6% , and vertical strain ε_v (ratio of settlement of crown/the initial height) was 1% and 0.4% , respectively. Figures 2.11 (a) and (b) show the variance in acceleration at the basement and crown when compared to the shaking table. As shown in the Figure, the maximum acceleration at the crown of the slope (A point) is greater than at other locations (B and C points) in both cases, and its tendency is significant for $w_0=43\%$. Under the same conditions, the behavior of pore water pressure normalized by the initial effective overburden pressure

σ'_{v0} was depicted in Figure 2.12. When $w_0=37\%$, it is clear that pore water pressure fluctuates frequently with cyclic loadings. The pore water pressure ratio for $w_0=43\%$, on the other hand, is greater than $\Delta u/\sigma'_{v0}=1$ indicating beginning liquefaction. However, slope failure did not occur with cyclic loadings at that time. This means that a volcanic slope with $w_0=43\%$ has cyclic mobility, as seen in dense sand.

2.4.2 *Studies on the combined effect of rainfall and earthquake*

Although the unexpected impacts of complex natural catastrophes have long been known, as mentioned in Chapter 1, only very few studies have been conducted on this topic. Some outstanding studies on the failure mechanism behavior of embankments subjected to freeze-thaw action in combination with rainfall or earthquake can be mentioned: the field monitoring results in Kawamura et al., 2013 [30], the model experiments in Kawamura et al., (2016) [31]; the proposed early warning criteria in Zhu et al., (2021) [89]; or overview of hazard events and research in Baselt and Heinze (2021) [1]. Regarding the stability of the slope under the dual hazard of rainfall and earthquake, the number of studies is even smaller, these studies often use data from actual complex disasters in the past. The majority of these researches are case studies of actual complex disasters in the past. In many cases, even though earthquakes have not caused slope collapse, they can leave long-term effects such as cracks or structural looseness at some local points. If adequate post-earthquake remedial measures are not taken, this can make it easier for water to penetrate and slopes to become weaker during the rainy season. Therefore, the previous earthquake could be one of the causes of slope collapse due to rainfall.

Nomura et al., (2014) [58] showed an example of a slope in Tochigi prefecture that collapsed by rainfall after the 2011 Tohoku Earthquake (Great East Japan Earthquake) with an M_w of 9.0~9.1. Which, the seismic disturbances in the slope are believed to be one of the reasons for the failure. The authors suggested that in general, after a large earthquake, landslides are thought to be more frequent with less rainfall than before the earthquake. Evidence to support this assumption can be easily found after the previous great earthquakes around the world. The $M_w7.7$ Chi-chi earthquake in September 1999 severely affected central Taiwan. In July 2001, almost 2 years later that earthquake, The Toraji typhoon produced strong precipitation of 650 mm per day and created widespread landslides in central Taiwan and areas of eastern Taiwan. The average area of a typhoon-related landslide is 2.1 ha/landslide, which is double the size of a 1999 Chi-chi earthquake-induced landslide, as reported in Wang et al., (2003) [81]. About 65% of typhoon-related landslides occurred in the affected region of the Chi-chi earthquake.

The above-mentioned assumption that the Toraji typhoon-related landslide in 2001 was a secondary calamity of the Chi-chi earthquake was confirmed by Wang et al., (2004) [82]. According to the interpretation from aerial pictures, around 30% of the typhoon-related landslides were caused by the outward spreading of earthquake-induced landslides, implying

that the strata near the earthquake-induced were fractured by the Chi-chi seismic shaking. The failure rate of a stratum or rock formation is calculated by the proportion of landslide area to stratum area. In the same stratum, typhoon-related failure rates were generally higher than earthquake-induced failure rates, implying that many earthquake-induced landslides could be widened during the Toraji typhoon. Figure 2.13 shows the frequency of rain-induced, earthquake-induced, and typhoon-related landslides against slope location (A) and slope angle (B). Due to the difference in mechanism, the distribution of landslides caused by rain and earthquakes is different in both cases. Rain-induced landslides occurred mostly on the lower sections of slopes, whereas earthquake-induced landslides occurred primarily on the upper sections. Furthermore, earthquake-induced landslides were centered on slope angles of 40 degrees, but rain-induced landslides relocated to slopes dipping approximately 30 degrees. These results might be due to ground motion being enhanced on the higher and steeper slopes and rainfall being concentrated on the lower and gentler slopes. However, the distribution of typhoon-related landslides was similar to that of earthquake-induced landslides. Field reconnaissance revealed tension fractures on upslopes and failed materials on mid-slopes following the Chi-chi earthquake. It is clear that the spread of the Toraji typhoon-induced landslides was connected to the Chi-chi earthquake occurrence.

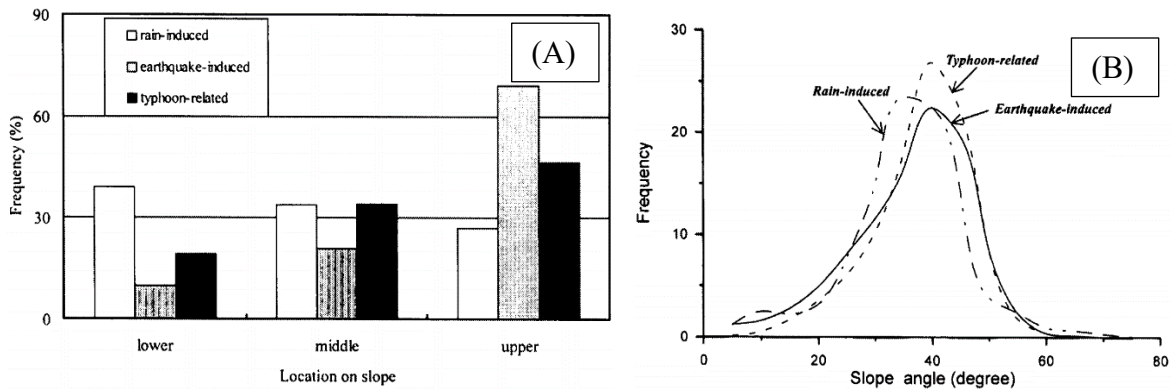


Figure 2.13 Frequency of each type of landslide (A) slope location (B) slope angle (Wang et al., (2004) [82]).

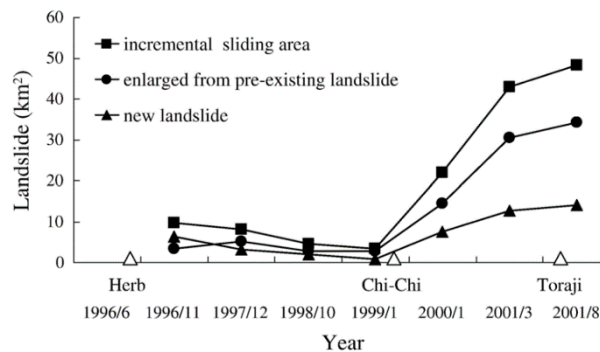


Figure 2.14 Different types of landslides in each satellite image (Lin et al., (2006) [39]).

Lin et al., (2006) [39] compared the occurrence of landslides in the Choushui River watershed using eight satellite photographs from 1996 to 2001 to assess the impact of the 1999 Chi-Chi earthquake on subsequent rainfall-induced landslides. According to the study, the Chi-Chi earthquake not only caused severe coseismic landslides but also severely disrupted the surface strata surrounding the epicenter. Following the severely disturbed surface strata, torrential rainfalls in 2000 and 2001 generated more landslides than the earthquake itself. When compared to data gathered from photos prior to the earthquake, it is clear that the density of rainfall-induced landslides rose dramatically after the earthquake, as did the locations where landslides occurred, as can be seen in Figure 2.14. Although Typhoon Herb in 1996 dropped more rain than Typhoon Toraji in 2001, Herb caused just 9.77 km² of landslides, but Toraji caused 48.8 km² of landslides--nearly five times the size of those caused by Herb.

Shieh et al (2009) [65] analyze variability in rainfall threshold for debris flow between 1999 and 2006 (critical rainfall for debris flow triggering) after the Chi-Chi earthquake. Results show that the rainfall threshold for debris flow was remarkably lower just after the Chi-Chi Earthquake, but gradually recovered. The rainfall threshold after 7 years of the earthquake was still lower than the original level prior to the earthquake. This variability in rainfall threshold is closely related to the amount of sediment material in the initiation area of debris flow, which increased rapidly due to landslides resulting from the earthquake. This variation in rainfall threshold is strongly tied to the amount of sediment material in the debris flow's commencement location, which grew significantly owing to landslides caused by the earthquake. The rainfall threshold was drastically reduced during the first year following the Chi-Chi earthquake due to an increase in silt material. Heavy rains, on the other hand, activated the silt material, generating debris flows and carrying sediment downstream. The rainfall threshold steadily recovered over time as silt material decreased.

Similarly, tens of thousands of landslides in the Wenchuan region of China were caused by extreme rainfall following the devastating M_w7.9 earthquake in May 2008 (Marui and Nadim (2009)). According to Fan et al., (2018) [8], most co-seismic landslides were confined to hillslopes and ravines, but there was an abundance of loose co-seismic landslide debris on the slopes following the earthquake, which later served as source material for rainfall-induced debris flows or shallow landslides. Heavy rains in the central section of the Wenchuan Earthquake-affected region generated 72 debris floods on September 24, 2008. Tang et al., (2009) [70] documented the process of debris flow commencement and movement in the research locations, as well as field observations on the roles of rainfall, lithology, and the existence of faults. Following the earthquake, the critical amount of accumulated precipitation and the hourly rainfall intensity required to initiate debris flow was most likely reduced compared to pre-earthquake values. The debris flow from the Xishanpo gully generated a substantial accumulation in the already destroyed city of

Beichuan. It is concluded that the whole area shaken by the Wenchuan Earthquake is now more vulnerable to debris flows, which might be triggered by locally severe rainfall.

Heavy rainstorms occurred in regions devastated by the 2008 Wenchuan Earthquake from August 12 to 14, 2010, causing catastrophic debris flows known as "the 8.13 debris flows". According to Xu et al., (2012) [84], the 8.13 debris flows are positioned along the seismic fault because the source materials are primarily loose deposits of landslides generated by the Wenchuan Earthquake. The major causes of these debris flows are the presence of huge volumes of these loose materials on the slopes and the emergence of high-intensity rainstorm events. The real discharge of the 8.13 debris flows is substantially more (up to ten times) than the values computed using Chinese rules, emphasizing that design standards for debris flow mitigation in earthquake zones must be improved. Finally, the authors introduced new debris flow mitigation measures that proved effective during the 2011 heavy rainy season. Following the 8.13 events, check dams, along with a sediment trap and a diversion tunnel built in the upstream part of Wenjia gully, successfully separated and diverted the water and solid materials, preventing new catastrophic debris flows. Furthermore, the construction of a flexible drainage system with reinforced stone cages successfully prevented lateral erosion along the erosion channels of potential debris flows.

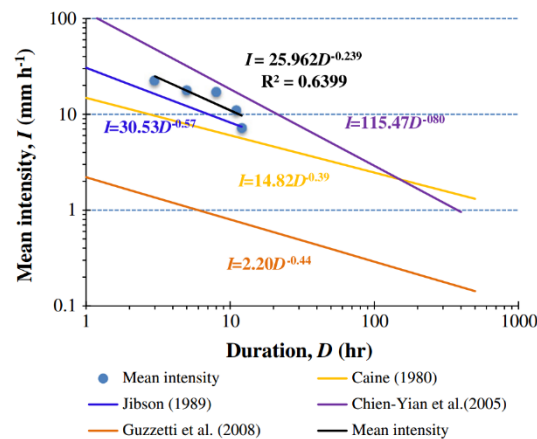


Figure 2.15 Intensity–duration graph for five debris flow events in the Wenjia torrent compared with previous research (Tang et al., (2012) [71]).

Through field reconnaissance, measurements, and aerial picture interpretation, Tang et al., (2012) [71] investigated the locations and structural characteristics of 20 in the 8.13 debris flows in the Qingping region of southern China. Among these, the devastating tragedy in the Wenjia catchment was caused by extensive erosion in loose material, which was deposited by a rock avalanche during the 2008 Earthquake event. From an overview of the Wenjia watershed debris flow fan, the debris flow dam, and the submerged region of Qingping's recently restored dwellings, it can be seen that a huge quantity of avalanche deposits in the lower stretch of the stream has led to the occurrence of debris flows. The

biggest debris flow occurrence was caused by rainfall with a peak intensity of 38.7 mm/h. Rainfall data from five debris flow incidents in the Wenjia stream were used to develop a basic rainfall intensity-duration relationship for initiating debris flows, which was then compared to other rainfall duration thresholds from across the world, as shown in Figure 2.15. As demonstrated by Chien-Yuan et al., (2005) [6], debris flows in the Qingping area were often generated by rainfalls with substantially lower hourly intensity and cumulative precipitation than those connected with the Chi-Chi earthquake area in Taiwan in Chien-Yuan et al., (2005) [6]. It can be seen from the above research that in earthquake-prone areas, the post-seismic debris-flow threat can last for decades.

Also happened in Sichuan province, the Lushan earthquake (April 20, 2013) unavoidably sparked further debris flow activity (Guo et al., (2021) [11]). During the rainy season, debris flows were generated twice in more than 20 gullies shortly after the earthquake (May 23 and July 9), as reported in [11]. Some gullies experienced their first-ever debris flow, according to historical records. Considering the same area, the initiating rainfall quantities and peak rainfall intensities were both substantially lower than those of the 2012 storm. However, the newly produced gully debris flows were much larger. The explanation was an increase in the amount of accessible loose debris as a result of the 2013 Lushan earthquake. Even with the relatively modest quantity of rainfall, this supply of loose particles might fuel debris flows. Debris flows were common and widespread throughout the region from 2014 to 2018. The volumes, however, were rather tiny. In contrast, the debris flows that followed the August 19-22, 2019 rainstorm event are rated as the most devastating in recorded history. The spatial distribution of material sources and production processes in the Desheng gully debris flow can be found in Guo et al., (2021) [11]). Desheng Gully is located in the Baoxing River's upstream portion, where debris flows were not observed before 2019. Recovery of natural vegetation, remaining solid material reduction, and control projects for debris flow control all play major roles in increasing the threshold of rainfall conditions necessary for starting debris flows.

Figure 2.16 shows the production mechanism of debris flows. Earthquakes are not thought to be the primary cause of debris flows, but rather the source of the plentiful loose materials in the original channel. Rainfall is the precipitating element for debris flows. High-velocity runoff can erode loose material quickly and significantly (Figure 2.16(a) and (b)). The surface flow concentrates loose debris, which leads to additional eroding of the channel bed by progressive bulking effect. The channel incision procedure exposes a free surface of diluvium along the channel, which might result in significant lateral erosion (Figure 2.16(c)). The channel bed was made up of either loose coarse material from local lower-gradient slope failures or poorly consolidated soils, which are extremely prone to runoff erosion (Figure 2.16(d)). The process of consecutive channel incision and erosion then converts a water flow into a debris flow. There is the possibility of debris flows becoming obstructed in limited

parts; nevertheless, when the loose slope is subjected to mass failure by the eruption of the blockage, the debris flow volume and velocity can be significantly amplified.

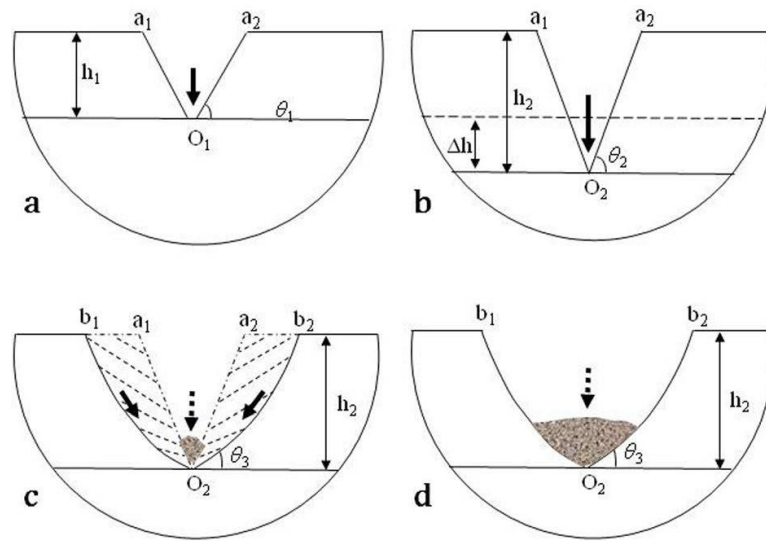


Figure 2.16 Debris-flow formation process (Guo et al., (2021) [11]).

Yang et al., (2015) [85] used the Stability Index MAPping model to assess and investigate slope stability following the 2013 Lushan earthquake in several rainfall scenarios as light rainfall, moderate rainfall, heavy rainfall, and rainstorm. The model parameters were adjusted to account for the major impact of severe earthquakes on geological settings. An increase in rainfall intensity leads to an increase in unstable areas. Despite varying rainfall circumstances (light rainfall, moderate rainfall, heavy rainfall, and rainstorm), the diverse distribution of slope instability is closely associated with the dispersion of earthquake intensity. According to the authors, seismic strength and rainfall are both important determinants in post-earthquake slope stability.

From the lessons learned above, one of the most severe worries about the 2016 Kumamoto earthquake in Japan was that it occurred so close to the rainy season which led to a high risk of post-seismic landslides. Many slopes in the affected area were loosened and left in a vulnerable state. As predicted, heavy rains over the Kumamoto prefecture in June 2016 prompted massive landslides and debris flows (Goda et al (2016) [10]). Matsunaga et al., (2019) [45] also depicted the subsequent rise in hillside failures as an example of the consequence of rainfall as a secondary disaster. As can be seen, the number of disasters in the event of post-earthquake rainfall is large due to the long-term effects of the earthquake described above. This led to a large number of studies on the effects of previous earthquakes on landslides or debris flows caused by subsequent rainfall, leading to many proposed guidelines. For example, Nomura et al., (2014) [58] recommended that landslide incidence thresholds should be reduced following big earthquakes of level 5+ on the Japanese scale.

On the contrary, the less attention paid to the case of post-rainfall earthquakes could be a reason for the enormous losses of this type of double disaster.

Mishima and Kimura (1970) [49] reported the embankment failure and landslide during the 1968 Tokachi-oki earthquake. About embankment, severely damaged highway and railway embankment areas coincide with areas of heavy rainfall, with the exception of banks on plateaus or along foothills. The majority of banks are made up of volcanic ash or fine sands with a poor homogeneity coefficient. Figure 2.17 depicts the collapse characteristics of a typical bank composed of volcanic ashes at Kami-Metoki. Regarding landslides, it is worth noting that the inclination of the natural slopes where the landslide occurs is quite gentle and concentrated in a small range from 20 to 25 degrees. The slide locations were covered with thick volcanic ash consisting of loam and pumice. The occurrence of many landslides can be attributed to volcanic ash containing a lot of water, resulting in saturation and high pore water pressure after four days of heavy rain, and they are in an earthquake-induced liquefaction-prone state. So with the results of field investigations, the decisive role of rainfall on landslide and embankment collapse may be demonstrated by the facts that there was adequate rainfall amount over the affected regions prior to the occurrence of the earthquake and that the locations with greater rainfall overlap with the areas that suffered more damage.

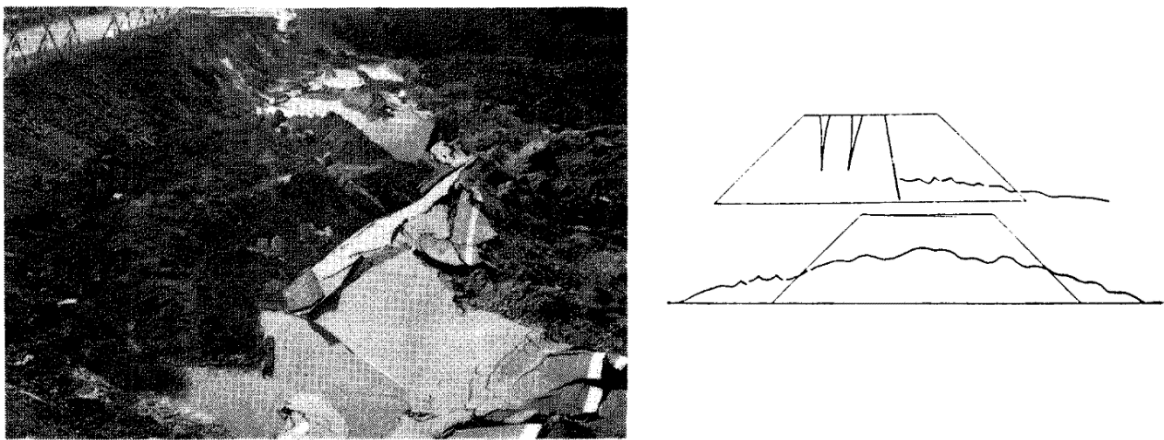


Figure 2.17 Failure situation of volcanic ashes bank at Kami-Metoki (Mishima and Kimura (1970) [49]).

Uzuoka et al., (2005) [79] conducted a field investigation of the characteristics of two landslides during Earthquake No. 526 in May (Dateshita landslide) and Earthquake No. 726 in July (Nishisaruta landslide), 2003, in Miyagi, Japan. The situation of the two landslides can be seen in Figure 2.18. For a week before the Dateshita landslide, no rainfall had been recorded at Tsukidate. Therefore, the soil at a depth of several meters in the upper section of the collapsed layer was unsaturated. Despite having a very loose fill structure, the unsaturated soil with high suction was not destabilized for a long time before the earthquake.

Then the collapsed soil was easily fluidized under the effect of cyclic shear. The composition of the slope is mainly pyroclastic sediments which generally crush its particles during shearing (Miura et al., (2003) [51]), which may have contributed to the high fluidity of the collapsed soil in addition to the loose state. In contrast, It had rained for a week before the earthquake that caused the Nishisaruta landslide, and the accumulated precipitations of 114 mm were measured for 3 days. Rainfall was considered by the authors as an important feature that exacerbated the Nishisaruta landslide. Under the effect of rain, the entire upper part of the slope was said to be saturated. Consequently, the main failure of the slide occurred at the upper part of the slope. The residual strength, after undrained cyclic shear loading, of the collapsed soil was much larger than that of the collapsed soil at Dateshita. This could also be an indication that previous rain was one of the causes of the Nishisaruta landslide because the two earthquakes have similar magnitudes.

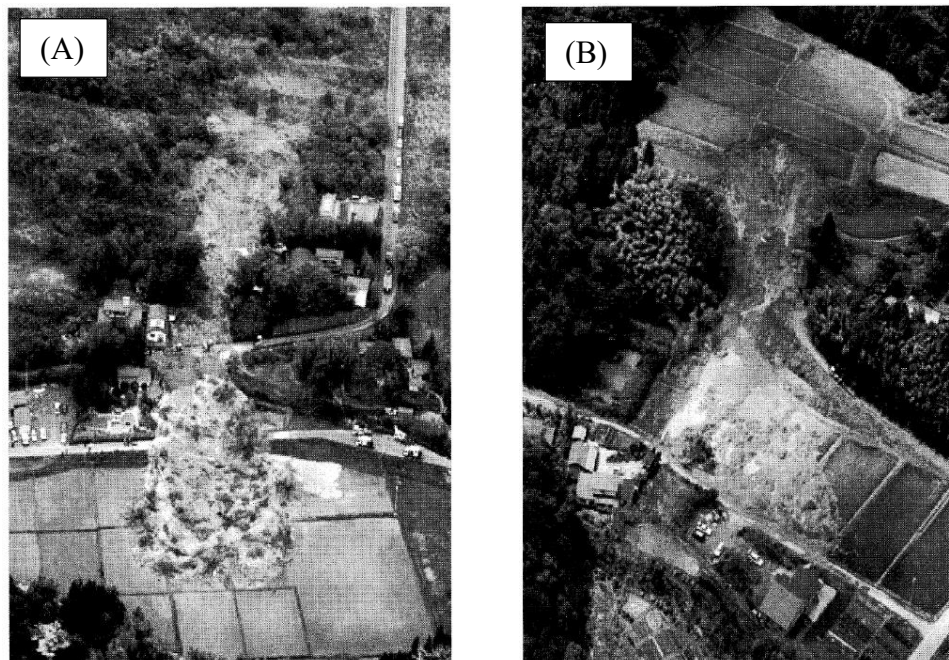


Figure 2.18 Aerial view of earthquake-induced landslides in Miyagi, Japan in 2003 (A) Dateshita landslide, (B) Nishisaruta landslide (Uzuoka et al., (2005) [79]).

In 2004, many significant rain events hit Japan, resulting in some landslide disasters such as the one in Yamakoshi Village. The total quantity of rain reported for the Niigata-Fukushima Heavy Rain (from July 10 to July 14) and the Fukui Heavy Rain (from July 16 to July 18) were 428 mm and 272 mm, respectively. Since 1993, rainfall amount in Niigata prefecture peaked in 2004. However, large landslides did not occur during this heavy rainfall period. Then, on October 20, typhoon No. 23 repeated the torrential rains of 100 mm in this area. The Chuetsu earthquake (2004 Mid-Niigata Prefecture earthquake) happened three days after the storm, leading to hundreds of landslide disasters as reported by Sassa et al.,

(2006) [62]. The authors presented the Soil Water Index (SWI) provided by the Japan Meteorological Agency as a criterion for assessing the amount of water stored below the ground surface. Based on SWI, an efficient technique for estimating landslide disaster probability is proposed by comparing the values of SWI for past landslide disasters. As shown above, major landslides did not occur during the July heavy rains although the maximum value for the period 1994 to 2003 in this area was exceeded. This is explained by the lower permeability of the slopes in the Tertiary weathered mudstone area of Niigata compared with the standard granitic slopes used by SWI. The authors suggested the necessity of reconsideration of the precipitation parameters.



Figure 2.19 The Higashi Takezawa landslide and the head scarp of previous landslides (Sassa et al., (2006) [62]).

Sassa et al., (2006) [62] also discussed the difference between the consequence of the 2004 Mid-Niigata Prefecture earthquake with those of the Hyogoken-Nambu earthquake, which occurred in January 1995, the dry season, with no rainfall before the earthquake. The energy of the Mj7.2 Hyogoken-Nambu earthquake with an epicentral depth of 17 km was higher than that of the M6.8 earthquake in Mid-Niigata Prefecture with an epicentral depth of 13 km. However, the quantity and scale of landslides caused by the Mid-Niigata Prefecture earthquake were substantially bigger. The earthquake triggered hundreds of landslides with widths of more than 50 m and 12 large-scale landslides with volumes greater than 1 million cubic meters, while the only notable landslide triggered by the Hyogoken-Nambu earthquake was the Nikawa rapid landslide (volume of $1.1-1.2 \times 10^5 \text{ m}^3$ and width of 125 m). This big difference might be explained by the impact of heavy rainfall preceding the Mid-Niigata Prefecture earthquake

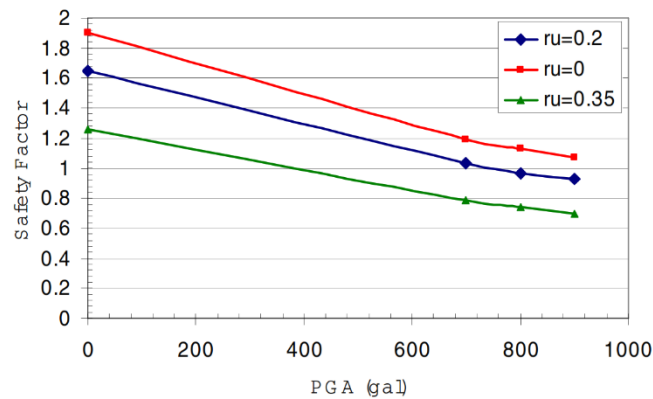


Figure 2.20 Decrease in Factor of Safety with Peak Ground Acceleration of the earthquake at different values of r_u (Tuladhar et al., (2007) [77]).

Among the landslides caused by the 2004 Mid-Niigata prefecture earthquake, the Higashi Takezawa landslide occurred within past landslide masses and created the largest dam over the river near the toe of the landslides, inflicting significant property destruction, as presented in Tuladhar et al., (2007) [77]. The overview of that landslide can be seen in Figure 2.19 with red arrows showing the head scarp of the current landslide and a curved line with red arrows presenting the head scarp of the previous landslide. The landslide was caused at the interface between two radically diverse geological layers: the upper layer of heavily weathered and loose sandy soil and the lower layer of mudstone. Soil samples were taken from these two layers to conduct laboratory tests. Shear tests and X-ray fluorescence tests were conducted to respectively measure friction angle and chemical index to assess the weathering index of the soil specimen. The results showed that the weathering degree of sandy soil in the upper part is higher than that of mudstone in the lower layer. In both kinds of soil, the residual friction angle decreases proportionately with the increase in weathering. That internal friction angle was used to determine the dynamic safety factor of slopes with different peak ground accelerations based on the Newmark method, as shown in Figure 2.20. In the figure, the different values of pore water pressure ratio r_u can also represent the different seasons. The significant impact of pore water pressure on the dynamic safety factor of the landslide was proved through the fact that it decreased exponentially with the increase in water pressure. It can be seen from Figure 2.20 that the safety factor of the slope is still higher than 1 in the dry season ($r_u = 0$) even with the earthquake with a PGA of 900 gals. When r_u increases to 0.35, a PGA of 400 gals is sufficient to produce instability. These results imply that the typhoon that occurred 3 days before the earthquake may have played a significant influence in the landslides. If the earthquake occurred during the dry season or if the soil mass was not loosened by the tremendous rainfall of the typhoon, the magnitude of the 2004 Mid-Niigata prefecture earthquake is insufficient to induce failure.

In contrast to those post-rainfall earthquake-induced disasters mentioned above, the motivation behind the 2006 Southern Leyte mudslide (Philippines) has been controversial

among experts. The fact that the magnitude of the earthquake was so small has led to the idea that it was a rainfall-only disaster. The characteristic of that massive rock slide-debris avalanche was detailed by Sassa et al., (2007) [63]. As can be seen in Catane et al., (2007) [3], the landslide's source region and deposits showed the projection of the Philippine Fault Zone and other geologic features while the close-up of the source region showed at least three primary failure planes: Fractures cut the bedrock in the top part of the segment; The slip surface (fault plane) is lined by the gouge; Sheared rocks and earlier landslide deposits form the mounds under the peak.

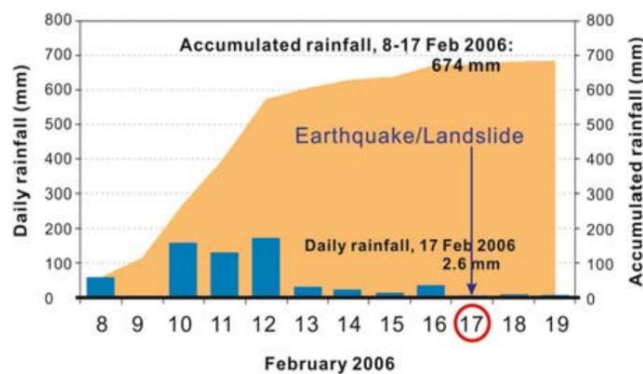


Figure 2.21 Rainfall record at the nearest station from the 2006 Leyte landslide (Sassa et al., (2007) [63]).

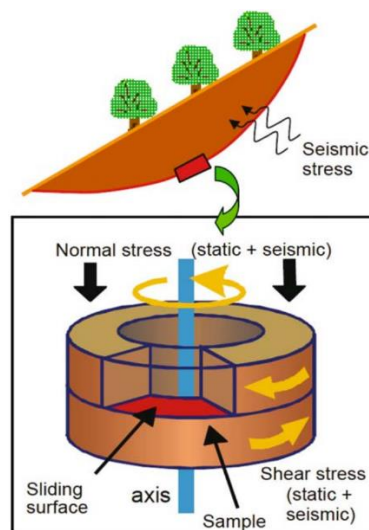


Figure 2.22 Concept of the stress-controlled dynamic-loading ring-shear apparatus (Sassa et al., (2007) [63]).

The rainfall data record at the nearest station from the landslide was shown in Figure 2.21 (Sassa et al., (2007) [63]): Heavy rainfall with a total amount of 571.2 mm over 5 days from 8 to 12 February (459.2 mm for 3 days from 10 to 12) were measured before the landslide. This high quantity of precipitation should have raised the groundwater level and

pore water pressure within the slope. Experts generally agree that excessive precipitation a week before the failure contributed to its circumstances. However, considering the rainfall on 13-17 February was little, it was likely that the peak of groundwater level had passed before the landslide on 17 February. Because of that 5-day delay between the heaviest rainfall and the landslide, as well as the fact that Southern Leyte usually receives high overall amounts of precipitation, the hypothesis of precipitation as the sole cause became unconvincing.

With an official death toll of 1126, this landslide was the greatest single landslide disaster in the world since the 2001 Las Colinas landslide caused by the M_w 7.7-7.9 El-Salvador earthquake. However, the nearby earthquake occurred at about the same time as the landslide only had a magnitude of 2.6, which made the role of that minor ground shaking still uncertain. It is also possible that the earthquake did not cause the landslide, but that the landslide produced ground shaking, which was recorded as an earthquake. Because earthquake-induced landslides are often generated by large earthquakes, it is difficult to persuade both landslide and earthquake experts that such a minor earthquake may create a massive landslide. Sassa et al., (2007) [63] used the result of a ring-shear simulation experiment to support the view that the landslide was caused by a combination of rainfall and earthquake. The concept for the undrained stress-controlled dynamic loading ring shear device can be seen in Figure 2.22. This apparatus tries to simulate the geotechnical formation of a sliding surface and the post-failure motion by reproducing the stresses acting on the potential sliding surface in the slope, including static stress from the soil layer's self-weight, seismic stress from an earthquake, and pore-pressure increase from rainfall. The test results of the Leyte landslide clearly demonstrated that even a very minor earthquake can be the essential trigger of a landslide when the stability of the slope has already been weakened owing to rains and the groundwater table has been near the critical level. In contrast, the authors also suggested that a severe earthquake does not always cause a large-scale landslide if the groundwater level is lower than the likely sliding surface.

The unpredictable consequences of the double disaster outlined by the above case studies as well as the analysis of the Hokkaido Eastern Iwate earthquake in Chapter 1 posed a requirement for verification. With that in mind, a number of studies have been done using numerical simulation. Matsumaru and Uzuoka (2016) [42] replicated the damage of the 2004 Niigata Chuetsu Earthquake including the recorded rainfall before this earthquake to examine the influence of rainfall on seismic activity. The behavior of unsaturated soil was modeled by a typical elastoplastic constitutive model and analyzed with a combination of three phases soil, water, and air. The results show that the embankment impacted by rainwater prior to the earthquake exhibited more deformation. The dynamic response with recorded heavy rainfall showed liquefaction as a result of the reduction in skeleton stress by earthquakes. As a result, the acceleration's reaction altered, and huge strains occurred. In

contrast, when only annual rainfall was applied, the appearance of liquefaction was minimal. From that comparison, the amount of rainfall before the earthquake clearly influenced the seismic behavior of the embankment. In addition, parametric analyses were also carried out to reveal that drainage and an impermeable roadbed might reduce the degree of saturation in the embankment. However, the embankment's seismic resistance remained low due to the low resistance to cyclic loading of material. The seismic behavior of the embankment was significantly enhanced by the use of high-quality embankment material.

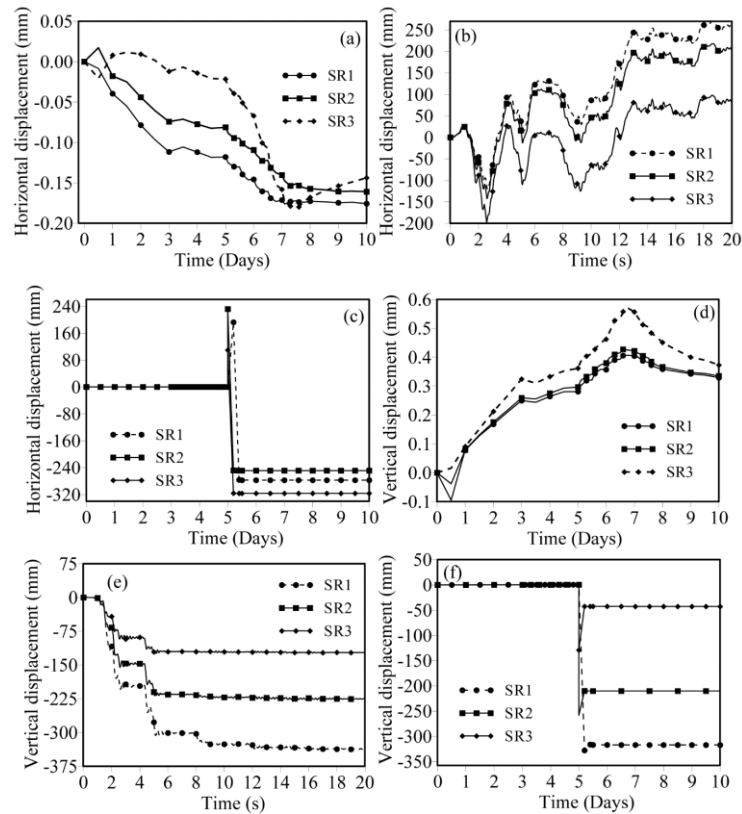


Figure 2.23 Horizontal and vertical displacement at slope crown (a) (d) Rainfall, (b) (e) Earthquake, (c) (f) Rainfall – Earthquake (Vickneswaran and Ravichandran (2020) [80]).

Vickneswaran and Ravichandran (2020) [80] used a numerical simulation with the acceleration of the 1940 El-Centro earthquake that attacked Imperial Valley, California to compare the effect of rainfall and erosion or rainfall and earthquake with a single hazard. The model of embankments was built with PLAXIS 2D, a combined geotechnical-hydrological finite element program capable of connecting soil deformation and flow behavior. To explore the influence of steepness on the stability and deformation behavior of earth slopes, investigations were performed for different slope ratios SR1 (1.5:1), SR2 (2:1), and SR3 (3:1). The results show that the factor of safety dropped as the slope ratio decreased. Figure 2.23 shows the horizontal and vertical displacement of the crown point in different cases. As can be seen, dual hazards lead to greater slope movement and lower factor of safety

when compared with single hazard, i.e., rainfall-only and earthquake-only (Figure 2.23). Further, it was found that the factor of safety has an inverse relationship with erosion and the duration of rainfall.

Current commercial software often analyzes slope stability using the phi-c reduction method in finite element models like Plaxis or limit equilibrium methods like GeoSlope or GeoStudio. Input for analysis of Geoslope is also based on finite element method such as SEEP/W module determines the infiltration of rainwater according to Darcy's law or QUAKE/W module calculates excessive pore water pressure due to inertia force according to the cyclic stress ratio, ... It can be seen that difficulties of general finite element method in the simulation of the granularity of the soil lead to the imprecision of some actual phenomena, such as the effect of rainfall on soil structure or the rearrangement of soil particles caused by earthquakes, ... For that reason, studies based on the results of model experiments are still indispensable.

2.4.1.3. Research on post-earthquake rainfall by model test

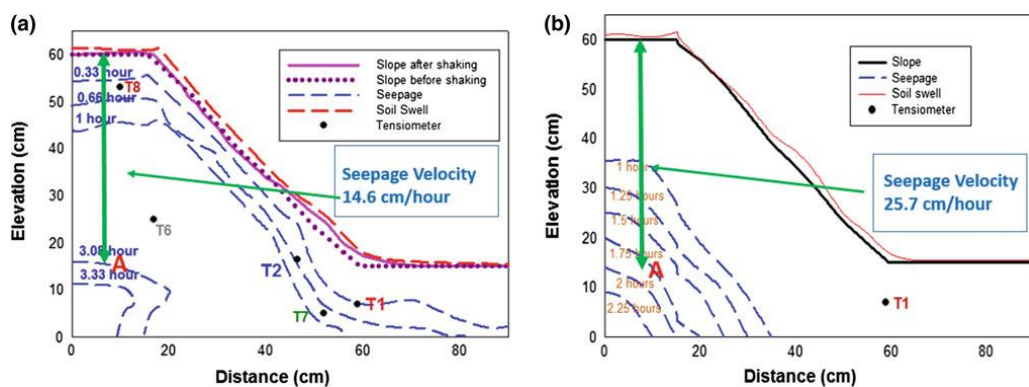


Figure 2.24 Movement of wetting fronts and seepage velocity of rainwater (a) post-earthquake rainfall test, (b) rainfall-only test (Tiwari et al., (2017a) [75]).

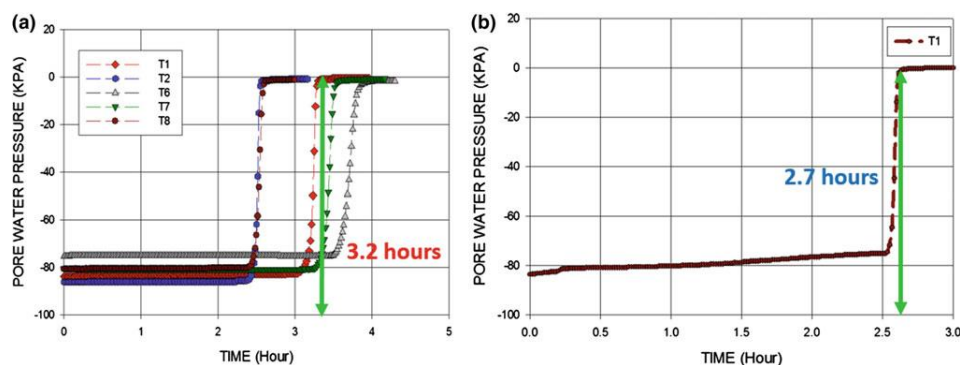


Figure 2.25 Variation of suction (a) post-earthquake rainfall test, (b) rainfall-only test (Tiwari et al., (2017a) [75]).

Among dual hazards, few studies investigated the failure of embankments subjected to post-earthquake rainfall by model experiments. Tiwari et al., (2017a) [75] compare the slope

stability in the case of rainfall only and post-earthquake rainfall. The movement of the wetting fronts with time for two laboratory-prepared models subjected to post-seismic rainfall and rainfall without earthquake is observed visually for comparison. The time it took for the wetting front to reach a certain point (point A in Figure 2.24) was also used to calculate the seepage velocity. Figure 2.24 clearly shows that the time necessary for total saturation of the model subjected to earthquake loading was longer than the time required for complete saturation of the model not subjected to any shaking. A comparison of the results from the tensiometers (Figure 2.25) also agrees with the observations made of the wetting fronts. As the wetting front passes through the position of the tension meter, suction rapidly reduces and reaches a value of zero. With the time required for the suction to reduce to a value of zero at the same location, the slope subjected to rainfall without an earthquake shows a smaller number than the slope subjected to post-earthquake rainfall. The instrumentation used in that study could only measure negative pore water pressure, so the above-calculated seepage velocities were used as input for the numerical analysis. Figure 2.26 shows that the factor of safety for the slope subjected to rainfall following earthquake shaking was higher than the slope subjected to rainfall without any earthquake shaking.

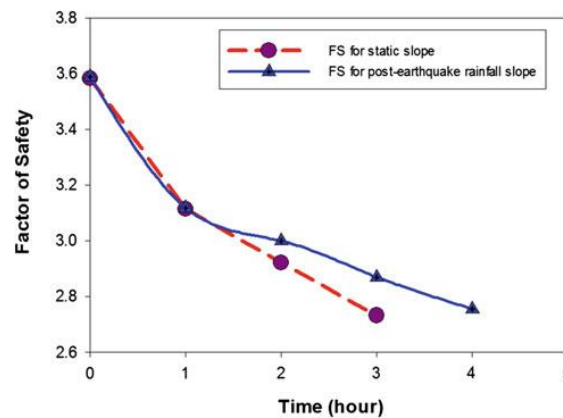


Figure 2.26 Comparison of safety factors in post-earthquake rainfall test and rainfall-only test (Tiwari et al., (2017a) [75]).

Tiwari et al., (2017b) [76] conducted similar research with different materials. A slope was shaken on a shake table with varied amplitudes and frequencies of seismic movements before being subjected to rainfall to measure the change in suction and seepage velocity. The investigation found that the seepage velocity dropped by around 40% following the shaking event. This is mostly due to a decrease in the slope's void ratio as a result of seismic stresses. The deformation and seepage velocity data from the laboratory tests were utilized to validate the numerical analysis. The change in the factor of safety of the slope with a length of rainfall in two cases is shown in Figure 2.27. For the reasons stated above, the static factor of safety was lower than the post-earthquake factor of safety. In that study, slopes compacted at lower relative densities (larger void ratios) settled following seismic loading, increasing soil

density. That phenomenon lowered the seepage velocity in the slope and increased the safety factor.

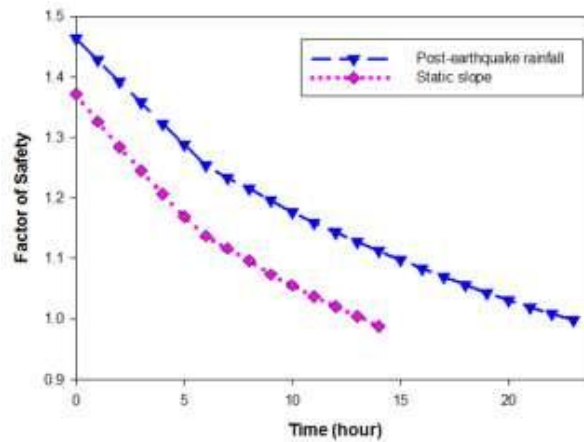


Figure 2.27 Comparison of safety factors in post-earthquake rainfall test and rainfall-only test (Tiwari et al., (2017b) [76]).

Kawamura et al., (2016) [31] and Kawamura and Miura (2014a) [29] clarified the rainfall-induced failure of volcanic slopes subjected to earthquakes for both water contents. Figure 2.28 shows the behavior of pore water pressure and the changes in the degree of saturation, respectively for $w_0=37\%$. In that case, with a prior cyclic loading of 280 gals, a shear strain of $\gamma=2.8\%$ was obtained in the model tests. In this situation, basement pore water pressure and saturation (pw2 and sm2) progressively rise with time. The first slope failure (failure 1) is caused by changes in pore water pressure and saturation degree at the toe of the slope. After that, the second slope failure (failure 2) is caused by developments of pore water pressure and saturation degree at the crown (pw1 and sm1). The model test was then continued until it reached the same depth as the slip line at 38%. (final failure). The schematics of slope forms during model tests are shown in Figure 2.29. It is clear that the failure pattern is nearly similar to that without cyclic stress (rainfall only).

The test for $w_0=43\%$ is similarly conducted, as shown in Figure 2.30. A shear strain of $\gamma=1.6\%$ was created by cyclic loading of 280 gals in advance for the model slope of $w_0=43\%$. Despite the fact that pore water pressure is considerable, as illustrated in Figure 2.30(a), rainfall-induced collapse does not occur in this situation. This is due to cyclic loadings increasing both slope density and saturation degree. Indeed, following seismic loadings, the degree of compaction D_c increased by up to 23% compared to the starting condition, and the degree of saturation rose by 1% (see Figure 2.30(b)). For model slopes having $\gamma=1.6\%-4\%$ for $w_0=43\%$, a similar result was obtained. In contrast, slope failure occurred for model slopes having less than $\gamma=1.6\%$.

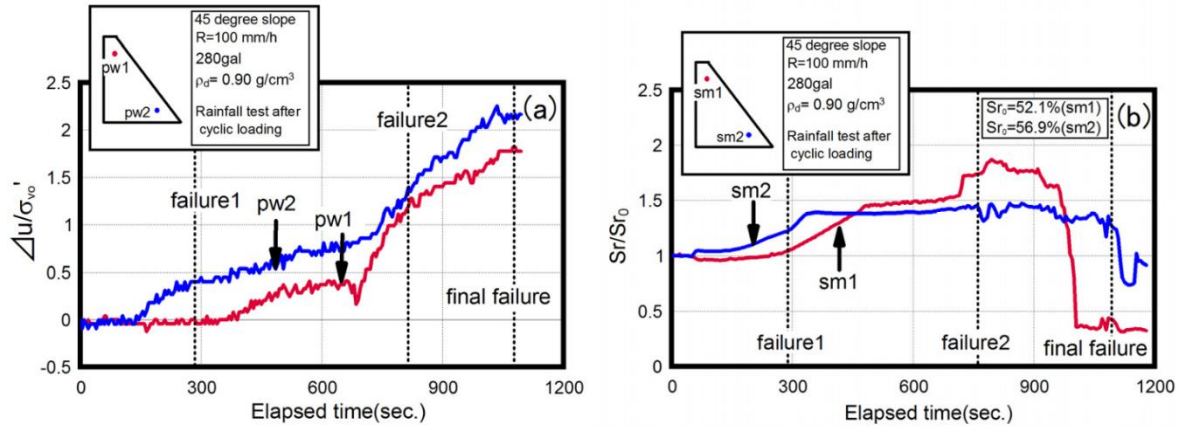


Figure 2.28 Changes in pore water pressure and saturation degree during rainfall test after cyclic loadings for $w_0=37\%$: (a) pore water pressure, (b) saturation degree (Kawamura and Miura (2014a) [29]).

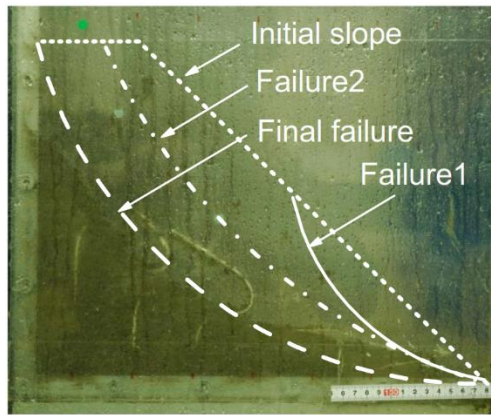


Figure 2.29 Schematics of failed slope shape for $w_0=37\%$ (Kawamura and Miura (2014a) [29]).

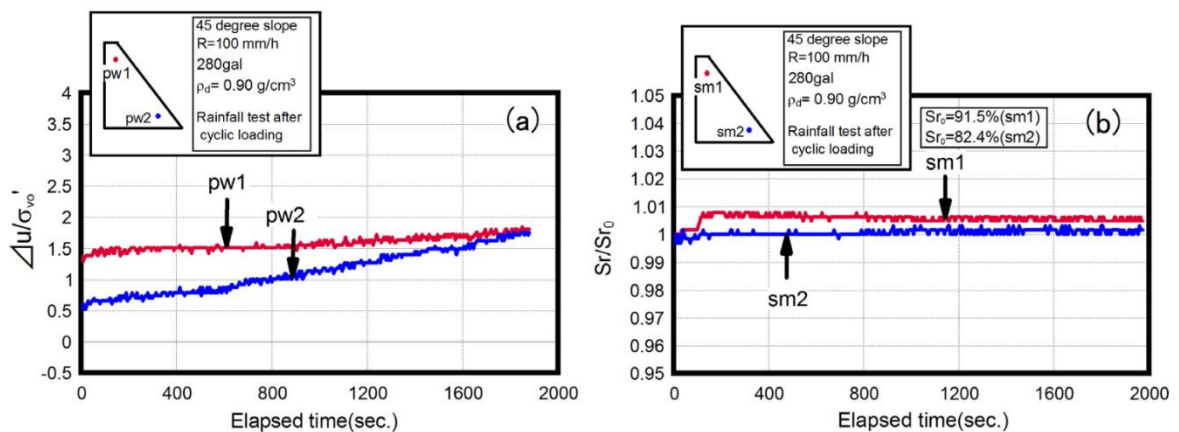


Figure 2.30 Changes in pore water pressure and saturation degree during rainfall test after cyclic loadings for $w_0=43\%$: (a) pore water pressure, (b) saturation degree (Kawamura and Miura (2014a) [29]).

The relationship between the failure time ratio in both cases and shear strain caused by cyclic loadings is summarized in Figure 2.31. In which, the failure time ratio is the elapsed time at ultimate failure normalized by that of the rainfall only in the case of $w_0=37\%$. As can be seen, the elapsed time at failure reduces with increasing shear strain in the case of $w_0=37\%$, while it slightly increases until $\gamma=1\%$ and then declines for more than $\gamma=4\%$ in the case of $w_0=43\%$. For the instance of $w_0=43\%$, there is no failure zone in the range of seismic-induced shear strain from 1.6% to 4%. As can be seen, slope failure seems to change depending on the stress-strain history caused by cyclic loadings.

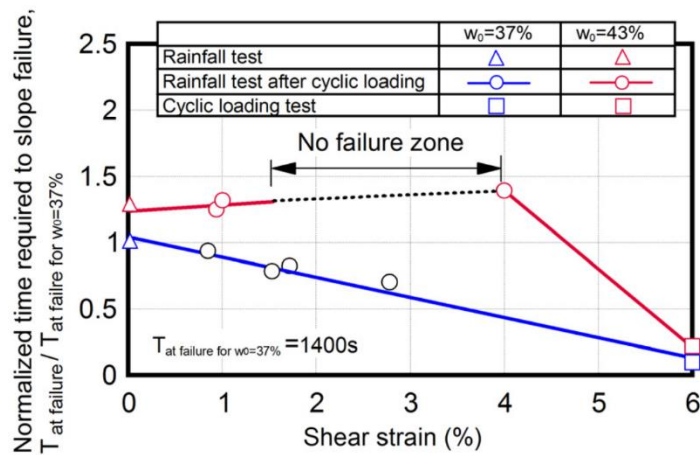


Figure 2.31 Required time until slope failure (Kawamura and Miura (2014a) [29]).

2.4.1.4. Research on Post-rainfall earthquake by model test

In the case of post-rainfall earthquakes, the number of research is even smaller than in the above case. Tiwari et al., (2013) [73] poured rainfall of 0.5 mm/min at two slopes constructed by loose sand with 30 and 40 degrees in 3 hours. The real-time moisture meter is not used during the test. Instead, soils at different locations were taken to measure saturation at the end of the experiment, as shown in Figure 2.32. Besides, shear strength was also measured with the direct shear device. That strength corresponding degree of saturation is shown in Figure 2.33. As can be seen, when the degree of saturation increases, apparent cohesion drops. For all points after the rainfall test, the friction angle was changed to about 30° from 34° in dry conditions. The data are used for stability analysis, which indicates that a seismic coefficient of 0.21 is enough to cause failure. However, the slope catastrophically failed at a seismic acceleration of 0.5g. The above-mentioned decrease in cohesion due to previous rainfall may result in failure when the slope is subjected to a subsequent earthquake. It is quite obvious that the value of allowable load when designing with software is smaller than the actual destructive force, which ensures safety for the design.

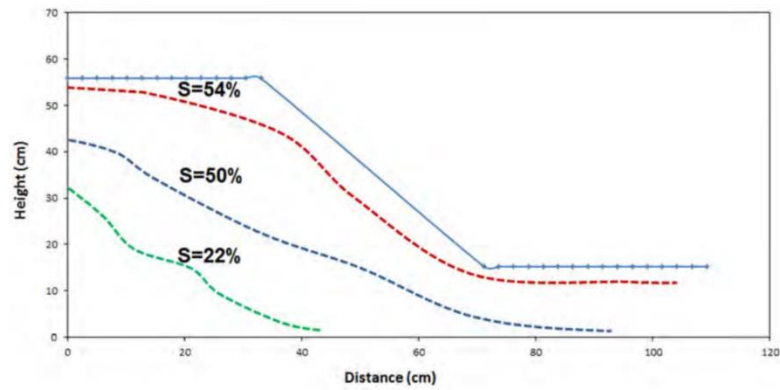


Figure 2.32 Changes in saturation degree in the embankment after 3 hours of rainfall (Tiwari et al., (2013) [73]).

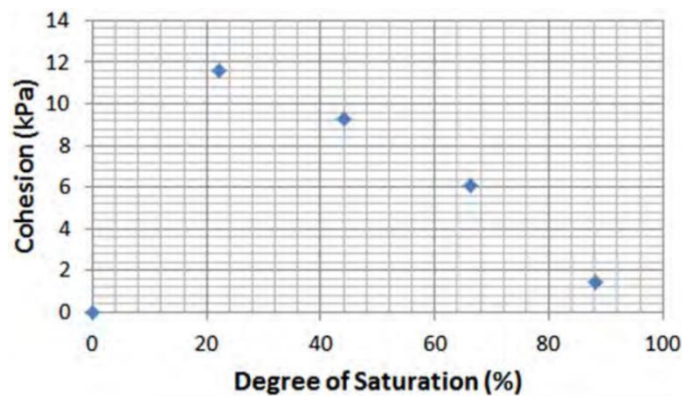


Figure 2.33 Changes in cohesion with saturation degree (Tiwari et al., (2013) [73]).

Tiwari et al., (2016) [74], based on the experimental results on soil samples collected from Southern California, conclude that both the rainfall before and after the earthquake can lead to the instability of the slopes. The infiltration rate of rainwater in the slope is increased by the earthquake effect. Therefore the seepage rate in the case of rainfall after the earthquake will be higher than in the reverse case.

2.5 Research of physical and mechanical properties of volcanic soils

Because of the specific behavior of volcanic soil as discussed in Chapter 1, the study of the mechanical and physical properties of this soil has attracted the interest of many authors around the world. Ng & Chiu (2001) [55] performed a series of triaxial tests and found that saturated loose volcanic soils behave like clay or sand under different conditions of stress path. Nguyen et al., (2018) [57] conducted column tests and numerical analyses to investigate differences in the amount of infiltration and runoff water between bare and grassed volcanic soil. Miura et al., (2003) [51] clarified the mechanical behavior of coarse-grained volcanic soils in Hokkaido, Japan, and evaluated the effect of particle breakage on their mechanical behavior. Ng and Pang (2000) [56] investigated the soil–water characteristic curve of completely decomposed volcanic soil in Hong Kong with different initial conditions by a conventional and a newly modified extractor. Hernandez et al., (2018)

[15] used mineralogical characterization tests and thermogravimetric analysis and found the high irreversibility of the characteristics of compacted volcanic soils depending on the water content before compaction.

As discussed in Chapter 1 on the importance of fine particle content to the mechanical behavior of volcanic soils, studies on this issue were widely performed by elemental tests. Liu and Yang (2014) [40] investigated the small-strain shear modulus of volcanic soil from northeastern Japan and found that this parameter rises significantly when particles smaller than 63 μm are removed from the original soils. Matsumura and Tatsuoka (2019) [44] demonstrated that the compacted volcanic soil's dry density and the molding water content have a notable effect on its cyclic undrained strength; however, the trend of these relationships varies depending on the content of the fine particles. Dao (2018) [7] studied the piping and the boiling phenomenon of saturated Komaoka volcanic soil (see Figure 2.34).

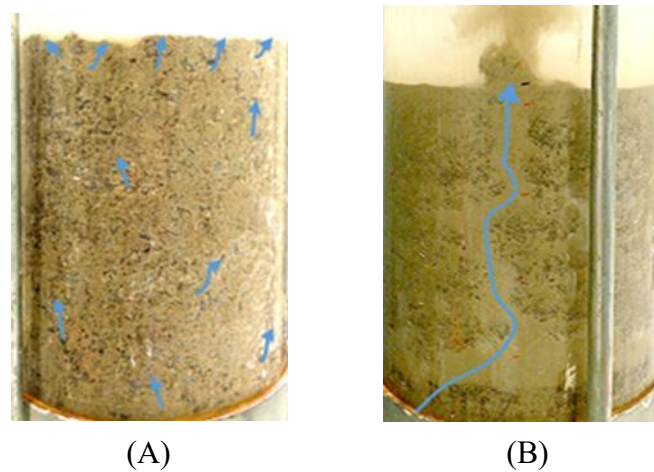


Figure 2.34 Piping test results of Komaoka volcanic soils: (A) piping, (B) boiling (Dao (2018) [7]).

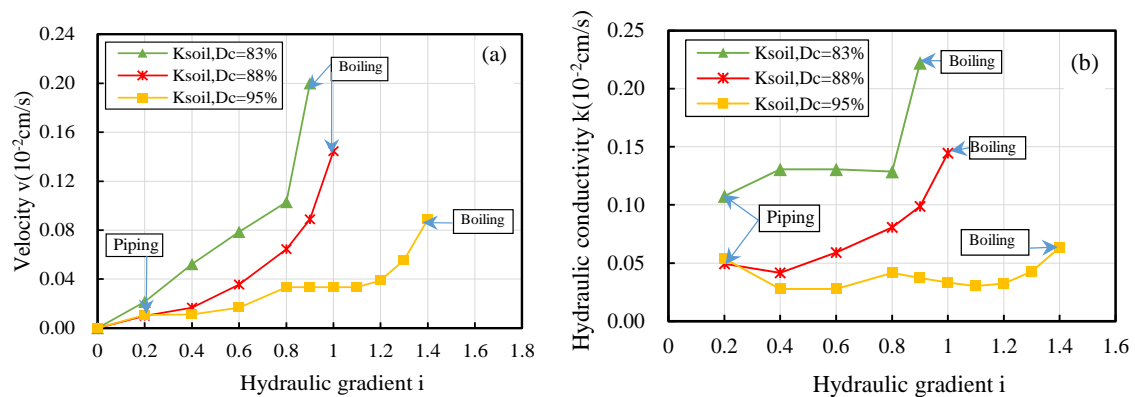


Figure 2.35 Change in results of Ksoil with different compaction degrees (a) velocity (b) hydraulic conductivity (Dao (2018) [7]).

Before discussions on the effect of fines content, the relationship between hydraulic gradient and flow velocity of Komaoka volcanic soil with the different degrees of compactions D_c of 83, 88, and 95% were investigated, as shown in Figure 2.35. As can be seen, internal erosion started at $i=0.2$ in all cases. The erosion process caused the migration of fine particles inside the pores of coarse particles. When $i=0.2$, a little fine particle was lost from the test specimen in the K_{soil} with $D_c=83\%$. This leads to a rise in void ratio, as well as an increase in hydraulic conductivity until $i=0.4$. From that point to $i=0.8$, the relationship between hydraulic gradient and hydraulic conductivity was recognized as approximately linear at this stage, and internal erosion was not detected during that time. In contrast, the permeability of the K_{soil} with compaction degrees of 88% and 95% is reduced until $i=0.4$. This might be because the process of soil compaction causes a significant decrease in the pore size of the samples, preventing the movement of fine particles and incorporating them into the filter fabric. After $i=0.4$, fine particles were washed out by seepage flow. As a result, effective porosity increased, resulting in an increase in permeability. Finally, the phenomenon of “boiling” occurred. These results suggest that the performance of the primary fabric of samples constructed by Komaoka volcanic soil can be influenced by the degree of compaction. The main fabric serves as a filter for fine particles carried by seepage flow. A high degree of compaction for the same volcanic soil sample results in a high value of the critical hydraulic gradient for the start of boiling. Yet, the internal erosion process of compacted materials with $D_c>88\%$ is nearly the same.

The results of piping tests of saturated Komaoka volcanic soil with different fine contents but the same dry density and water content at compaction are shown in Figure 2.36. In the figure, the hydraulic behavior of these test samples was similar and indicated that the internal erosion according to Darcy’s law occurred in all samples. As can be seen in the relationship between hydraulic gradient i and velocity v (Figure 2.36(A)), the piping phenomenon occurred early at $i = 0.2$, and the critical hydraulic gradient corresponding to the occurrence of the boiling phenomenon was 1.4, 1, and 0.6 for $K_{8.5A}$, K_{soil} , and K_{40A} , respectively. This implied that the permeability of compacted volcanic soil is affected by the increase in fine grains. Furthermore, the difference in hydraulic conductivity of $K_{8.5A}$, K_{soil} , and K_{40A} as shown in Figure 2.36(B) was explained by the fine grains clogging to coarser particles and then being released. The tendency of water to flow through the pore network and wash out the fine particles was particularly obvious in samples with high fine content such as K_{40A} . The loss of fine particles increased permeability and led to internal instability of the soil, so the boiling phenomenon of sample K_{40A} was recorded with the smallest hydraulic gradient.

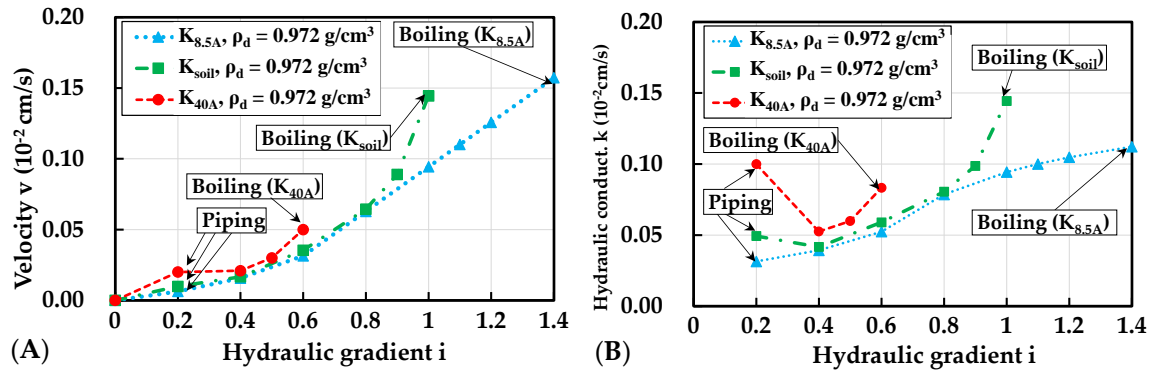


Figure 2.36 Piping test results of Komaoka volcanic soil (A) velocity (B) hydraulic conductivity (Dao (2018) [7]).

Due to obvious difficulties, the number of studies on the effect of fine particle content using modeling experiments is very limited. Kawamura and Miura (2013) [27] Kawamura and Miura (2014a) [29] investigated the increment of fines content before and after different tests ΔFc (%) for many types of volcanic soil, as shown in Figure 2.37. ΔFc rises as the initial water content increases. It is important to mention that particle breakage rises with rainfall-induced stress histories. This means that failures of unsaturated volcanic slopes with crushable particles can be attributed to a shearing resistance decrease caused by particle breakage during rainfall. Miura et al., (2003) [51] reported that reduction in shearing resistance caused by particle breaking. Accurate estimation of the softening of slope surfaces is important for the stability of volcanic slopes; in particular, its influence is attributed to the reduction of shearing resistance due to particle breakage.

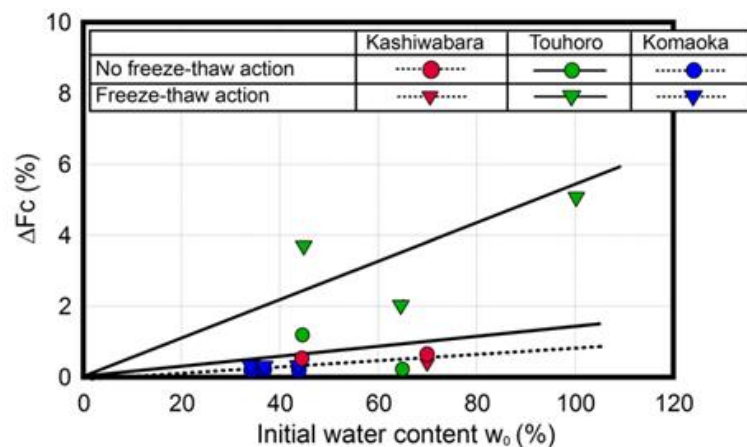


Figure 2.37 Changes in the increment of finer content ΔFc after rainfall test (Kawamura and Miura (2014a) [29]).

2.6 Summary

The slope stability under the effect of rainfall and earthquakes has been studied for a long time by various methods. Especially after the proposal of Rocha (1957) [61], the model

was applied to bring understanding in many areas of geoengineering. This method has been applied to study the failure mechanism of embankments under the independent effect of rainfall (Kawamura 2013), and earthquake (Kawamura 2014). The model is also initially applied to study the mechanism of double disasters such as in the case of post-earthquake rainfall ([75], [76]), and post-rainfall earthquakes ([73], [74]). However, the results still have many limitations due to objective difficulties. With the development of current equipment, these studies need to be completed. Despite the wide occurrence of volcanic soils and the hazards associated with their tendency to become highly unstable during earthquakes and heavy precipitation, there are relatively few published studies on their geotechnical characterization, much fewer attempts to identify common properties and formulate a generic model for their behavior. Based on an analysis of the current state of research in this area, the remaining issues include:

- Studying the earthquake-induced failure mechanism of volcanic embankments subjected to rainfall based on the results of model experiments;
- Influence of fine grain content and initial water content on the stability of embankment under the independent and combined effects of rainfall and seismic loadings:
- Compare the impact order of rainfall and earthquake on the slope failure.

Therefore, these problems were focused to solve on in the following chapters.

CHAPTER 3:

SOIL MATERIALS AND TESTING METHODS

3.1 Introduction

To fill in the gap of knowledge discussed in Chapter 2, Komaoka volcanic coarse-grained soils were reconstituted as samples for model experiments in this study. This chapter presents the physical and mechanical properties of the test specimens. The data on soil material including compaction characteristics was investigated in previous research. Because of its importance to this study, it was briefly summarized and further explained and discussed. After that, the specifications of the test apparatus which contains a shaking table and spray nozzle were shown. During the tests, measuring devices including pore water pressure transducers, soil moisture meters, and acceleration meters were utilized to provide an understanding of the failure of volcanic embankments under rainfall and seismic loadings. The similarity laws used in model tests were built and the preparation of the model embankment was illustrated. In order to provide fundamentals and to grasp the effects of geotechnical conditions on the mechanical behavior of volcanic coarse-grained soils, the test conditions were chosen with various cases of initial water content, and fine particle contents, ... Besides, the influence of external factors were clarified with the dissipation time between rainfall and earthquake, or the order impact of rainfall and earthquake in test conditions.

3.2 Test materials

The original material used in this study is the volcanic coarse-grained soils derived from Shikotsu caldera's ejecta, Hokkaido, Japan (see Figure 3.1). This soil, hereafter referred to as Komaoka volcanic soil, is the sample adopted for the construction of a series of physical model tests as well as the full-scale embankment (e.g., Chapter 5). It is estimated that the eruption age for Komaoka volcanic soil belonging to Shikotsu primary tephra was 31,000 ~ 34,000 years and was flow deposits (the notation is Spfl; Shikotsu pumice flow deposits). Spfl is the same type of Shikotsu caldera liquefied by the 2018 Hokkaido Eastern Iwate Earthquake, as reported in [33]. Besides, volcanic soils, including Spfl, which have been utilized for residential embankments have repeatedly liquefied due to the strong earthquakes

in the past; examples include Hokkaido Nansei-oki (1993), Hokkaido Toho-oki (1994) and Tokachi-oki (1968 and 2003). The physical properties of Spfl in comparison with those of Toyoura sand are shown in Table 3.1. The natural water content of Spfl is ignored in this table because it is easily changed in the event of rainfall or earthquakes due to its loose deposition in nature. The fines of Komaoka volcanic soil were classified into non-plastic material (NP) according to Atterberg limits, the liquid limit is 46.7%, plastic limit is NP).

Table 3.1 Physical properties of Komaoka volcanic soil and Touyouura sand

Parameters	Komaoka volcanic soil	Touyouura sand
Soil particle density, ρ_s (g/cm ³)	2.47	2.68
Maximum void ratio, e_{max}	2.25	0.96
Minimum void ratio, e_{min}	1.21	0.64
Mean grain size, D_{50} (mm)	0.27	0.18
Coefficient of uniformity, U_c	46	1.5
Natural fines content, F_c (%)	26.0~42.6	0

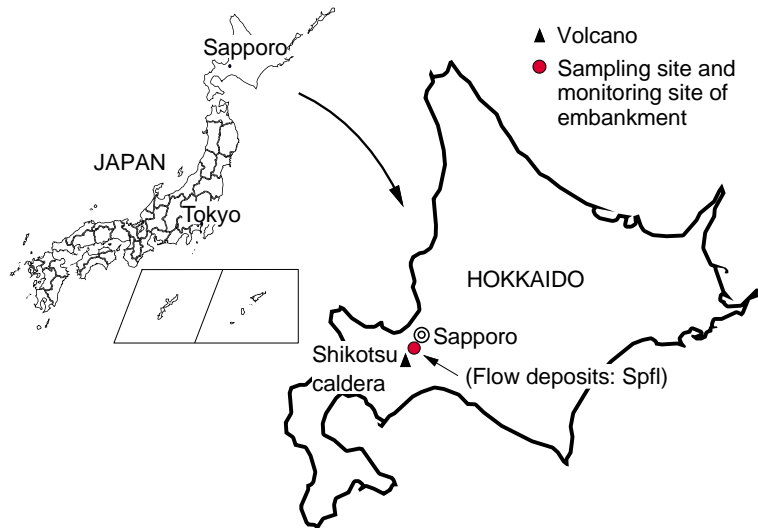


Figure 3.1 Locations of sampling and monitoring site of embankment in this study

Similar to elemental experiments, the material sample K_{soil} ($F_c = 27\%$) in this study was obtained by removing particles larger than 9.5 mm from the Spfl to reduce errors due to the scale effect. As discussed in Chapter 2, Hieu et al., (2017) [16] used the elemental experiment to investigate the influence of fine particle content on the hydraulic activity and permeability of Komaoka volcanic soils, which will be verified and compared in this study. In that way, the experimental samples were prepared in the same manner as in [16]. From K_{soil} , the fine particle content was adjusted to produce samples $K_{8.5A}$ ($F_c = 8.5\%$) and K_{40A} ($F_c = 40\%$). The grain size distribution, which was determined according to the procedure

in JGS 0131-2009 [22], and the physical properties of the test samples are shown in Figure 3.2 and Table 3.2, respectively.

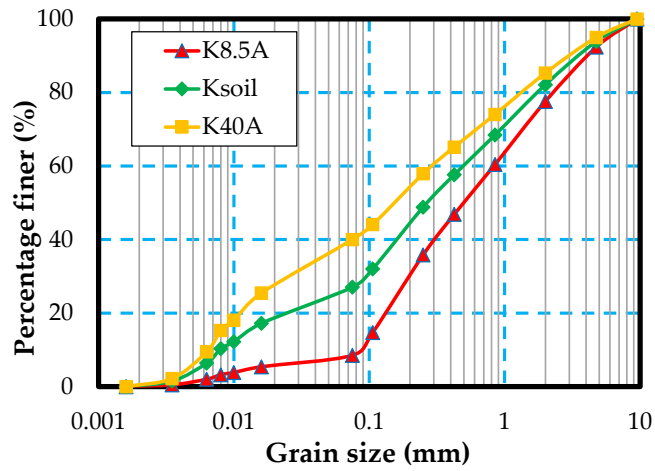


Figure 3.2 Grain size distribution of test samples in this study, according to [23].

Table 3.2 Physical properties of test samples in this study.

Parameters	K _{8.5A}	K _{soil}	K _{40A}
Fine particles content, F_c (%)	8.5	27	40
Optimum water content, w_{opt} (%)	35.81	34.32	31.20
Maximum dry density, $\rho_{d max}$ (g/cm ³)	1.0412	1.1049	1.1241
Mean grain size, D_{50} (mm)	0.50	0.27	0.16
Uniformity coefficient, U_c	10.6	62.5	42.8
Soil particle density, ρ_s (g/cm ³)	2.5289	2.5203	2.5134
Maximum void ratio, e_{max}	2.76	2.25	2.46
Minimum void ratio, e_{min}	1.30	1.21	1.25

Since Komaoka soil particles are fragile and easily broken by compaction [16], the compaction curves of the test samples in this study are determined by a non-repetitive method (A-b method of JGS 0711-2009 [23]), as shown in Figure 3.3. The compaction effort was equal to 550 kJ/m³. Although the optimum water content is different, the peaks of these curves are all located near the line of $S_r = 65\%$. As can be seen, the optimum saturation is almost similar with different fine content. The dry densities corresponding to these peaks are called the maximum dry density $\rho_{d max}$ and were used as the base data to calculate the compaction degree D_c in the model experiments, such as the test conditions in Section 3.3.3. The influence of fine particle content on optimum water content and maximum dry density, obtained from these three compaction curves, is shown in Figure 3.4. As can be seen, an increase in fine content leads to an increase in the maximum dry density, but a decrease in optimum water content. Compaction by standard mortar or by roller in model tests is a

process by which soil particles rearrange to reduce volume and increase density. Therefore, soils with a higher fine content more readily allow fine grains to enter the voids between larger particles, resulting in easier compaction and density increase. However, greater density also means less porosity and space to hold water. Figure 3.5 shows the maximum and minimum void ratio according to JGS 0161-2009 [24]. In the figure, the increase in fine content also leads to a decrease in the minimum void ratio. The compaction behavior of soil samples with different fine content shows a similar trend between dry conditions and optimum water content conditions. In contrast, the maximum void ratio in Figure 3.5 related to the loose condition shows that the K_{soil} has a higher dry density or lower void ratio than $K_{8.5A}$ and K_{40A} . In addition, the variation in e_{max} was higher than that in e_{min} , predicting that an increase in compaction degree reduces the effect of fine particle content.

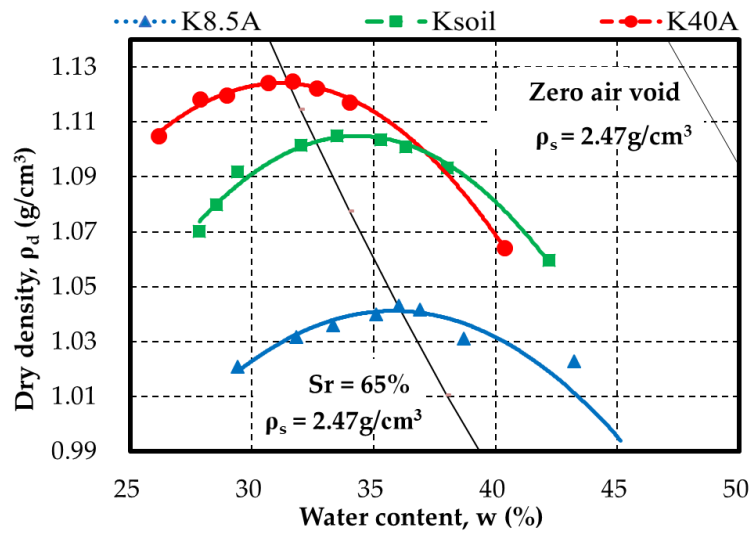


Figure 3.3 Compaction curve of test samples in this study, according to the A-b method [16].

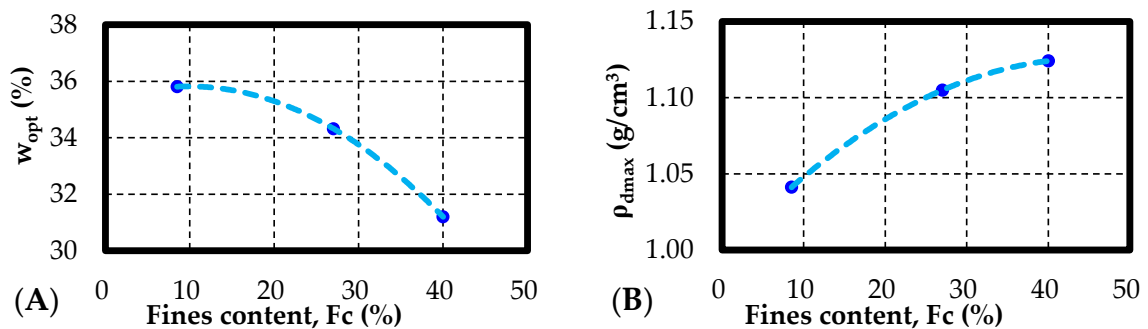


Figure 3.4 Influence of fines contents on compaction features of Komaoka volcanic soil (A) optimum water content w_{opt} , (B) and maximum dry density ρ_{dmax} .

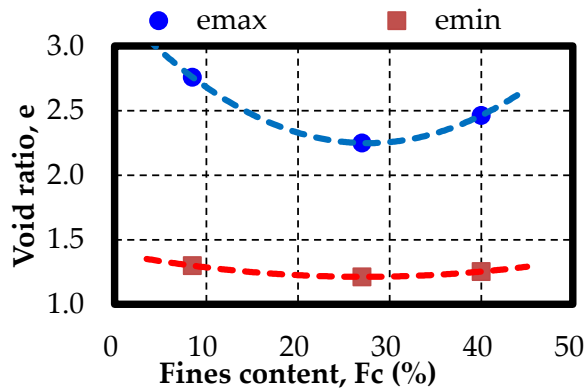


Figure 3.5 Maximum and minimum void ratio of Komaoka volcanic soils with different fine particle contents.

Due to the size of the test apparatus, the influence of different fine contents on soil particle density cannot be taken into account by experiments. Therefore, the soil particle density ρ_s for $K_{8.5A}$, K_{soil} , and K_{40A} in this study were calculated by the formula in Equation (1) and data proposed by Matsumura (2014) [43]:

$$\rho_s = \sum \rho_{si} x_i \quad (3.1)$$

where ρ_{si} is the soil particle density of each grain size shown in Table 3.3 and x_i is the content of this size in the soil sample.

Table 3.3 Soil particle density of each grain size [43].

Grain Size (mm)	4.75 ~ 9.50	2.00 ~ 4.75	0.85 ~ 2.00	0.425 ~ 0.85	0.25 ~ 0.425	0.106 ~ 0.25	0.075 ~ 0.106	<0.075
Index i	1	2	3	4	5	6	7	8
Soil particle density, ρ_{si} (g/cm ³)	2.595	2.591	2.569	2.587	2.519	2.444	2.414	2.484

3.3 Test apparatus and procedures

3.3.1 Test equipment

Table 3.4 Specifications of the shaking table used in this study

Parameters	Value
Maximum loading weight (N)	1500
Amplitude	±50 mm
Frequency	0.05Hz ~ 5 Hz
Wave	Regular wave (sinusoidal form)
Control system	AC-Servo motor, Hydraulic control

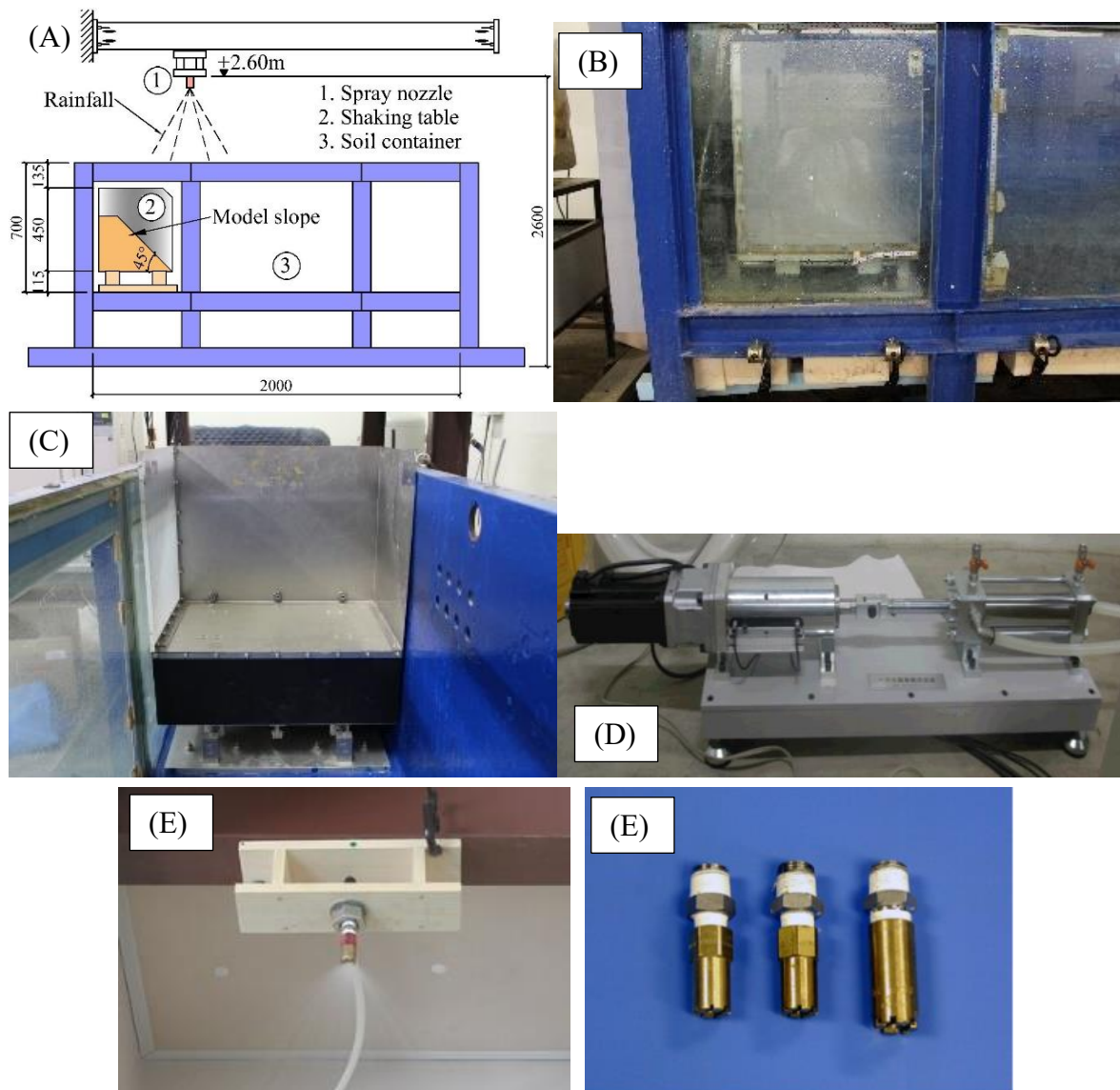


Figure 3.6 Overall view of test apparatus in this study. (A) Overall view (B) Side view (C) Front view (D) 1-dimensional vibration loading device (E) Spray nozzle.

Figure 3.6 shows the overall view of the test apparatus used in this study to investigate the behavior of embankments subjected to rainfall and earthquakes. The internal dimensions of the model soil tank are 2000 mm long, 700 mm high, and 600 mm wide. The side of this tank is fitted with a 20 mm thick tempered glass to allow monitoring of the deformation and phenomena occurring with the slope during the tests. In the soil tank, the model embankment was prepared in a shaking table with dimensions of 400 mm in length, 450 mm in height, and 580 mm in width. Friction on the sides of this table is eliminated by applying grease. The computer controls the one-dimensional vibration loading device attached under the shaking table through a hydraulic cylinder to apply a wave with specifications shown in Table 3.4. The support system for the spray nozzle can be adjusted

in position and height so that the entire slope receives rainwater, and the rainfall intensity is managed by the valve system. Two digital cameras were used to record the phenomena on the front and side of the slope. Rainfall from the slope bottom was drained by a pump as necessary.

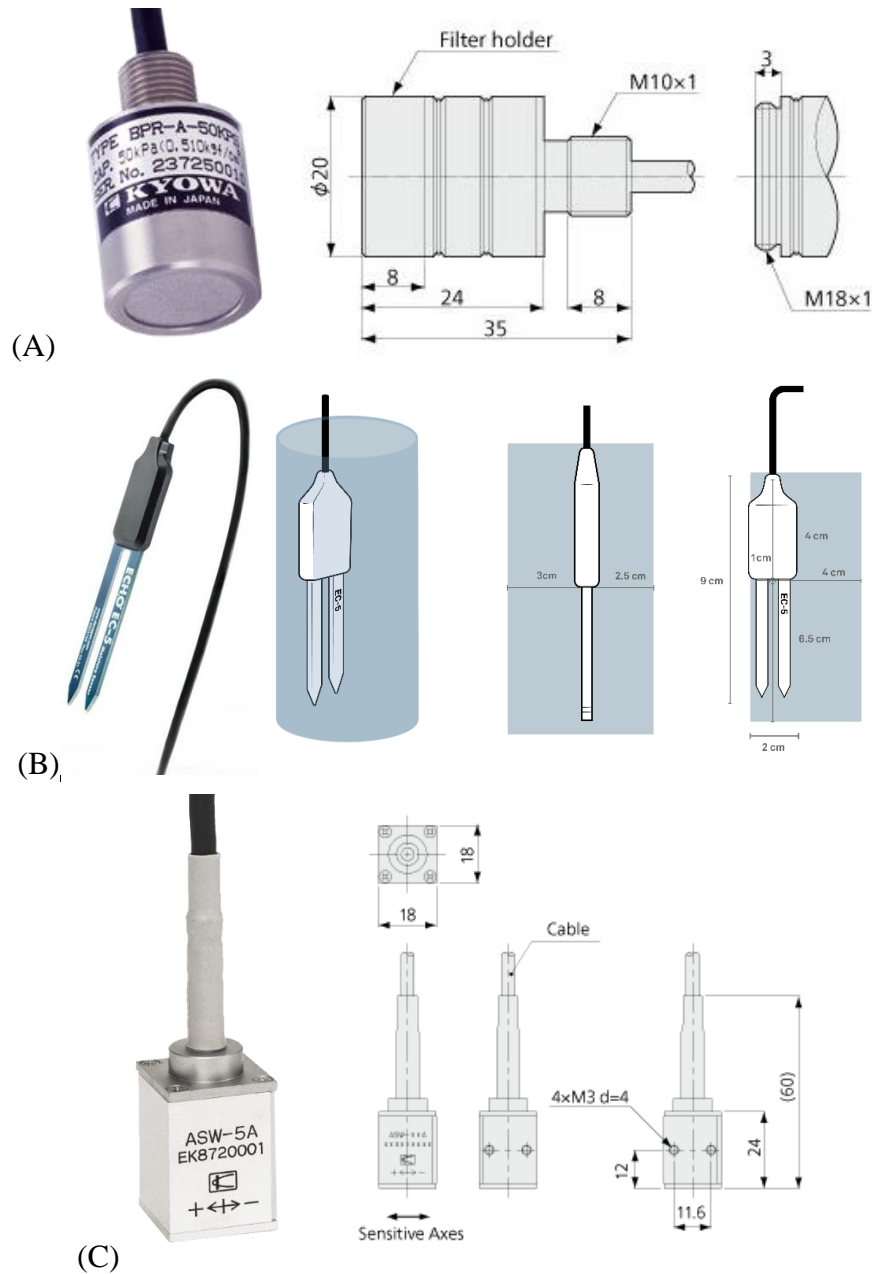


Figure 3.7 Measuring devices in this study (A) Pore water pressure transducer (B) Soil moisture meter (C) Acceleration meter

The types of measuring devices used in this study are listed in Table 3.5. All devices are small-sized gauges for model experiments (see Figure 3.7). Through the soil–water characteristic curve of compacted Spfl [43] as shown in Figure 3.8, Kawamura et al., (2021) [33] demonstrated that the influence of suction on the mechanical behavior of this soil can

be ignored when the saturation is greater than 60% along the wetting path. Thus, the use of BPR-A-50KPS to monitor pore water pressure in the post-rainfall earthquake experiments with high soil moisture conditions in this study is completely appropriate.

Table 3.5 Specification of measuring devices in this study

Measuring device	Pore water pressure transducer	Soil moisture meter	Acceleration meter
Type	Small-sized gauge for model experiments	Volumetric water content (VWC) sensor	Oil damping
Manufacturer	Kyowa	METER Group	Kyowa
Name	BPR-A-50KPS	ECH ₂ O EC-5	ASW-2A
Range	0 - 50 kPa	0 – 100% (VWC)	±19.61m/s ² (±2G)
Specifications	[36]	[46, 47]	[37]

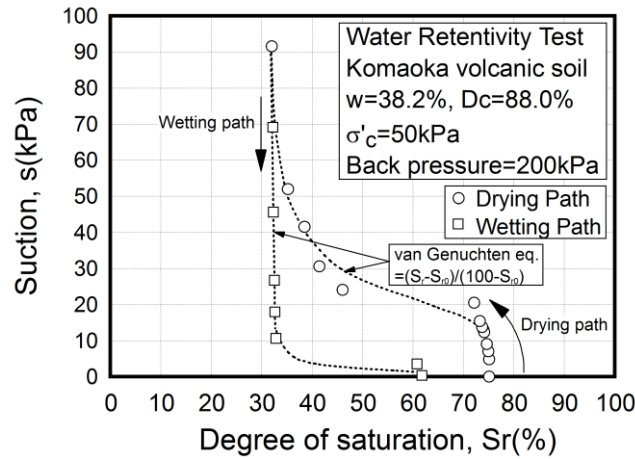


Figure 3.8 Soil-water characteristics curve of Komaoka volcanic soil [43]

Soil moisture meters were calibrated on several slope density conditions. However, variations in soil moisture attributed to dilatancy induced by the deformation of slopes during model testing were not evaluated in Chapter 4 due to the difficulty in defining their behavior. The measured volumetric water content θ was used to calculate the water content w and saturation degree S_r discussed in Chapter 4 by Equations (3.2) and (3.3).

$$w = \frac{\theta \rho_w}{\rho_d} 100\% \quad (3.2)$$

$$S_r = \frac{w \rho_s}{e} = \frac{w \rho_s}{\frac{\rho_s \rho_w}{\rho_d} - 1} \quad (3.3)$$

Which, ρ_d is the dry density of samples shown in Table 3.6, and ρ_w is water density (1g/cm^3). ρ_s is above-mention soil particle density, and e is the void ratio. The settings for these devices will be described in section 3.3.2.

3.3.2 Model embankment preparation

The shape and dimensions of the model embankments with the locations of measurement equipment are depicted in Figure 3.9. In this study, three acceleration meters, three pore water pressure transducers, and six soil moisture meters were used. Besides, the shear strain γ was calculated from the displacement of the six kite strings inserted during the preparation of the slope model (see Figures 3.10 and 3.11). Shear strain, acceleration, pore water pressure, and saturation degree were the parameters for understanding the slope failure mechanism.

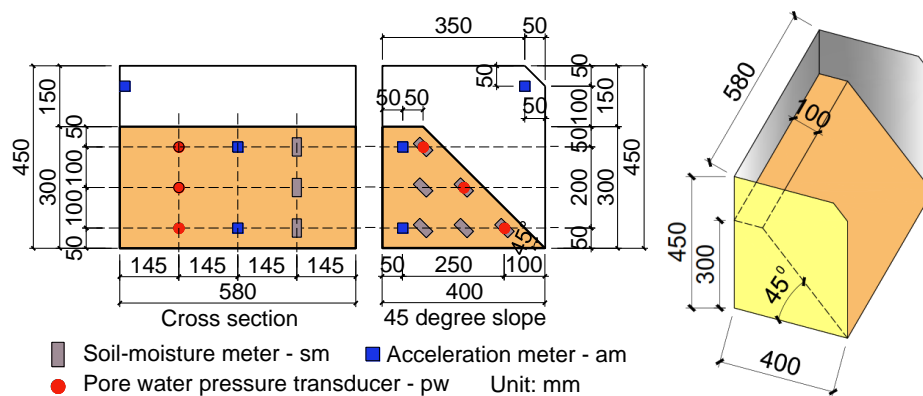


Figure 3.9 Shape and dimensions of model embankments and setting positions of measuring instruments.



Figure 3.10 The initial shape of the model embankments (A) front view (B) side view.

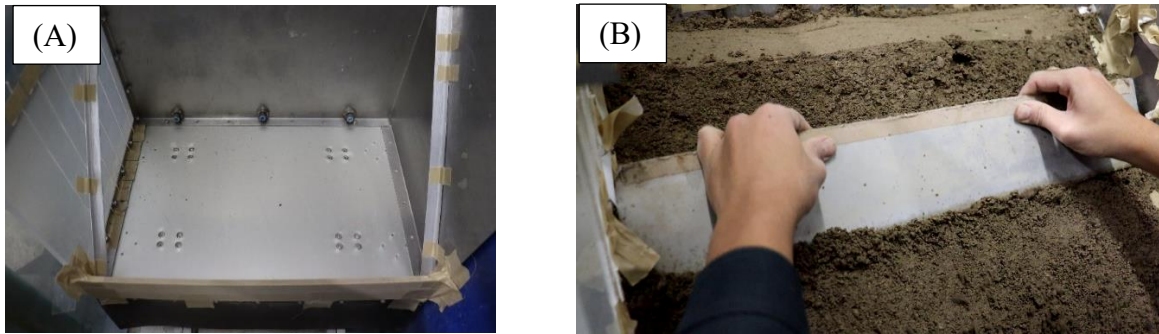


Figure 3.11 Slope preparation (A) Kite strings and side aluminum sashes (B) Excessive soil removal

The slope preparation method:

The volume of the embankment was calculated from the dimensions and shape of the model embankment shown in Figure 3.9. The volume and density in Table 3.6 were then used to compute the required soil mass for the test. Finally, the mass of dry soil and water was determined by the initial water content in Table 3.6. The soil is dried in an oven at 110⁰C for at least 1 day before being mixed with water. Two aluminum sashes were installed on either side to provide the slope with a defined shape and angle (see Figure 3.11). The sample was then sprinkled and settled uniformly to be homogeneous. For each 5 cm thick layer, a roller with a weight of 127.4N was used to compact to ensure dry density (degree of compaction) for the whole slope. The number of compactions is 4 times per 1 layer. The fluctuation in dry density during compaction is limited to 5% to reduce the effect of the variance in compaction density on the failure behavior. The compaction process at the initial water content is carried out so that the constituent particles are not broken. This process was continued until the embankment reached the specified height. After that, excess soil was removed from the slope surface by carefully sliding the iron plate with a sharp cutting edge on the aluminum sashes.

3.3.3 Test conditions

Since the three soils have different optimum water content, the curves in Figure 3.3 are adjusted as shown in Figure 3.12 by normalizing the water content with the optimum water content of each soil type. As shown in figure 3.12, the test cases in this study are marked with the symbol ■, which lies on the dashed lines representing the compaction degree of $D_c=90\%$ by compaction method in model tests described in section 3.3.2. This degree of compaction was chosen to reduce the effect of internal erosion as discussed in Chapter 2. Similar to maximum dry density, optimum water contents were used as the base to determine the initial conditions of the tests in this study as shown in Table 3.6.

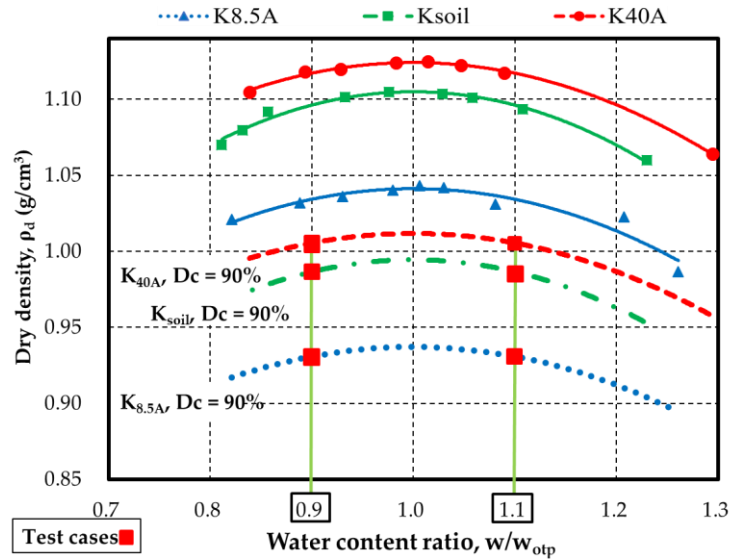


Figure 3.12 Adjusted compaction curves and test conditions

Figure 3.13 shows the relationship between permeability and initial water content by Dao (2018) [7] and Matsumura (2014) [43]. To examine that by model test and focus on the effect of initial water content on the mechanical behavior of compacted volcanic soils, the initial water content ratio w_0/w_{opt} is set at 0.9 and 1.1, representing the dryer and wetter sides of the optimum water content (in practice, the soil is usually compacted around w_{opt} in Japan). Through comparison, the influence of the difference in initial water content during compaction in the same dry density condition on the slope failure phenomenon was investigated. Because of the different specific initial water content values, these experiments are collectively referred to as the "dry cases" and the "wet cases" for all 3 kinds of soil.

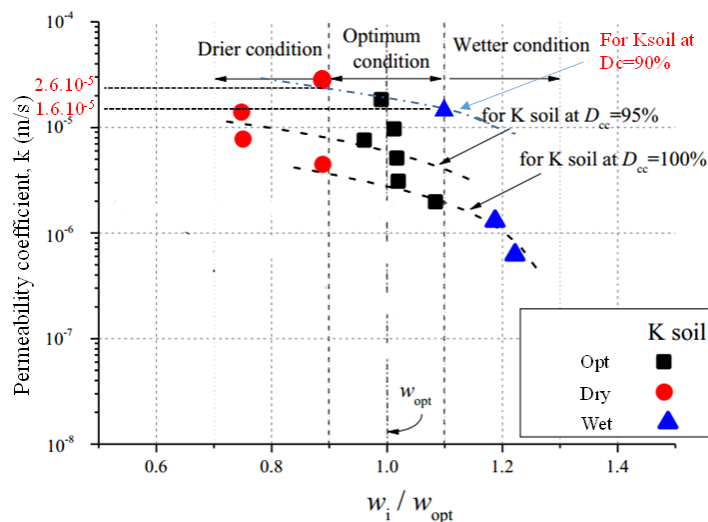


Figure 3.13 Relationship between permeability and initial water content (Dao (2018) [7] and Matsumura (2014) [43])

As discussed in previous Chapters, the effect of the impact order of external force was clarified by comparing the slope stability under post-rainfall earthquakes in this study with the results of post-earthquake rainfall cases in Kawamura et al., (2016). To ensure a basis for comparison, the experimental conditions in these cases were also chosen similar to those in Kawamura et al., (2016) [31], as summarized in Table 3.7. Besides, given the fact that real earthquakes might happen at any moment following the end of rainfall, seismic loadings in this study were applied to the model slope according to 3 typical cases based on different pore water pressure conditions before earthquakes:

- Case (i): pw1 is higher than pw2;
- Case (ii): pw1 and pw2 reach the lowest value;
- Case (iii): pw2 is higher than pw1.

in which, pw1 and pw2 are the pore water pressure at the upper part and lower part of the slope, respectively.

Table 3.6 Test conditions to clarify the effect of finer contents

Parameters	K_{8.5A}	K_{soil}	K_{40A}
Fines content (%)	8.5	27	40
Slope angle (⁰)	45	45	45
Length of base (mm)	400	400	400
Initial water content in dry cases (%)	32	31	28
Initial water content in wet cases (%)	39	38	34
Rainfall intensity (mm/h)	100	100	100
Acceleration (m/s ²)	2.8	2.8	2.8
Degree of compaction (%)	90	90	90
Dry density (g/cm ³)	0.93	0.99	1.00
Void ratio	1.72	1.55	1.50
Rainfall-only experiments			
Rainfall time (minutes)	≥30	≥30	≥30
Failure time in dry cases (minutes)	10	10	9
Failure time in wet cases (minutes)	8	14	15
Post-rainfall earthquake experiments (Dry cases)			
Rainfall time (min.)	5	5	4.5
Shear strain after rainfall (%)	3.88	4.68	3.11
Number of cycles	100, 200	100, 200	100, 200
Post-rainfall earthquake experiments (Wet cases)			
Rainfall time (min.)	4	7	7.5
Shear strain after rainfall (%)	4.70	4.37	3.89
Number of cycles	100, 200	100, 200	100, 200

Table 3.7 Test conditions to clarify the effect of impact order of external force

Parameters	Post-earthquake rainfall	Post-rainfall earthquake
	Kawamura et al., (2016) [31]	(This study)
Material	Komaoka volcanic soil	
Slope angle ($^{\circ}$)	45	
Length of base (mm)	400, 750	400
Initial water content	37, 43	
Degree of compaction (%)	85	
Dry density (g/cm^3)	0.9	
Rainfall intensity (mm/h)	100	
Acceleration (m/s^2)	2.8	2.8, 3.2
Number of cycles	20	

3.3.4 Similarity laws of model tests

Similar laws are the condition for selecting soil materials for the model test and also the basis for determining the magnitude of loadings and impacts applied to the model based on desired conditions in the prototype. Due to several inaccuracies such as the scale effect, the soil particle effect, and the confining pressure effect, it is difficult to precisely recreate mechanical behavior on model embankments, particularly in the 1g field. However, it is well known that physical modeling in model testing can enhance our knowledge (Kawamura et al., (2010) [26], Kawamura and Miura (2013) [27], Kawamura and Miura (2014) [30]).

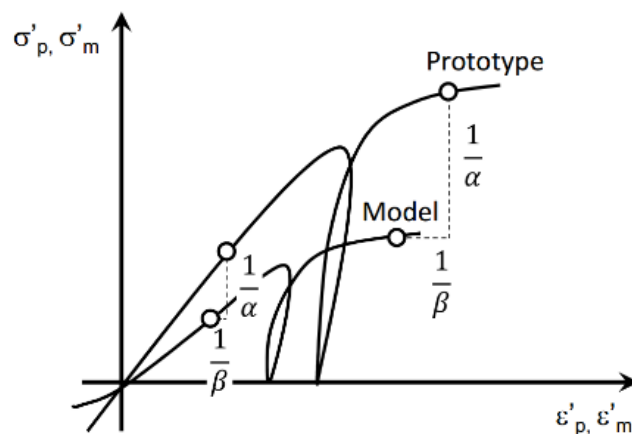


Figure 3.14 Stress-strain relationship between prototype and model (Rocha (1957) [61])

Figure 3.14 shows the first idea of Rocha (1957) [61] in his attempt to use the information obtained from model tests in geotechnical engineering: The material of the model must have a stress-strain diagram that is produced from the diagram of the prototype by multiplying the ordinates by $1/\alpha$ and $1/\beta$ in the vertical and horizontal axes. This condition

needs to be satisfied for any triaxial loading to which cylinders of the materials are subjected and for the strain in any direction. Then a physical modeling approach was suggested based on that stress-strain relationship, in which force ratios on mechanical behavior were synchronized in the model and prototype. It is obvious that rigid adherence to general similarity laws is not possible due to the complexity of soil properties. Accuracy here is required by the problem itself. As in soil mechanics, accepting simplified hypotheses changes the laws of similarity. For example, the deformation of the soil is assumed to be proportional to the stress when working in the elastic region. Then the similarity laws only require that the model materials have elastic moduli proportional to the similar modulus of the prototype and have an equal Poisson coefficient. Another simple case is problems that deal with failure and ignore non-linear relationships between stress and strain, the conditions apply only for stress and strain values at the time of failure, namely the cohesion and angle of internal friction. In contrast, for general problems, the number of conditions can be increased. For example, when it is necessary to consider strain as a function of time, the relationship graph of deformation and time of the homologous material should obey the similarity laws. When studying the flow of the liquid phase, to consider the buoyancy of the solid phase due to its immersion in the liquid phase, the porosity of the prototype and the model materials must be equal.

The stress(σ) - strain (ε) relationship of soil material in the model and prototype according to the concept in Figure 3.14 were presented by Equations (3.2) and Equation (3.3). Then the fundamental scaling (model/prototype) of length (L), time (T), density (ρ), and gravity acceleration (g) were shown in Equations (3.4) to (3.7).

$$\sigma_m/\sigma_p = 1/\alpha \quad (3.4)$$

$$\varepsilon_m/\varepsilon_p = 1/\beta \quad (3.5)$$

$$L_m/L_p = 1/\lambda \quad (3.6)$$

$$t_m/t_p = 1/\lambda_t \quad (3.7)$$

$$\rho_m/\rho_p = 1/\lambda_\rho \quad (3.8)$$

$$g_m/g_p = 1/\lambda_g \quad (3.9)$$

The interdependence between these scales needs to be eliminated in order to retain only the independent scales. First, the time scale is expressed as the scale of length and gravity acceleration as shown in (3.8). Then, the stress scale is also reproduced as the scale of length, gravity acceleration, and density by deducing from the self-weight formula as in (3.9).

$$t_m/t_p = 1/\lambda_t = (\lambda_g/\beta\lambda)^{0.5} \quad (3.10)$$

$$\sigma_m/\sigma_p = 1/\alpha = 1/(\lambda_\rho\lambda_g\lambda) \quad (3.11)$$

Thereafter, by synchronizing the ratios of force on influence factors for each other, physical modeling can be obtained for acceleration (a) in Equation (3.10), deformation (d) in Equation (3.11), and deformation modulus (E) in Equation (3.12). The scale of permeability (k) is also determined by Darcy's law as shown in Equation (3.13). The state of stress at the failure of the material of the prototype and model are σ_p , σ'_p and σ_p/α , σ'_p/α , respectively. Hence Mohr's circles of the prototype and model materials are congruent, resulting in congruent envelope lines. Based on this analysis, the scale for Friction ($\tan\phi$), and Cohesion (c) was derived in Equation (3.14) and Equation (3.15).

$$a_m/a_p = 1/\lambda_g \quad (3.12)$$

$$d_m/d_p = 1/(\beta\lambda) \quad (3.13)$$

$$E_m/E_p = \beta/(\lambda_p\lambda_g\lambda) \quad (3.14)$$

$$k_m/k_p = \lambda_p/(\beta\lambda/\lambda_g)^{0.5} \quad (3.15)$$

$$\tan\phi_m/\tan\phi_p = \alpha/(\lambda_p\lambda_g\lambda) \quad (3.16)$$

$$c_m/c_p = 1/(\lambda_p\lambda_g\lambda) \quad (3.17)$$

In addition, if the stress-strain relationship is expressed by a hyperbolic model, the scaling of strain can be theoretically derived as Equation (3.16). The details of the procedure were described by Kokusho (2014) [34]. Besides, Equation (3.17) can be applied for 1g model testing and Equation (3.18) can be applied in the case that soil in the prototype was used as model material. Apply Equation (3.16) to (3.18) to the general scaling in Equation (3.9) to (3.14), the similarity laws were obtained as summarized in Table 3.8 for 1g model testing if the same material as that in the prototype is adopted. The more general conditions of similarity a material satisfies, the more information can be obtained from the experiment.

$$1/\beta = 1/\lambda^{0.5} \quad (3.18)$$

$$g_m/g_p = 1/\lambda_g = 1 \quad (3.19)$$

$$\rho_m/\rho_p = 1/\lambda_p = 1 \quad (3.20)$$

The use of prototype soil itself for the model tests is simple and satisfy some assumption of Rocha (1957) [61]. However, it is easy to see from these above calculations that not all prototype soils can be used as materials for 1g model experiments in all problems. Now we consider the suitability of Komaoka volcanic coarse-grained soil in rainfall and earthquake experiments in this study by its stress-strain relationship. Figure 3.15 shows the results of consolidated undrained triaxial tests (\overline{CU} tests) for Komaoka volcanic soils in terms of the relationship between the stress ratio σ_1'/σ_3' and shear strain γ (Kawamura et al., (2021) [33]. In the figure, the Poisson's ratio is 0.5 to calculate the shear strain in \overline{CU} . As a

result, an angle of internal friction of 38° and cohesion of 0 kN/m^2 was estimated. In Figure 3.15 (a), the stress-strain relationship is affected by the difference in effective confining pressure. However, if the strain was normalized by the square root of σ_c' as in Figure 3.15 (b) the stress-strain curves fit for each other, and peak points roughly lie on the same hyperbola.

Table 3.8 Similarity laws applied in 1g model experiments where the prototype soils are used as test materials

Parameters	Scale (Model/Prototype)
Length (L)	$1/\lambda$
Time (t)	$1/\lambda^{0.75}$
Density (ρ)	1
Acceleration (a)	1
Stress (σ)	$1/\lambda$
Strain (ε)	$1/\lambda^{0.5}$
Deformation (d)	$1/\lambda^{1.5}$
Deformation modulus (E)	$1/\lambda^{0.5}$
Permeability (k)	$1/\lambda^{0.75}$
Friction ($\tan\phi$)	1
Cohesion (c)	$1/\lambda$

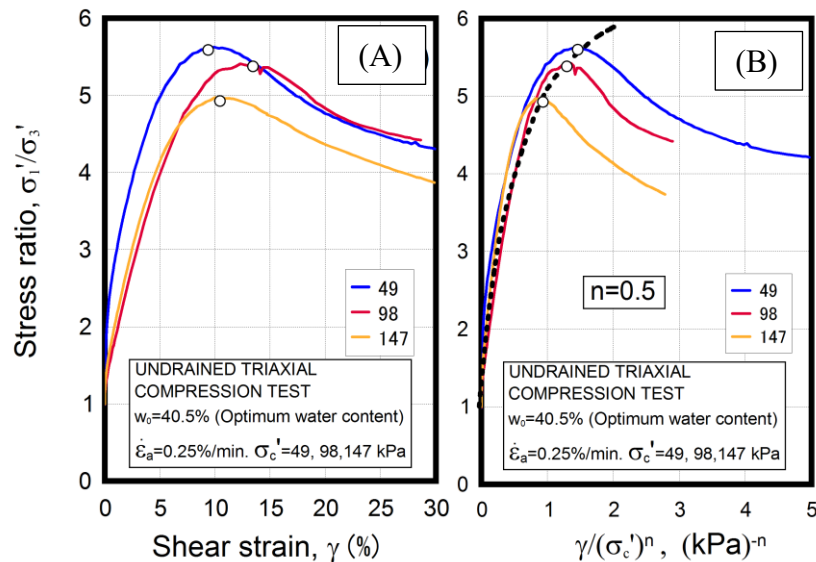


Figure 3.15 Consolidated undrained triaxial test results of Komaoka volcanic soils
 (A) Relationship of σ_1'/σ_3' and γ , (B) Relationship of σ_1'/σ_3' and $\gamma/(\sigma_c')^{0.5}$ [34]

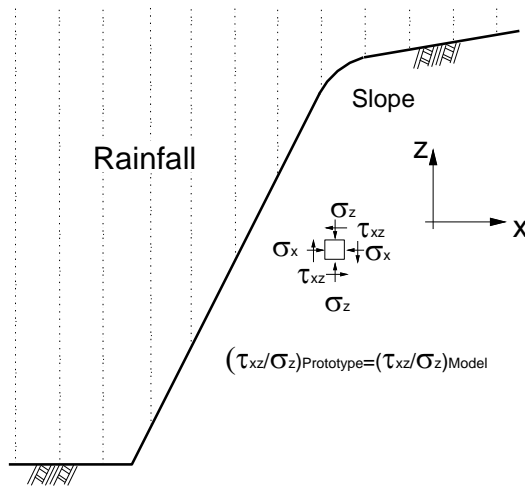


Figure 3.16 Test concept for 1g model test

Table 3.9 Similarity laws were applied in this study.

Parameters	Scale (Model/Prototype)
Length (L)	$1/\lambda$
Earthquake acceleration (a)	1
Rainfall intensity (R)	1
Stress ratio in element in slope (σ)	1
Strain in element in slope (ε)	1
Pore water pressure ratio ($\Delta u / \sigma_v'$)	1
Saturation degree ratio (S_r / S_{r0})	1
Deformation (d)	$1/\lambda$

Based on the consideration of the above discussion, the relationship between stress and normalized strain is unique, which leads to the possibility of using prototype Komaoka soils as model material according to the satisfaction of Rocha's assumption. Therefore, the strength of soil can be assumed to vary proportionally by the normalization of effective confining pressure, as described in Figure 3.16. Namely, the conventional way of thinking for element testing is taken in that of the 1g model testing. According to this technique, the mechanical behavior at the failure of slope elements for the 1g model corresponds with those at failure in the real field if rainfall intensity and seepage speed in the model are consistent with those in the prototype (Permeability of Komaoka volcanic soil is a high value of more than 10^{-5} m/s). Owing to this, rainfall intensity which was assumed to occur in the real field was directly applied to the slope surface. As a result, the similarity of dependency on time regarding the development of pore water pressure and the consolidation phenomenon may be not required theoretically. Additionally, note that the pore water pressure value obtained from model testing can be similarly evaluated as a true value. Consequently, reproduction by model testing is theoretically enabled for cohesionless soils such as Komaoka volcanic

soils, although the assumption that a model and a natural physical phenomenon occur by the same mechanism is required (Kawamura et al., (2010) [26]). In addition, the effect of suction on mechanical behavior until failure was small because the degree of saturation was more than 60 % in test ranges, as discussed above. To summarize, Similarity laws applied in this study are shown in Table 3.9.

3.3.5 Test procedures

Definition of slope failure

Kawamura and Miura (2013) [27] monitored the failure phenomenon of the model embankments through the PIV method and found that the saturation reached its peak value when the shear strain was 4–6%, independent of the differences in soil material, rainfall intensity, slope angle, and permeability of the bottom layer; after that, the embankment collapsed. Therefore, the moment when the shear strain γ reaches 6% is also defined as slope failure.

Rainfall amount in post-rainfall earthquake experiments:

Firstly, rainfall-only experiments were conducted. In which, the rainfall corresponding to the shear strain $\gamma = 6\%$ was set as R_0 . In post-rainfall earthquake tests, rainfall amounts of $0.5R_0$ were applied to the slope before carrying out seismic loadings to quantitatively evaluate the effect of the previous rainfall on the collapse of the model embankments.

The procedure for post-rainfall earthquake experiments used in this study is presented as follows:

1. Adjust the type, position, and water pressure of the spray nozzle installed at height G.L. + 2.6 m to obtain the rainfall intensity at the specified value of 100 mm/h. The acceleration is also set at 280 m/s^2 ;
2. After the slope model is completed, spray water from the spray nozzle and simultaneously start measuring the pore water pressure transducers, soil moisture meters, and acceleration meters;
3. When the amount of rainfall reaches a predetermined value, finish the rainfall test and carry out the seismic loading test.

In the present study, each test was performed at least two times.

3.4 Summary

Similar to other volcanic soils in Hokkaido, Komaoka has liquefied many times under the influence of major earthquakes in history. The fine content of Komaoka volcanic soil ranges from 26.0 % to 42.6 %. The fines were classified into non-plastic material (NP). The physical model tests in this study were conducted on the embankments constructed from 3 types of soil with different amounts of fine content: $K_{8.5A}$, K_{soil} , and K_{40A} . They are prepared with initial water contents on the dry side and wet side as the boundary of optimum water content. In addition, the relationship between the initial water content and dry density

of test materials was examined based on A-b compaction test methods. Results indicated that an increase in the number of fine particles of Komaoka volcanic soils leads to the decrease of optimum water and the increase of maximum dry density, respectively. The apparatus combined shaking table and spray nozzle were used to investigate the mechanical behavior of volcanic embankments subjected to rainfall and earthquake. Based on the similarity laws, the phenomenon that occurred with the prototype can be estimated by monitoring of model. The model embankment was built by the compacting method at the compaction degree of 90%. Pore water pressure, saturation degree, acceleration, and shear strain are data of tests, which were discussed in Chapter 4.

PHYSICAL MODEL TEST RESULTS AND ANALYSIS

4.1 Introduction

With the materials, equipment, and procedures presented in the previous Chapter, a series of 1g model experiments were performed. Rainfall-only experiments were conducted at first until failure occurred at the model embankment. Through comparison of the failure phenomenon and measured data, the influence of fine particle content on embankment failure mechanism due to rainfall was clarified. In these experiments, the rainfall corresponding to the moment when the shear strain reached 6% was set as the total rainfall amount R_0 . In the post-rainfall earthquake experiment, the model embankment was first subjected to a rainfall of $0.5R_0$. After the rainfall stopped, seismic loads were applied. The earthquake resistance of the embankment that has been subjected to previous rainfall was clarified under different conditions of initial water content and fine particle amount. In addition to clarifying the effect of dissipation time, earthquakes were applied at different moments as described in Chapter 3. Finally, the post-rainfall earthquake experiments were conducted under the same conditions as the post-earthquake rainfall experiments in Kawamura et al., (2016) [31]. The comparison is made to highlight the influence of the order of external forces on the stability of the volcanic slope.

4.2 Influence of initial water content and fines content on the stability of volcanic embankments under rainfall and earthquake

Similar to other research by 1g model experiments and conventional approach to element testing, the variation in water content in soils during rainfall and earthquake tests in this study was depicted by saturation ratio S_r/S_{r0} , which is the saturation degree S_r normalized by its initial value S_{r0} . Along with that, the reduction in shear strength of the embankment was evaluated through the pore water pressure ratio $\Delta u/\sigma_v'$. In this, the change in pore water pressure Δu was normalized by the effective overburden pressure σ_v' which was updated with the above-mentioned measured water content.

4.2.1 Effect of fines content on slope stability during rainfall

First, rainfall-only experiments were conducted for all three samples with a rainfall duration of at least 30 minutes or until slope failure. The influence of fine particle content on the mechanical behavior of volcanic embankments during rainfall is discussed below.

4.2.1.1. Dry cases

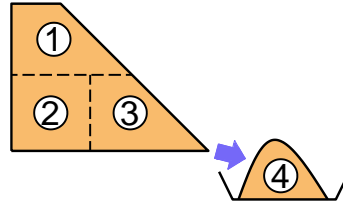


Figure 4.1 Sieving test areas in this study.

As shown in Figure 2.37, the increment of fine content in the Komaoka volcanic soil after rainfall experiments was nearly zero, implying that there is almost no particle breakage due to rainfall for this soil. However, because of their lightweight and no cohesion, the fine particles easily move in the pores between the coarse particles under the effect of rainwater. In this study, an attempt to understand the trend of this migration was made by examining the grain size distribution with sieving tests in different parts of the embankments (Areas 1, 2, 3) and in the washed-out part (Area 4), as shown in Figure 4.1. The results shown in Table 6 imply that the fine particles in all three types of soil tend to move from Areas 1 to Areas 2 and 3 because of gravity and rainfall. It can also be seen that the fine particle content of Area 3 was greater than those of Area 2 in all three cases even though the direction of rainwater is towards Area 2 (shown by the movement direction of the wetting front in the next section). This may be due to fine particles moving with rainwater due to the piping phenomenon in the saturation region from Area 1 to Area 3. When the secondary failure had not yet occurred, the soil in Area 4, which was generated by runoff, consisted mainly of fine particles.

Table 4.1 Fines content inside embankment after 30 minutes of rainfall (dry cases)

Test samples	Fc1 (%)	Fc2 (%)	Fc3 (%)	Fc4 (%)	m4 (kg)
K _{8.5A}	5.47	8.61	9.12	12.68	6.22
K _{soil}	24.24	27.34	28.49	38.49	0.84
K _{40A}	37.07	40.24	41.18	53.33	1.02

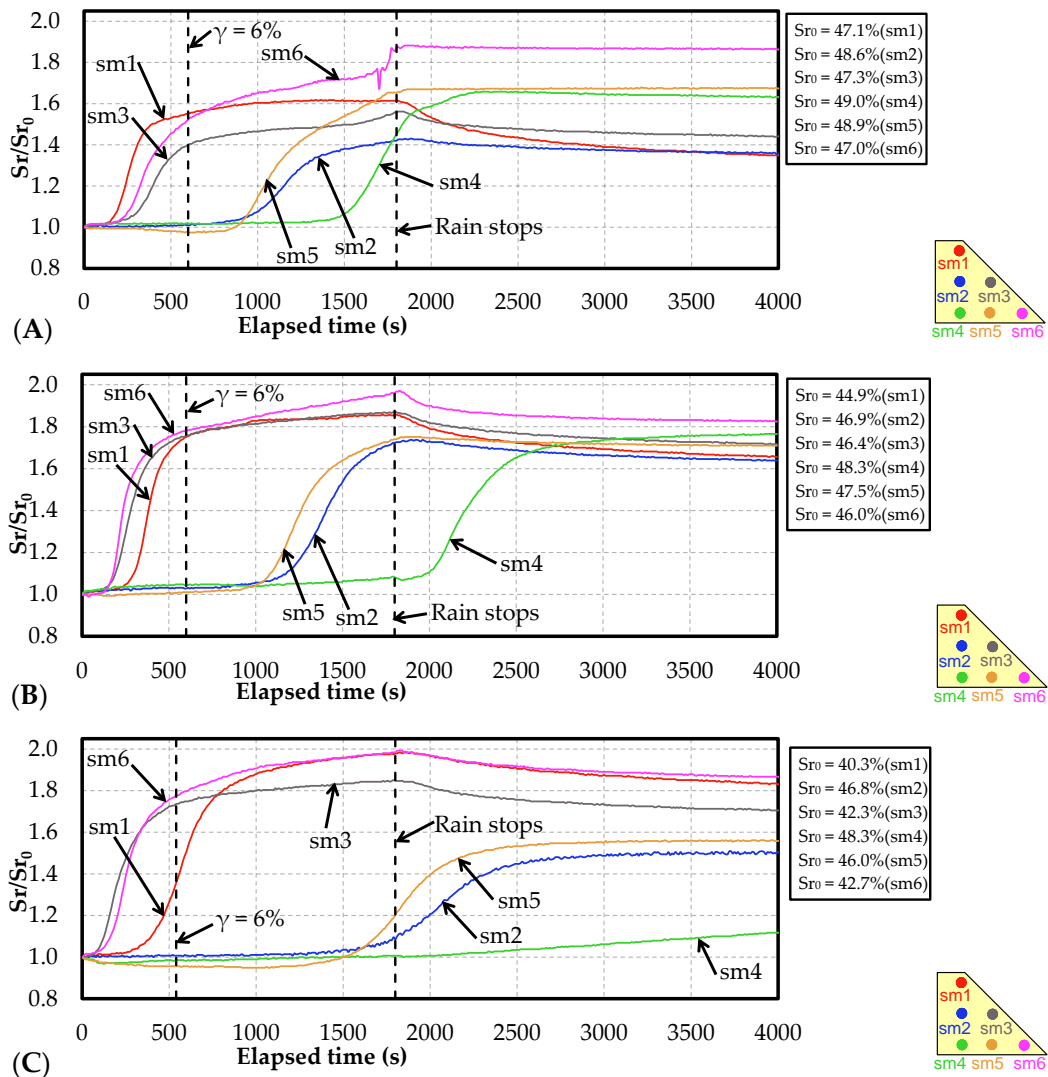
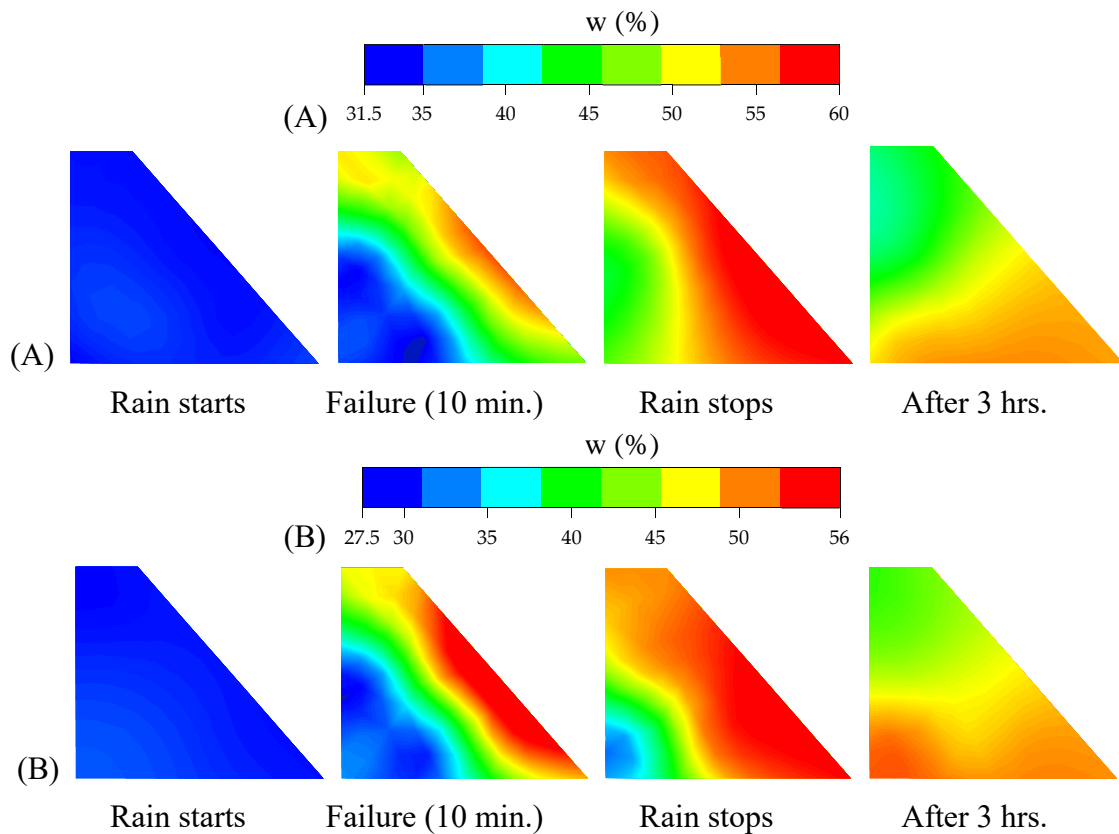


Figure 4.2 Changes in saturation degree during rainfall tests (A) $K_{8.5A}$, (B) K_{soil} , and (C) K_{40A} (dry cases)

The variation in saturation degree during the rainfall tests is shown in Figure 4.2. Under the effect of rainfall, the value of each meter started to increase at different moments depending on their locations. All three samples showed a similar trend: sm6, sm3, and sm1 located closest to the surface increased first; then sm5 and sm2 increased, and finally, sm4 increased. If the meters lie on the same wetted front, their values start to increase together and show the same trend, as noted in sm1, sm3, and sm6 or sm2 and sm5. At the time of failure corresponding to shear strain reached 6%, the saturation conditions inside the embankment in three cases were also similar: sm1, sm3, and sm6 increased to near steady values while the other meters remained at the original value. However, as the rainfall continued, the different hydraulic conductivity between the three soils caused the difference in the speed of the wetting front in the embankment. This difference can be more easily observed in the water content distribution shown in Figure 4.3, which was obtained by linear interpolation from the six measurements inside the slope and the direct measurements at the

boundary of the embankment before and after the experiments. In the figure, sample $K_{8.5A}$ showed the highest permeability: after 30 min of rainfall, except for the deepest meter sm4 which increased to a rather high value, the meters sm1, sm2, sm3, sm5, and sm6 increased to their maximum value, as shown by the fact that they were no longer increase when the rainfall stopped. For K_{soil} , sm4 did not start to increase after 30 min of rainfall. In particular, K_{40A} showed the lowest permeability: sm2 and sm5 did not even reach their maximum value. The effect of fine particle content on the hydraulic conductivity of volcanic soil in this study seems to be more obvious than it was in [7], which can be explained as follows: Under the same dry density in [7], the loss of fines content only leads to an increase in the average size of pores. However, a decrease in fine particle content directly results in the void ratio under the same compaction degree condition in this study. Therefore, the decrease in permeability in the latter case was more significant. After the rainfall stopped, sample $K_{8.5A}$ showed the fastest drainage rate (sm6 did not decrease because it was exposed after failure), followed by K_{soil} and the slowest, which was K_{40A} .



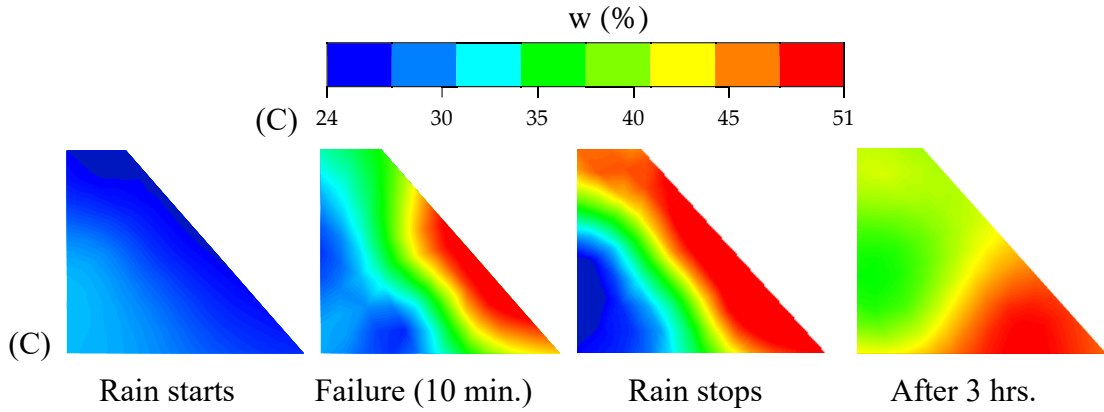


Figure 4.3 Water content distribution inside model embankments during and after rainfall tests (A) $K_{8.5A}$, (B) K_{soil} , and (C) K_{40A} (dry cases)

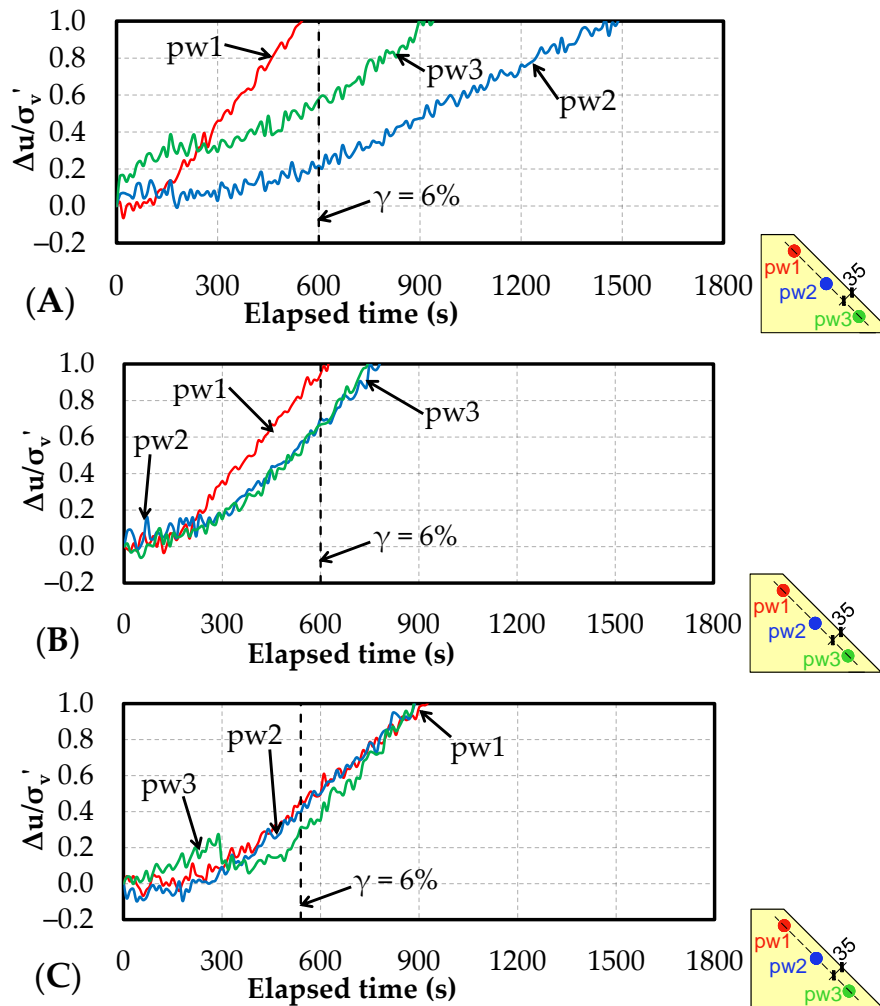


Figure 4.4 Change in pore water pressure during rainfall tests (A) $K_{8.5A}$, (B) K_{soil} , and (C) K_{40A} (dry cases)

The change in pore water pressure during rainfall is shown in Figure 4.4. In the case of $K_{8.5A}$ and K_{soil} , pw1 near the crown of the embankment increased faster than pw2 and pw3.

Then, flow deformations occurred at the base of the slope when pw3 exceeded 1. For K_{40A} , the rate of increase in pore water pressure was lower than that of $K_{8.5A}$ and K_{soil} . The values at three positions, pw1, pw2, and pw3, were almost the same. When the shear strain reached 6%, the pore water pressure was quite small compared with the other two cases. Another difference in K_{40A} was that the value of pw3 did not decrease for 3 h after the rainfall had stopped. The saturation degrees sm4, sm5, and sm6 of K_{40A} also showed an upward trend after rainfall instead of decreasing as was the case of $K_{8.5A}$ and K_{soil} . This can be explained through the movement of fine particles. As mentioned above, the fine content in Area 3 was always greater than in Areas 1 and 2. This migration trend led to the concentration of a large amount of fine grain at the toe of the slope. Fine particles combined with coarser particles made their size larger than the size of the pores, which prevented water and soil from continuing to move through that pore. This blocking effect in the basement made it difficult to drain and thus increased the groundwater table in the embankment as can be seen in the K_{40A} case.

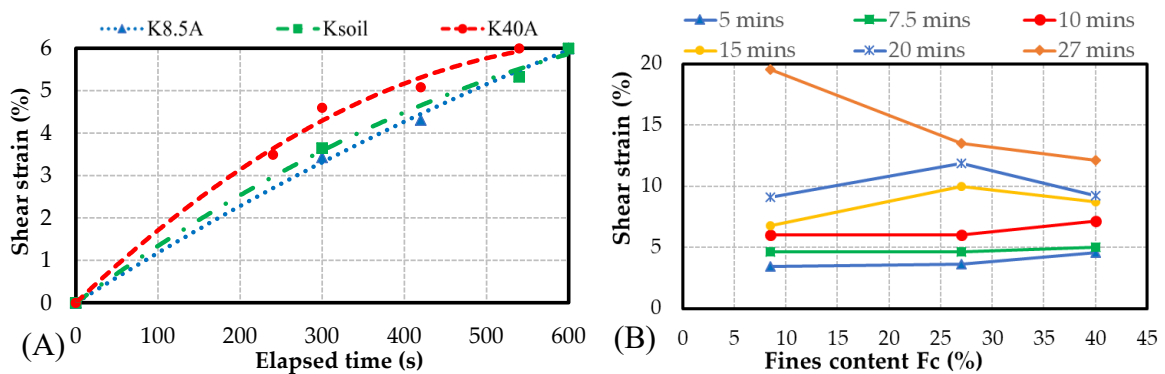


Figure 4.5 Change in rainfall-induced shear strain (dry cases) (A) Shear strain changed with time (B) Shear strain changed with fines content

The increment of shear strain during rainfall is shown in Figure 4.5, (A) is the change of shear strain over time, and (B) is the relationship between shear strain and fine particle content. As can be seen in Figure 4.5(A), when the shear strain was less than 6%, these relationships were almost linear for all three samples. Failure time for $K_{8.5A}$ and K_{soil} was 10 min and for K_{40A} was 9 min. Since the increase in pore water pressure during this period of K_{40A} was smaller, the faster failure rate of this soil sample is considered to be due to its smaller shear strength (internal friction angle). Thus, although an increase in fine content was shown to reduce soil permeability, it had almost no effect on rain-induced slope failure when the shear strain was less than 6%. After the shear strain exceeded 6%, it sharply increased at 27 min for the $K_{8.5A}$ embankment along with secondary failure, which was not observed for K_{soil} and K_{40A} during 30 min of rainfall, as shown in Figure 4.5(B). Even in another experiment when the precipitation time was increased to more than 1 hour,

secondary failure did not occur with K_{40A}. This difference can be explained through the failure pattern of K_{8.5A} and K_{40A} shown in Figure 4.6. In the case of K_{8.5A}, along with the increment of pore water pressure, the flow deformation that occurred at the base of the embankment led to the fast development of a larger slip line. However, the other parts in the model slope except for the slip line showed almost no change. In contrast, the K_{40A} embankment did not show slip line or gully erosion, but a small local failure appeared on the entire slope surface leading to a gradual reduction in size. Even when the pore water pressure exceeded 1, the flow deformation did not occur. The surface failure for K_{40A} can be attributed to the fine grains migration in the embankment as described above, because fine particles play an important role in the construction of K_{40A}'s soil structure, not just filling the voids as in the case of K_{8.5A} (see Figure 4.7). When the soil was gradually saturated, the flow of water inside the embankment became more difficult, leading to a decrease in the movement of fine particles. As a result, the rate of increase in shear strain for K_{40A} was reduced.

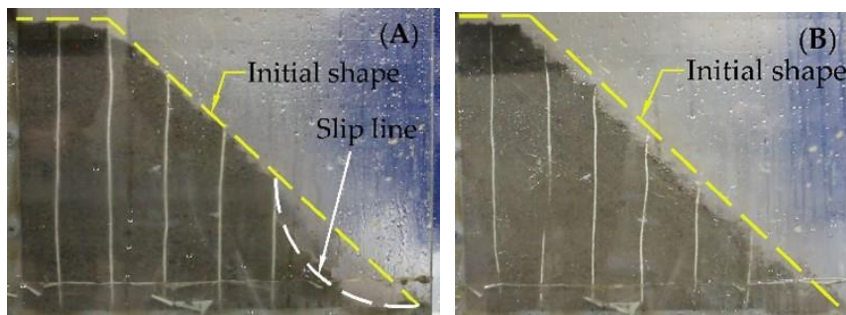


Figure 4.6 Rainfall-induced failure type of model embankments (A) K_{8.5A} and (B) K_{40A} (dry cases)

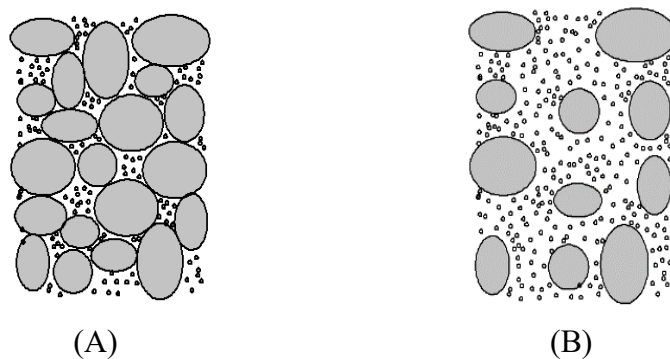


Figure 4.7 Grains distribution of Komaoka soils (A) K_{8.5A}, (B) K_{40A}

4.2.1.2. Wet cases

Figure 4.8 shows the changes in pore water pressure during rainfall in wet cases. The trend, in these cases, is almost the same as in the dry case. The value and increase of pw1 were quite much higher than that of pw2 and pw3 in the case of K_{8.5A} and K_{soil}, and almost

equal to that of pw3 in the case of K_{40A} . When the shear stress reached 6% with $K_{8.5A}$ and K_{soil} , the pore water pressure ratio was close to 1. While at the failure time of K_{40A} , this ratio was still much less than 1. The difference in the changes in pore water pressure between the wet cases and dry cases may be only the elapsed time. The growth rate of pore water pressure is approximately equal between the two initial water contents in the case of $K_{8.5A}$. With K_{soil} and K_{40A} , this speed in the wet cases is slower.

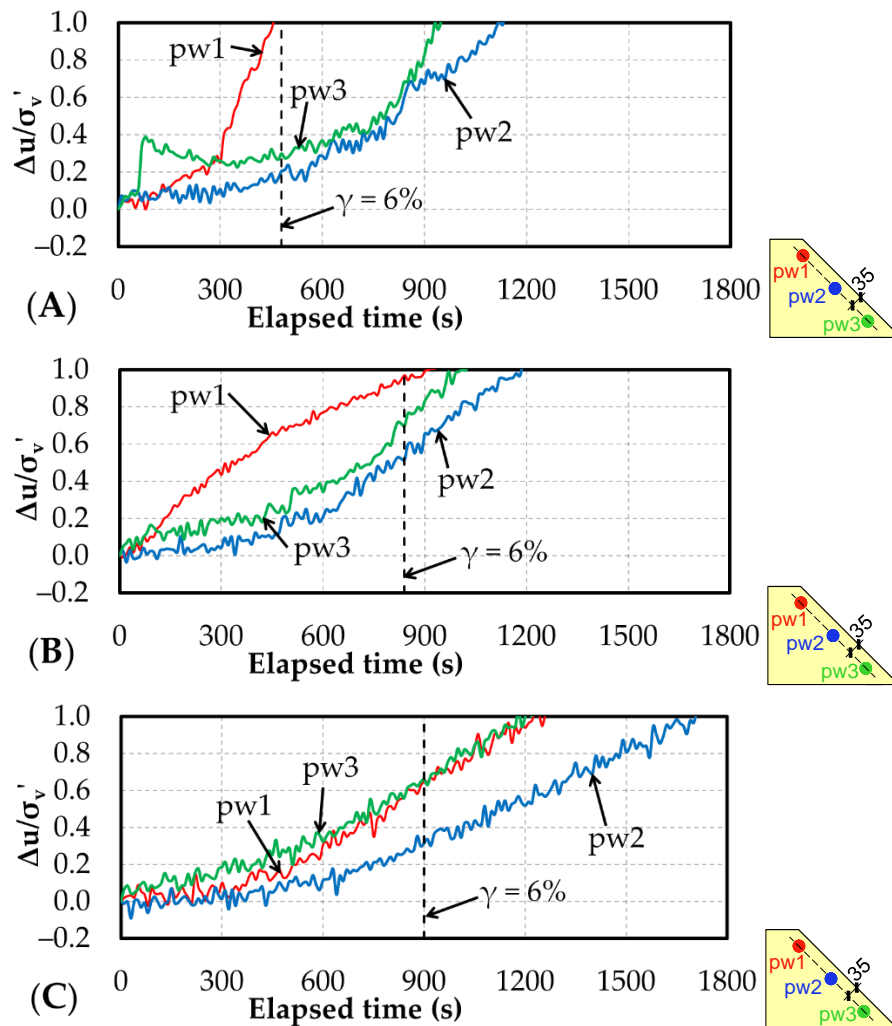


Figure 4.8 Change in pore water pressure during rainfall tests (A) $K_{8.5A}$, (B) K_{soil} , and (C) K_{40A} (wet cases)

The rate of infiltration of rainwater into the embankment can be seen more clearly through the variation of saturation degree shown in Figure 4.9. In the dry cases, at about 9 to 10 minutes (failure time in dry cases), sm1, sm3, and sm6 of all 3 soil samples were almost reaching the stable value. Whereas for the wet cases, these values are still quite low in the case of K_{soil} and K_{40A} . Sm1, sm3, and sm6 of these two soil samples were only close to the steady state at about 14 to 15 minutes, which is also the failure time in wet cases. In contrast, the infiltration rate of $K_{8.5A}$ is almost the same in both cases of initial water content. It can

be seen that the saturation at the time of shear strain reaching 6% is quite similar for all 3 soil types in both dry and wet cases. The tendency to decrease permeability as fine particle content increases was even more evident in wet cases due to the rather high permeability of $K_{8.5A}$. Based on these results, the tendency to decrease permeability at the same degree of compaction as shown in Figure 3.13 is confirmed in the model experiment for K_{soil} and K_{40A} . These are two types of soil with similar and higher fine grain content than the one used by Matsumura (2014) [43] and Dao (2018) [7] in elemental experiments. With $K_{8.5A}$, the infiltration rate is high and almost equivalent independent of the water content at the time of compaction.

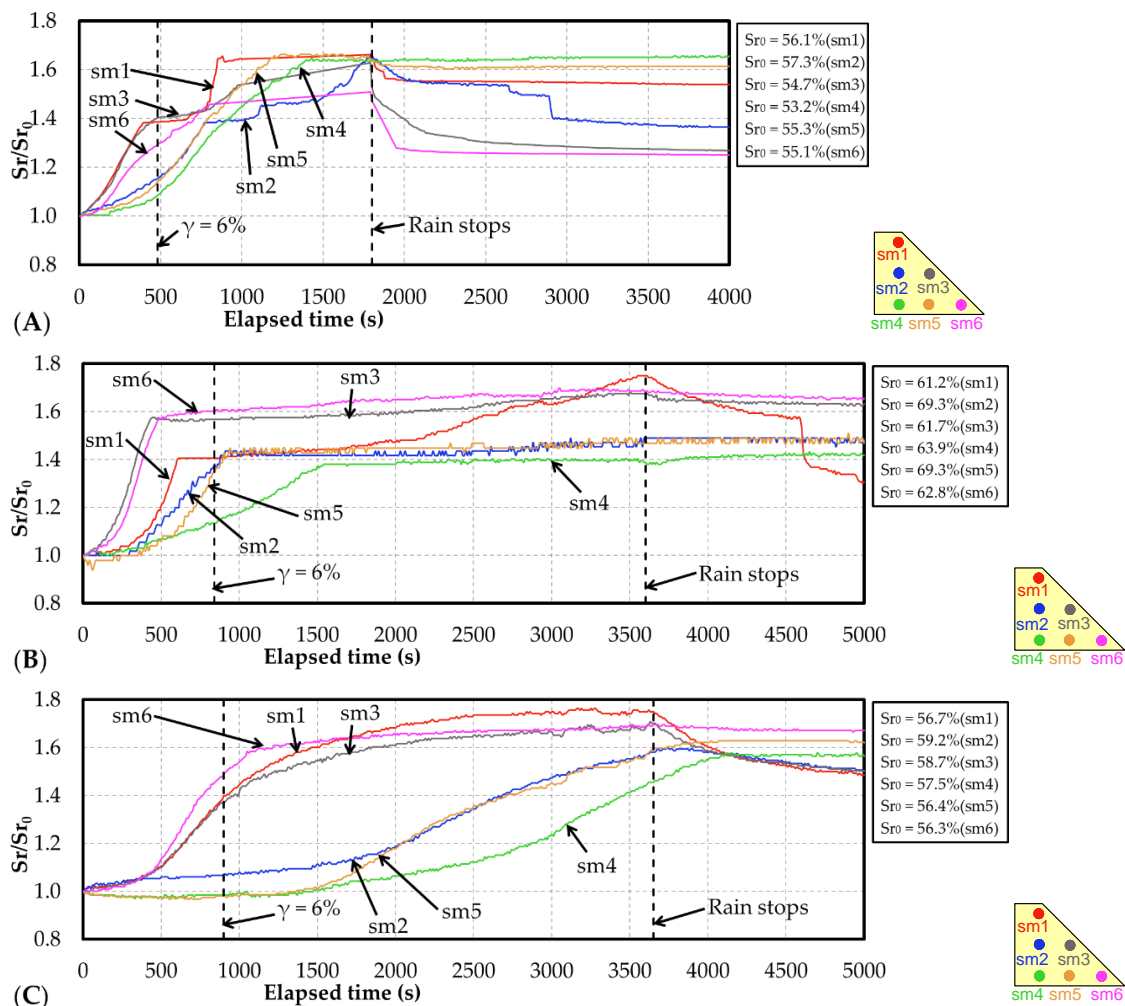


Figure 4.9 Changes in saturation degree during rainfall tests (A) $K_{8.5A}$, (B) K_{soil} , and (C) K_{40A} (wet cases)

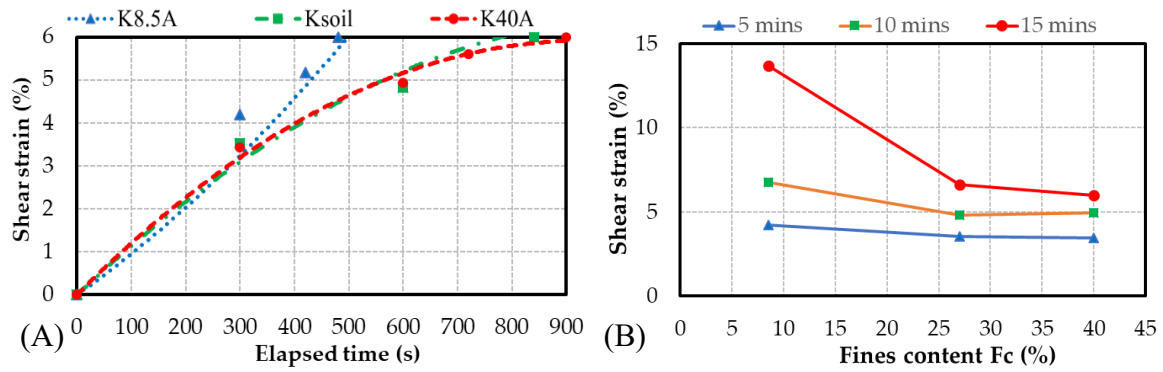


Figure 4.10 Change in rainfall-induced shear strain (wet cases) (A) Shear strain changed with time (B) Shear strain changed with fine content

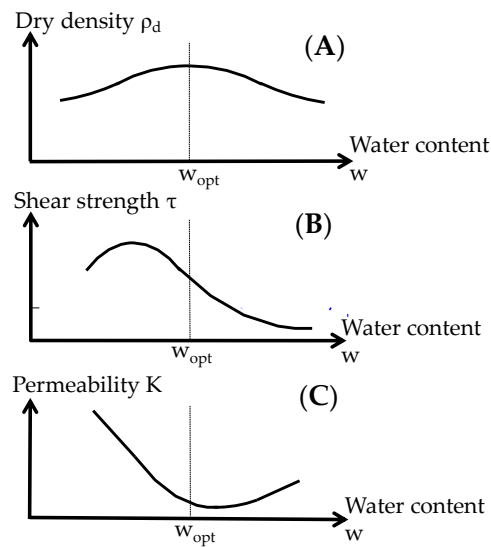


Figure 4.11 Changes in the mechanical and physical behavior of volcanic soils with water content (A) dry density, (B) shear Strength, (C) and permeability [30].

The increase of shear strain over time in rainfall-only experiments of model embankments with different fine contents was summarized in Figure 4.10(A). As can be seen in Figure 4.10(B), the increment of fines content leads to the slower develop of shear strain at any time during rainfall test, that trend is more clear at longer rainfall time. Thus, the rate of increase in the shear strain of the model embankment is proportional to the permeability of the material in the wet cases. Compared with the dry cases, the failure time of the wet cases is shorter with $K_{8.5A}$ and longer with K_{soil} and K_{40A} . Hayashi and Kawamura (2019) [12] proposed the influence of water content on the dry density, shear strength, and permeability of volcanic soil, as shown in Figure 4.11. Comparing the behavior of compacted volcanic soils on the dry and wet sides of the optimum water content, the dry density is similar but the shear strength and permeability on the dry side show higher values. It can be seen that the trend shown in Figure 4.11(A) and 4.11(C) is similar to the results in Figure 3.3 and Figure 3.13, respectively. As soil moisture increases (e.g., due to rainfall), soil properties

follow similar curves. The dry soil becomes wet and the permeability decreases until the soil is completely saturated. This may be the reason why the rainfall experiments in this study lead to a similar trend when the soil is on the dry and wet sides of the optimum water content. Although the shear strength of the volcanic soil compacted on the wet side is lower than it is on the dry side as shown in Figure 4.11(B), this only affects the rainfall-induced failure of the embankments when the permeability is high enough, as in the case of $K_{8.5A}$. In the wet case of K_{soil} and K_{40A} , the increase in the shear stress was suppressed due to their low permeability making it difficult to increase the pore water pressure. From the results of the dry and wet cases, both the differences in shear strength and permeability have an effect on the failure of volcanic embankments under rainfall.

4.2.2 Failure of embankments with different fine contents under post-rainfall earthquake

As the fine content varied, the samples in earthquake-only tests of this study showed similar mechanical behavior and shear strain (less than 2% after 400 cycles), implying that fine particle content had no significant effect on the seismic resistance of compacted volcanic soils at a compaction degree of 90%. However, this behavior is no longer correct in the post-rainfall earthquake experiments presented below.

The cumulative rainfall up to the time of failure mentioned in Section 4.2.1 was set as the total rainfall amount R_0 :

In dry cases:

- For K_{40A} : $R_0 = 100 \text{ mm/h} \times 9 \text{ min} = 100 \text{ mm/h} \times 0.15 \text{ h} = 15 \text{ mm}$;
- For $K_{8.5A}$, K_{soil} : $R_0 = 100 \text{ mm/h} \times 10 \text{ min} = 100 \text{ mm/h} \times 0.17 \text{ h} = 17 \text{ mm}$.

In wet cases:

- For $K_{8.5A}$: $R_0 = 100 \text{ mm/h} \times 8 \text{ min} = 100 \text{ mm/h} \times 0.13 \text{ h} = 13 \text{ mm}$;
- For K_{soil} : $R_0 = 100 \text{ mm/h} \times 14 \text{ min} = 100 \text{ mm/h} \times 0.23 \text{ h} = 23 \text{ mm}$;
- For K_{40A} : $R_0 = 100 \text{ mm/h} \times 15 \text{ min} = 100 \text{ mm/h} \times 0.25 \text{ h} = 25 \text{ mm}$.

In this section, the model embankment was first subjected to the precipitation of R equal to $0.5R_0$. As a result, the rainfall-induced shear strain was 3.88% for $K_{8.5A}$, 4.69% for K_{soil} , 3.11% for K_{40A} (dry cases), and 4.70% for $K_{8.5A}$, 4.37% for K_{soil} , 3.89% for K_{40A} (wet cases). After the rainfall had stopped for 90 s, seismic loadings were applied when the residual pore water pressure was still high. The total number of cycles was 100 and 200, divided into five applying times, each time was about 75 seconds apart.

4.2.1.1. Dry cases

The response acceleration due to post-rainfall earthquakes at different locations inside the model embankment is shown in Figure 4.12. The previous rainfall caused this behavior not to retain the periodicity as in the earthquake-only experiment, but the acceleration at the upper parts was always higher than that at the lower parts of the slope. The maximum values of the acceleration at the crown area in the case of $K_{8.5A}$, K_{soil} , and K_{40A} were 5.51, 4.43, and 4.33 (m/s^2), respectively. It can be seen that these values were

higher than the value of 3.2 m/s² in the case of the earthquake-only experiment. This is considered to be due to the deformation and the change in soil structure generated by previous rainfall.

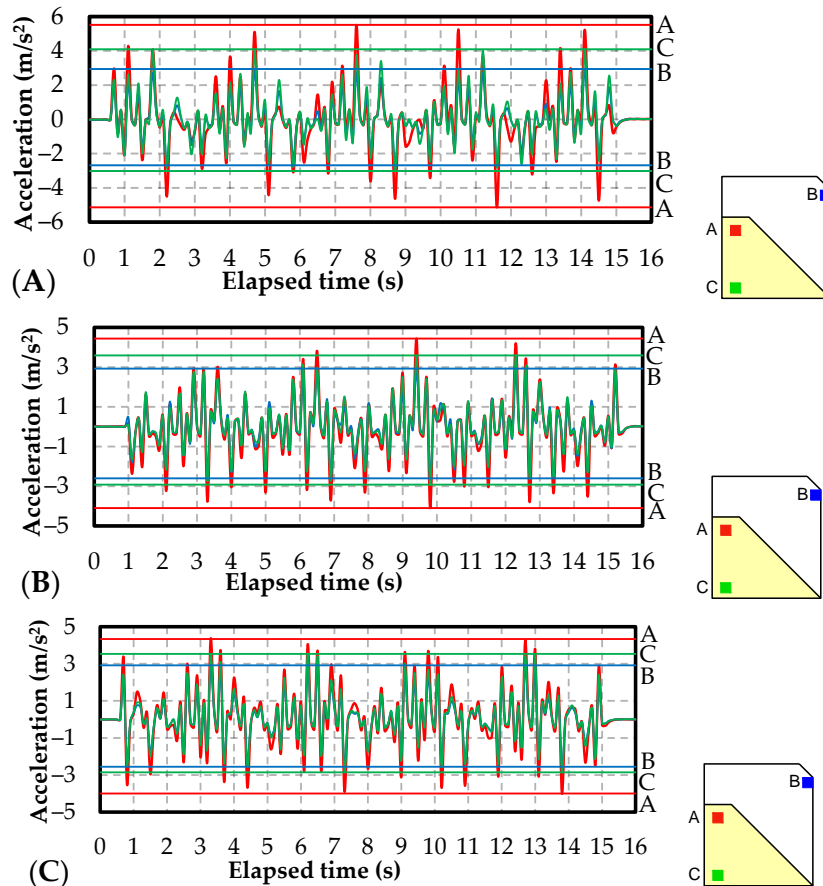


Figure 4.12 Variation in accelerations during earthquakes at shaking table and basement, the crown of embankments subjected to rainfall (A) K_{8.5A}, (B) K_{soil}, (C) K_{40A} (dry cases)

The behavior of saturation degree under the post-rainfall earthquake is shown in Figure 4.13. As can be seen, the variation during rainfall was similar to that of the beginning of the rainfall-only experiment: sm1, sm3, and sm6 started to increase due to the infiltration of rainwater but did not yet reach their maximum value while sm2, sm4, and sm5 were almost unchanged. When cyclic loadings were applied, a general trend was observed for all three samples: sm1, sm3, and sm6 increased while sm2 and sm5 decreased. In which, the change in sm1 and sm2 was more obvious than that of sm6 and sm5. Under the effect of seismic loadings, the particles rearrange, and the pore size changes, leading to the movement of water in the pore. Through the change in the distribution of water content before and after the earthquake as shown in Figure 4.14, we can see that the cyclic loadings have the effect of pushing water from the inside to the outside of the model embankment. Another point worth noting for the K_{40A} case was the difficulty of drainage after earthquakes, which occurred not only in the basement but also in the upper parts of the slope. Thus, cyclic

loadings can cause a blocking effect due to fine particle concentration at any point in the K_{40A} embankment.

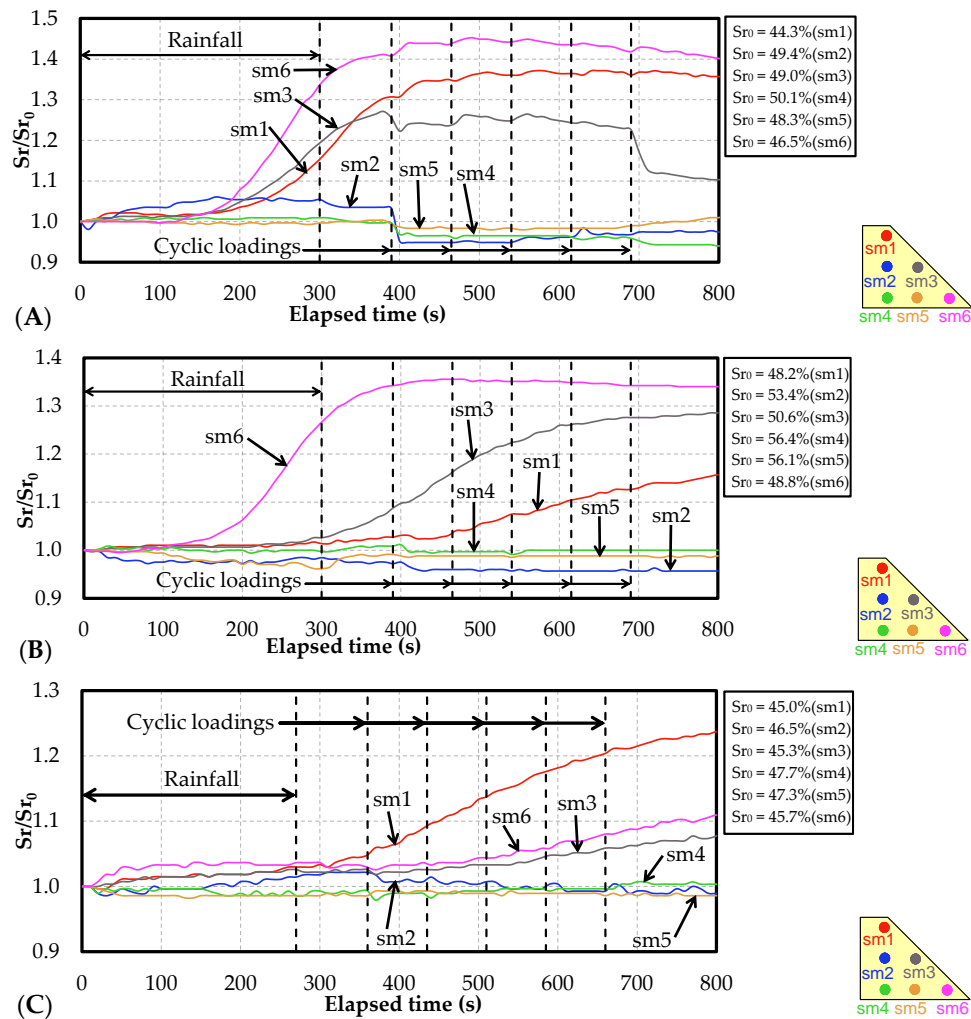


Figure 4.13 Changes in saturation degree during post-rainfall earthquake tests (A) $K_{8.5A}$, (B) K_{soil} , and (C) K_{40A} (dry cases)

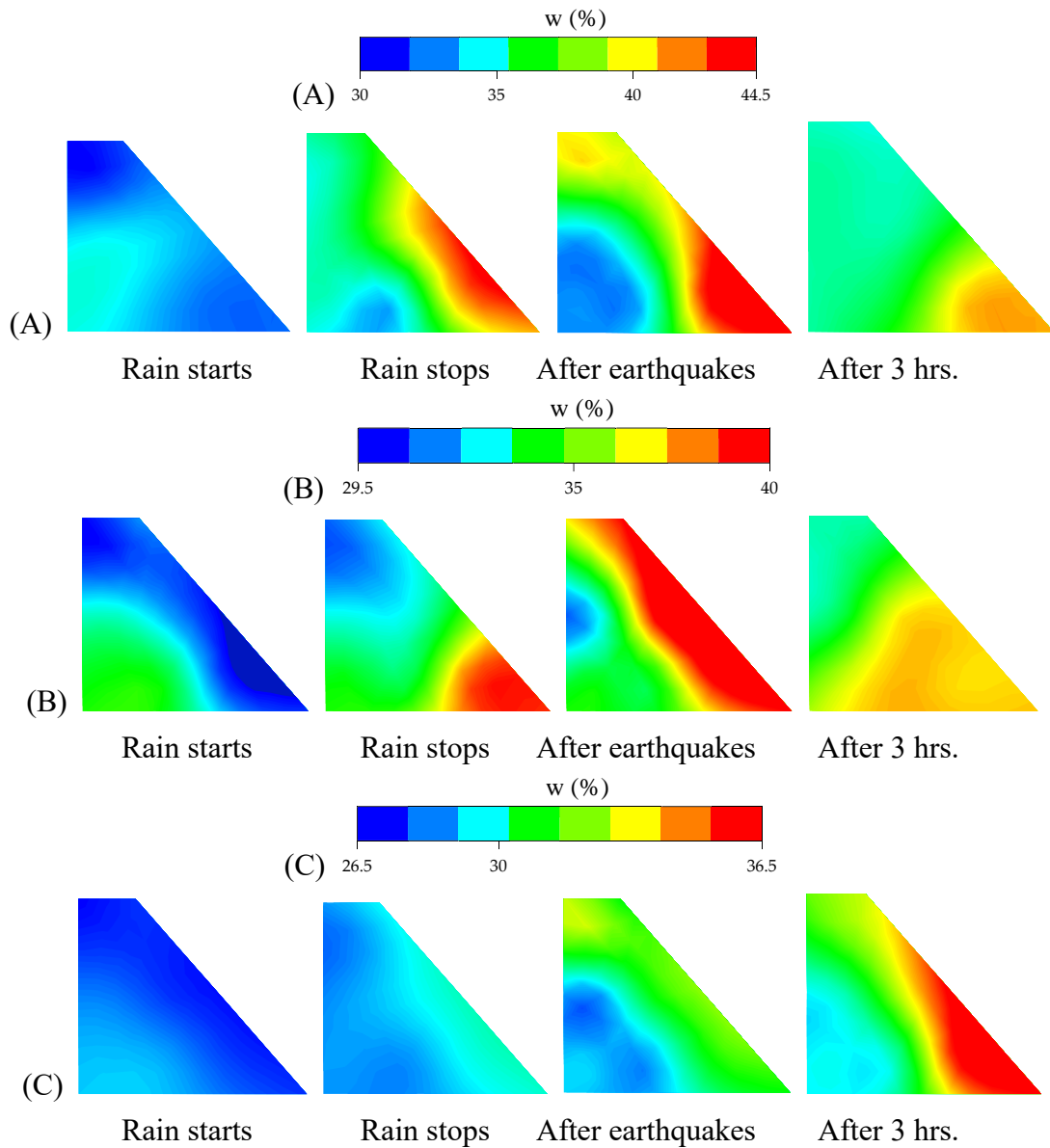


Figure 4.14 Water content distribution inside model embankments during and after post-rainfall earthquake tests (A) K_{8.5A}, (B) K_{soil}, and (C) K_{40A} (dry cases)

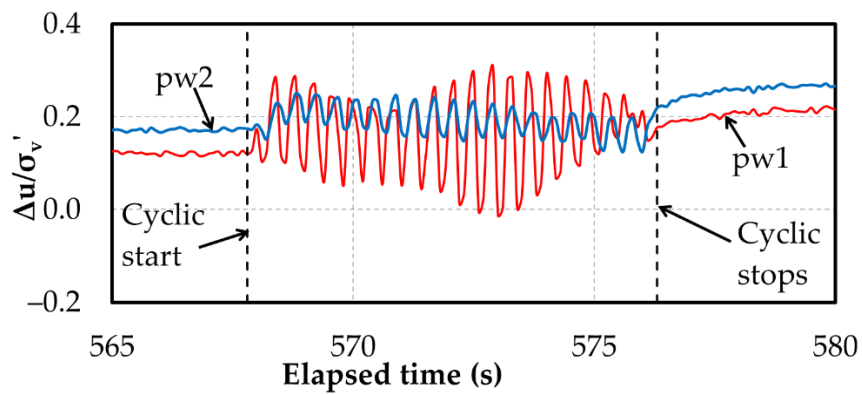


Figure 4.15 Pore water pressure during seismic loadings

Figure 4.15 shows the rapid change of pore water pressure during seismic loadings of volcanic embankments subjected to rainfall. Similar to the case of earthquake-only experiments as shown in Figure 2.11, the pore water pressure changed periodically under earthquakes. As the shaking table begins to move, it forces the slope back causing volume contraction and a decrease in voids, increasing pore water pressure. When the shaking table returns to its original position, the soil on the slope has a large degree of freedom, and the pores between the particles increase, so the pore water pressure decreases. The amplitude of this periodical change in pore water pressure was greatest in the case of $K_{8.5A}$. The change in pore water pressure during post-rainfall earthquakes is shown in Figure 4.16. Similar to the rainfall-only experiment, the measured values at the positions of pw1, pw2, and pw3 both increased during rainfall, and the difference between them was small. Figure 4.16 ignored the rapid variations shown in Figure 4.15 and focused on the changing trend of pore water pressure after earthquakes. As presented in the above section, earthquakes cause pore water to move outwards. Therefore, pw1, pw2, and pw3 placed near the slope surface increased together under the effect of cyclic loadings. It can be seen that the increase in pw1 near the crown of the slope was larger than that of pw2 and pw3. In the case of $K_{8.5A}$, the pore water pressure at pw1 exceeded one at the first time of seismic loading and the flow deformation near the crown caused slope failure. During the 4th seismic loading, the pore water pressure of pw3 increased suddenly, causing the shear strength to rapidly decrease, the two soil sections were separated, creating cracks that were recorded near the basement. Pw1 in the case of K_{soil} reached a value of one at about the 70th cycle, corresponding to the total shear strain due to rainfall and earthquake surpassing 6%. In the case of K_{40A} , pw1 was still less than one after 100 cycles and only exceeded one at about the 140th cycle. This is because the shear strain due to rainfall was smaller in this case. As can be seen in most tests, the point of shear strain due to rainfall and earthquake reaching 6% was relatively close to the time when the pore water pressure ratio reached one. Thus, the measurement of pore water pressure still plays an important role in assessing slope stability.

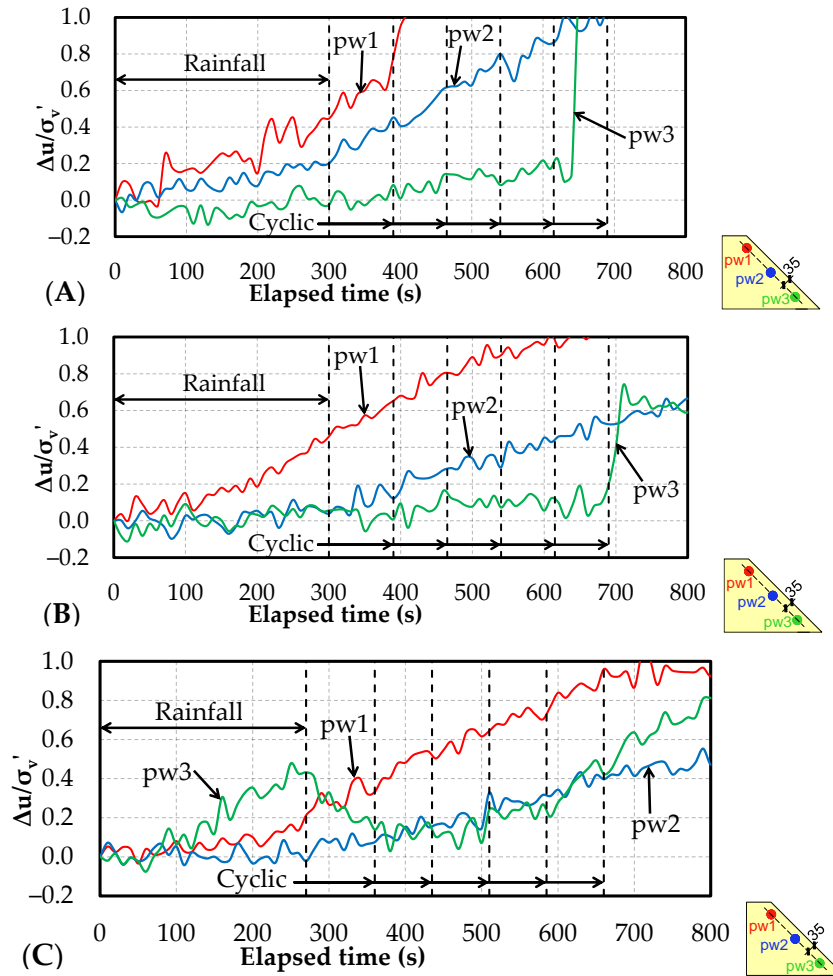


Figure 4.16 Changes in pore water pressure during post-rainfall earthquake tests (A) $K_{8.5A}$, (B) K_{soil} , and (C) K_{40A} (dry cases)

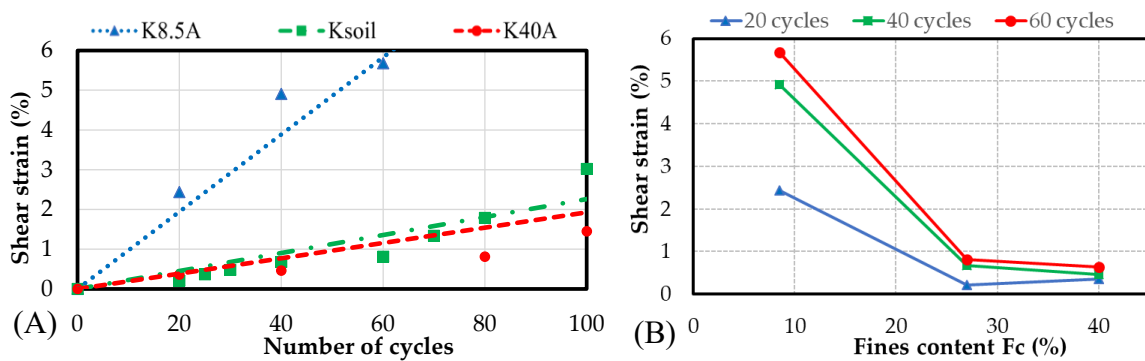


Figure 4.17 The earthquake-induced shear strain of embankments subjected to previous rainfall (dry cases) (A) Shear strain changed with number of cycles (B) Shear strain changed with fines content

The increase in the earthquake-induced shear strain of embankment subjected to previous rainfall is shown in Figure 4.17(A). In the figure, $K_{8.5A}$ showed much higher values while the behavior of K_{soil} and K_{40A} was almost similar. The failure form of these two soils

was also the settlement of the entire embankment due to the rearrangement effect of seismic loadings while the failure due to flow deformations and cracks was recorded in the case of $K_{8.5A}$ as mentioned above. As shown in Figure 4.17(B), the growth rate of shear strain decreases sharply when the fine grain content increases from 8.5% to 27% and remains almost unchanged when the fine grain content increases from 27% to 40%. Soils with small fine particle contents have higher hydraulic conductivity and pore water pressure is easier to increase during post-rainfall earthquakes. Meanwhile, high fines content soils, which have a small void ratio, increased their density even more during rainfall. Therefore, seismic loadings have difficulty rearranging the particles to reduce pore size and increase pore water pressure. In addition, the increase in density also makes the stabilizing force due to self-weight more advantageous than the earthquake-induced destabilizing horizontal force. However, the characteristics that increase this resistance to seismic loadings in K_{soil} and K_{40A} are similar. This explains the relationship between shear strain and fine particle content shown in Figure 4.17(B). As the fine content increases and exceeds a certain limit, its effect diminishes because fine particles occupy most of the voids in the soil. For these reasons, the earthquake resistance of compacted volcanic soil is subjected to previous rainfall increases with the increase in fine particle content. However, this strength does not increase further after the fine particle content exceeds a certain threshold of about 27% in this study.

4.2.1.2. Wet cases

Figures 4.18 and 4.19 show the behavior of pore water pressure and saturation degree of model embankments during post-rainfall earthquakes in wet cases. As shown in Figure 4.18, the development of pore water pressure in wet cases was faster compared with those in dry cases for all 3 soil samples. In the dry cases, only the pore water pressure of $K_{8.5A}$ suddenly increases when facing cyclic loadings (pw1 in the first loading and pw3 in the fourth loading) while the other value shows a gradual increase. In the wet cases, the ratio of pw3 near the basement of the slope in $K_{8.5A}$ increases rapidly and exceeds the value of 1 in the first loading. The same is shown on the fourth loading for pw1 near the crown of K_{40A} . The pw1 ratio K_{soil} also spiked suddenly and exceeded 1 on the third loading although it dropped after that.

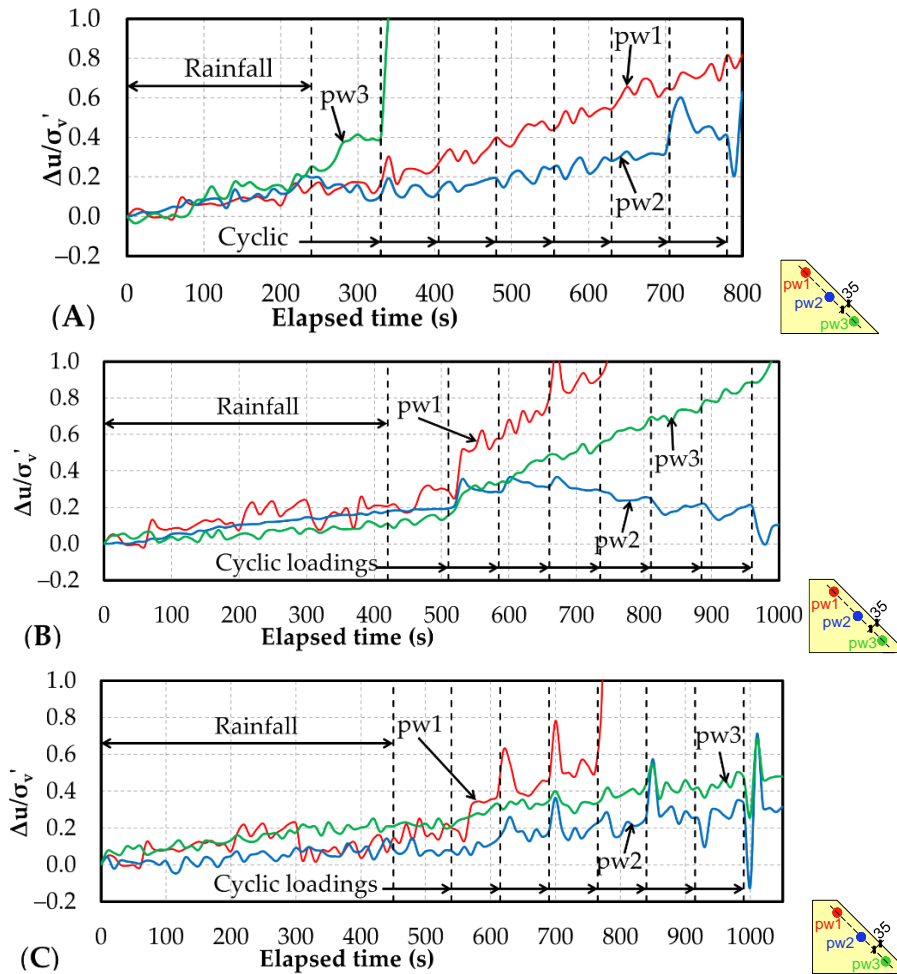


Figure 4.18 Changes in pore water pressure during post-rainfall earthquake tests (A) $K_{8.5A}$, (B) K_{soil} , and (C) K_{40A} (wet cases)

With the change of saturation degree shown in Figure 4.19, the trend is similar to dry cases: when seismic loadings were applied; values of meters near the slope surface (sm1, sm3, and sm6) showed an increasing trend while those in meters inside the slope (sm2, sm4, and sm5) tended to stay the same or decrease. Thus, the tendency of seismic loadings to move water from the inside to the outside of the embankment is observed in both cases of the initial water content. The difference is that the change of saturation degree in each shaking of the wet cases is more obvious and stronger than that of the dry cases, similar to the variation of pore water pressure.

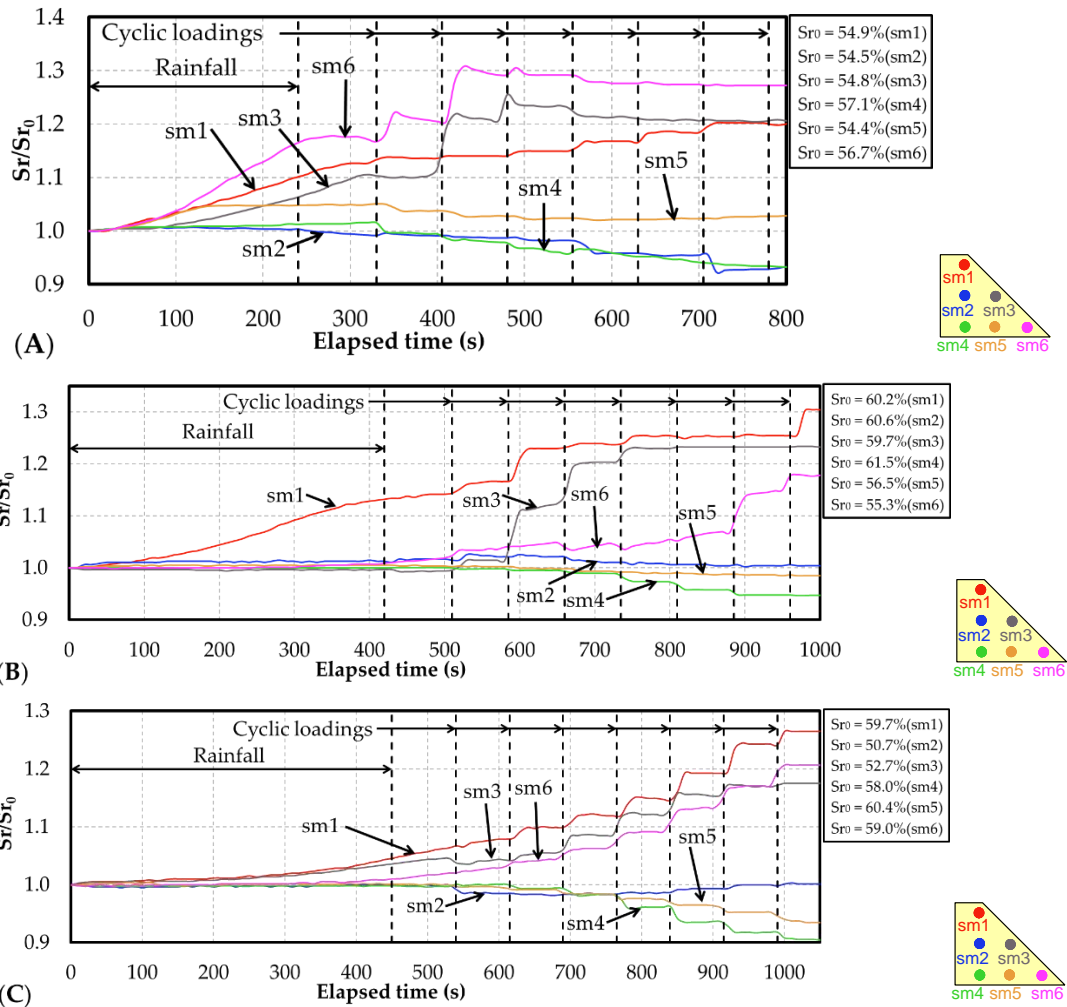


Figure 4.19 Changes in saturation degree during post-rainfall earthquake tests (A) K_{8.5A}, (B) K_{soil}, and (C) K_{40A} (wet cases)

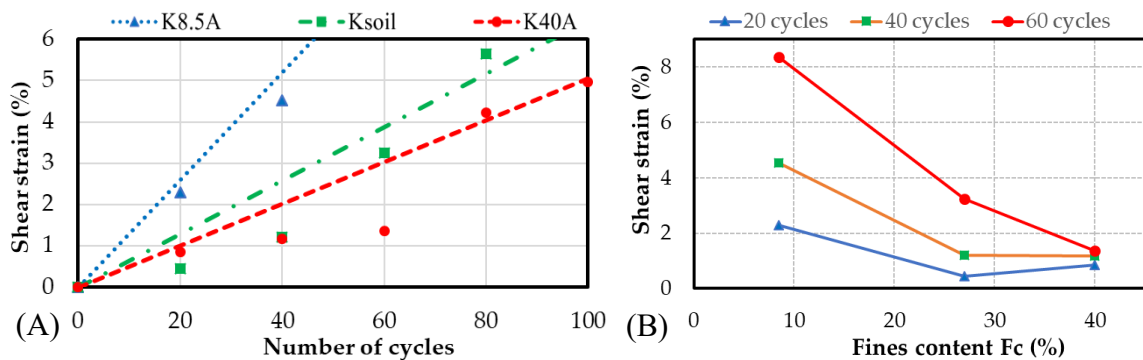


Figure 4.20 The earthquake-induced shear strain of embankments subjected to previous rainfall (wet cases) (A) Shear strain changed with number of cycles (B) Shear strain changed with fines content

The change of shear strain due to cyclic loadings in wet cases of model embankments subjected to rainfall is shown in Figure 4.20. Both the relationship between shear strain and cyclic numbers in Figure 4.20(A) and the relationship between shear strain and fine grain

content in Figure 4.20(B) show the same trends as dry cases behaved in Figure 4.17: The increase in shear strain of $K_{8.5A}$ is the fastest, followed by K_{soil} , and the slowest is K_{40A} . The failure types of $K_{8.5A}$ and K_{40A} are shown in Figure 4.21. As can be seen, the $K_{8.5A}$ also showed the flow deformation near the basement and the crack near the crown (see Figure 4.21(A)). However, the slope failure of K_{soil} and K_{40A} is more serious than dry cases. The liquefaction was observed near the crown of the slope at the cycle when the pore water pressure ratio of $pw1$ exceeded 1, as shown in Figure 4.21(B). The rapid and severe failure in the wet cases compared with the dry cases may be attributed to the influence of the decreasing trend in shear strength shown in Figure 4.11(B). This trend is only shown for $K_{8.5A}$ in the case of rainfall-only but is shown for all 3 soil types when model embankments were subjected to lateral driven forces in seismic loadings. Another reason is that embankments in the wet cases were subjected to longer periods of rainfall than in the dry cases. Although the post-rainfall shear strain of the two cases was relatively equal, the longer precipitation period may cause a greater effect on the soil texture and reduce the shear strength. This has led to a rapid increase in shear strain when the embankment is subjected to cyclic loadings.

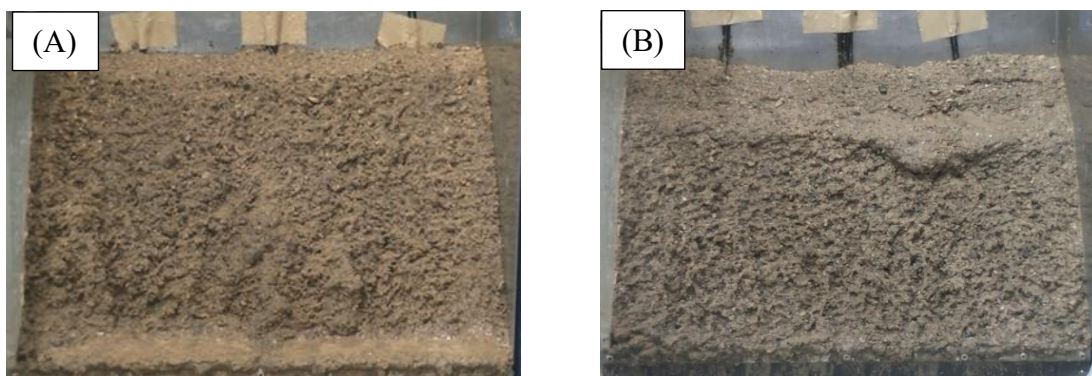


Figure 4.21 Earthquake-induced failure type of model embankments subjected to rainfall
(A) $K_{8.5A}$, (B) K_{40A} (wet cases)

4.3 Effect of dissipation time between rainfall and earthquake

Since natural earthquakes can occur at any time after the rainfall stops, we applied seismic loadings to the model slope according to 3 typical cases corresponding to 3 moments:

- Case (i): $pw1$ is higher than $pw2$;
- Case (ii): $pw1$ and $pw2$ reach the lowest value;
- Case (iii): $pw2$ is higher than $pw1$.

Where $pw1$ and $pw2$ are the pore water pressure at the crown and the basement of the embankment, respectively.

Figure 4.22 shows the change in the pore water pressure ratio in the case of (i).

Because of seepage, the pore water pressure inside the embankment rises immediately when the rain begins. After reaching a certain value, this increase slows down. After the rainfall had stopped for about 60 to 100 seconds, seismic loadings were applied when the residual pore water pressure was still high. As can be seen in Figure 4.22, the pore water pressure of pw1 suddenly increased (compared to before the earthquake) and exceeded 1 in both cases due to the response characteristics and rapid seismic loadings. On the other hand, the pore water pressure of pw2 shows 2 different trends when subjected to 20 cycles: an increase in the wet case and a decrease in the dry case. This is presumed to be due to the development of negative excess pore water pressure under the effects of unsaturation and dilatancy. Similar to the pore water pressure, the saturation degree also showed a rapid change at the time of seismic loadings. The front view camera confirmed flow deformation at the crown of the slope in both initial water content.

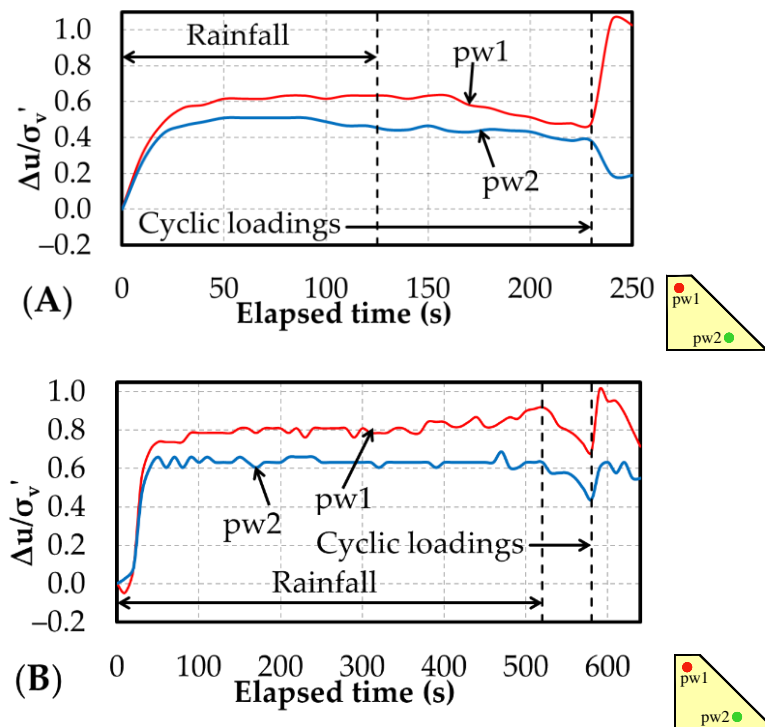


Figure 4.22 Changes in pore water pressure and saturation degree in the case of (i) (A) Dry case (B) Wet case

Next, in case (ii), the failure did not occur under an acceleration of 2.8 m/s^2 as in (i) and (iii) for both initial water contents. Therefore, the change in pore water pressure in the embankment upon failure under case (ii) was studied with an acceleration of 3.2 m/s^2 , as shown in Figure 4.23. Similar to case (i), the values of pw1 and pw2 decreased with the time from the end of rainfall. When the dissipation time was extended to about 10-15 minutes, the pore water pressure at both locations decreased to zero, and then the seismic loading tests were carried out. Although both pw1 and pw2 in both initial water content cases had been at

the lowest value before earthquakes, they changed immediately and showed an increasing trend after 20 cycles. The pw1 value exceeded 1, and flow deformation in the upper area was observed. A difference from case (i) is the appearance of transverse cracks near the crown of the slope. Regarding the saturation degree when seismic loadings were applied, the dry case showed a small change, while the wet case showed almost no change.

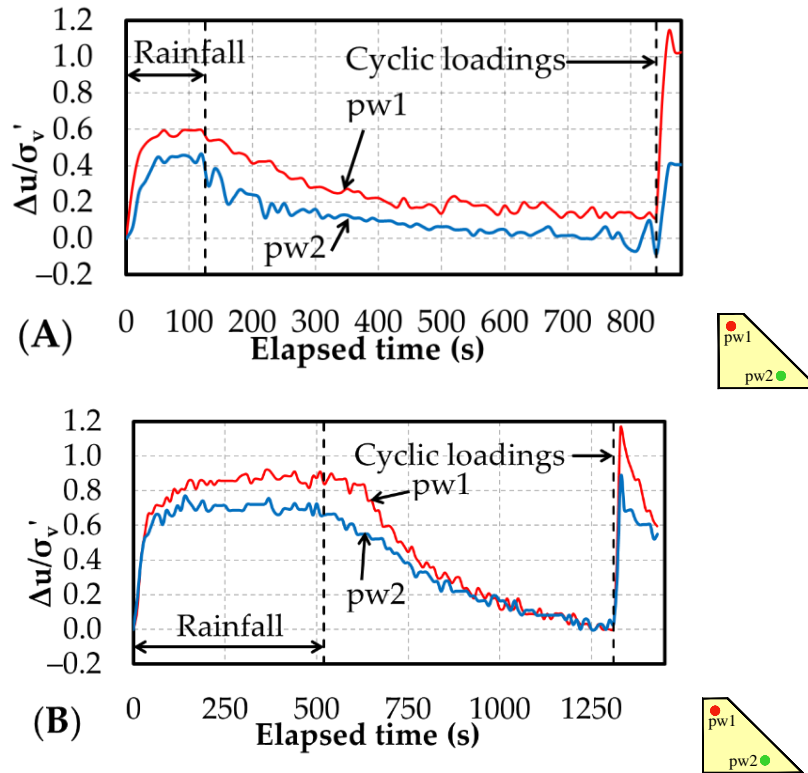


Figure 4.23 Changes in pore water pressure and saturation degree in the case of (ii) (A) Dry case (B) Wet case

Finally, Figure 4.24 shows the change in pore water pressure in case (iii). In more than 2 hours after the end of the rainfall, the pore water pressure decreased as in case (ii) and then increased again because the water penetrates the bottom of the embankment and the consolidation of the soil occurs over time. At that time, pw2 showed a higher value compared with pw1 in both cases of initial water content. This may be due to the drainage process making the water move from the inside of the embankment to the crown. When seismic loadings were applied, both excess pore water pressure ratios of pw1 and pw2 exceeded 1 and showed greater values than cases (i) and (ii). Flow deformation was confirmed almost simultaneously in both the upper and lower parts of the slope. The cracks caused by seismic loading were longer than in case (ii) and appeared both at the crown and the upper part of the slope. Focusing on the degree of saturation, a trend is common for both initial water content: sm1 sharply increases and sm2 sharply decreases right after being subjected to the seismic loadings.

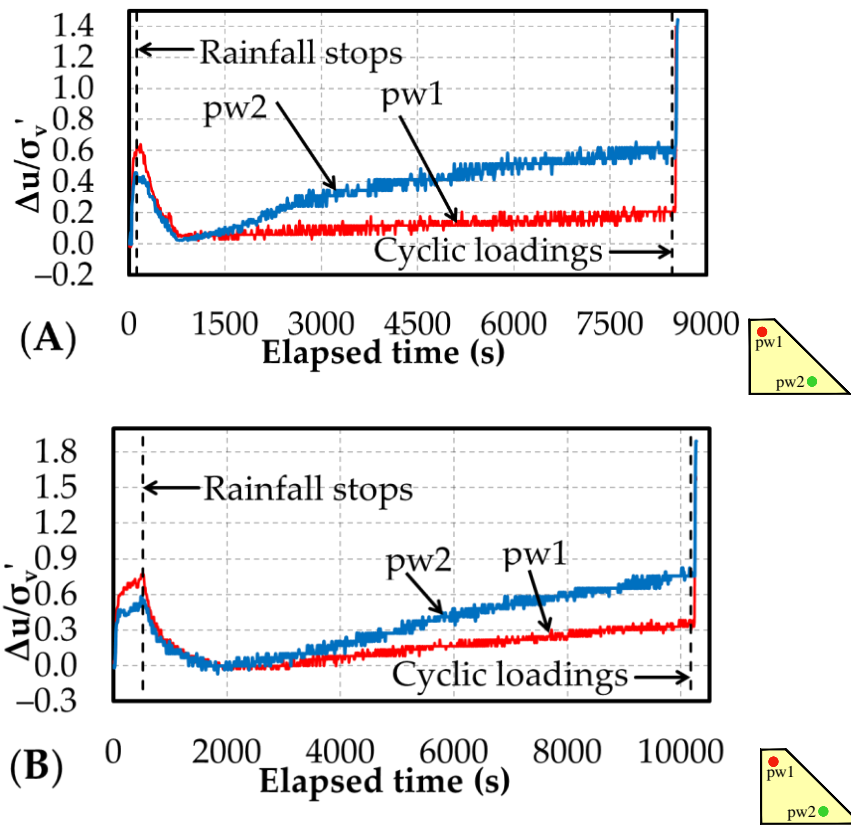


Figure 4.24 Changes in pore water pressure and saturation degree in the case of (iii) (A) Dry case (B) Wet case

Phenomenologically, when seismic loadings were applied to the soil that was still wet due to rainfall in case (i), failure occurred, but cracks did not appear. On the contrary, in cases (ii) and (iii), the soil has become drier, so the response of the embankment to seismic loadings is similar to that in the case without rainfall. Moreover, the length, width, and density of the cracks in cases (ii) and (iii) were larger than those in the case of earthquakes only. The failure type of model slope is shown in Figure 4.26 with flow deformations and cracks highlighted in cyan and yellow, respectively. When the slope in the dry cases was subjected to the seismic without previous rainfall, the pore water pressure changed periodically. After the end of the loadings, it did not accumulate but returned to its original value. Thus, the slope still works within the elastic limit. In contrast, in the case of rainfall before the earthquake, accumulation in pore water pressure immediately occurred. It can be seen that the rainfall caused the soil structure to separate and the soil to be plastically deformed. In the case of earthquake-only tests with w_0 higher than optimum water content, the pore water pressure ratio exceeded 1, but the slope did not collapse after 20 cycles, which shows the cyclic mobility of the slope. Compared with the case of rainfall before seismic loadings, when the pore water pressure ratio exceeded 1, the slope collapsed.

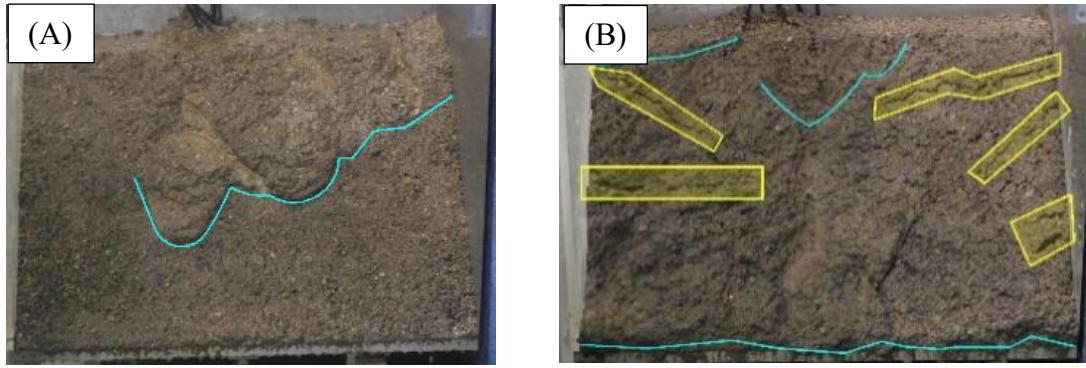


Figure 4.25 Model embankment at failure (A) case (i) (B) case (iii).

In this study, besides the rainfall amount of $R=0.5R_0$, we also performed other rainfall tests such as $0.3R_0$, $0.6R_0$, and $0.7R_0$ to get different shear strains with the model slope. After that, seismic loadings were applied and the different failure times were confirmed. Figure 4.25 shows the relationship between failure time caused by seismic loadings and the rainfall-induced shear strain under different conditions of pore water pressure. The seismic failure time in Figure 4.25 was normalized by Equation 4.1.

$$R_{ft}^{r \rightarrow s} = \frac{T_{fs}}{T_{fs0}} \quad (4.1)$$

where T_{fs} is the failure time due to seismic loadings of model embankments that were subjected to previous rainfall, while T_{fs0} is the failure time due to seismic loadings only. From Figure 4.25, it can be seen that the seismic failure time decreases inversely proportional to the shear strain due to rainfall in all 3 cases. In both cases of initial water content, at the same shear strain, the failure time was the longest in case (ii), followed by that in case (iii), and the shortest failure time was in case (i). The difference is more obvious in dry cases. Since the dissipation time in case (iii) is longer than in case (ii), the impact of the previous rainfall on the earthquake resistance of model embankments is assumed to be smaller. However, the failure time of case (iii) is shorter and the increase of pore water pressure is higher than that of case (ii). This implies that it is necessary to add drainage pipes on the embankment body because drainage when concentrated in one location can also lead to risks. As mentioned above, the effect of dissipation or the residual pore water pressure existing in the slope cannot be ignored.

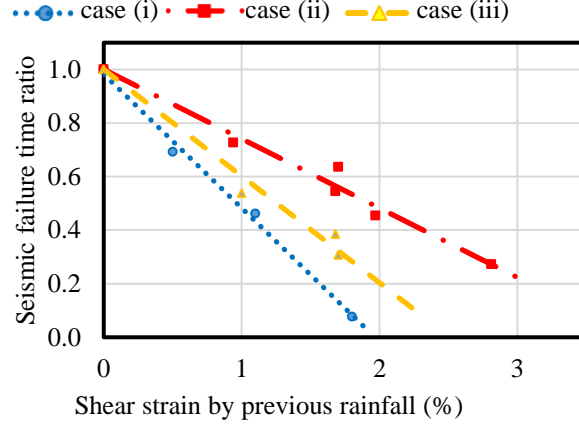


Figure 4.26 Relationship between seismic failure time ratio and rainfall-induced shear strain in different conditions of pore water pressure (Dry case)

4.4 Effects of different orders of rainfall and earthquakes on slope failures

In this section, the result of this study will be compared with the case where seismic loadings were applied before rainfall in Kawamura et al., (2016) [31]. Due to the difficulty in equally evaluating the effect of rainfall and seismic loadings, the failure time in the case of earthquake → rainfall will be normalized by Equation 4.2 in the same way as the above section.

$$R_{ft}^{s \rightarrow r} = \frac{T_{fr}}{T_{fr0}} \quad (4.2)$$

where T_{fr} is the failure time due to rainfall of model slopes that were subjected to previous seismic loadings, while T_{fr0} is the failure time due to rainfall only. In general, when a research object is firstly affected by event A and then is collapsed by event B, the failure time ratio is calculated as follows:

$$R_{ft}^{A \rightarrow B} = \frac{T_{fB}}{T_{fB0}} \quad (4.3)$$

where T_{fB} is the event B-induced failure time of the research object that was subjected to event A in the past, while T_{fB0} is the failure time due to only event B. The smaller the value of the failure time ratio $R_{ft}^{A \rightarrow B}$, the greater the effect of event A on the resistance to failure due to event B of the research object.

Figure 4.27 presents the relationship between failure time ratio and shear strain caused by previous external force in the 2 initial water content cases (data for rainfall → earthquake are taken according to case (i)). When seismic loadings are applied first, the model slopes with the dryer and wetter initial water content show 2 different trends. The

failure time decreases as the shear strain generated by seismic loadings increases in the dry case. In the wet case, when the shear strain increases, the failure time still increases until γ reaches 4% and after that, it decreases. When rainfall is applied first, 2 initial water content model slopes show the same trend, and the failure time is shorter compared with the case of earthquake→rainfall for the same shear strain generated. This difference can be explained as follows. In the case of a post-rainfall earthquake, the volumetric weight of the soil is increased by rainfall, which leads to the increase of the vertical driving forces in the slope. After that, seismic loadings will create horizontal driving force and further decrease the shear strength because the generated instantaneous pore water pressure superimposes the pore water pressure caused by the seepage flow. On the other hand, when seismic loadings are applied first, although they increase the pore water pressure, they also increase soil density due to the compaction effect. This will cause subsequent rainfall to take a longer time to loosen the soil structure to destabilize the slope. These results mentioned above lead to a need for appropriate evaluation of embankments under complex disasters taking into account the order of effects of external forces.

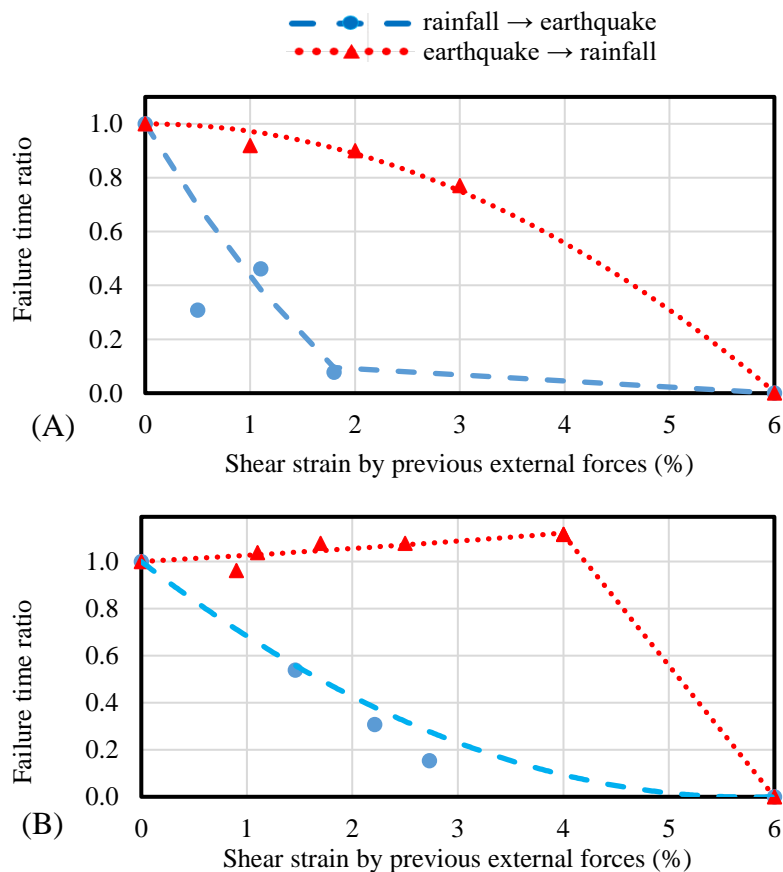


Figure 4.27 Relationship between failure time ratio and shear strain generated by previous external forces (A) Dry cases (B) Wet cases

However, the above results may change with variations in soil materials, tests, and

measuring equipment, as well as inherent errors such as the scale effect. In any case, further discussions in this direction will be required.

4.5 Summary

A series of rainfall and seismic tests were carried out on model embankments made of Komaoka volcanic coarse-grained soil. The soil samples were generated with three different fine particle concentrations (K8.5A, Ksoil, and K40A), with the starting water content set at 0.9 (dry cases) and 1.1 (wet cases) of optimal water content. In the post-rainfall earthquake, seismic loadings were applied at three distinct pore water pressure situations inside the embankments. The findings of this investigation were compared to the post-earthquake rainfall test in Kawamura et al., (2016) [31]. From that, the following results were found:

(1) The rainfall-induced residual pore water pressure and water retention condition inside the slope play an important role in evaluating the stability of embankments under subsequent earthquakes.

(2) The fine particle content has a great influence and must be taken into account when studying the stability of the volcanic embankment under the independent or combined effects of rainfall and earthquake. At the same degree of compaction, the permeability of volcanic soils decreases with the increase in the fine grain content.

(3) The earthquake resistance of the compacted volcanic embankment subjected to previous rainfall increases as the fine content increases. Even so, this increment in seismic strength is not significant when the fines content was higher than 27%;

(4) The permeability of the compacted soil on the wet side of the optimum moisture content is less than it is on the dry side when the fine grain content of the soil is sufficiently large. In contrast, embankments compacted on the wet side exhibit less resistance to subsequent earthquakes under the same shear strain due to previous rainfall.

(5) In studying the slope under complex hazards, even if the previous shear strain induced is similar, the stability of the slope may change due to the different order of rainfall and seismic loadings.

DISCUSSIONS ON STABILITY EVALUATION OF VOLCANIC SLOPES

5.1 Introduction

In this Chapter, the experimental results in Chapter 4 will be discussed and compared with studies using elemental experiments as well as disaster reports. Based on the behavior of the water content of the soil during experiments, a simple method to evaluate the stability of the volcanic embankment is also proposed. Next, the field observations of the Komaoka volcanic soil were analyzed. Based on that, pore water pressure prediction based on historical data is carried out by applying machine learning techniques. In addition, the prediction of water content based on soil images is also studied with deep learning models.

5.2 Model test results in comparison with previous research

Using the same material as this study, Matsumura (2014) [43] investigated the effect of increment of fine content due to particle breakage on cyclic shear behavior through a series of cyclic undrained triaxial tests on compacted Komaoka volcanic soil with different fine content samples. The author found that as the fine particle content increases, the relationship between cyclic strength and dry density is proportional until the fine content is less than a certain threshold, after which it changes to inversely proportional. This fine content threshold was likely to be water content dependent: The higher the water content of the specimen, the lower the threshold of the fine content. When the soil moisture is equal to that of the model experiments in this study, the threshold suggested in [43] is around 32%, and the declining behavior of cyclic strength appears to be weak after that. The elemental experiments apply many ideal conditions, and the saturation progress in the triaxial experiments is not the same as the natural process. Therefore, it is necessary to verify these results with experiments that are closer to the field conditions. In the case that the increase in soil moisture was due to rainfall in the model tests in this study, the influence of fine particle content on cyclic strength confirmed a similar trend with Matsumura (2014) [43].

As mentioned above, the area selected for sampling in this study is one of the sites that experienced many major earthquakes including the 2018 dual disaster [21, 32, 83]. As

described in Chapter 1, Ishikawa et al., (2021) [21] reported the road cracks and subsidence in Sapporo City caused by the 2018 earthquake (magnitude of M6.7), which was not recorded in the 2003 Tokachi-oki earthquake (magnitude of M8.0). The authors suggested that one of the reasons for the difference in the damage situation between these two severe earthquakes was the rainfall from Typhoon Jebi that preceded the 2018 earthquake. The rise of the groundwater level, which was reported in [21], may also be due to the blocking effect similar to that behavior of volcanic soils with high fine particles in the model experiment in this study. In the above-mentioned liquefaction disaster in the Satozuka district, the topography was formed by the pumice sand from the crater of Shikotsu Lake filling the old valleys. Watabe and Nishimura (2020) [83] performed element tests on samples generated by real conditions before the earthquake to offer credible scenarios of the recorded disaster. The results of undrained cyclic triaxial tests showed that in spite of high fine content (more than 40%), the volcanic soils compacted on the wet side of optimum water content were still quite prone to be liquefied. The reason is considered to be the loose condition of the soil although compacted on the wet side of optimum water content. The presented microscopic photographs showed the loose soil structure created with the aggregates formed by fine particles and an inter-pore network between these aggregates. The high angularity of these aggregates creates friction resulting in the need for a higher compaction effort to densify the soil. Therefore, the authors also suggested that if the fill material had been sufficiently compacted, the earthquake would not have caused liquefaction over such a wide area. The earthquake-only model experiments in this study partially proved this suggestion by recording the high cyclic strength of the compacted volcanic soils at a compaction degree of 90%. Furthermore, the effect of previous rainfall, which was only included as a potential factor in the disaster scenario in [83], was confirmed in this study. It can be seen that the conclusions from the model test results in this study are similar to the previously published elemental experiment results or disaster reports for the same soil material. Moreover, an additional note raised by this study is that groundwater table lowering should be provided special attention in volcanic soils with a high fine-grained content of about 40% or more. In contrast, embankments with a sharp reduction in fine particle content due to the washing effect of rainfall should also be assigned a higher warning level. From the results of model tests, increasing the fine particle content of the volcanic soil was shown to reduce the hydraulic conductivity as well as the rate of increase in the shear strain of the embankment under rainfall and earthquake. Therefore, the selection of the filling material with high fine content soil or a mixture of sand and fine grain is proposed in this study as a solution for engineering design in mitigating the impacts of dual disasters. For economic purposes, it is necessary to provide a reasonable threshold for this increase. Furthermore, volcanic soils with a high fine-grained content of 40% exhibited some negative behaviors in this study such as difficulty in drainage and blocking effects which may cause an increase in the

groundwater table. Based on the analysis performed in Chapter 4, a fine particle content of 27% is recommended as a reference value for the design of embankments constructed by cohesionless soil materials such as Komaoka volcanic soil.

5.3 Stability evaluation method

From Figures 4.2 and 4.9, the variation in the saturation degree during rainfall tests obtained in this study is typified as shown in Figure 5.1. On the other hand, Figure 5.2 shows the change in soil infiltration capacity during rainfall presented by Horton (1939) [17]. It can be seen from these two figures that the water content in the soil gradually increases while the permeability gradually decreases. When the soil is completely saturated and cannot hold any more water, the saturation degree converges while the infiltration capacity reaches its minimum value. This relationship implies that changes in saturation degree over rainfall time can be expressed similarly to that of infiltration. The formula corresponding to the diagram in Figure 5.2 which determines the infiltration capacity of soil $f(t)$ over rainfall time t is shown in Equation 5.1 [17].

$$f(t) = f_c + (f_0 - f_c)e^{-kt} \quad (5.1)$$

where f_0 is the initial infiltration capacity, f_c is the final infiltration capacity, and k is the shape coefficient.

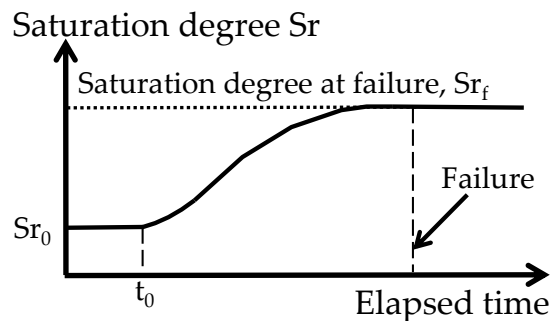


Figure 5.1 Typical variation in the saturation degree during rainfall tests in this study.

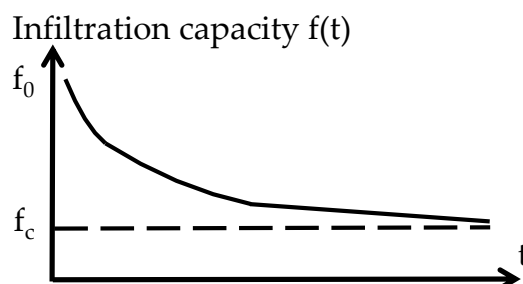


Figure 5.2 Diagram of soil infiltration capacity during rainfall based on Horton's concept (Horton (1939) [17]).

With the above-mentioned similarity, the same way was used to illustrate the time-dependent change in water content $w(t)$ as shown in Equation 5.2:

$$\begin{cases} w(t) = w_0 & \text{when } t < t_0 \\ w(t) = w_f + (w_0 - w_f)e^{-n(t-t_0)} & \text{when } t \geq t_0 \end{cases} \quad (5.2)$$

where w_0 and w_f are the water content at the initial and failure conditions, respectively; while n is the shape coefficient of the curve. The time t_0 is added as the starting moment of the rise in water content to account for the difference in position in the slope. Based on the behavior of saturation degree obtained from the experiments, t_0 is assumed to depend on the distance to the slope surface and the soil permeability. The interesting point is that the coefficient n seems to be independent of k and equal to 0.008 (sm1, sm3, sm6) or 0.005 (sm2, sm5) in this study for all three soil samples of $K_{8.5A}$, K_{soil} , and K_{40A} . Thus, the remaining unknown of the above equation is the water content at failure w_f which is investigated in the following section.

From the model test results, the relationship between initial water content w_0 and water content at failure w_f is summarized and illustrated in Figure 5.3. In addition to the results of the model tests in this study (dashed line), the data for the same material of Komaoka volcanic coarse-grained soil in Kawamura et al., (2021) [33] (solid line) were added for comparison purposes. As shown in the figure, the results of all three soil samples lie on the same curve in both the rainfall-only experiments and the post-rainfall earthquake experiments. The effect of dual disasters is demonstrated by the fact that the water content at failure in the case of seismic loadings is smaller. Moreover, the “rainfall-only” curve in this study is close to the “no freeze-thaw action” curve in [34] while the “post-rainfall seismic loadings” curve in this study is close to the “freeze-thaw action” curve in [34]. As can be seen, despite the different failure mechanisms, the failure point of slope in some specific cases (such as earthquake after rainfall and freeze-thaw action) is still similar. The relationship between both water contents in this study can also be expressed by a power function, similar to [34], as follows:

$$w_f = \beta w_0^\gamma \quad (5.3)$$

where values of coefficients β and γ are shown in Table 5.1. These values combined with Equation 5.3 can be considered a simple method to evaluate slope stability in practice with the measured water content as the object of assessment.

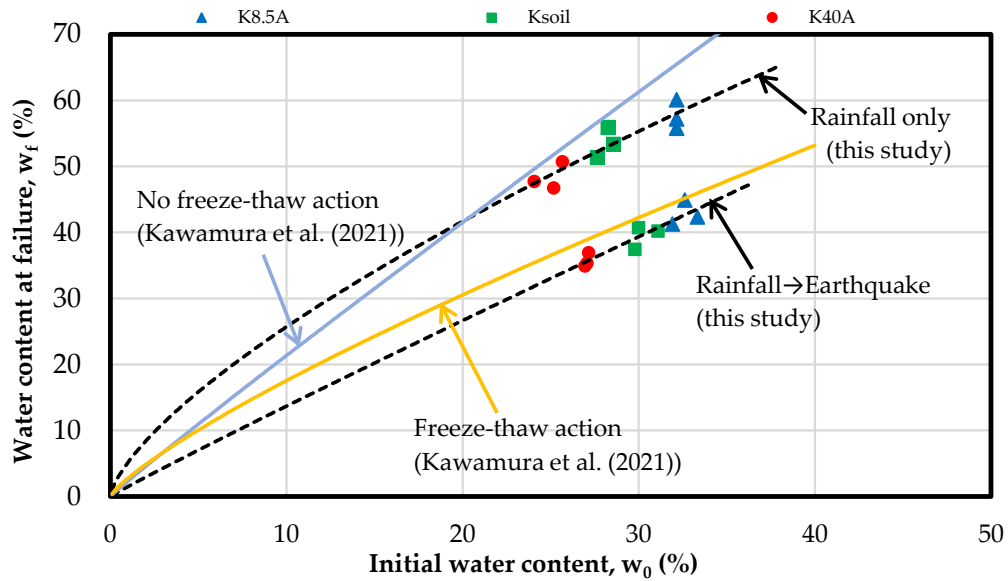


Figure 5.3 Relationship between water content at initial and failure conditions for Komaoka volcanic soil.

Table 5.1 Values of β and γ in this study

$w_f = \beta w_0^\gamma$	β	γ
Rainfall only	5.15	0.70
Post-rainfall earthquake	1.50	0.96

The framework for that evaluation of slope stability can be summarized as follows:

(1) based on the reason that may cause a slope failure, estimate the line of water content in Figure 5.3.

(2) Investigate the initial water content w_0 at the setting positions of measurement instruments such as soil moisture meters.

(3) Use Equation 5.3 to calculate predicted water content at failure w_f .

(4) Monitor the change in water content w such as increase during rainfall.

(5) Evaluate the condition of slope based on the relationship between measured water content w and the curve provided by w_0 , w_f , and Equation 5.2.

(6) If the monitoring data of water content reaches the predicted value, the failure of the slope will be predicted.

(7) Finally, evaluate slope stability by taking the geometric conditions of slopes into account.

In this way, it is possible to evaluate slope stability if such a relation can be obtained for an in-situ slope, and slope failure can be predicted if the water retention capacity in a slope is estimated by monitoring water content.

5.4 Prediction of water retention characteristic of Komaoka soil

5.4.1 Pore water pressure forecasting

Forecasting is the practice of creating predictions based on evidence from the past and present. Prediction is a related but broader phrase. Risk and uncertainty are fundamental to forecasting and prediction; it is generally accepted that indicating the degree of uncertainty associated with projections is a good practice. Forecasting may be done in two ways: qualitatively or quantitatively. Qualitative forecasting approaches are subjective, relying on the opinions and judgments of customers and experts; they are useful when historical data is unavailable. They are typically used for mid to long-term choices. Quantitative forecasting models, on the other hand, are used to anticipate future data as a function of previous data. They are acceptable for usage when historical numerical data is available and it is plausible to infer that some of the data patterns will persist into the future. These strategies are typically used for making short- or intermediate-term choices. Different methods may lead to a different level of forecasting accuracy. In any case, the data must be up to date so that the forecast can be as accurate as possible.

5.4.1.1 Evaluation metric of prediction

In statistical modeling, regression analysis is a set of statistical processes for estimating the relationships between a dependent variable and one or more independent variables. Thus the prediction task in this section is a regression analysis. The essential step in any model such as machine learning models is to evaluate the accuracy of the model. The metrics commonly used to evaluate the performance of the model in regression analysis are listed as follows. In a test or valid dataset with n elements, the element i has the value y_i and is predicted by the model to be y_{pi} .

Mean absolute error: known as the average of the absolute difference between the dataset's actual and anticipated values. It calculates the dataset's residuals' average.

$$MAE = \frac{1}{N} \sum_{i=1}^N |y_i - y_{pi}| \quad (5.4)$$

It is easy to see that MAE is a non-differentiable function in the general case. Therefore, we need to use a differentiable function that makes it easier to perform mathematical operations than MAE . Mean Squared Error: known as the mean of the squared difference between the data set's original and forecasted values. It calculates the residuals' variance.

$$MSE = \frac{1}{N} \sum_{i=1}^N (y_i - y_{pi})^2 \quad (5.5)$$

When a measure with the same units as the variable is needed, *RMSE* is used instead of *MSE*. Root Mean Squared Error: known as the square root of Mean Squared error. It calculates the standard deviation of residuals.

$$RMSE = \sqrt{MSE} = \sqrt{\frac{1}{N} \sum_{i=1}^N (y_i - y_{pi})^2} \quad (5.6)$$

The coefficient of determination or R-squared: known as the percentage of the dependent variable's variation that the regression model can explain. Since the score is scale-free, it will always be less than one regardless of how big or tiny the numbers are.

$$R^2 = 1 - \frac{\sum_{i=1}^N (y_i - y_{pi})^2}{\sum_{i=1}^N (y_i - \bar{y})^2} \quad (5.7)$$

where \bar{y} is the mean value of y_i :

$$\bar{y} = \frac{1}{N} \sum_{i=1}^N y_i \quad (5.8)$$

The lower value of *MAE*, *MSE*, and *RMSE* implies higher accuracy of a regression model. However, a higher value of R square is considered desirable. In addition, to ensure accuracy in the general case, models need to avoid overfitting which is defined in mathematical modeling as the creation of an analysis that correlates too closely or perfectly to a specific set of data and may thus fail to fit additional data or predict future observations correctly.

5.4.1.2 Monitoring of full-scale cut slopes and embankments

The purpose of in-situ testing is to clarify the slope failure mechanism of embankments constructed by volcanic soil in cold regions such as Hokkaido. Full-scale embankments and a cut slope were constructed by Komaoka volcanic coarse-grained soils at a testing site in Sapporo city, Japan (North latitude: 42°57'13", East longitude: 141°21'46"), which is similar to the sampling site of material for model tests in previous Chapters. Figure 5.4 shows a whole view of the testing site while figure 5.5 shows the measurement device for cut slopes.

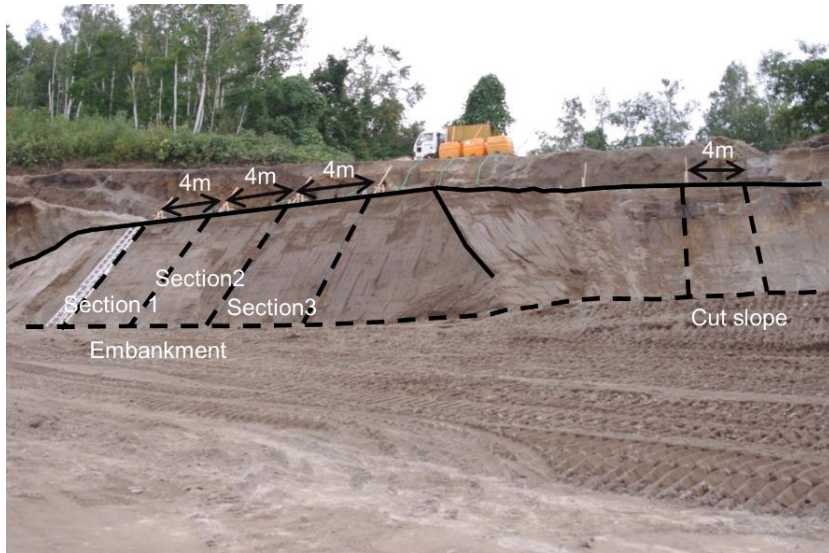


Figure 5.4 Full-scale cut slopes and embankments

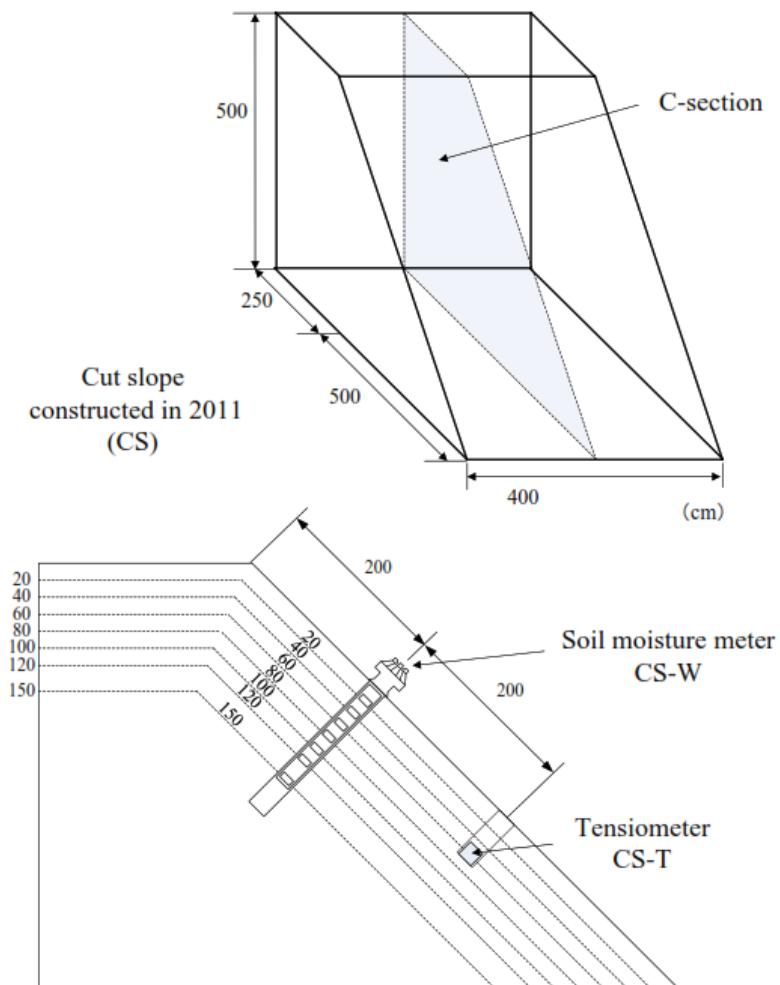
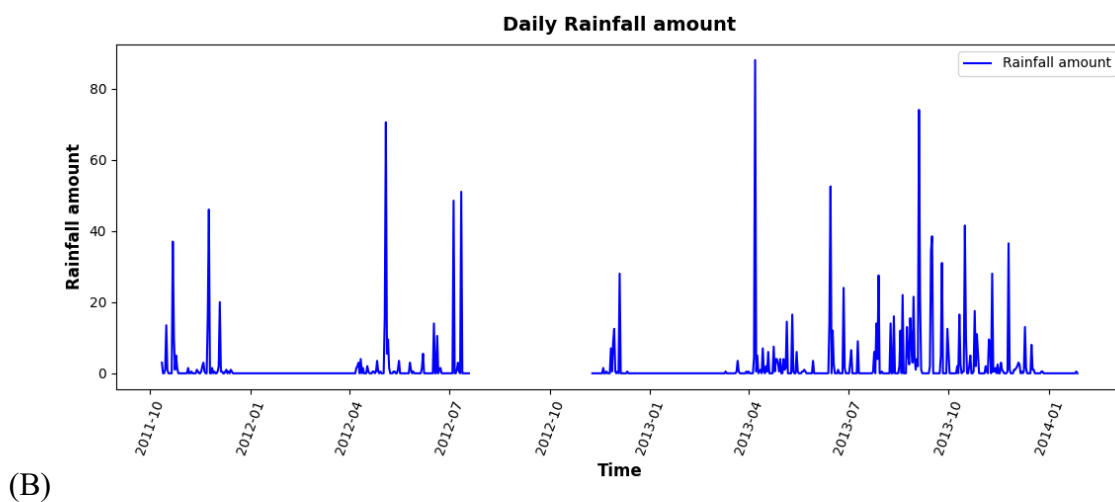
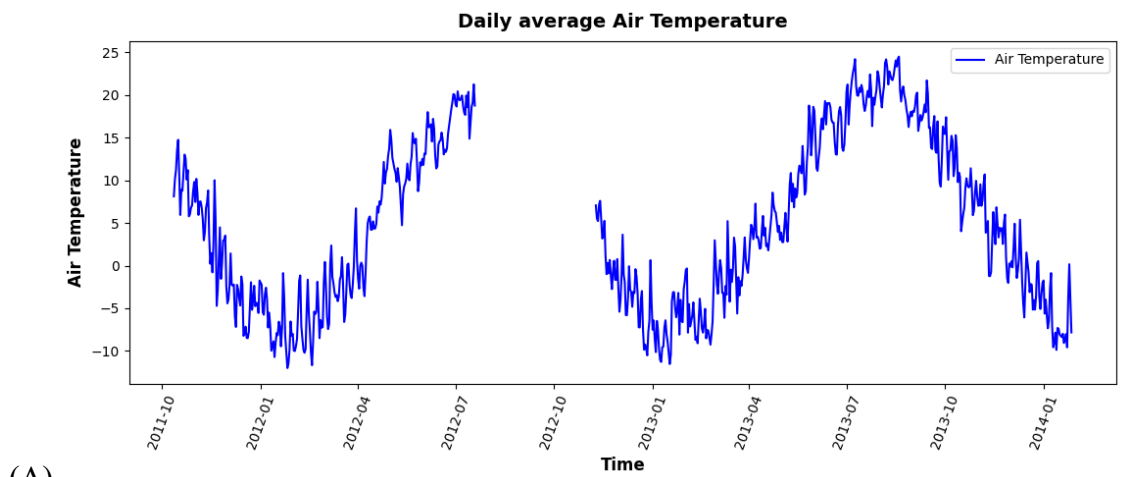


Figure 5.5 Locations of monitoring instruments of cut slopes

The full-scale embankment FE-2011 and the cut slope CS were constructed in

September 2011 for the purpose of in-situ measurement. The results and discussion of monitoring and the rainfall-induced slope failure phenomenon that actually occurred on FE-2011 have been revealed by Kawamura and Miura (2014b) [30] and Kawamura et al., (2013) [28]. Thus, because the FE-2011 embankment led to some slope failures, a new embankment FE-2012 was constructed using the same soil material next to FE-2011 in October 2012. The field monitoring of FE-2012 can be found in Kawamura et al., (2021) [33]. The measured data for the cut slope is shown in Figure 5.6. There are 2 phases of measurement, phase 1 is from 2011 to July 2012 and Phase 2 is from November 2012 to January 2014. It can be seen that each year pore water pressure increases sharply on two occasions: during the thawing and rainy seasons. This is typical behavior of soil in cold regions like Hokkaido. It can be seen that pore water pressure is highly dependent on season and weather.



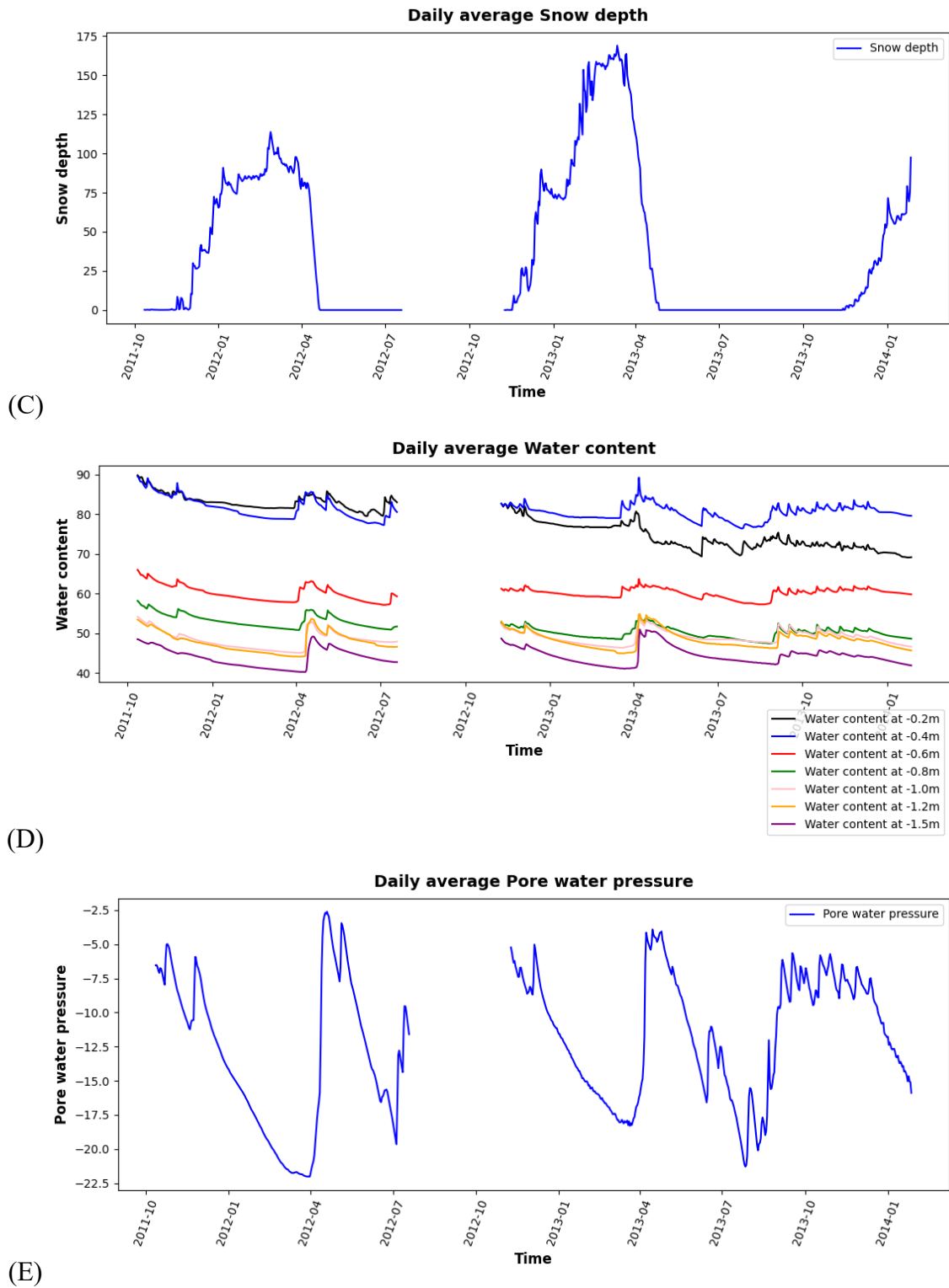


Figure 5.6 Measured data of cut slope (A) Air temperature (B) Rainfall amount (C) Snow depth (D) Water content (E) Pore water pressure

In this section, the forecasting task will be introduced step by step on pore water pressure data in phase 2 of the cut slope. The dataset covers 445 days from November 9, 2012, to January 27, 2014. The dataset will be divided by 80% (356 days) for the training

set and 20% (corresponding to 89 days) for the testing set (see Figure 5.7).

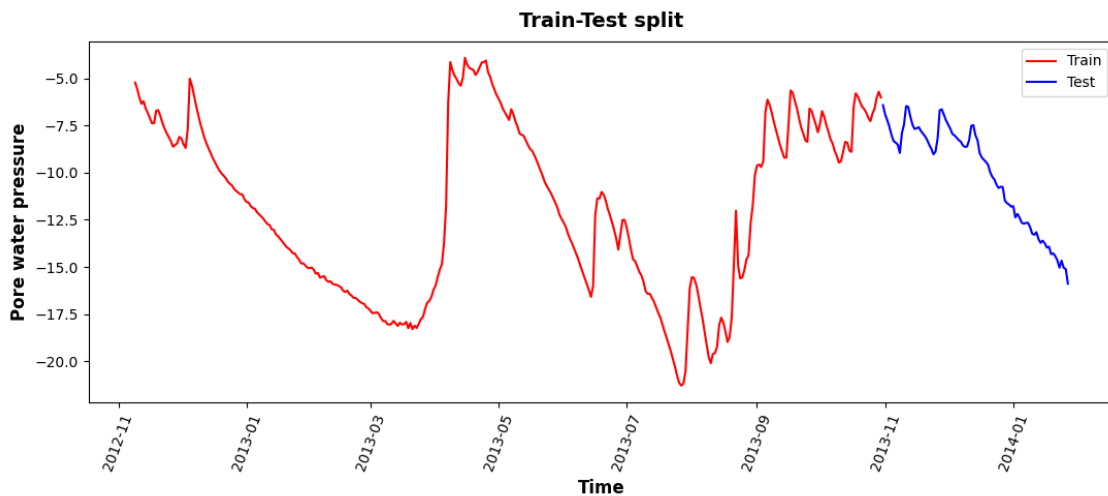


Figure 5.7 Train-Test split

5.4.1.3 Data Characteristics

In this section, the characteristics of pore water pressure data are examined accordingly based on the components of Time series data as shown in Figure 5.8.

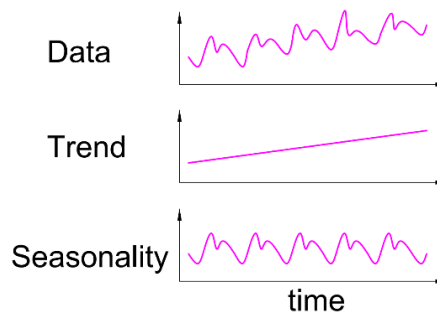


Figure 5.8 Time series data components

a. Trend

A trend component of time series shows a long-term shift in the mean of series that increases or decreases with time. The trend is the slowest-moving element of a series, signifying the most important time scale. The moving average plot can demonstrate the type of trend that a time series has. The average of the data inside a sliding window of some set width was used to compute a moving average of a time series. Each point on the graph reflects the average of all series values that fall inside the window on each side. The goal is to smooth out any short-term swings in the series, leaving just the long-term changes. A change must occur over a longer length of time than seasonal fluctuations in order to be considered a component of the trend. To display a trend, we use an average over a longer time than any seasonal period in the collection. In Figure 5.19, the moving average trend of

pore water pressure (blue line) was plotted with a sliding window of 365 days. With the input of the time feature (time index: day), that trend was tried to be simulated by linear regression as shown in the green line.

Linear regression: a method that predicts future occurrences by establishing a linear connection between an independent variable and a dependent variable. It is a statistical approach used for predictive analysis in data science and machine learning.

One note is that the linear trend is shown in Figure 5.9 only because it produces a smaller error than the nonlinear trend and not because the nonlinear trend cannot be regressed. Every time linear regression was used in this study, the output variable can depend on its previous values with an order different than 1. The word "linear" in "linear regression" can be misleading in that the value being regressed can only be linearly dependent on the variables. However, if you take the example of adding more variables of z_k equal to x_k^2 , it is possible to obtain a value that has a quadratic dependency with the variable.

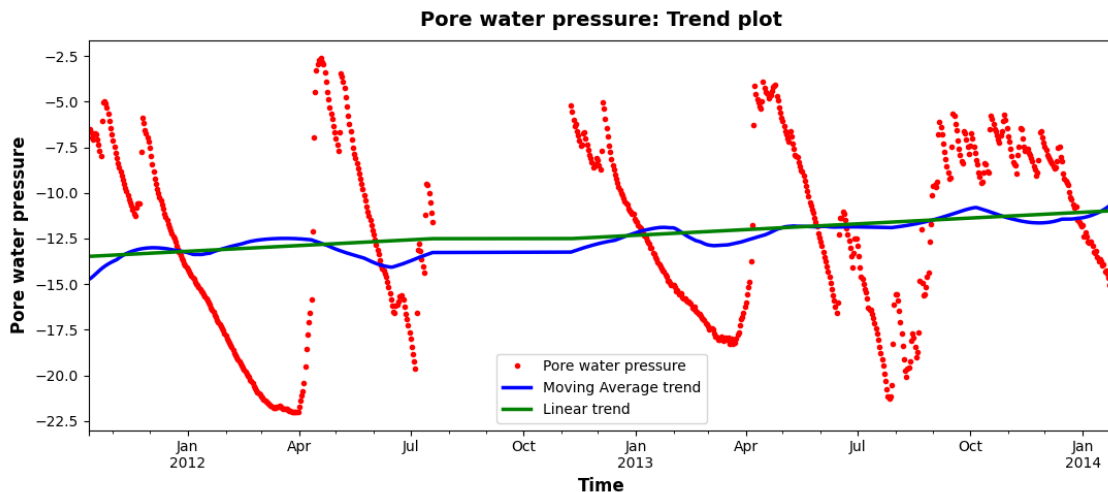


Figure 5.9 Moving average plot of pore water pressure data

b. Seasonality

Seasonality occurs when the mean of a time series changes on a regular, periodic basis. Seasonal changes often follow the clock and calendar, with repeats occurring throughout a day, a week, or a year. Seasonality is driven by natural world cycles or societal behavior standards, depending on the source of data. Figure 5.10 depicts the yearly seasonality of pore water pressure when data is shown in relationship with the day of the year.

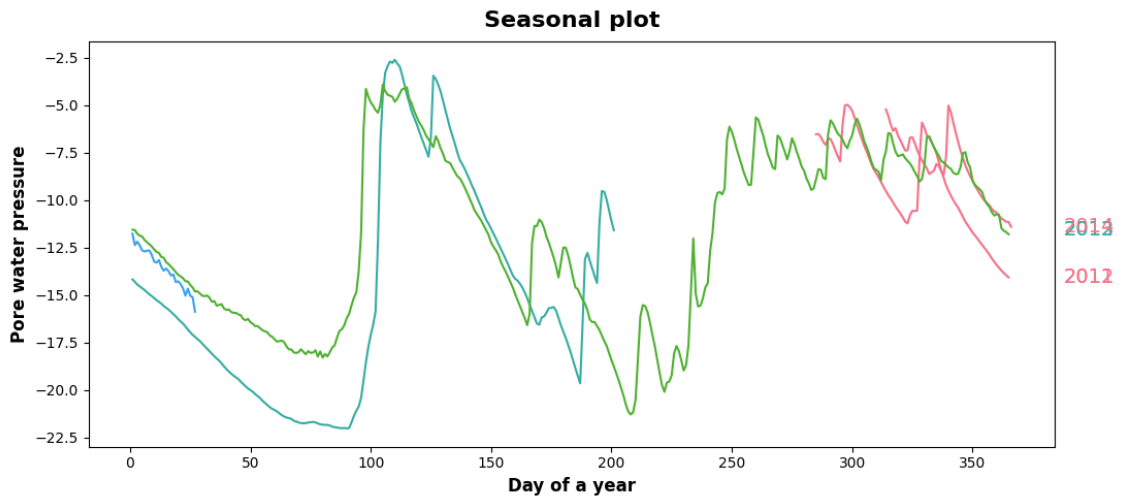


Figure 5.10 Seasonal plot of pore water pressure data

Similar to the previous section, the seasonality was tried to simulate by linear regression. For the input, there are two kinds of features that model seasonality: indicator and Fourier.

Seasonal indicator: If days of a year were used as 365 features, the model would obviously be overfitted when forecasting. Figure 5.11 shows the regressive result when the month indicator was used as 11 features, the coefficient of determination was 0.7308

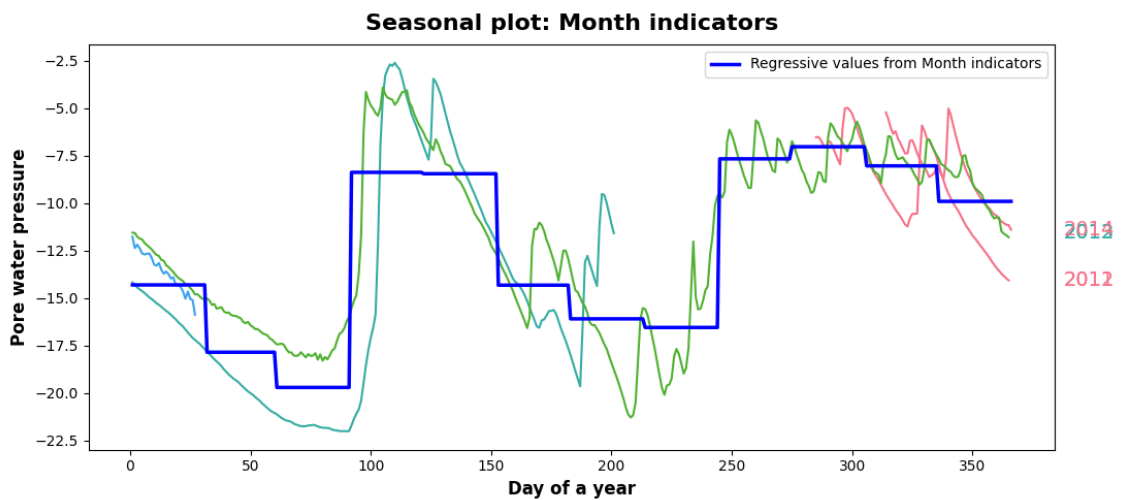


Figure 5.11 Seasonality regressed by Month indicator

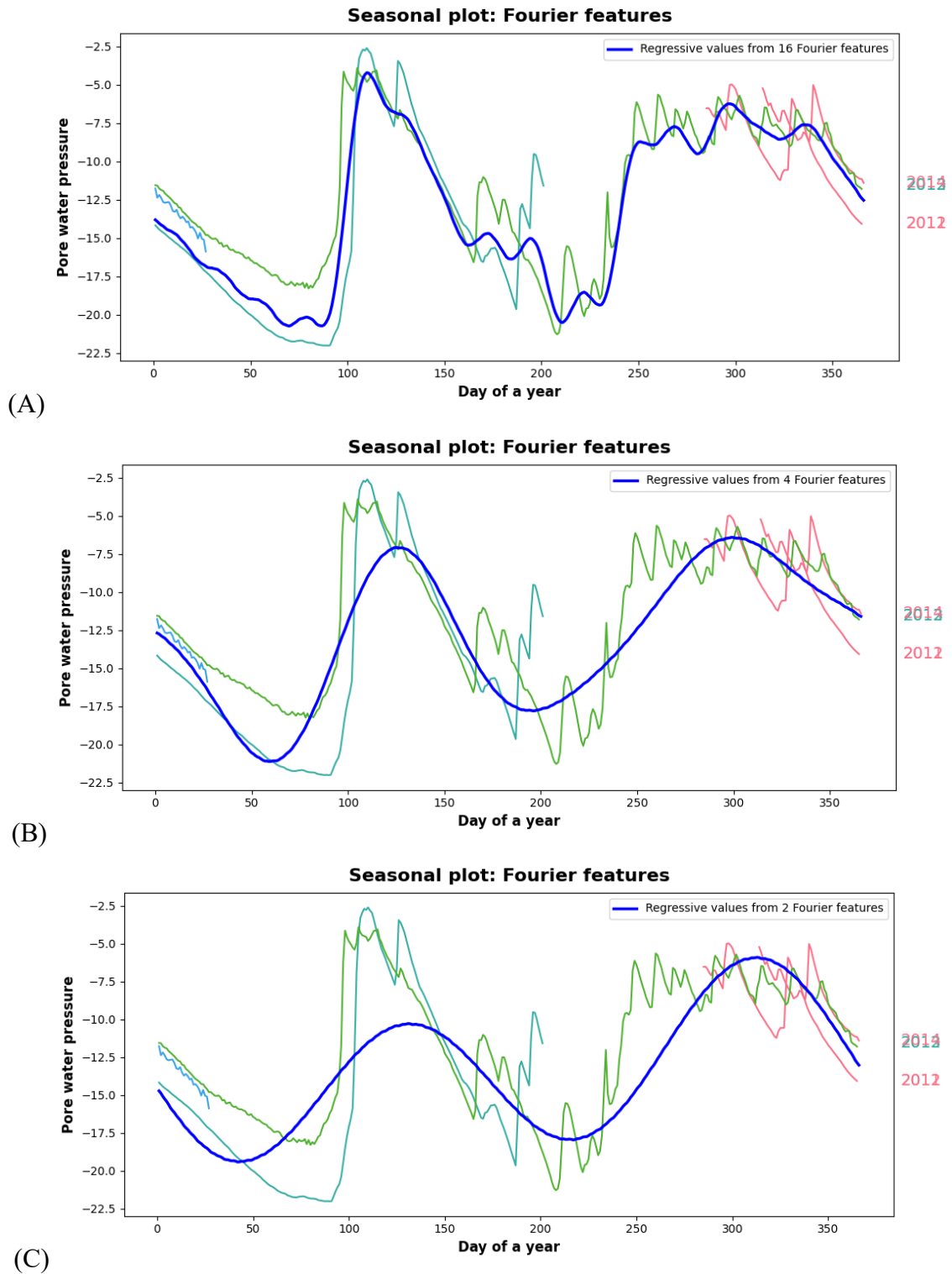


Figure 5.12 Seasonality regressed by Fourier features (A) 16 features (B) 4 features (C) 2 features

Fourier: Fourier characteristics are pairs of sine and cosine curves, one pair for each season's potential frequency, beginning with the longest. Rather than developing a feature for each date, Fourier features are used to try to capture the general form of the yearly curve

with a few features. The objective is to incorporate periodic curves with the same frequency as the seasonality in Figure 5.12 in the training data. The curves utilized are the sine and cosine trigonometric functions.

Figures 5.12(A), (B), and (C) show the Seasonality regressed by 16, 4, and 2 Fourier features, respectively. The coefficient of determination is 0.8895 for 16 features, 0.7588 for 4 features, and 0.6325 for 2 features. The increase in features raises the accuracy but also increases the overfitting risk. The number of Fourier pairs can be chosen through the periodogram as shown in Figure 5.13. The periodogram shows the strength of the frequencies in a time series. Specifically, the value on the y-axis of the graph is $(a^2 + b^2)/2$, where a and b are the coefficients of the sine and cosine at that frequency (as in the Fourier Components plot above). Since the pore water pressure increases twice a year as described above, the periodogram reaches its highest value at semiannual. From left to right, the periodogram drops off after Quarterly, four times a year. Therefore, four Fourier pairs can be chosen to model the annual season as in Figure 5.12(B).

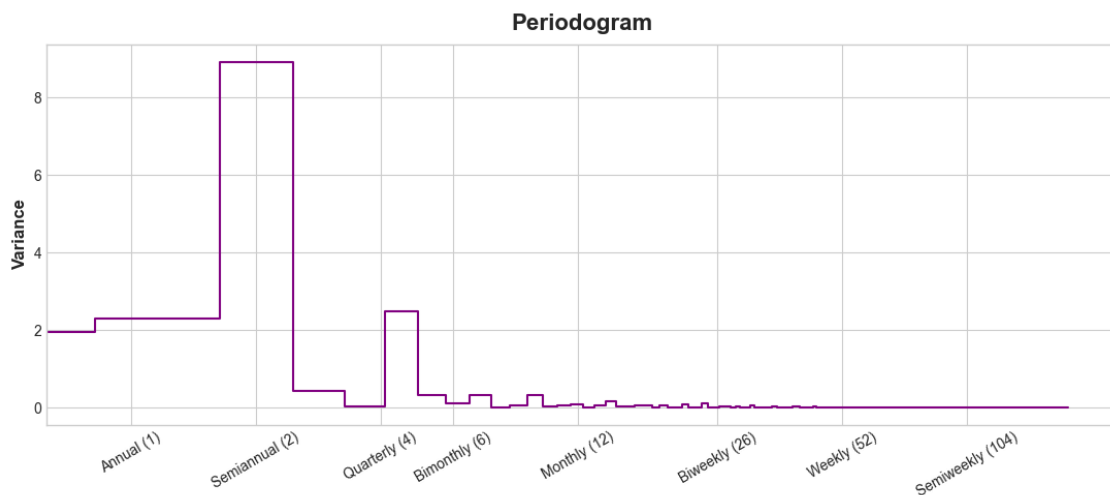


Figure 5.13 Periodogram of pore water pressure

Comparing Figures 5.11 and 5.12, the difference between the 2 above-mentioned features can be derived. The first kind, indicators, is best for a season with few observations, like a weekly season of daily observations. The second kind, Fourier features, is best for a season with many observations, like an annual season of daily observations, where indicators would be impractical.

c. Serial Dependence

The serial dependency of time series data cannot be demonstrated by time series visualization, but rather by using lag plots, as seen in Figure 5.14. In which the link between pore water pressure value and its lag characteristic was demonstrated. Lag features were

created by reversing the value in its index in one or more steps. These lag graphs show that there is a substantial and seemingly linear link between present pore water pressure and historical pressure. The numbers in the charts represent the most generally used measure of serial dependency, known as autocorrelation, which is essentially the correlation between a time series and one of its lags. Pore water pressure has an autocorrelation of 0.99 at lag 1, 0.98 at lag 2, and so on.

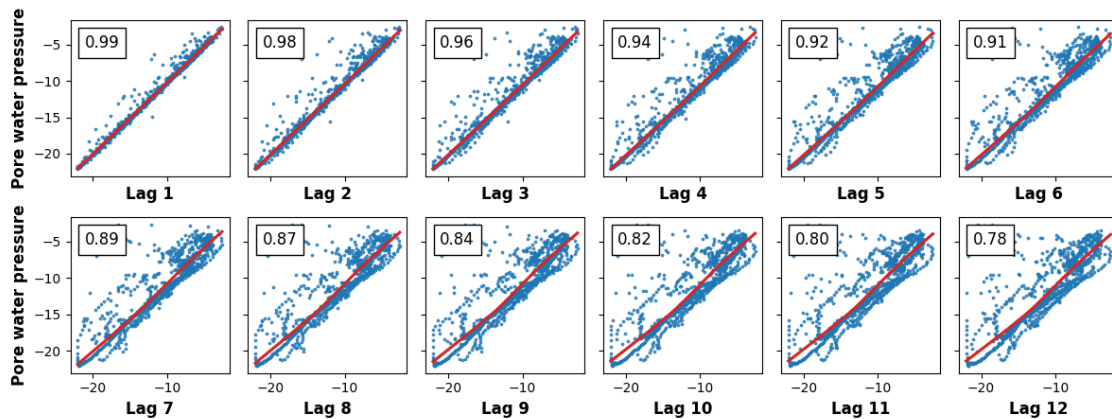


Figure 5.14 Lag plots of pore water pressure

It is often not necessary to include every lag with a high autocorrelation when selecting lags to utilize as features. In Figure 5.14, the autocorrelation at lag 2 might be completely due to "decayed" information from lag 1, or it could be a correlation carried over from the previous stage. If lag 2 does not provide anything new, there is no purpose to include it if lag 1 already exists. The number of lag features to employ may be determined by visualizing the partial autocorrelation, also known as a correlogram, as seen in Figure 5.15. The partial autocorrelation describes the correlation of a lag after accounting for all preceding lags, as well as the amount of "new" correlation that the lag provides. Because delays 1 through 4 in the picture are outside the intervals of "no correlation" (in blue), we might use them as features for pore water pressure data.

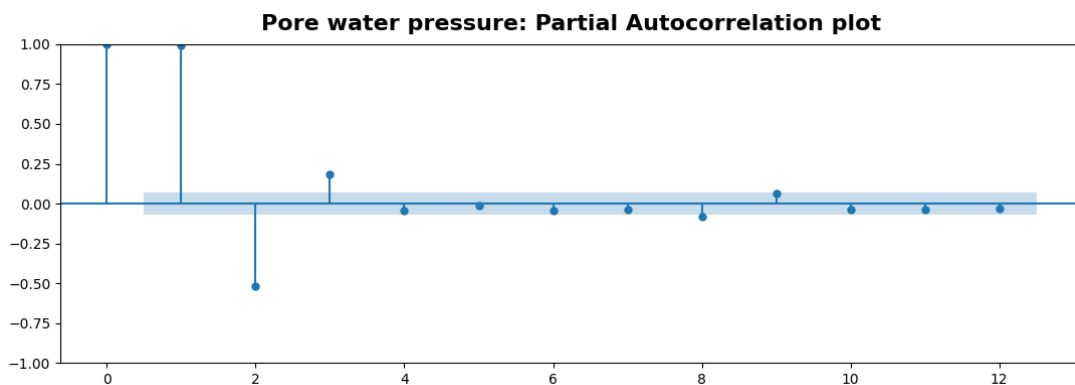


Figure 5.15 Partial Autocorrelation plot of pore water pressure

5.4.1.4 Forecasting results and discussion

a. Long-term forecasting

First, the forecasting for all dates in the test set will be discussed. This will provide a long-term view of the behavior of pore water pressure over a long period of time. Based on the properties of the pore water pressure data analyzed above, regression models can be built to forecast future values with self-values. Each of those models will forecast the value at a single point or step in time. To produce the forecast for multiple target steps, four common strategies can be used:

Multioutput model: Use a model that naturally provides numerous outputs. This method is simple and efficient, however, it is not applicable to all algorithms.

Direct strategy: Train a separate model for each step: one model forecasts one step ahead, another two steps ahead, and so on, thus having a different model anticipate each step might assist. The disadvantage is that training a large number of models can be computationally costly.

Recursive strategy: Train a single one-step model and use its forecasts to update the lag features for the following step. We feed a model's 1-step forecast back into that same model to utilize as a lag feature for the following forecasting step using the recursive technique. We only need to train one model, but because mistakes spread from step to step, projections for extended horizons may be erroneous.

DirRec strategy: A hybrid of the direct and recursive techniques in which a model is trained for each step and forecasts from prior stages are used as fresh lag features. Each model is gradually given an extra lag input. The DirRec technique can capture serial dependency better than Direct since each model always has an up-to-date set of lag characteristics, but it can also suffer from error propagation like Recursive.

In the following section, some well-known pre-built models based on recursive strategy were applied. The results are shown in Figure 5.16 with the red line representing the true value and the blue line representing the predicted value.

Naïve approach: One of the simplest methods, produces projections that are equal to the most recently observed value. If the time series is thought to be seasonal, the seasonal naive method may be more suited when projections are equal to the previous season's value. This approach works well for economic and financial time series, which frequently feature patterns that are difficult to anticipate regularly and precisely. Simple forecasts can also serve as a baseline against which more advanced models can be compared (see Figure 5.16(A)).

AutoRegressive (AR): employs linear regression to generate one prediction at a time and feeds the results back into the model. The sequence of the dependencies between the output value and the input variable - its past values (lags) at earlier time steps - is specified in AR-X(p). When establishing the model, the number of steps or lag duration must be given.

The results are shown in Figure 5.16(B).

MA (Moving Average): a strategy to model univariate time series, eliminating all seasonality but maintaining patterns in time series data. This is written as $MA(q)$, where q is the trend's order. In the results shown in Figure 5.16(C), the order of the trend is set to 1.

AutoRegressive Moving Average (ARMA): AutoRegression (AR) and Moving Average (MA) models are combined. This is known as the $ARMA(p,q)$ model, where p represents the order of the AR portion and q represents the order of the MA part. The results are depicted in Figure 5.16(D)

AutoRegressive Integrated Moving Average (ARIMA): has the following three components:

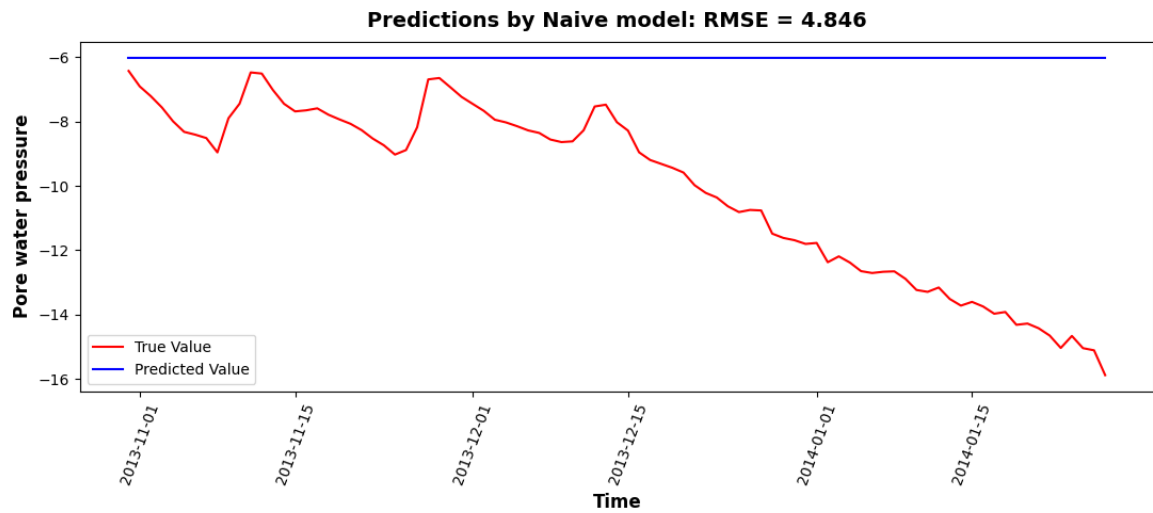
- (i) $AR(p)$, the autoregressive component.
- (ii) The integrated component (I) denotes that the data has been replaced with the difference between the current observation and the prior time step.
- (iii) $MA(q)$, or moving average.

$ARIMA(p, d, q)$ represents this model, where p , d , and q determine the order of the $AR(p)$, $I(d)$, and $MA(q)$ models, respectively. Figure 5.16(E) depicts the findings.

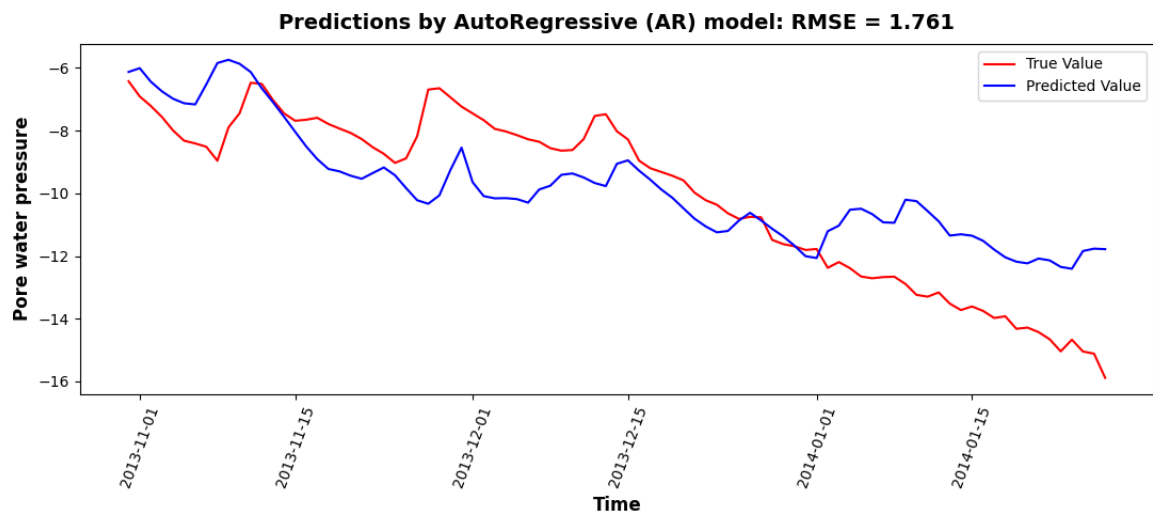
Despite the fact that ARIMA models are quite strong, optimizing the proper parameters for ARIMA models can be time-consuming. Auto ARIMA similar is a common implementation for solving this problem.

Auto ARIMA: Discover the best order for an ARIMA model automatically. The auto-ARIMA approach aims to find the best parameters for an ARIMA model before settling on a single-fitted ARIMA model. The results are depicted in Figure 5.16(F).

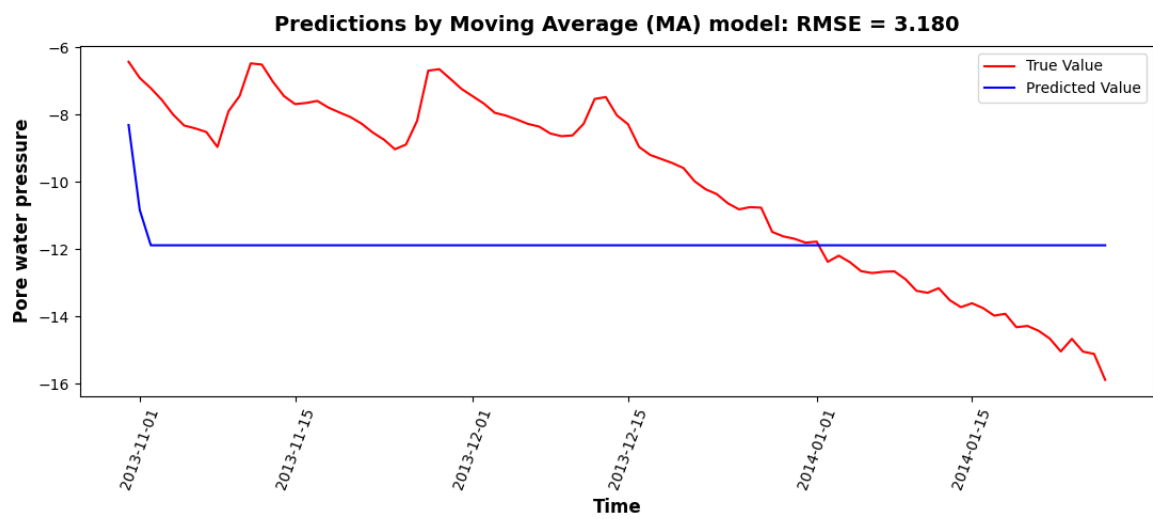
Seasonal AutoRegressive Integrated Moving Average (SARIMA): an extension of the ARIMA model that allows for seasonal AR, I, and MA modeling. Seasonal ARIMA models are designated as $ARIMA(p,d,q)(P, D, Q)_m$, where m is the number of seasons and P, D, Q (uppercase) are the autoregressive, differencing, and moving average components for the seasonal element of the ARIMA model. The results are shown in Figure 5.16(G).



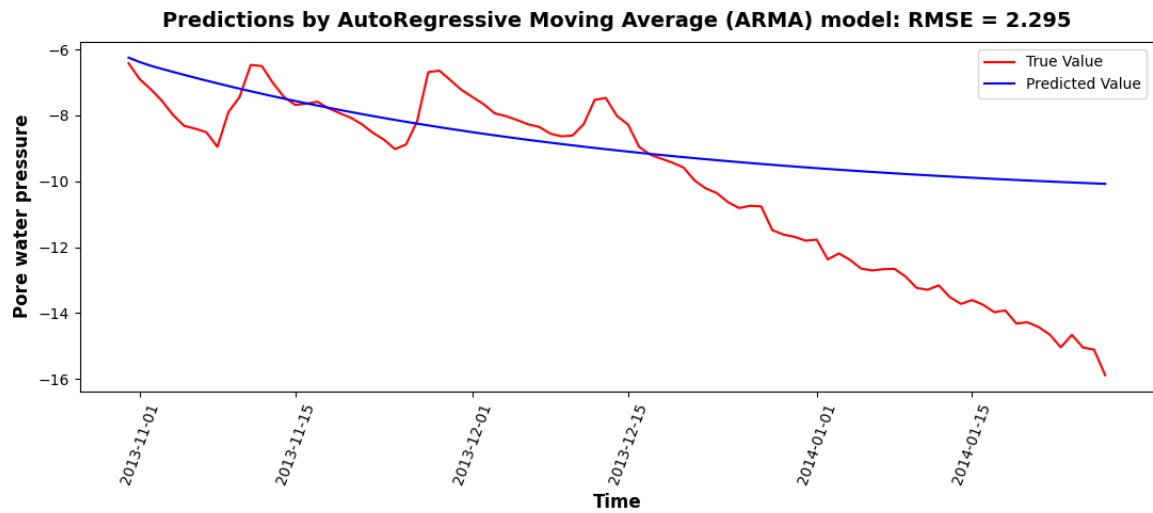
(A) Naïve approach



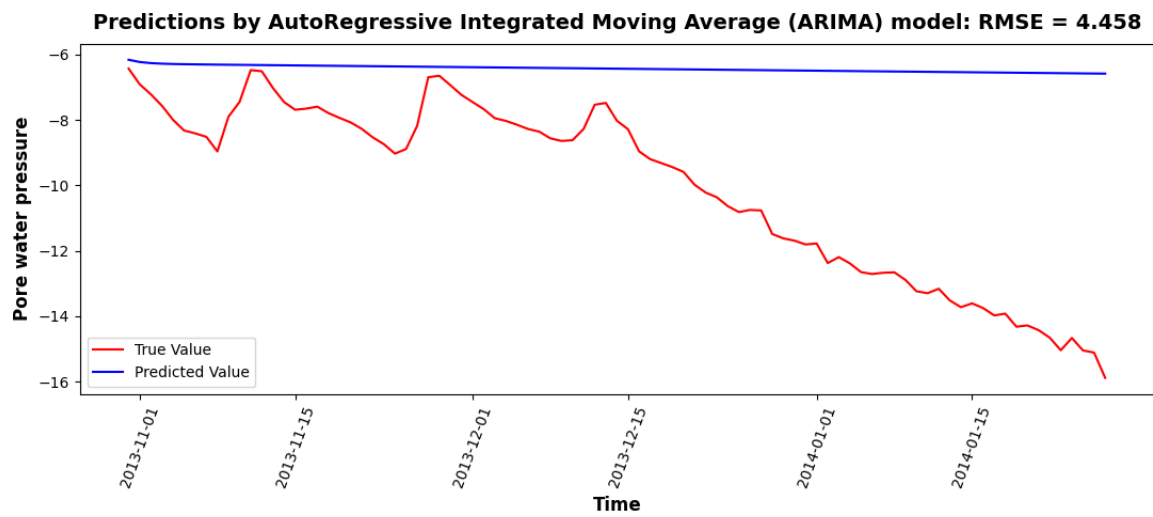
(B) AutoRegressive



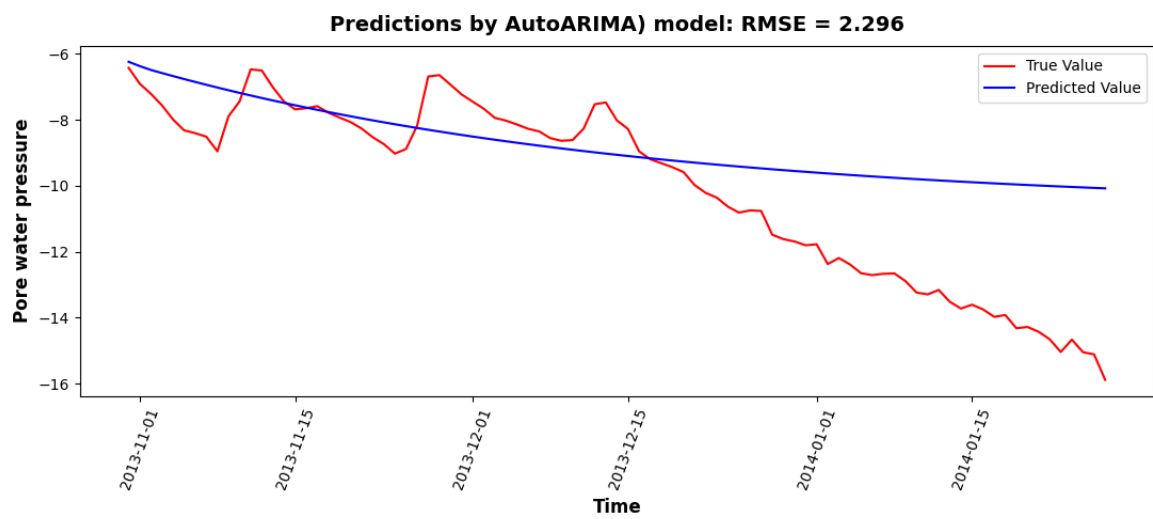
(C) Moving Average



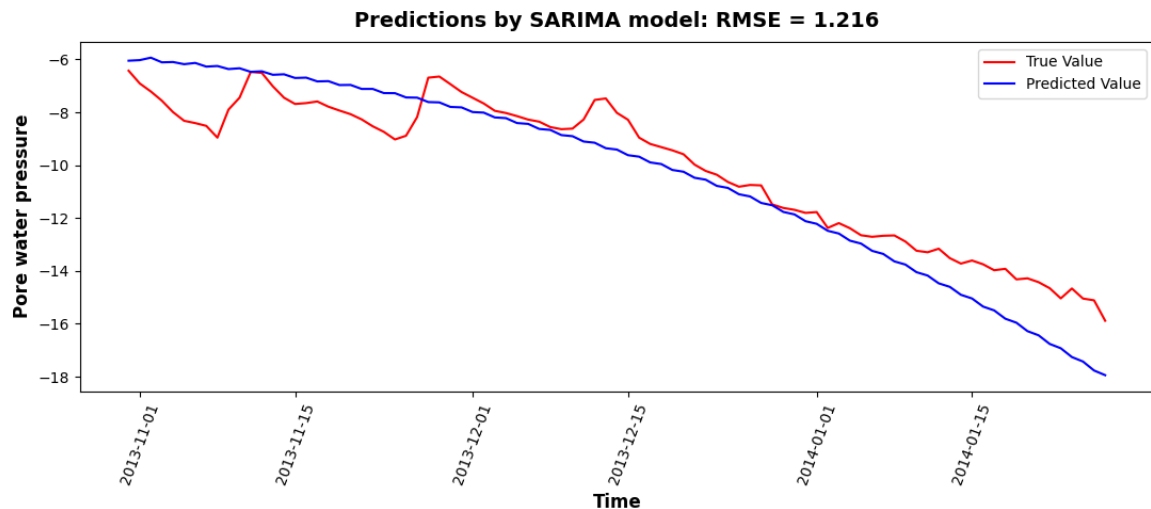
(D) AutoRegressive Moving Average



(E) AutoRegressive Integrated Moving Average



(F) Auto ARIMA



(G) Seasonal AutoRegressive Integrated Moving Average

Figure 5.16 Results in long-term forecasting

Thus, it can be seen that the models can work effectively when predicting many steps. As mentioned above, new values need to be constantly updated to improve the accuracy of the model. This work will be discussed in the next section.

b. Forecasting with daily updated data

Using lag features as input and current pore water pressure value as output, the dataset now looks like a supervised learning problem for machine learning. In addition to a linear regressor, some machine learning models were introduced to use in this section:

- **Ridge regressor**: a technique for calculating the coefficients of multiple-regression models where the independent variables are highly correlated. It has been applied in a variety of domains such as econometrics, chemistry, and engineering [41].
- **Lasso regressor** (least absolute shrinkage and selection operator): a regression analysis approach that conducts variable selection as well as regularization to improve the predictability and interpretability of the final statistical model [9].
- **Extreme Gradient Boosting (XGBoost)**: an open-source software package that provides a framework for regularizing gradient boosting. It has lately acquired a lot of attention and popularity as the algorithm of choice for many winning teams in machine learning contests [5].
- **Random Forest** (random decision forests): an ensemble learning approach for classification, regression, and other problems that works by building a large number of decision trees during training. For classification problems, the random forest output is the class chosen by the majority of trees. The mean or average forecast of the individual trees is returned for regression tasks. Random decision forests compensate for decision trees' tendency to overfit their training set. In general, random forests outperform choice trees. However, data features might have an

impact on their performance [2].

- **Elastic Net:** a regularized regression approach in statistics that linearly integrates the L1 and L2 penalties of the lasso and ridge methods in the fitting of linear or logistic regression models [91].
- **Support vector machines:** supervised learning models with related learning algorithms that examine data. Given a set of training examples, each labeled as belonging to one of two categories, an SVM training method builds a model that assigns new instances to one of two categories, making it a non-probabilistic binary linear classifier. In order to maximize the distance between the two categories, SVM converts training instances to points in space. Then, new instances are categorized in that same space by which side of the gap they fall after being mapped into it. [14].

Although machine learning models can fully meet the prediction requirements. A deep learning model is also introduced in this section that aims to be applied to more complex problems.

- **Artificial neural networks:** computer systems based on the biological neural networks that make up animal brains. An ANN is made up of linked neurons that are often aggregated into layers. The connections between neurons, known as edges, can send a signal - a real number determined by some non-linear function of the sum of preceding neurons - to the next neuron. Neurons and edges usually have a weight that changes as learning progresses [78].

The prediction results are shown in Figure 5.17 and the errors of the models are summarized in Table 5.1. It can be seen that the models have improved accuracy markedly compared with those in the previous condition. With the above-mentioned deep serial dependency, it is easy for the models to learn the relationship between the lag feature and the target and use it to make accurate predictions. These results confirm that new data must be continuously updated to improve the performance of the model. This problem poses a requirement for the application of technologies such as IoT to sensors and measurement systems in the field for pore water pressure and soil moisture.

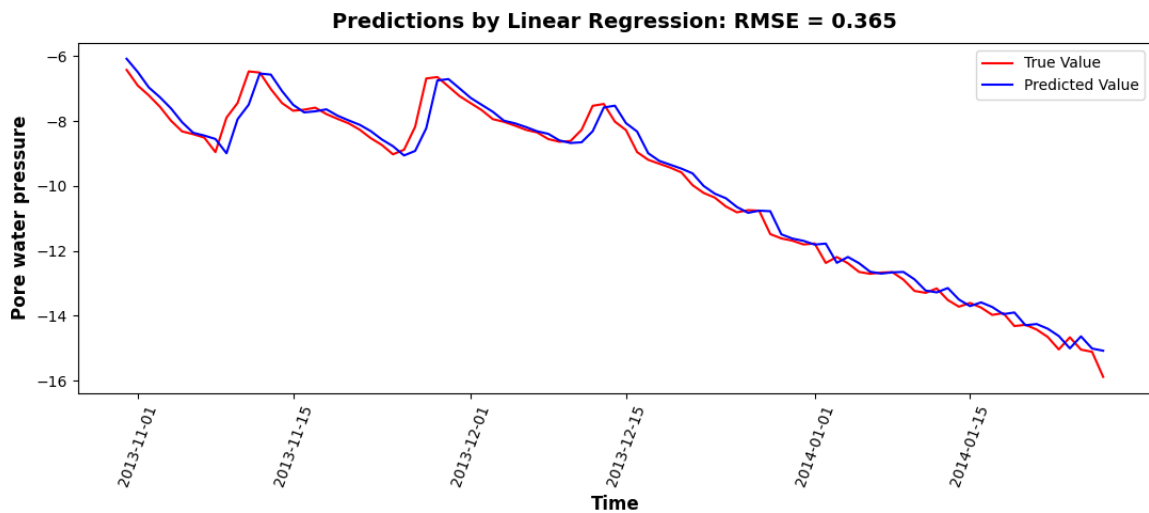
Table 5.2 Case definition and results

Table 5.2a. Case definition

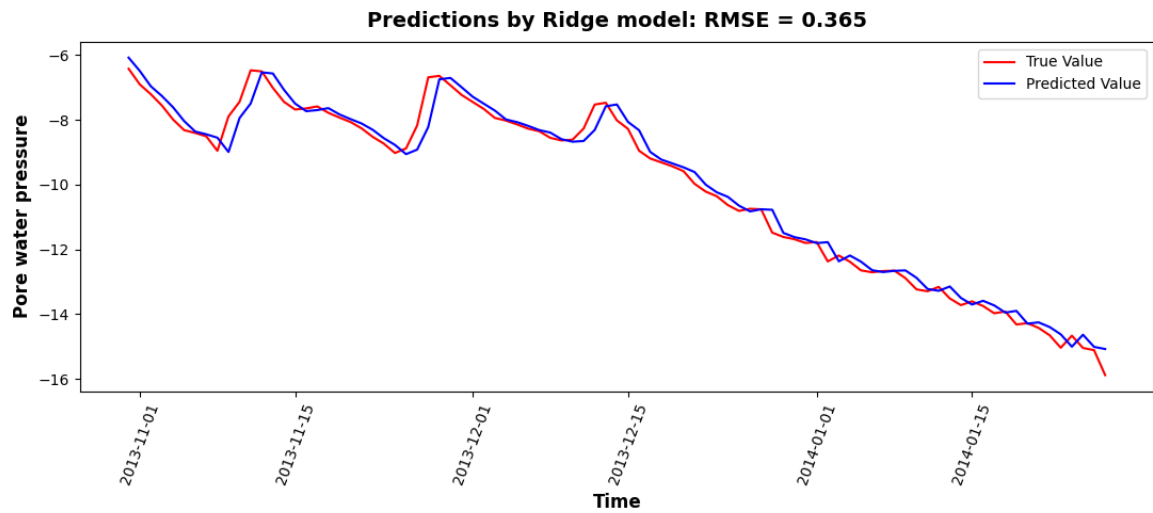
Parameters	Case 1	Case 2	Case 3
Definition	Historical pore water pressure data is daily updated	Historical pore water pressure data is daily updated combined with climate data	Forecasting with only climate data
Input	Lag features	Lag features Time features Air temperature Rainfall amount Snow depth	Time features Air temperature Rainfall amount Snow depth

Table 5.2b. RMSE of machine learning models

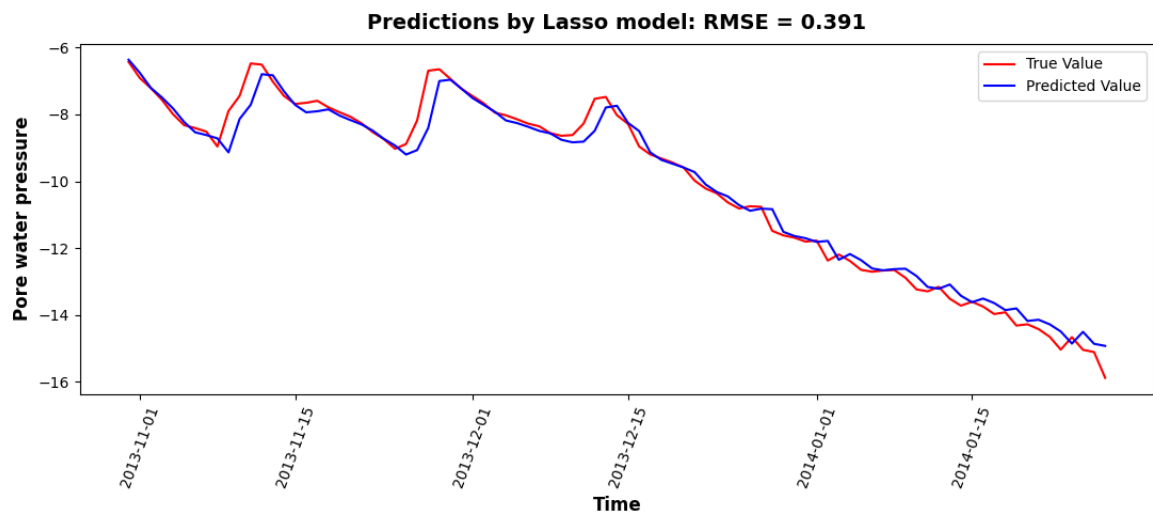
Model	Case 1	Case 2	Case 3
Linear regressor	0.365	0.328	3.094
Ridge regressor	0.365	0.328	3.094
Lasso regressor	0.391	0.349	3.019
XGBoost	0.633	0.414	2.102
Random forest	0.589	0.375	1.934
Elastic Net	0.390	0.374	3.015
SVM	0.366	1.850	2.272
ANN	0.401	0.546	2.482



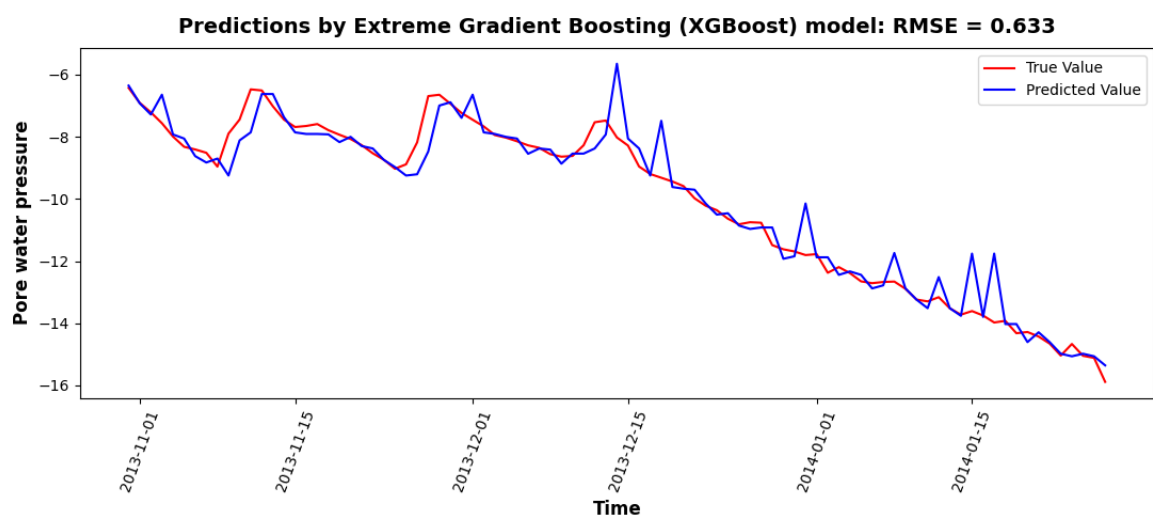
(A) Linear regressor



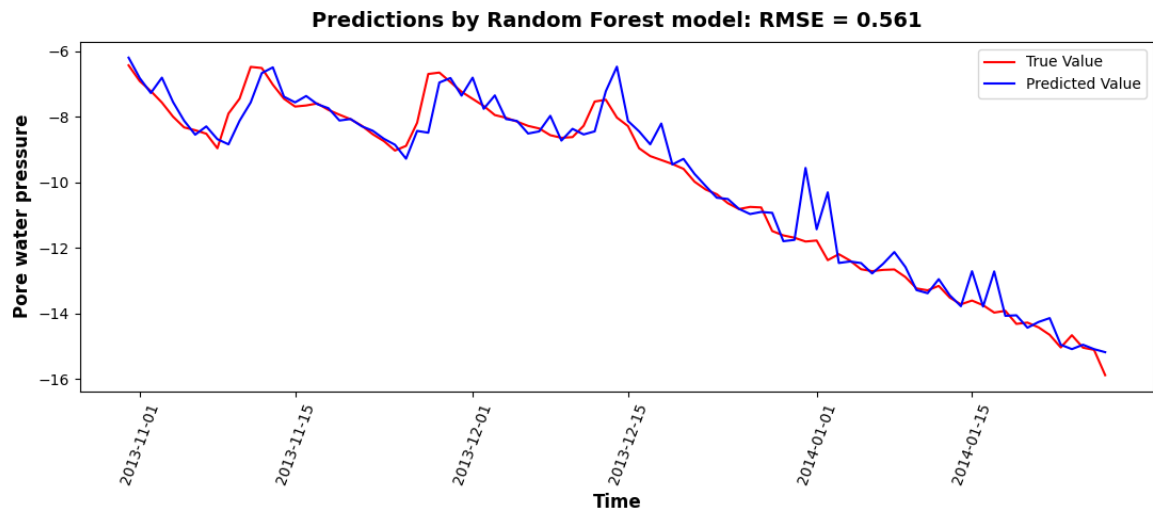
(B) Ridge regressor



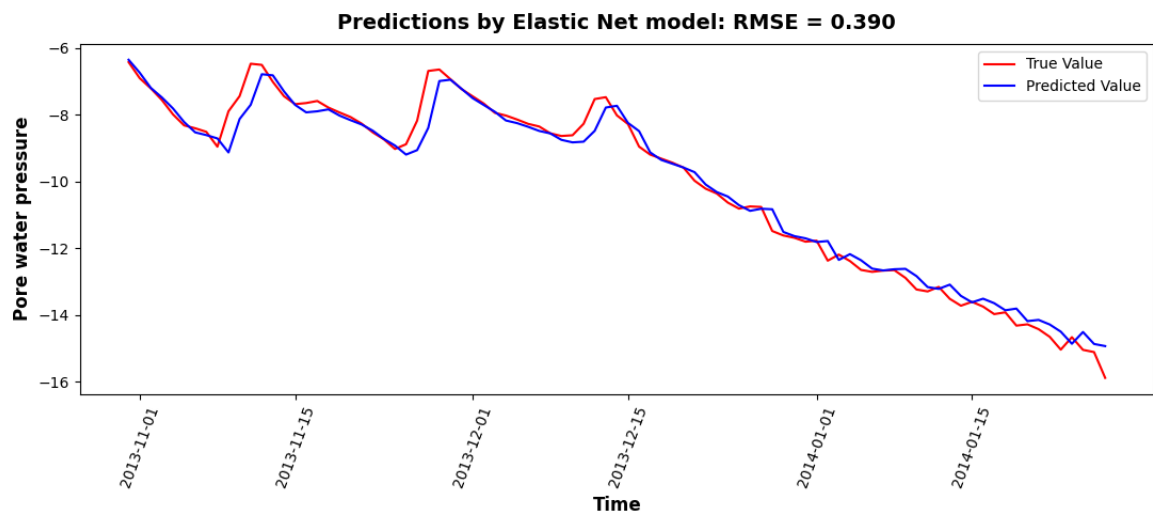
(C) Lasso regressor



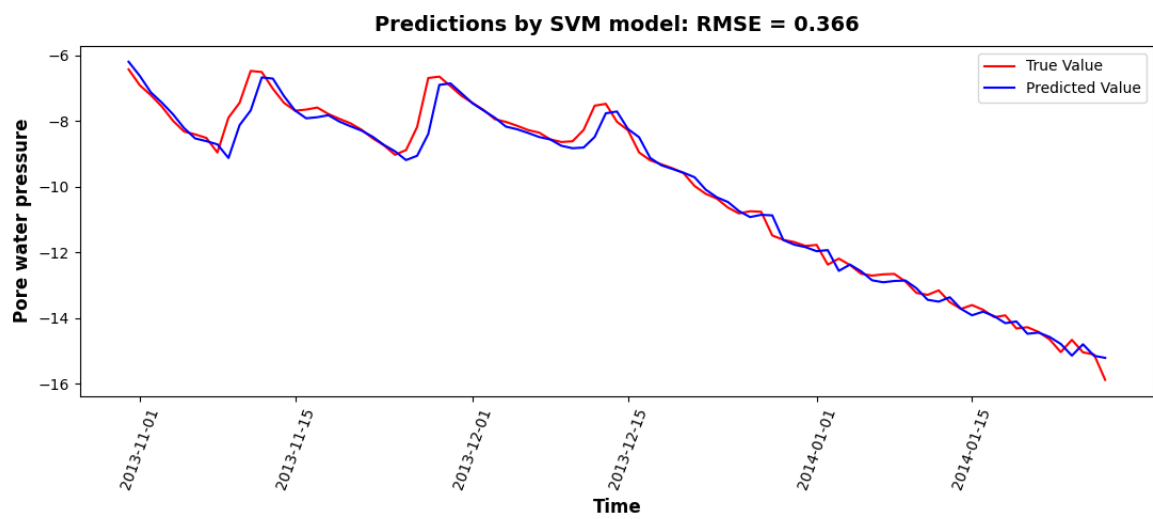
(D) XGBoost



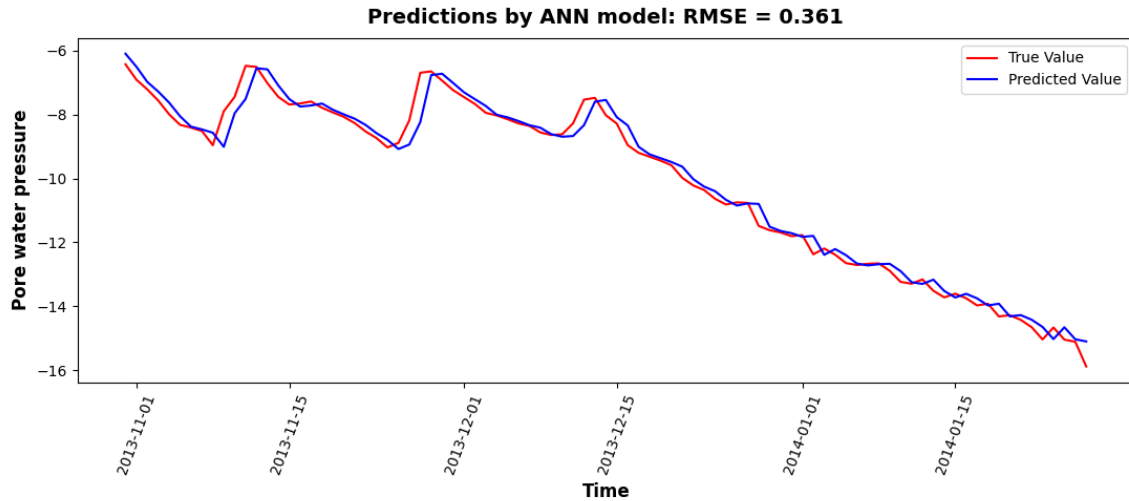
(E) Random Forest



(F) Elastic Net



(G) SVM



(H) ANN

Figure 5.17 Forecasting results with daily updated data

c. Forecasting with daily update data and climate data

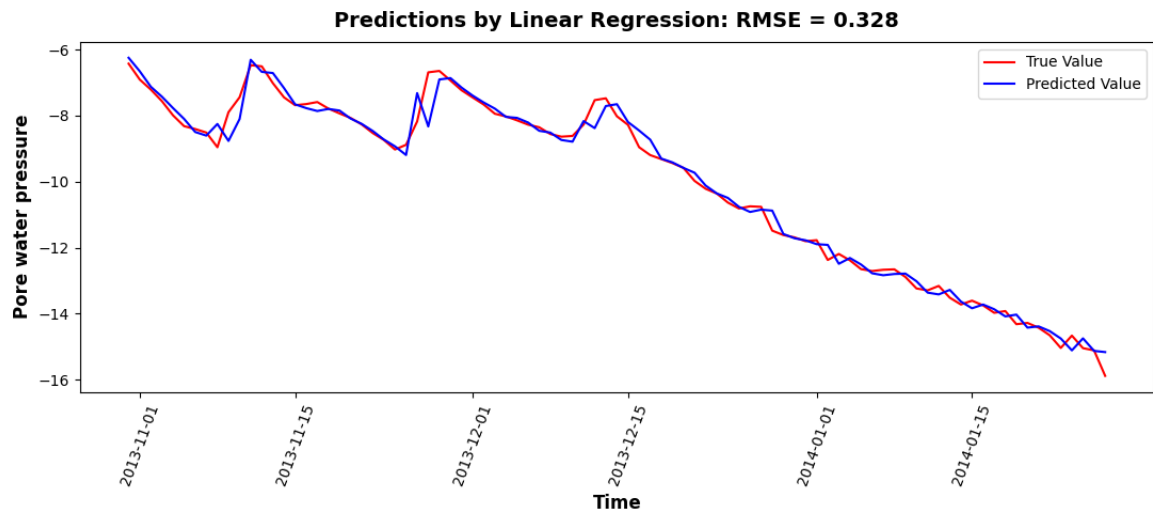
It is easy to see that with the model based only on previous values, the prediction was only following these data. In addition to the lag feature in the previous section, we add weather data as input to the models. Added features include:

- Time features;
- Air temperature;
- Rainfall amount;
- Snow depth.

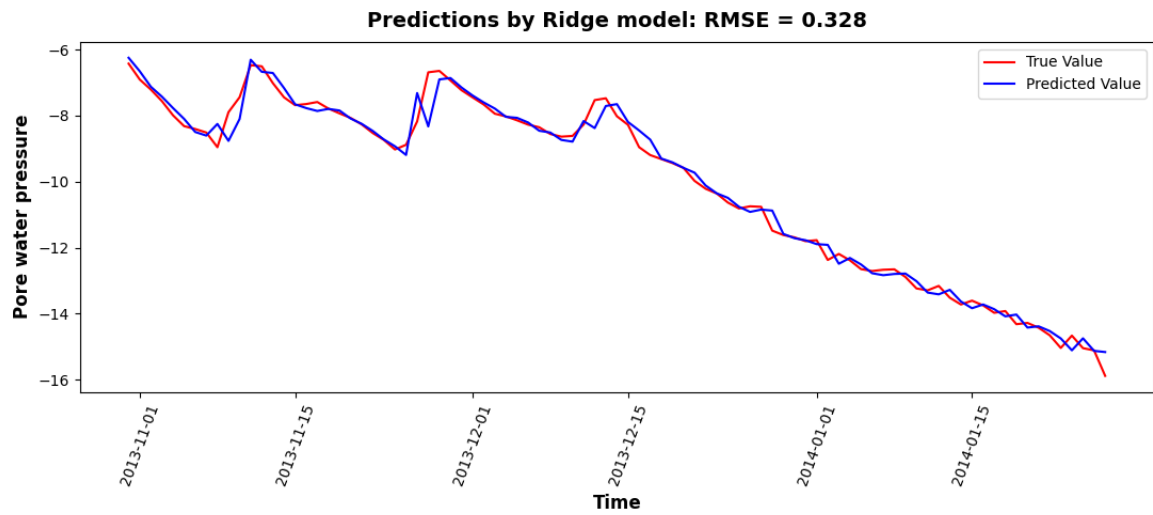
The forecasting results are shown in Table 5.1 and Figure 5.18. Because the pore water pressure data was strongly related to the climate data, the performance of models was once more time improved. Moreover, compared with the previous case, the prediction has shown the initiative to the change of weather. However, the SVM and ANN models generate more errors than in the previous case. These overfit of the models can be attributed to the small number of training sets. After training, the XGB and Random Forest models evaluated the importance of features as shown in Table 5.2. It can be seen that the lag feature is still the main input data used.

Table 5.3 Feature importance of forecasting with daily update data and climate data

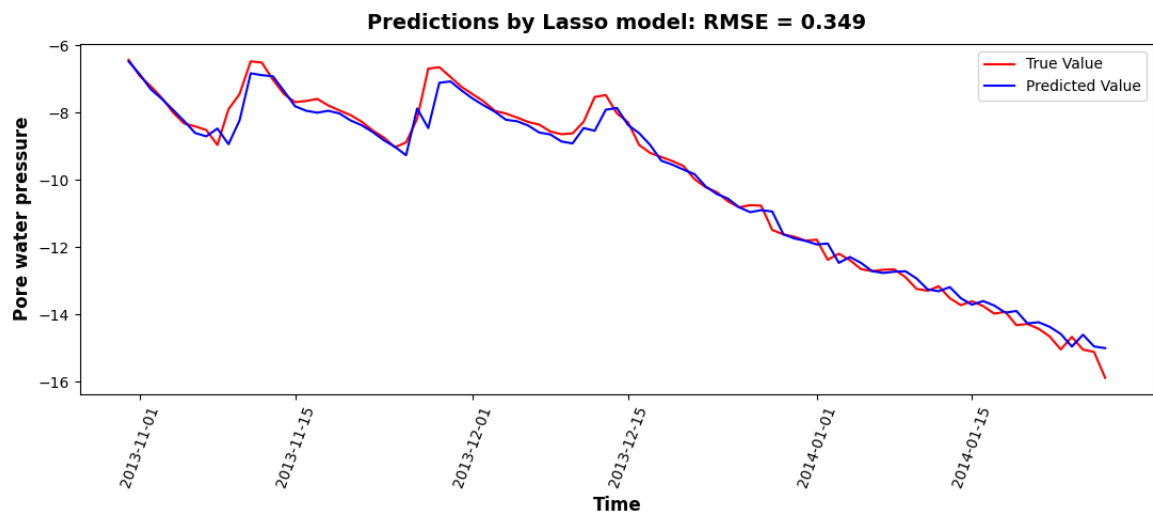
Feature	XGB	Random Forest
Lag features	97.22%	98.36%
Time features	0.75%	0.61%
Air temperature	0.16%	0.20%
Rainfall amount	1.21%	0.54%
Snow depth	0.66%	0.29%



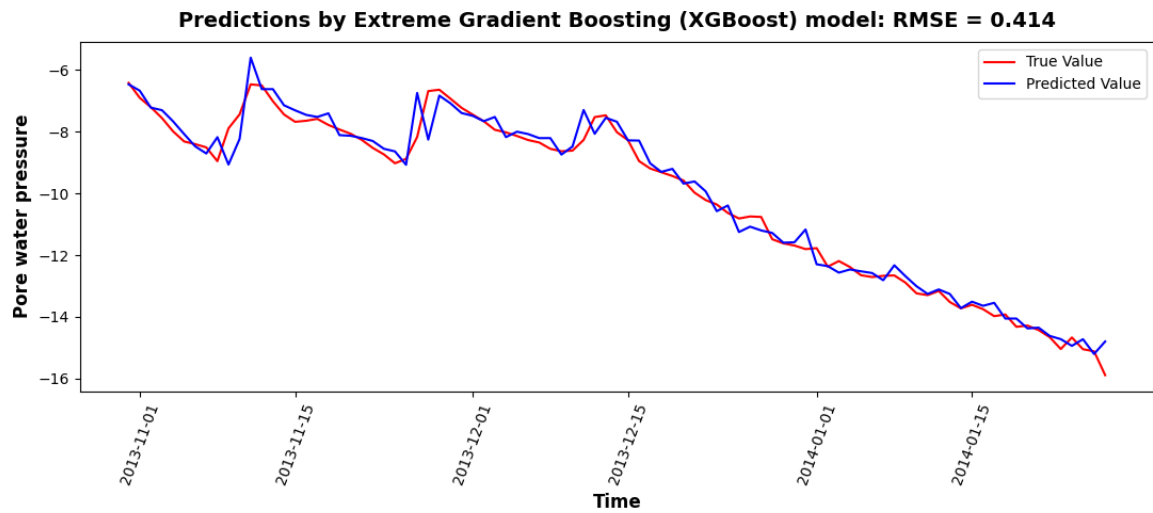
(A) Linear regressor



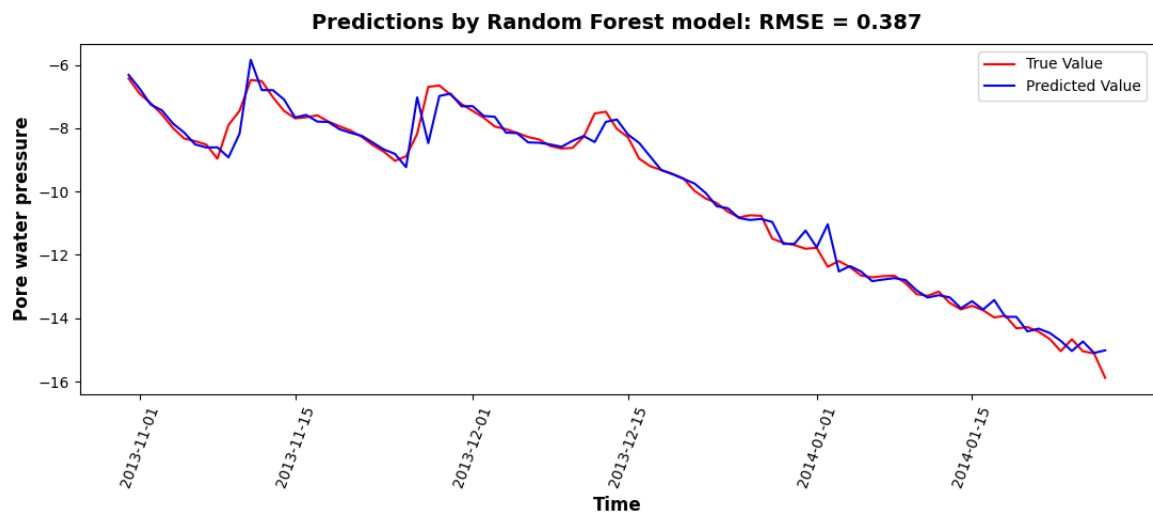
(B) Ridge regressor



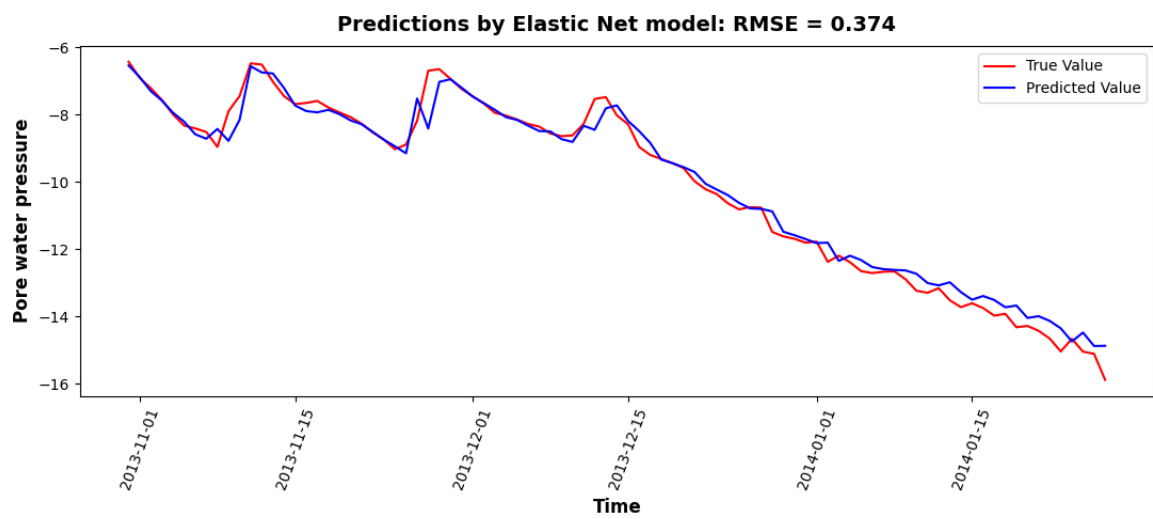
(C) Lasso regressor



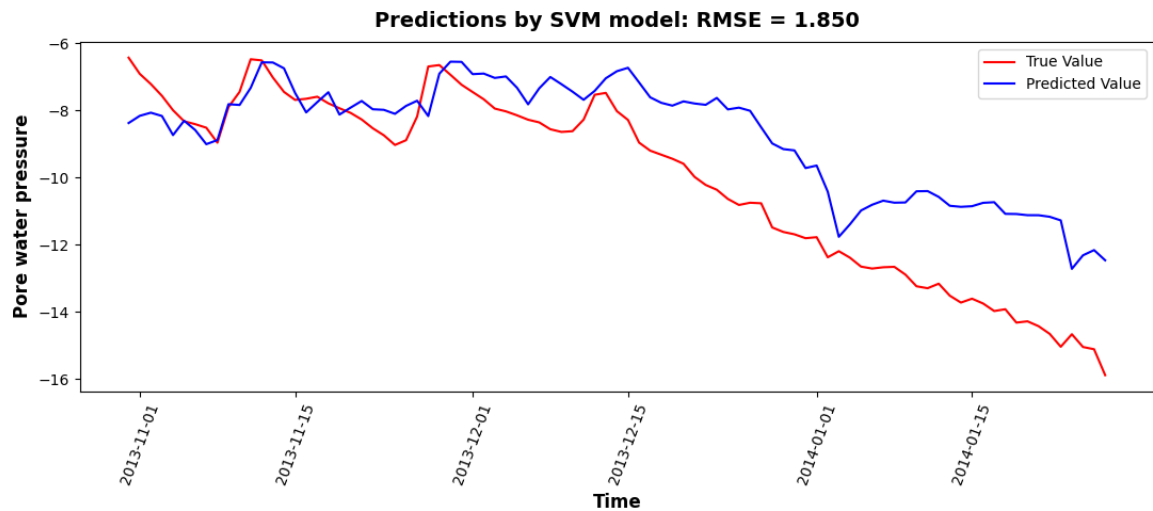
(D) XGBoost



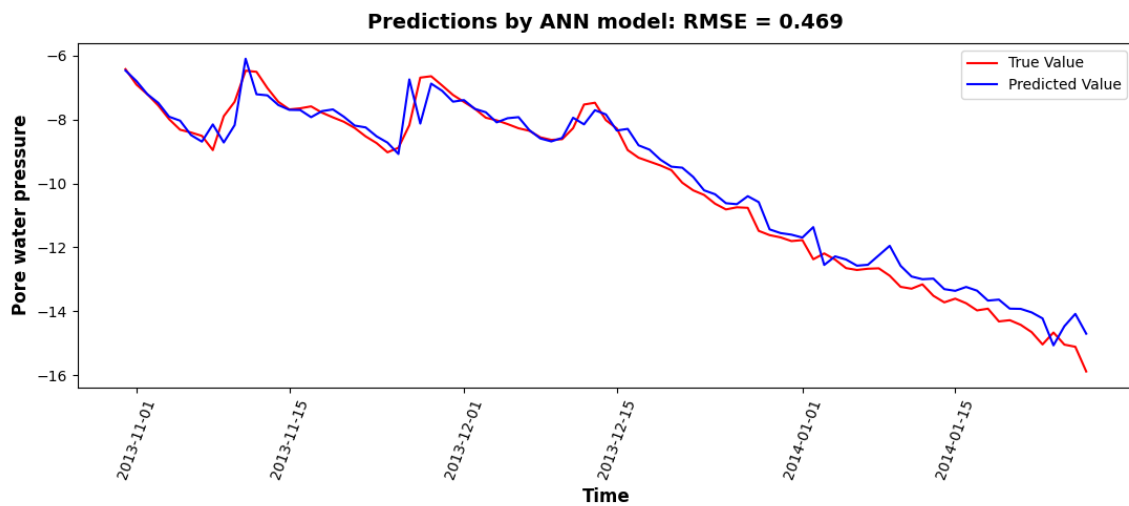
(E) Random Forest



(F) Elastic Net



(G) SVM

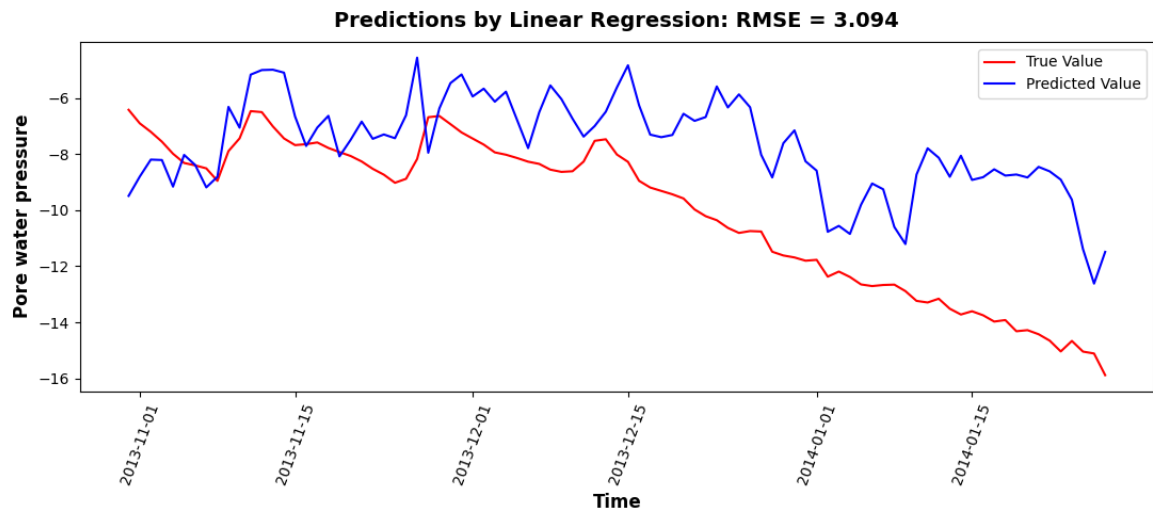


(H) ANN

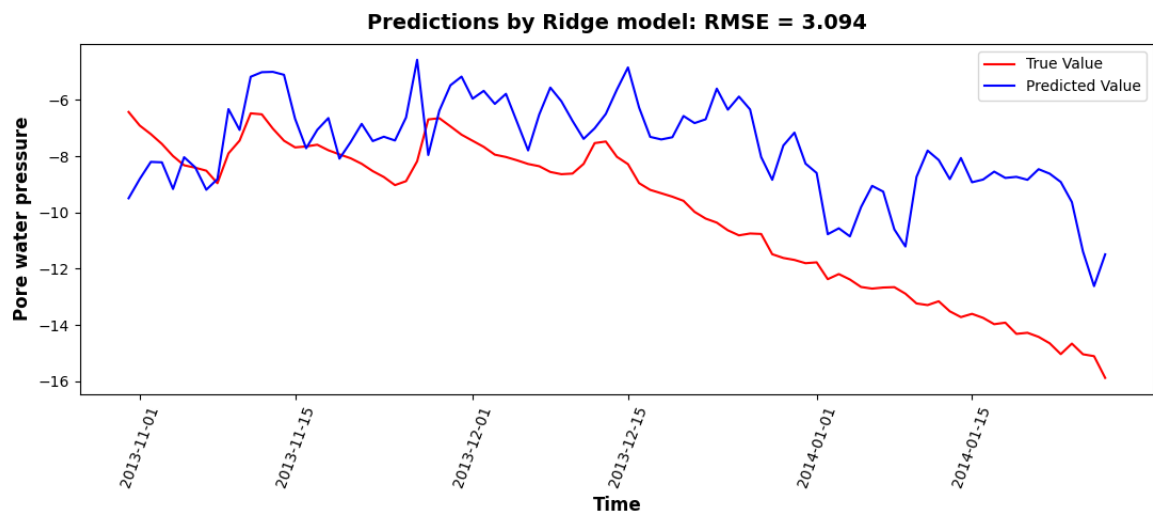
Figure 5.18 Forecasting results with daily update data and climate data

d. Forecasting with only climate data

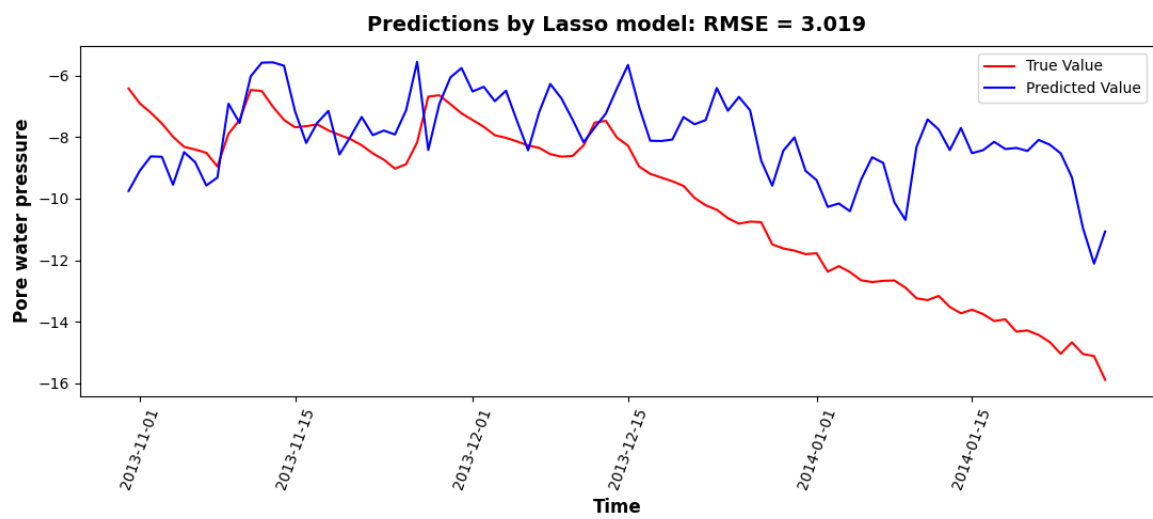
The presumptive condition in this section is that the data collected in the past is incomplete. We will remove the lag feature and let models forecast based solely on weather data. The results are shown in Figure 5.19. It can be seen that the models can still work, but the efficiency has decreased markedly. The importance of features is shown in Table 5.3. Time features were the most important input for both the XGB and Random Forest models.



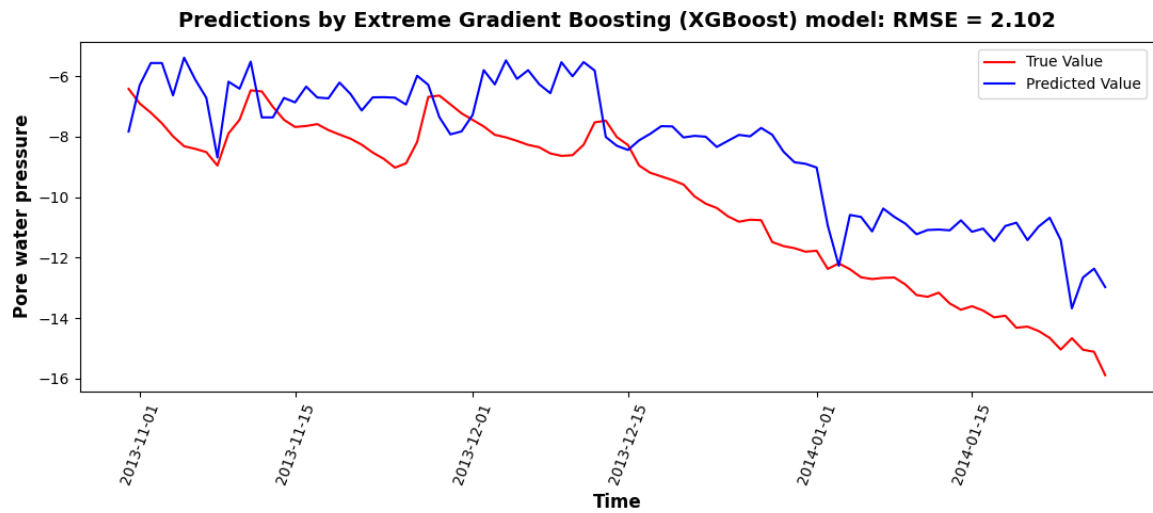
(A) Linear regressor



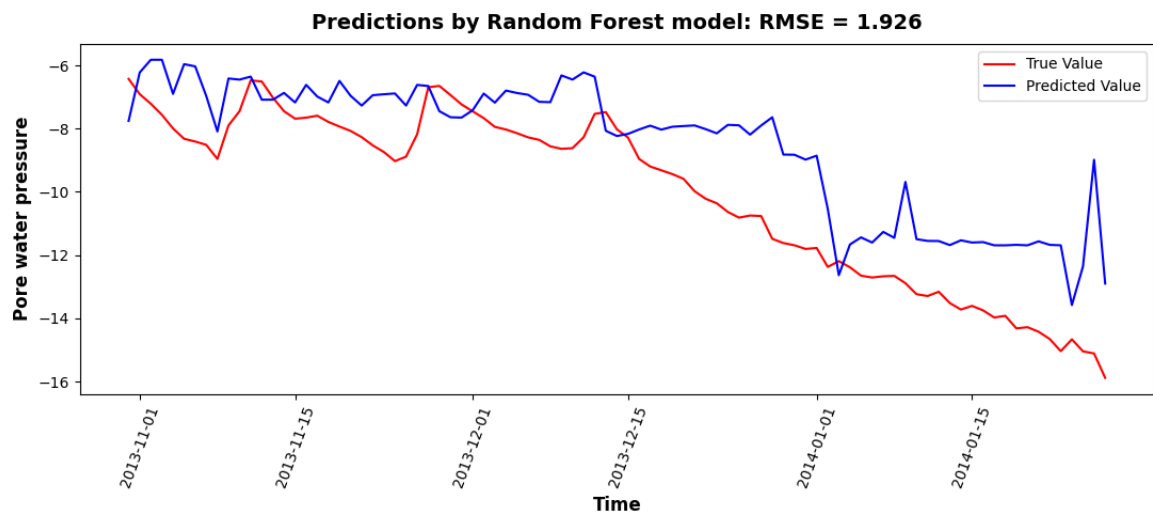
(B) Ridge regressor



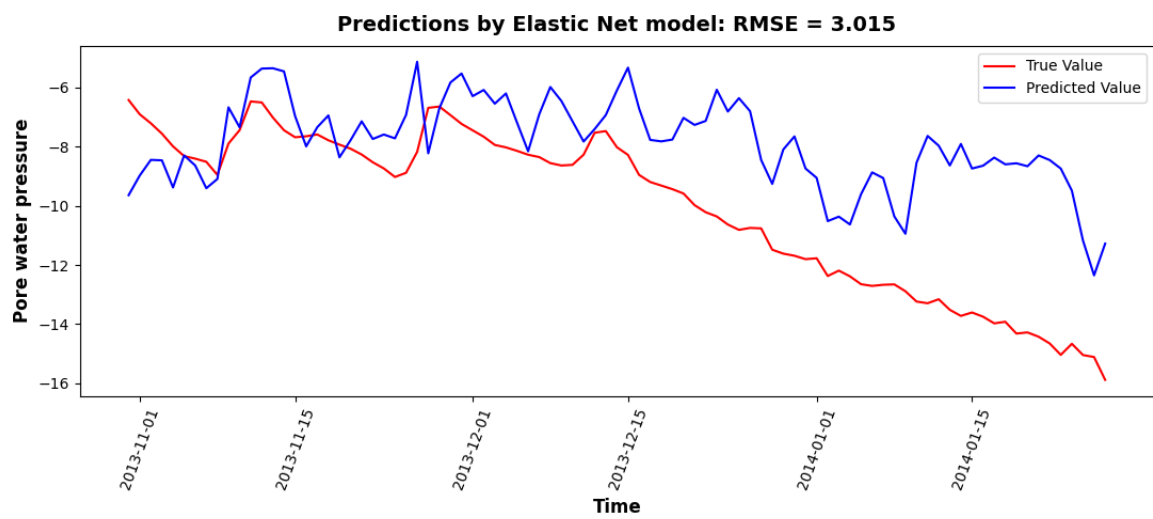
(C) Lasso regressor



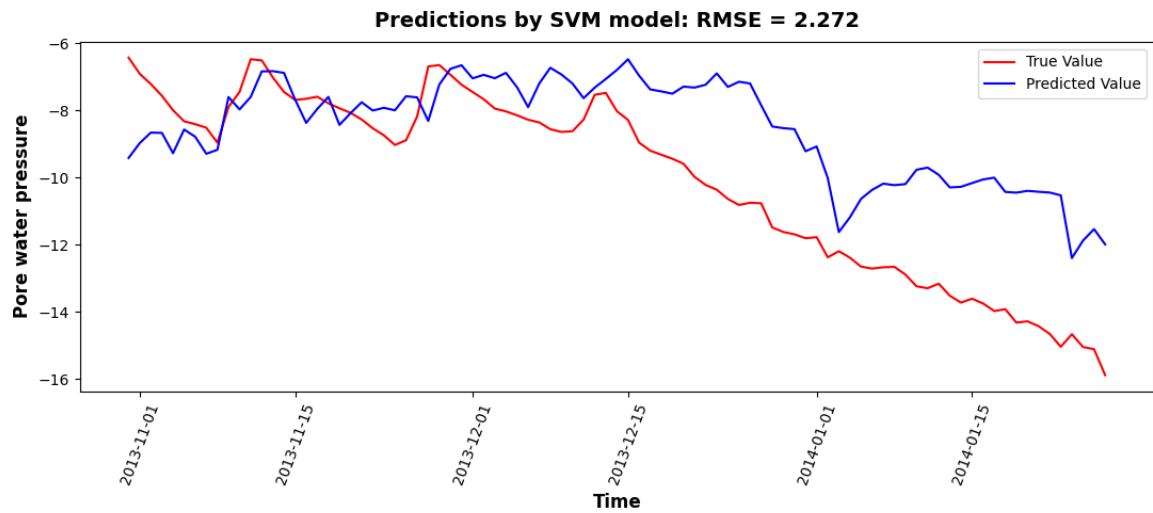
(D) XGBoost



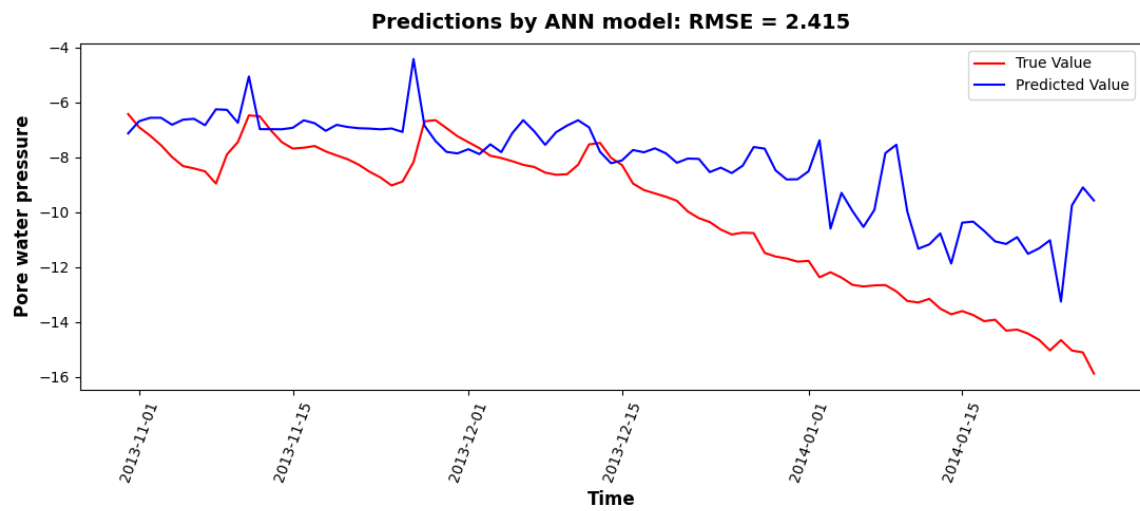
(E) Random Forest



(F) Elastic Net



(G) SVM



(H) ANN

Figure 5.19 Forecasting results with only climate data

Table 5.4 Feature importance in the case of Forecasting with only climate data

Feature	XGB	Random Forest
Time features	64.13%	49.29%
Air temperature	3.96%	23.73%
Rainfall amount	1.78%	1.96%
Snow depth	30.13%	25.02%

5.4.2 Water content prediction based on soil images

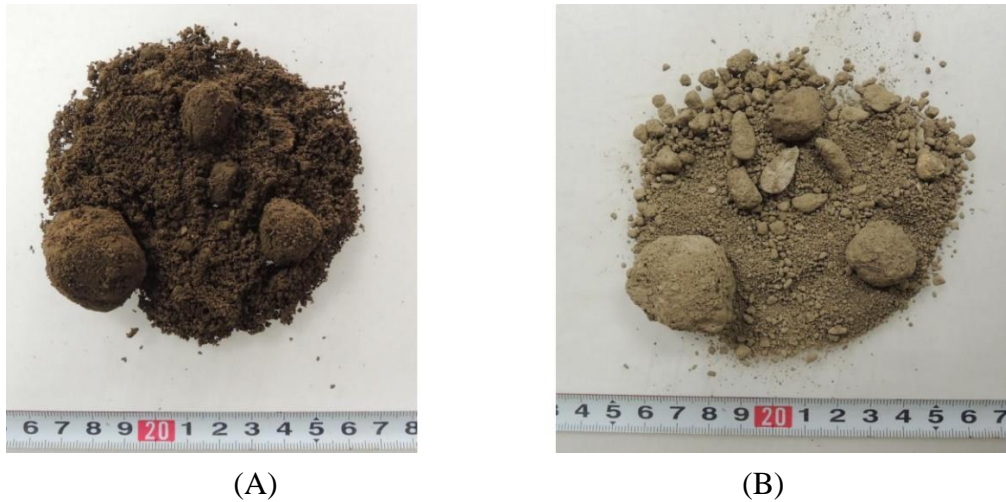


Figure 5.20 Komaoka volcanic soil (A) Wet condition (B) Dry condition

Figures 5.20 (A) and (B) show the original Komaoka volcanic soil at natural water content and after oven-drying for 24 hours, respectively. Komaoka volcanic soil is composed of particles that vary in grain size, which turn whitish after drying. Although different particle sizes have different shapes and colors, the color of the soil is highly dependent on the color of the fine particles that surround the coarse grains due to their high content. When the water is poured on any material like cloth, sand, or concrete; their colors will change (they become darker). The reason is the refractive index of the material and water is different. When the light falls on the surface of wet material, very little light is reflected compared with dry material. In the case of soils, the amount of organic matter, and the types of minerals present in a soil affect its color. Which, iron minerals can impart many colors to soils, which change in color as they become wet or dry out. It can be seen that there are many reasons for volcanic soils to change color as their moisture changes. This implies using images of soils to predict their water content. This section will examine the feasibility and accuracy of applying artificial intelligence in this work

5.4.2.1 Methods

When the working object is images instead of numbers, applying the ANN network as above will lead to a huge amount of computation as well as overfitting. This led to the need to adopt a convolutional neural network (CNN), a specially designed network for processing pixel data.

Convolutional neural networks: multilayer perceptrons that have been regularized. Multilayer perceptrons are typically completely connected networks, which means that each neuron in one layer is linked to all neurons in the following layer. These networks' "full connectivity" renders them prone to data overfitting. Regularization, or preventing overfitting, is commonly accomplished by punishing parameters during training (such as

weight decay) or cutting connectivity (skipped connections, dropout, ...) [59].

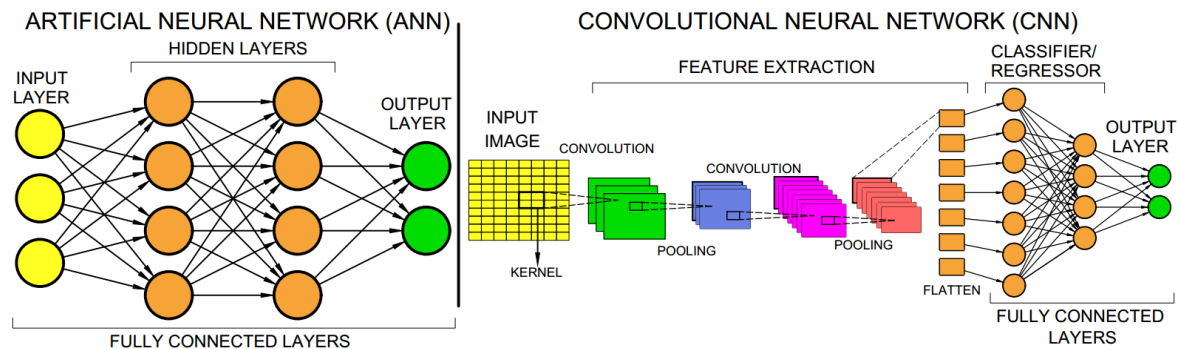


Figure 5.21 Artificial Neural Networks (ANN) and Convolutional Neural Networks (CNN)

However, deep learning networks are often quite massive in size. Training from scratch can take weeks to get the weights that make the model work effectively. That is the motivation for transfer learning.

Transfer learning: a machine learning research subject that focuses on preserving information obtained while addressing one problem and applying it to another but a similar challenge. In practice, reusing or transferring knowledge from previously learned tasks for the learning of new tasks has the potential to dramatically increase a reinforcement learning agent's sampling efficiency [90].

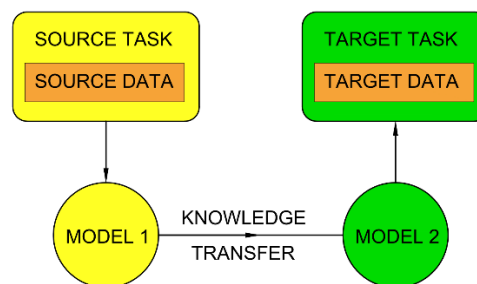


Figure 5.22 Transfer learning mechanism for deep learning in this study.

The transfer learning used for deep learning in this study can be explained in Figure 5.22. The source task is the classification task for ImageNet, a dataset containing more than 14 million training images across 1,000 object classes. Then the model with weights obtained from the source task will work as a feature extractor in the source task – Water content prediction. In this section, 3 following pre-trained models were used:

VGG16: one of the VGG models or VGGNet, a 16-layer CNN model initially introduced by Simonyan and Zisserman (2014) [66]. Figure 5.23 depicts the design of VGG16. VGG16 is a pretty large network with 138 million parameters and 16 layers, including three fully linked and 13 convolutional ones. The simplicity of the VGGNet16

design, on the other hand, is its key selling point.

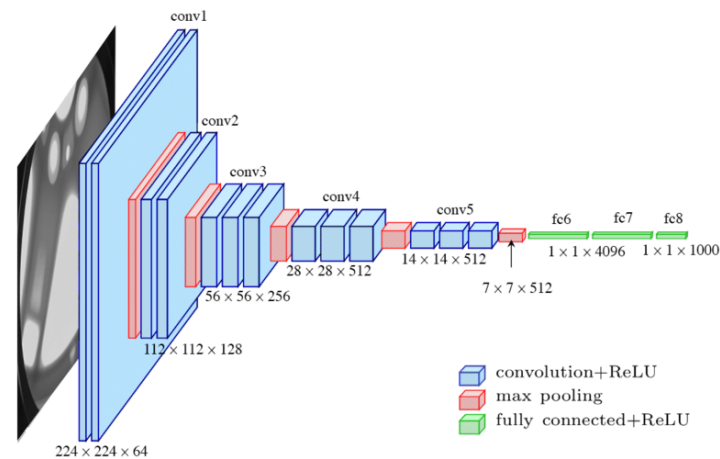


Figure 5.23 VGG16 architecture

Residual Neural Network (ResNet): He et al., (2015) [13] introduced a deep learning model for computer vision applications that can handle hundreds or thousands of convolutional layers. Previous CNN designs encountered the "vanishing gradient" problem while attempting to enhance performance by adding more layers. Skip connections" is ResNet's creative solution to this problem. ResNet stacks several identity mappings (convolutional layers that do nothing at first), skips those levels, and reuses the prior layer's activations. By condensing the network into fewer layers, skipping speeds up initial training. The network is then retrained, and all layers are enlarged, allowing the leftover elements of the network, known as residual parts, to explore more of the feature space of the input picture.

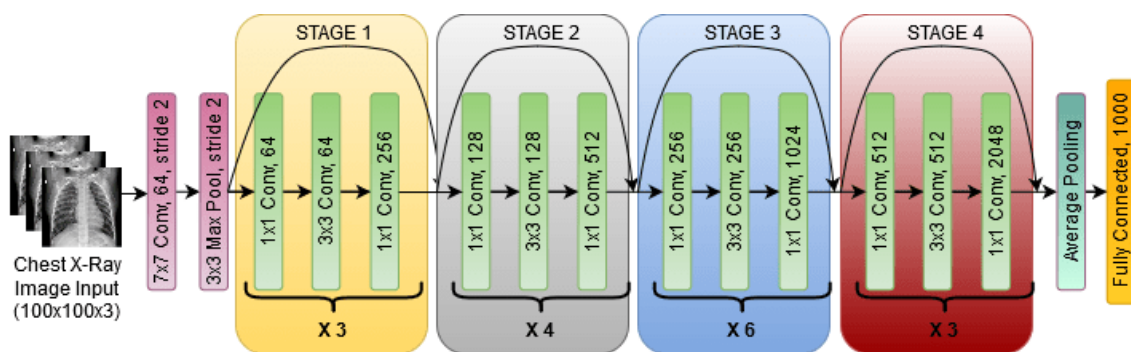


Figure 5.24 Resnet architecture

Inception Network: Szegedy et al., (2014) [69] introduce a deep neural network with an architectural design that comprises repeated components referred to as Inception modules. The researchers' key assumption while creating the Inception network was that highly

performant deep neural networks needed to be vast, with numerous additional layers and units inside these levels. Convolutional neural networks gain from extracting features of different sizes to do this. Figure 5.25 depicts the architecture of the Inception network.

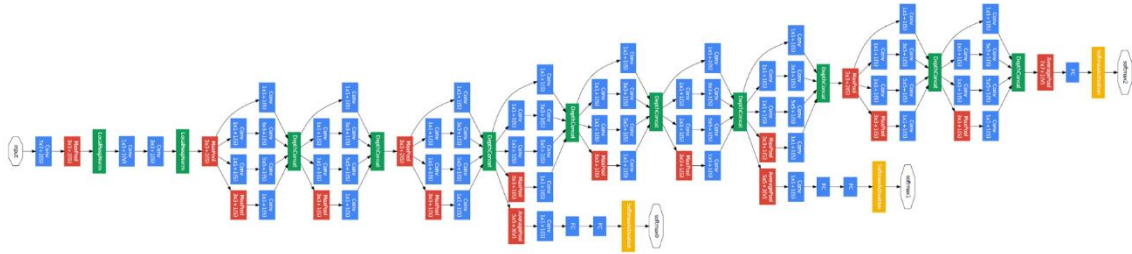


Figure 5.25 Inception architecture

5.4.2.2 Results and discussions

Komaoka volcanic coarse-grained soils were prepared at different water contents from 0% to 50%, with the water content of each sample spaced by 5%. 100 photos will be taken with each sample. The deep learning models will be applied to three cases as shown in Table 5.1. In the case of A, the models will be used for classification, a familiar task of computer vision. A special point in this problem is that the labels are numeric (“0”, “5”, ..., “50”), which suggests the application of regression as defined in the previous section. Therefore, case B has been proposed with the same settings as case A but regression procedures were used instead of classification procedures. The number of images in each soil type will be divided by 80% for training and 20% for testing. Similar to case B, case C applies regression procedures but tries to predict intermediate water content. This is the case of simulating the condition when the image data is incomplete. The model is only trained with soil images at 0%, 10%, ..., and 50% moisture and then tested with 5%, 15%, ..., and 45% images. The training process of the models is shown in Figure 5.26.

Table 5.5 Test conditions

Parameters	Case A	Case B	Case C
Type	Classification	Regression	Regression
Training data: Label [quantity of image]	0% [80], 5% [80], 10% [80], 15% [80], 20% [80], 25% [80], 30% [80], 35% [80], 40% [80], 45% [80], 50% [80]	0% [80], 5% [80], 10% [80], 15% [80], 20% [80], 25% [80], 30% [80], 35% [80], 40% [80], 45% [80], 50% [80]	0% [100], 10% [100], 20% [100], 30% [100], 40% [100], 50% [100]
Testing data: Label [quantity of image]	0% [20], 5% [20], 10% [20], 15% [20], 20% [20], 25% [20], 30% [20], 35% [20], 40% [20], 45% [20], 50% [20]	0% [20], 5% [20], 10% [20], 15% [20], 20% [20], 25% [20], 30% [20], 35% [20], 40% [20], 45% [20], 50% [20]	5% [100], 15% [100], 25% [100], 35% [100], 45% [100]

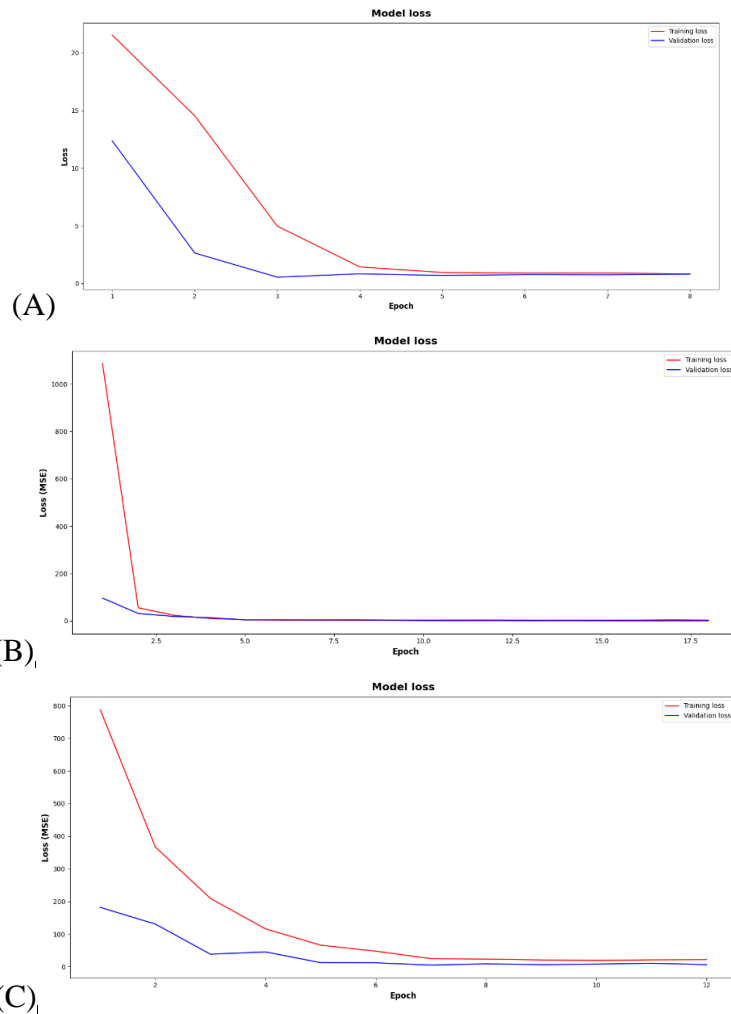


Figure 5.26 Training process (A) Case A (B) Case B (C) Case C

In the case of A, model VGG16 performed quite impressively and quickly reached an accuracy of 94% after 5 epochs. However, even if the accuracy reaches 100%, for the error of water content to be within 1%, we need to collect images of the soil at all moisture 1% apart. In the case of B, RMSE is 1.59 and R2 is 0.94. Thus, it can be seen that the deep learning model can also perform a regression task on the image similar to the classification task. However, similar to case A, to be able to apply case B in practice, the number of images required for training is very large. In the case of C, RMSE is 1.95 and R2 is 0.85. Thus, it can be seen that the models can completely predict the intermediate moisture. However, the error is still relatively high. This may be because lighting conditions greatly affect the color of soils in images.

The results of the test set of different models are shown in Table 5.1. The VGG16 model gives the smallest error, followed by ResNet and Inception for the largest error. In the original task of these pre-trained models - the Imagenet dataset, InceptionV3 has the highest accuracy of 78.95%, followed by ResNet-152 with 75.57% accuracy, and VGG-16 with 74.40% [19]. This leads to the conclusion that the performance of the models is different for different problems. In the problem of soil moisture prediction, the images are relatively similar, the difference is mainly in color. Therefore, it is possible that the models with multi-branch architecture like ResNet and Inception are more easily overfit and produce large error results.

Figure 5.27 summarizes the results of the VGG16 model when applying different dimensions for the input image. It can be seen that in both cases B and C, the prediction error decreases sharply when the input image size is from 32x32 to 128x128, reaches the smallest value when the input image is 256x256, and increases in the case of 512x512. Thus, importing a larger image does not always give a smaller error. This should be noted because working with large images consumes more resources and time.

Some examples of prediction results in case C with the VGG16 model are shown in Figure 5.28. Actual and predicted moisture in Figures 5.28(A), (B), (C), and (D) are 5% and 6.21%; 15% and 14.45%; 25% and 22.72%; 35% and 33.82%, respectively. It can be seen that the average error is 1.95%, but the difference between the images is quite large. Some images have an error of less than 1%, but some images have an error of more than 3%. So even if the average error is low, we still need to pay attention to the maximum error. In general, deep learning models need much improvement to be able to be applied to the prediction of soil moisture in practice.

Table 5.6 Test results in different models

Metrics	VGG16	Resnet	Inception
MAE	2.00792	2.74027	3.25524
MSE	5.30935	10.91262	15.84919
RMSE	2.30420	3.30343	3.98110
R- Squared	0.78735	0.56292	0.36520

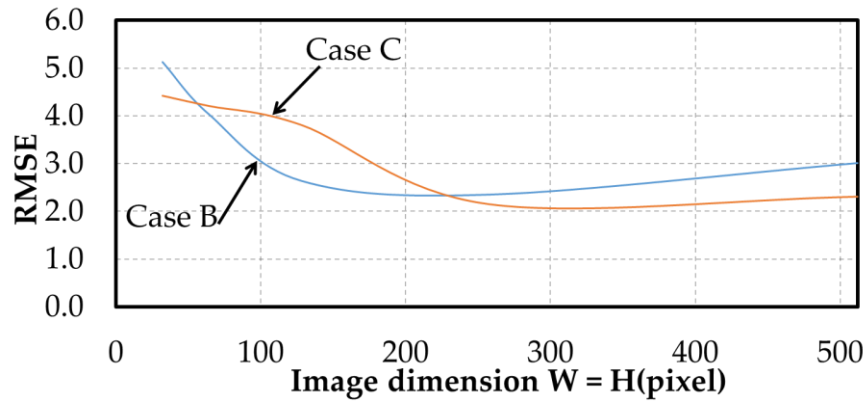


Figure 5.27 Test results in different input image dimensions

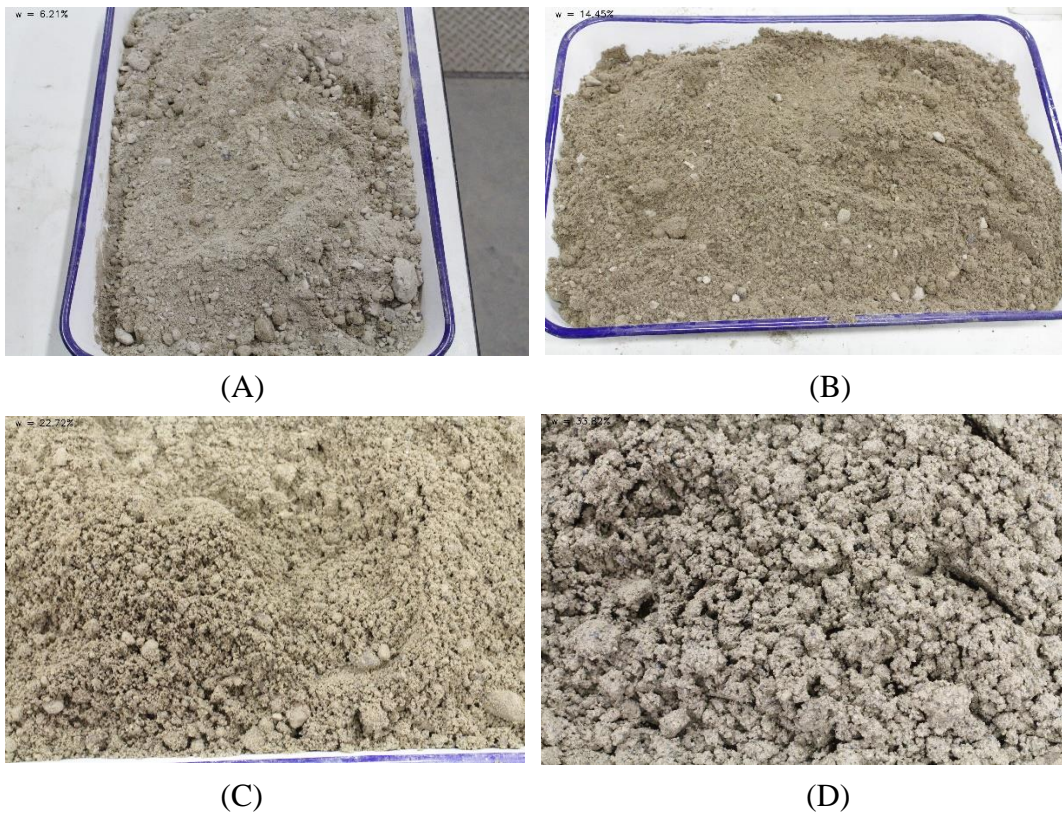


Figure 5.28 Example of prediction results

(A) $w = 5\%$ (B) $w = 15\%$ (C) $w = 25\%$ (D) $w = 35\%$

5.5 Summary

Based on the change in soil infiltration capacity, a simple method to evaluate slope stability in practice with the measured water content as the object of assessment was proposed. Pore water pressure data may be predicted using machine learning techniques. Daily data updates enhance forecast accuracy greatly. Climate data can also help to reduce prejudice. In contrast to the positive findings obtained when using artificial intelligence to anticipate pore water pressure from time series data, the use of computer vision for the prediction of volcanic soil moisture from photographs found several problems. The models need to be improved further in order to match the needs given out in reality.

CONCLUSIONS AND SUGGESTIONS

6.1 Introduction

This chapter presents the findings obtained from this study and some suggestions for further research.

6.2 Conclusions

A series of rainfall and earthquake experiments on model embankments constructed by Komaoka volcanic coarse-grained soil was conducted. The soil samples were prepared with 3 different amounts of fine particle contents ($K_{8.5A}$, K_{soil} , K_{40A}) while the initial water content was chosen at 0.9 (dry cases) and 1.1 (wet cases) of optimum water content. In post-rainfall earthquakes, the seismic loadings were applied at 3 different conditions of pore water pressure inside the embankments. The results of this study were compared with the test of post-earthquake rainfall in Kawamura et al., (2016) [31]. The physical model test results were also compared with previous research including element tests and disaster reports. Besides, modern techniques of artificial intelligence were applied to predict the water retention characteristics of volcanic slopes. There are some conclusions obtained from the research results as follows:

(1) The previous rainfall plays an important role in evaluating the stability of embankments under subsequent earthquakes through water retention conditions inside the slope such as rainfall-induced residual pore water pressure and saturation degree.

(2) The fine particle content has a great influence and must be taken into account when studying the stability of the volcanic embankment under the independent or combined effects of rainfall and earthquake. At the same degree of compaction, the permeability of volcanic soils decreases with the increase in the fine-grained content. The earthquake resistance of the compacted volcanic embankment subjected to previous rainfall increases as the fine content increases. Even so, this increment in seismic strength is not significant when the fines content was higher than 27%;

(3) Initial water content has a great influence on the mechanical behavior, infiltration characteristics, and failure phenomenon of embankments due to rainfall and/or earthquakes. The permeability of the compacted soil on the wet side of the optimum moisture content is

less than it is on the dry side when the fine grain content of the soil is sufficiently large. In contrast, embankments compacted on the wet side exhibit less resistance to subsequent earthquakes under the same shear strain due to previous rainfall.

(4) When embankments are subjected to dual disasters, the slope stability may be various for different orders of earthquake and rainfall even though the preceding received shear strain is similar. This leads to a need for appropriate evaluation of embankments under complex disasters taking into account the order of effects of external forces.

(5) A simple method to evaluate slope stability in practice with the measured water content as the object of assessment was proposed based on the change in soil infiltration capacity.

(6) Machine learning models can be applied to predict pore water pressure data. Daily data updates significantly improve prediction accuracy. Climate data can also contribute to reducing bias. In contrast to the promising results in applying artificial intelligence to time series data forecasting of pore water pressure, the application of computer vision to the prediction of volcanic soil moisture from images encountered many difficulties. The models need more improvement to enhance their performance to meet the requirements set out in reality.

6.3 Suggestions for future research

In further studies, it is recommended that consideration is given to:

- Investigate the influence of fines content on the mechanical behavior of volcanic coarse-grained soils in the same condition of coefficient of uniformity ($K_{8.5B}$, K_{40B} soil in [16]).
- Integrate the procedure of model test with the use of an X-ray CT scanner and PIV method to increase the understanding of fines particle movement and shear strain observation.
- Use the results of physical model tests to verify the results obtained from numerical simulation with embankment constructed by volcanic coarse-grained soils.
- Studying the forecasting with a longer dataset of pore water pressure and water content, in combination with specified techniques for time series data like RNN, LSTM

ACKNOWLEDGEMENT

I always believe that all the people that we are fortunate to meet in life, whether short or long, bring value to our growth journey. It would therefore be impossible to acknowledge here all the individuals and organizations for whom I was able to complete my doctoral course as well as this thesis. Even so, they will all always hold a special place in my heart.

First and foremost, I would like to express my deepest gratitude to my advisor, Professor Shima Kawamura, for his patient guidance, caring, inspiration, motivation, and a vast amount of knowledge and experience shared. Not only did I learn a lot from his creativity and problem-solving skills, but also from the kindness and positive energy he shared with us. Above all, Professor Kawamura will always be my future role model.

My gratitude extends to the members of my examination committee: Professor Yukihiro Kohata and Professor Katsutoshi Kimura for their insightful comments and constructive suggestions which have helped me to improve the quality of my research.

I would like to thank the Japan Science and Technology Agency as well as all the staff of Muroran IT who are behind the SPRING project. In addition to financial support for living expenses and research funds, seminars on interdisciplinary research and computer science have really opened up many new doors for me in my research.

As an international student, I would also like to say a word of thankfulness to the Centre for International Relations for helping us adjust to life in Japan.

Further, I would like to express my respect and great thanks to the persons who opened up this opportunity for me, Dr. Duong Quang Hung and especially Dr. Dao Minh Hieu, who still gives me advice every day.

Besides, I am deeply grateful to the members of the Geo-disasters prevention engineering laboratory for their hard work and efforts together. Special thanks to Dr. Nguyen Thi Thao Van, Mr. Masaya Sato, Mr. Yuta Kubo, Mr. Eiji Takase, and also the alumni who carried out the model experiments before we enrolled. As for Mr. Takumi Inaba, my language skills have been impotent when trying to describe the meaning of what you have done for me.

Further, I also sincerely thank Mr. Tetsuo Abe of Nexco West and the members of the Geotechnical Laboratory of Nexco Research Institute for their kind recommendation and precious support. One month of internship here has brought me valuable experiences that will definitely help me a lot in my future work.

I greatly appreciate the daily help of Vietnamese students at Muroran IT: Dr. Le Khac Hung, Dr. Pham Quang Vuong, Dr. Nguyen Thanh Thu, Dr. Ta Quy Hung, Mr. Nguyen Hoang Nam, and Mr. Nguyen Ngoc Hieu. You guys helped me through the hardest days of living away from home.

Last but not least, I would like to thank my parents and siblings for their love and encouragement which have always been by my side. I will never forget the sacrifices made by my wife and daughter so that I can live this dream.

Muroran, September 2023

REFERENCES

- [1] Baselt, I., & Heinze, T. (2021). Rain, Snow and Frozen Soil: Open Questions from a Porescale Perspective with Implications for Geohazards. *Geosciences*. Vol. 11, Issue 9, p. 375. MDPI AG. <https://doi.org/10.3390/geosciences11090375>
- [2] Breiman, L. (2001). Random Forests. *Machine Learning*. Vol. 45, Issue 1, pp. 5–32. Springer Science and Business Media LLC. <https://doi.org/10.1023/a:1010933404324>
- [3] Catane, S. G., Cabria, H. B., Tomarong, C. P., Jr, Saturay, R. M., Jr, Zarco, M. A. H., & Pioquinto, W. C. (2006). Catastrophic Rockslide-Debris Avalanche at St. Bernard, Southern Leyte, Philippines. *Landslides*. Vol. 4, Issue 1, pp. 85–90. Springer Science and Business Media LLC. <https://doi.org/10.1007/s10346-006-0050-3>
- [4] Chakraborty, S., Puppala, A. J., Bheemasetti, T. V., & Das, J. T. (2021). Seismic Slope Stability Analysis of a Hydraulic Fill Dam. *International Journal of Geomechanics*. Vol. 21, Issue 1. American Society of Civil Engineers (ASCE). [https://doi.org/10.1061/\(asce\)gm.1943-5622.0001892](https://doi.org/10.1061/(asce)gm.1943-5622.0001892)
- [5] Chen, T., & Guestrin, C. (2016). XGBoost: A Scalable Tree Boosting System. In *Proceedings of the 22nd ACM SIGKDD International Conference on Knowledge Discovery and Data Mining*. KDD '16. ACM. <https://doi.org/10.1145/2939672.2939785>
- [6] Chien-Yuan, C., Tien-Chien, C., Fan-Chieh, Y., Wen-Hui, Y., & Chun-Chieh, T. (2005). Rainfall Duration and Debris-Flow Initiated Studies for Real-Time Monitoring. *Environmental Geology*. Vol. 47, Issue 5, pp. 715–724. Springer Science and Business Media LLC. <https://doi.org/10.1007/s00254-004-1203-0>
- [7] Dao, M.H. (2018). Stability Evaluation on Internal Erosion of Volcanic Coarse-Grained Soil. Doctoral Dissertation, Graduate School of Engineering, Muroran Institute of Technology, Hokkaido, Japan. <http://hdl.handle.net/10258/00009638>
- [8] Fan, X., Juang, C. H., Wasowski, J., Huang, R., Xu, Q., Scaringi, G., van Westen, C. J., & Havenith, H.-B. (2018). What We Have Learned from the 2008 Wenchuan Earthquake and Its Aftermath: A Decade of Research and Challenges. *Engineering Geology*. Vol. 241, pp. 25–32. Elsevier BV. <https://doi.org/10.1016/j.enggeo.2018.05.004>
- [9] Freijeiro-González, L., Febrero-Bande, M., & González-Manteiga, W. (2020). A Critical Review of LASSO and Its Derivatives for Variable Selection under Dependence among Covariates (Version 1). *arXiv*. <https://doi.org/10.48550/ARXIV.2012.11470>
- [10] Goda, K., Campbell, G., Hulme, L., Ismael, B., Ke, L., Marsh, R., Sammonds, P., So, E., Okumura, Y., Kishi, N., Koyama, M., Yotsui, S., Kiyono, J., Wu, S., & Wilkinson, S. (2016). The 2016 Kumamoto Earthquakes: Cascading Geological Hazards and Compounding Risks. *Frontiers in Built Environment*. Vol. 2. Frontiers Media SA. <https://doi.org/10.3389/fbuilt.2016.00019>
- [11] Guo, X., Chen, X., Song, G., Zhuang, J., & Fan, J. (2021). Debris Flows in the Lushan Earthquake Area: Formation Characteristics, Rainfall Conditions, and Evolutionary Tendency. *Natural Hazards*. Vol. 106, Issue 3, pp. 2663–2687. Springer Science and Business Media LLC. <https://doi.org/10.1007/s11069-021-04559-2>
- [12] Hayashi, M.; Kawamura, S. (2019). Effect of Particle Breakage on Permeability of Volcanic Coarse-Grained Soils. In *Proceedings of the 54th Japan National Conference on Geotechnical Engineering*, Saitama, Japan, 16-18 July 2019; Japanese Geotechnical Society: Tokyo, Japan; pp. 849–850. (In Japanese)
- [13] He, K., Zhang, X., Ren, S., & Sun, J. (2015). Deep Residual Learning for Image Recognition (Version 1). *arXiv*. <https://doi.org/10.48550/ARXIV.1512.03385>
- [14] Hearst, M. A., Dumais, S. T., Osuna, E., Platt, J., & Scholkopf, B. (1998). Support Vector Machines. *IEEE Intelligent Systems and their Applications*. Vol. 13, Issue 4, pp. 18–28. Institute of Electrical and Electronics Engineers (IEEE). <https://doi.org/10.1109/5254.708428>
- [15] Hernandez, O., Cordão Neto, M. P., & Caicedo, B. (2018). Structural Features and Hydro-Mechanical Behaviour of a Compacted Andesitic Volcanic Soil. *Géotechnique Letters*. Vol. 8, Issue 3, pp. 195–200. Thomas Telford Ltd. <https://doi.org/10.1680/jgele.18.00056>
- [16] Hieu, D. M., Kawamura, S., & Matsumura, S. (2017). Internal Erosion of Volcanic Coarse-Grained Soils and Its Evaluation. *International Journal of GEOMATE*. Vol. 13, Issue 38, pp.165-172. <https://doi.org/10.21660/2017.38.70411>
- [17] Horton, R. E. (1939). Analysis of Runoff-plat Experiments with Varying Infiltration Capacity. *Transactions, American Geophysical Union*. Vol. 20, Issue 4, p. 693. American Geophysical Union (AGU). <https://doi.org/10.1029/tr020i004p00693>
- [18] Iai, S. (1989). Similitude for Shaking Table Tests on Soil-Structure-Fluid Model in 1g Gravitational Field. *Soils and Foundations*. Vol. 29, Issue 1, pp. 105–118. Elsevier BV. <https://doi.org/10.3208/sandf1972.29.105>
- [19] Image Classification on ImageNet. Available online: <https://paperswithcode.com/sota/image-classification-on-imagenet> (accessed on July 2023).
- [20] Ishikawa, T., & Miura, S. (2011). Influence of Freeze-Thaw Action on Deformation-Strength

- Characteristics and Particle Crushability of Volcanic Coarse-Grained Soils. *Soils and Foundations*. Vol. 51, Issue 5, pp. 785–799. Elsevier BV. <https://doi.org/10.3208/sandf.51.785>
- [21] Ishikawa, T., Yoshimi, M., Isobe, K., & Yokohama, S. (2021). Reconnaissance Report on Geotechnical Damage Caused by 2018 Hokkaido Eastern Ibari Earthquake with JMA Seismic Intensity 7. *Soils and Foundations*. Vol. 61, Issue 4, pp. 1151–1171. Elsevier BV. <https://doi.org/10.1016/j.sandf.2021.06.006>
- [22] Japanese Geotechnical Society (2009). JGS 0131-2009; Test Method for Particle Size Distribution of Soils. JGS: Tokyo, Japan.
- [23] Japanese Geotechnical Society (2009). JGS 0711-2009; Test Method for soil Compaction Using a Rammer. JGS: Tokyo, Japan.
- [24] Japanese Geotechnical Society (2009). JGS 0161-2009; Test Method for Minimum and Maximum Densities of Sands. JGS: Tokyo, Japan.
- [25] Japanese Geotechnical Society, Hokkaido Branch, (2011). *Volcanic Soils for Engineers – Characteristics, Design, Construction and Disasters*. The Research Committee in Hokkaido Branch. JGS, pp. 1–130 (in Japanese).
- [26] Kawamura, S., Miura, S., & Yokohama, S. (2010). Mechanical Behavior of Anisotropic Sand Ground Beneath Structures Subjected to Cyclic Loading Such as Wave Loading. *Soils and Foundations*. Vol. 50, Issue 5, pp. 645–657. Elsevier BV. <https://doi.org/10.3208/sandf.50.645>
- [27] Kawamura, S., & Miura, S. (2013). Rainfall-Induced Failures of Volcanic Slopes Subjected to Freezing and Thawing. *Soils and Foundations*. Vol. 53, Issue 3, pp. 443–461. Elsevier BV. <https://doi.org/10.1016/j.sandf.2013.04.006>
- [28] Kawamura, S., Miura, S., Yokohama, S., Kudo, A., & Kaiya, N. (2013). Field Monitoring of Embankment Constructed by Volcanic Soil and Its Evaluation. *Geo-Congress 2013*. American Society of Civil Engineers. <https://doi.org/10.1061/9780784412787.037>
- [29] Kawamura, S., & Miura, S. (2014a). Stability of Volcanic Slopes in Cold Regions. *Journal of Geography and Geology*. Vol. 6, Issue 3. Canadian Center of Science and Education. <https://doi.org/10.5539/jgg.v6n3p34>
- [30] Kawamura, S., & Miura, S. (2014b). Failure of Volcanic Slopes in Cold Regions and its Prediction. *Procedia Earth and Planetary Science*. Vol. 9, pp. 143–152. Elsevier BV. <https://doi.org/10.1016/j.proeps.2014.06.010>
- [31] Kawamura, S., Miura, S., Dao, H. M., & Yamada, R. (2016). Rainfall-Induced Failure of Volcanic Embankments Subjected to Cyclic Loadings in Cold Regions. *Geo-China 2016*. American Society of Civil Engineers. <https://doi.org/10.1061/9780784480007.014>
- [32] Kawamura, S., Kawajiri, S., Hirose, W., & Watanabe, T. (2019). Slope Failures/Landslides over a Wide Area in the 2018 Hokkaido Eastern Ibari Earthquake. *Soils and Foundations*. Vol. 59, Issue 6, pp. 2376–2395. Elsevier BV. <https://doi.org/10.1016/j.sandf.2019.08.009>
- [33] Kawamura, S., Miura, S., & Matsumura, S. (2021). Stability Monitoring of Embankments Constructed by Volcanic Coarse-Grained Soil in Snowy-Cold Regions. *Journal of Cold Regions Engineering*. Vol. 35, Issue 1. American Society of Civil Engineers (ASCE). [https://doi.org/10.1061/\(asce\)cr.1943-5495.0000240](https://doi.org/10.1061/(asce)cr.1943-5495.0000240)
- [34] Kokusho, T. (2014). *Fundamentals of Earthquake Geo-Dynamics*. Kajima Institute Publishing Co. Ltd., Tokyo, Japan. (in Japanese)
- [35] Kusaka, H., & Takahashi, A. (2018). Estimation of Water Level in Road Embankment by Transient Unsaturated Seepage Analysis. *PanAm Unsaturated Soils 2017*. American Society of Civil Engineers. <https://doi.org/10.1061/9780784481684.019>
- [36] KYOWA. BPR-A-S Small-sized Pore Pressure Transducer—Technical Specifications. Available online: <https://www.kyowa-ei.com/eng/product/category/sensors/bpr-a-s/index.html> (accessed on 4 July 2023).
- [37] KYOWA. ASW-A Waterproof Acceleration Transducer—Technical Specifications. Available online: <https://www.kyowa-ei.com/eng/product/category/sensors/asw-a/index.html> (accessed on 4 July 2023).
- [38] Lee, K. Z.-Z., Jensen, N., Gillette, D. R., & Wittwer, D. T. (2019). Seismic Deformation Analysis of Embankment Dams Using Simplified Total-Stress Approach. *Journal of Geotechnical and Geoenvironmental Engineering*. Vol. 145, Issue 10. American Society of Civil Engineers (ASCE). [https://doi.org/10.1061/\(asce\)gt.1943-5606.0002135](https://doi.org/10.1061/(asce)gt.1943-5606.0002135)
- [39] Lin, C.-W., Liu, S.-H., Lee, S.-Y., & Liu, C.-C. (2006). Impacts of the Chi-Chi Earthquake on Subsequent Rainfall-Induced Landslides in Central Taiwan. *Engineering Geology*. Vol. 86, Issues 2–3, pp. 87–101. Elsevier BV. <https://doi.org/10.1016/j.enggeo.2006.02.010>
- [40] Liu, X., & Yang, J. (2014). Laboratory Measurement of Small-Strain Shear Modulus of Volcanic Soil. *Geo-Congress 2014 Technical Papers*. American Society of Civil Engineers. <https://doi.org/10.1061/9780784413272.012>
- [41] Marquardt, D. W., & Snee, R. D. (1975). Ridge Regression in Practice. *The American Statistician*. Vol. 29, Issue 1, pp. 3–20. Informa UK Limited. <https://doi.org/10.1080/00031305.1975.10479105>
- [42] Matsumaru, T., & Uzuoka, R. (2016). Three-Phase Seepage-Deformation Coupled Analysis about

- Unsaturated Embankment Damaged by Earthquake. *International Journal of Geomechanics*. Vol. 16, Issue 5. American Society of Civil Engineers (ASCE). [https://doi.org/10.1061/\(asce\)gm.1943-5622.0000699](https://doi.org/10.1061/(asce)gm.1943-5622.0000699)
- [43] Matsumura, S. (2014) Laboratory and In-Situ Studies on Mechanical Properties of Volcanic Soil Embankment in Cold Region. Doctoral Dissertation, Graduate School of Engineering, Hokkaido University, Hokkaido, Japan. <http://hdl.handle.net/2115/55883>
- [44] Matsumura, S., & Tatsuoka, F. (2018). Effect of Compaction Conditions and Fines Content on Cyclic Undrained Strength of Saturated Soils. *Soil Dynamics and Earthquake Engineering*. Vol. 112, pp. 152–161. Elsevier BV. <https://doi.org/10.1016/j.soildyn.2018.04.029>
- [45] Matsunaga, K., Matsuda, R., Matsuo, T., & Watanabe, I. (2019). The 2016 Kumamoto Earthquakes Landslide Disasters and Response. *International Journal of Erosion Control Engineering*. Vol. 11, Issue 4, pp. 131–137. Japan Society of Erosion Control Engineering. <https://doi.org/10.13101/ijece.11.131>
- [46] METER Group. ECH2O EC-5—Technical Specifications. Available online: <https://www.metergroup.com/en/meter-environment/products/ech20-ec-5/ech20-ec-5-tech-specs> (accessed on July 2023).
- [47] METER Group. Cited Publications for ECH2O EC-5. Available online: <https://www.metergroup.com/en/meter-environment/products/ech20-ec-5/cited-publications-ech20-ec-5> (accessed on July 2023).
- [48] Minardo, A., Zeni, L., Coscetta, A., Catalano, E., Zeni, G., Damiano, E., De Cristofaro, M., & Olivares, L. (2021). Distributed Optical Fiber Sensor Applications in Geotechnical Monitoring. *Sensors*. Vol. 21, Issue 22, p. 7514. MDPI AG. <https://doi.org/10.3390/s21227514>
- [49] Mishima, S., & Kimura, H. (1970). Characteristics of Landslides and Embankment Failures During the Tokachioki Earthquake. *Soils and Foundations*. Vol. 10, Issue 2, pp. 39–51. Elsevier BV. https://doi.org/10.3208/sandf1960.10.2_39
- [50] Miura, S.; Yagi, K. (1997). Particle Breakage of Volcanic Coarse-Grained Soils and Its Evaluation. *J. Geotech. Eng.* 1997, 561, 257–269. (In Japanese)
- [51] Miura, S., Yagi, K., & Asonuma, T. (2003). Deformation-Strength Evaluation of Crushable Volcanic Soils by Laboratory and In-Situ Testing. *Soils and Foundations*. Vol. 43, Issue 4, pp. 47–57. Elsevier BV. https://doi.org/10.3208/sandf.43.4_47
- [52] Mori, H., Chen, X., Leung, Y. F., Shimokawa, D., & Lo, M. K. (2020). Landslide Hazard Assessment by Smoothed Particle Hydrodynamics with Spatially Variable Soil Properties and Statistical Rainfall Distribution. *Canadian Geotechnical Journal*. Vol. 57, Issue 12, pp. 1953–1969. Canadian Science Publishing. <https://doi.org/10.1139/cgj-2019-0601>
- [53] Muraleetharan, K. K., Deshpande, S., & Adalier, K. (2004). Dynamic Deformations in Sand Embankments: Centrifuge Modeling and Blind, Fully Coupled Analyses. *Canadian Geotechnical Journal*. Vol. 41, Issue 1, pp. 48–69. Canadian Science Publishing. <https://doi.org/10.1139/t03-065>
- [54] NEXCO Research Institute, 2012. Standard Design Specifications Vol. 1 Earthworks (in Japanese).
- [55] Ng, C. W. W., & Chiu, A. C. F. (2001). Behavior of a Loosely Compacted Unsaturated Volcanic Soil. *Journal of Geotechnical and Geoenvironmental Engineering*. Vol. 127, Issue 12, pp. 1027–1036. American Society of Civil Engineers (ASCE). [https://doi.org/10.1061/\(asce\)1090-0241\(2001\)127:12\(1027\)](https://doi.org/10.1061/(asce)1090-0241(2001)127:12(1027))
- [56] Ng, C. W., & Pang, Y. W. (2000). Experimental Investigations of the Soil-Water Characteristics of a Volcanic Soil. *Canadian Geotechnical Journal*. Vol. 37, Issue 6, pp. 1252–1264. Canadian Science Publishing. <https://doi.org/10.1139/t00-056>
- [57] Nguyen, T. B., Tatsuya, I., & Srikrishnan, S. S. (2018). Rainfall Infiltration and Runoff Characteristics of an Unsaturated Volcanic Soil under Grass Cover. *PanAm Unsaturated Soils 2017. Second Pan-American Conference on Unsaturated Soils*. American Society of Civil Engineers. <https://doi.org/10.1061/9780784481684.015>
- [58] Nomura, Y., Okamoto, A., Kuramoto, K., & Ikeda, H. (2014). Landslide-Triggering Rainfall Thresholds after Major Earthquakes for Early Warning. *International Journal of Erosion Control Engineering*. Vol. 7, Issue 2, pp. 56–62. Japan Society of Erosion Control Engineering. <https://doi.org/10.13101/ijece.7.56>
- [59] O’Shea, K., & Nash, R. (2015). An Introduction to Convolutional Neural Networks (Version 2). arXiv. <https://doi.org/10.48550/ARXIV.1511.08458>
- [60] Robinson, J. D., Vahedifard, F., & AghaKouchak, A. (2017). Rainfall-Triggered Slope Instabilities under a Changing Climate: Comparative Study Using Historical and Projected Precipitation Extremes. *Canadian Geotechnical Journal*. Vol. 54, Issue 1, pp. 117–127. Canadian Science Publishing. <https://doi.org/10.1139/cgj-2015-0602>
- [61] Rocha, M. (1957) The Possibility of Solving Soil Mechanics Problems by the Use of Models. *Proceedings of the 4th International Conference on Soil Mechanics and Foundation Engineering*, London, UK, 12-24 August 1957; Butterworths Scientific Publications: London, UK, 1957; Volume 1, pp. 183–188. <https://www.issmge.org/publications/publication/the-possibility-of-solving-soil-mechanics-problems-by-the-use-of-models>

- [62] Sassa, K., Fukuoka, H., Wang, F., Wang, G., Okada, K. & Marui, H., (2006). Landslide Disasters Triggered by the 2004 Mid-Niigata Prefecture Earthquake in Japan. *Annals of Disas. Prev. Res. Inst.*, Kyoto Univ., No. 49 C, 2006, pp. 119-136.
- [63] Sassa, K., Fukuoka, H., Wang, F., & Wang, G. (2007). Landslides Induced by a Combined Effect of Earthquake and Rainfall. *Progress in Landslide Science* (pp. 193–207). Springer Berlin Heidelberg. https://doi.org/10.1007/978-3-540-70965-7_14
- [64] Schofield, A. N. (1980). *Cambridge Geotechnical Centrifuge Operations*. Géotechnique. Vol. 30, Issue 3, pp. 227–268. Thomas Telford Ltd. <https://doi.org/10.1680/geot.1980.30.3.227>
- [65] Shieh, C. L., Chen, Y. S., Tsai, Y. J., & Wu, J. H. (2009). Variability in Rainfall Threshold for Debris Flow after the Chi-Chi Earthquake in Central Taiwan, China. *International Journal of Sediment Research*. Vol. 24, Issue 2, pp. 177–188. Elsevier BV. [https://doi.org/10.1016/s1001-6279\(09\)60025-1](https://doi.org/10.1016/s1001-6279(09)60025-1)
- [66] Simonyan, K., & Zisserman, A. (2014). Very Deep Convolutional Networks for Large-Scale Image Recognition (Version 6). arXiv. <https://doi.org/10.48550/ARXIV.1409.1556>
- [67] Shinoda, M., Nakajima, S., Watanabe, K., Nakamura, S., Yoshida, I., & Miyata, Y. (2022). Practical Seismic Fragility Estimation of Japanese Railway Embankments Using Three Seismic Intensity Measures. *Soils and Foundations*. Vol. 62, Issue 4, p. 101160. Elsevier BV. <https://doi.org/10.1016/j.sandf.2022.101160>
- [68] Song, B., & Hao, X.-M. (2017). Study on the Influence of Rainfall Condition on the Stability of Railway Slope. *International Collaboration in Lifeline Earthquake Engineering 2016. Seventh China-Japan-US Trilateral Symposium on Lifeline Earthquake Engineering*. American Society of Civil Engineers. <https://doi.org/10.1061/9780784480342.051>
- [69] Szegedy, C., Liu, W., Jia, Y., Sermanet, P., Reed, S., Anguelov, D., Erhan, D., Vanhoucke, V., & Rabinovich, A. (2014). Going Deeper with Convolutions (Version 1). arXiv. <https://doi.org/10.48550/ARXIV.1409.4842>
- [70] Tang, C., Zhu, J., Li, W. L., & Liang, J. T. (2009). Rainfall-Triggered Debris Flows Following the Wenchuan Earthquake. *Bulletin of Engineering Geology and the Environment*. Vol. 68, Issue 2, pp. 187–194. Springer Science and Business Media LLC. <https://doi.org/10.1007/s10064-009-0201-6>
- [71] Tang, C., van Asch, T. W. J., Chang, M., Chen, G. Q., Zhao, X. H., & Huang, X. C. (2012). Catastrophic Debris Flows on 13 August 2010 in the Qingping Area, Southwestern China: The Combined Effects of a Strong Earthquake and Subsequent Rainstorms. *Geomorphology*. Vols. 139–140, pp. 559–576. Elsevier BV. <https://doi.org/10.1016/j.geomorph.2011.12.021>
- [72] Terzaghi, K. (1950). Mechanism of Landslides. *Application of Geology to Engineering Practice*. pp. 83–123. Geological Society of America. <https://doi.org/10.1130/berkey.1950.83>
- [73] Tiwari, B., Lewis, A., & Ferrar, E. (2013). Experimental Simulation of Rainfall and Seismic Effects to Trigger Slope Failures. *Geo-Congress 2013. Geo-Congress 2013. American Society of Civil Engineers*. <https://doi.org/10.1061/9780784412787.046>
- [74] Tiwari, B., Tran, D., Ajmera, B., Oli, H., & Stapleton, J. (2016). Effect of Pre-and Post-Earthquake Rainfall Events on the Deformation and Stability of Slopes. *Geotechnical and Structural Engineering Congress 2016. American Society of Civil Engineers*. <https://doi.org/10.1061/9780784479742.129>
- [75] Tiwari, B., Ajmera, B., & Tran, D. (2017a). Influence of Post-Earthquake Rainfall on the Stability of Clay Slopes (IPL-192). *Advancing Culture of Living with Landslides*. pp. 429–436. Springer International Publishing. https://doi.org/10.1007/978-3-319-59469-9_38
- [76] Tiwari, B.; Ajmera, B.; Tran, D.; Caballero, S. (2017b). Effect of Post-Earthquake Rainfall in Triggering Landslides; *Proceedings of the 19th International Conference on Soil Mechanics and Geotechnical Engineering, Seoul, Korea, 17–22 September 2017*; pp. 3533–3536. <https://www.issmge.org/publications/publication/effect-of-post-earthquake-rainfall-in-triggering-landslides>
- [77] Tuladhar, G. R., Tiwari, B., & Marui, H. (2007). Post Earthquake Evaluation of Higashi Takezawa Landslide Located at Niigata Prefecture of Japan. *Dynamic Response and Soil Properties. Geo-Denver 2007. American Society of Civil Engineers*. [https://doi.org/10.1061/40904\(223\)8](https://doi.org/10.1061/40904(223)8)
- [78] Uhrig R. E. (1995). Introduction to Artificial Neural Networks. *Proceedings of IECON '95 - 21st Annual Conference on IEEE Industrial Electronics, Orlando, FL, USA, 1995*, pp. 33-37 vol.1, <https://doi.org/10.1109/IECON.1995.483329>.
- [79] Uzuoka, R., Sento, N., Kazama, M., & Unno, T. (2005). Landslides During the Earthquakes on May 26 and July 26, 2003 in Miyagi, Japan. *Soils and Foundations*. Vol. 45, Issue 4, pp. 149–163. The Japanese Geotechnical Society. https://doi.org/10.3208/sandf.45.4_149
- [80] Vickneswaran, T., & Ravichandran, N. (2020). Multi-Hazard Analysis of Earth Slopes Using Coupled Geotechnical-Hydrological Finite Element Model. *Geo-Congress 2020. Geo-Congress 2020. American Society of Civil Engineers*. <https://doi.org/10.1061/9780784482797.007>
- [81] Wang, W.-N., Wu, H.-L., Nakamura, H., Wu, S.-C., Ouyang, S., & Yu, M.-F. (2003). Mass Movements Caused by Recent Tectonic Activity: The 1999 Chi-chi Earthquake in Central Taiwan. *Island Arc*. Vol. 12, Issue 4, pp. 325–334. Wiley. <https://doi.org/10.1046/j.1440-1738.2003.00400.x>

- [82] Wang, W.-N., Nakamura, H., Tsuchiya, S., Wu, S.-C., & Ouyang, S. (2004). Occurrences and Displacements of Landslides by an Earthquake with a Subsequent Rain: the 1999 Chi-chi Earthquake in Central Taiwan. *Journal of the Japan Landslide Society*. Vol. 41, Issue 4, pp. 366–374. Japan Landslide Society. https://doi.org/10.3313/jls.41.4_366
- [83] Watabe, Y., & Nishimura, S. (2020). Ground Movements and Damage in Satozuka District, Sapporo Due to 2018 Hokkaido Eastern Iburi Earthquake. *Soils and Foundations*. Vol. 60, Issue 5, pp. 1331–1356. Elsevier BV. <https://doi.org/10.1016/j.sandf.2020.04.007>
- [84] Xu, Q., Zhang, S., Li, W. L., & van Asch, Th. W. J. (2012). The 13 August 2010 Catastrophic Debris Flows after the 2008 Wenchuan Earthquake, China. *Natural Hazards and Earth System Sciences*. Vol. 12, Issue 1, pp. 201–216. Copernicus GmbH. <https://doi.org/10.5194/nhess-12-201-2012>
- [85] Yang, Z., Lan, H., Liu, H., Li, L., Wu, Y., Meng, Y., & Xu, L. (2015). Post-Earthquake Rainfall-Triggered Slope Stability Analysis in the Lushan Area. *Journal of Mountain Science*. Vol. 12, Issue 1, pp. 232–242. Springer Science and Business Media LLC. <https://doi.org/10.1007/s11629-013-2839-6>
- [86] Zelikson, A. (1969). Geotechnical Models Using the Hydraulic Gradient Similarity Method. *Géotechnique*. Vol. 19, Issue 4, pp. 495–508. Thomas Telford Ltd. <https://doi.org/10.1680/geot.1969.19.4.495>
- [87] Zhang, Y., Tang, H., Li, C., Lu, G., Cai, Y., Zhang, J., & Tan, F. (2018). Design and Testing of a Flexible Inclinometer Probe for Model Tests of Landslide Deep Displacement Measurement. *Sensors*. Vol. 18, Issue 2, p. 224. MDPI AG. <https://doi.org/10.3390/s18010224>
- [88] Zhang, J., Li, X., Chi, M., Yang, H., & Liu, C. (2019). Study on the Failure Mechanism of Slope under Rainfall by Strength Reduction FEM. IACGE 2018. International Conference on Geotechnical and Earthquake Engineering 2018. American Society of Civil Engineers. <https://doi.org/10.1061/9780784482049.046>
- [89] Zhu, Y., Ishikawa, T., Siva Subramanian, S., & Luo, B. (2021). Early Warning System for Rainfall- and Snowmelt-Induced Slope Failure in Seasonally Cold Regions. *Soils and Foundations*. Vol. 61, Issue 1, pp. 198–217. Elsevier BV. <https://doi.org/10.1016/j.sandf.2020.11.009>
- [90] Zhuang, F., Qi, Z., Duan, K., Xi, D., Zhu, Y., Zhu, H., Xiong, H., & He, Q. (2019). A Comprehensive Survey on Transfer Learning (Version 3). arXiv. <https://doi.org/10.48550/ARXIV.1911.02685>
- [91] Zou, H., & Hastie, T. (2005). Regularization and Variable Selection Via the Elastic Net. *Journal of the Royal Statistical Society Series B: Statistical Methodology*. Vol. 67, Issue 2, pp. 301–320. Oxford University Press (OUP). <https://doi.org/10.1111/j.1467-9868.2005.00503.x>